



Dipl.-Ing. Matthias Peter Maria Gruber, BSc

**Entanglement Spreading
in Integrable Spin Chains
with Inhomogeneities**

DOCTORAL THESIS

to achieve the university degree of
Doktor der technischen Wissenschaften

submitted to

Graz University of Technology

Supervisor

Priv.-Doz. Dr. Viktor Eisler
Institute of Theoretical and Computational Physics

Graz, December 2020

AFFIDAVIT

I declare that I have authored this thesis independently, that I have not used other than the declared sources/resources, and that I have explicitly indicated all material which has been quoted either literally or by content from the sources used. The text document uploaded to TUGRAZonline is identical to the present doctoral thesis.

Date, Signature

to Mama, Papa and Nana

Abstract

In the present thesis, we study the entanglement spreading in nonequilibrium dynamics of spin-1/2 chains following different quantum quenches and local operator excitations. In the second chapter, we introduce the models considered and the methods applied throughout the thesis. On the numerical side, we work within the matrix product state (MPS) framework, applying density-matrix renormalization group (DMRG) methods. Our results are presented in three chapters.

In chapter 3, we apply generalized hydrodynamics (GHD) to study the magnetization profiles after the geometric quench in the XXZ chain. The entanglement entropy dynamics are investigated for both interacting and noninteracting (XX) cases. For the latter, we can put forward a heuristic conformal field theory (CFT) ansatz. Eventually, we find a proportionality between subsystem magnetization fluctuations and the entanglement entropy after the geometric quench.

In chapter 4, the entanglement negativity is studied which, unlike the entropy, allows to measure the entanglement of mixed states and thus between noncomplementary intervals. The quench setup is chosen such that two free-fermion half chains are connected via a defect, thus breaking the translational invariance of the Hamiltonian. After a quench from equal fillings, a logarithmic increase of the negativity is found and a proportionality between negativity and $1/2$ -Rényi mutual information holds true. For different initial fillings, like the domain wall quench, a linear increase of the entanglement is observed, followed by a saturation to an extensive value. We are able to describe this behaviour within a quasiparticle ansatz in which pairs of entangled quasiparticles are created at the defect.

In chapter 5, we study the entanglement entropy after local fermionic excitations in the XXZ spin chain. These are superpositions of low-energy excitations which can be described via Bethe ansatz techniques. At first, we study the fermionic creation operator in the gapless phase and observe entropy profiles which are well described by a probabilistic spinon ansatz. The profile maxima after a Majorana excitation depend on the anisotropy. This behaviour is understood qualitatively within a Luttinger liquid theory. In the gapless phase, a modified Majorana excitation is studied, that creates an antiferromagnetic domain wall. Here, the excess entropy profiles are found to have a multiplicative factor related to the ground state entropy.

Kurzfassung

Diese Dissertation behandelt die Ausbreitung von Quantenverschränkungen in der Nichtgleichgewichtsdynamik von Spin-1/2-Ketten nach verschiedenen Quenches sowie Anregungen durch lokale Operatoren. In Kapitel 2 stellen wir die behandelten Modelle sowie die verwendeten Methoden in dieser Arbeit vor. In unseren numerischen Simulationen verwenden wir Matrixproduktzustände (MPS) und die Dichtematrix-Renormierungsgruppe (DMRG). Unsere Resultate sind in 3 Kapitel unterteilt.

In Kapitel 3 wenden wir *generalized hydrodynamics* (GHD) an, um die Magnetisierungsprofile nach dem geometrischen Quench in einer XXZ-Kette zu beschreiben. Die Dynamik der Quantenverschränkungen wird sowohl in wechselwirkenden als auch in nicht-wechselwirkenden (XX) Systemen untersucht. Für Letztere präsentieren wir einen heuristischen konforme Feldtheorie (CFT) Ansatz. Schlussendlich zeigen wir eine Proportionalität zwischen den Magnetisierungsfluktuationen eines Subsystems und der Quantenverschränkung nach dem geometrischen Quench.

In Kapitel 4 wird die *entanglement negativity* behandelt, die, anders als die *entanglement entropy*, die Quantenverschränkung von gemischten Zuständen, und damit auch zwischen nichtkomplementären Intervallen, messen kann. Unser Setup ist so gewählt, dass wir zwei freie-Fermionen-Halbketten mittels eines Defekts verbinden, wodurch die Translationsinvarianz des Hamiltonoperators gebrochen wird. Für eine identische Füllung der Halbketten beobachtet man ein logarithmisches Ansteigen der *negativity*, weiters zeigt sich eine Proportionalität zwischen der *negativity* und der 1/2-Rényi *mutual information*. Für unterschiedliche Füllungen, zum Beispiel beim *domain wall quench*, zeigt sich ein linearer Anstieg der *negativity*, gefolgt von einem extensiven Wert. Dieses Verhalten können wir mittels eines Quasiteilchenansatzes beschreiben, in dem die verschränkten Quasiteilchenpaare am Defekt erzeugt werden.

In Kapitel 5 untersuchen wir die Quantenverschränkung nach Anregungen durch lokale, fermionische Operatoren in der XXZ-Spinkette. Wir konzentrieren uns auf niederenergetische Anregungen, die mittels Bethe-Ansatz-Methoden beschrieben werden können. Zuerst untersuchen wir den fermionischen Erzeugungsoperator im kritischen Regime, der gut durch einen probabilistischen Spinonenansatz beschrieben wird. Nach einer Majorana-Anregung sieht man, dass die Maxima der Profile von der Anisotropie abhängig sind, was wir auch innerhalb der Luttinger-

Flüssigkeits-Theorie erklären können. In der nicht-kritischen Phase untersuchen wir eine modifizierte Majorana-Anregung, die eine antiferromagnetische *domain wall* erzeugt. Die darauffolgende Quantenverschränkung weist einen multiplikativen Faktor auf, der mit der Grundzustandsverschränkung zusammenhängt.

I would not call that *one* but rather *the* characteristic trait of quantum mechanics, the one that enforces its entire departure from classical lines of thought. By the interaction the two representatives (or ψ -functions) have become entangled.

- *Erwin Schrödinger*

Contents

1	Introduction	3
2	Models and Methods	13
2.1	Basics	13
2.2	Models	15
2.3	Bethe ansatz	18
2.3.1	Thermodynamic Bethe ansatz	22
2.4	Generalized Hydrodynamics	25
2.5	Entanglement measures	30
2.5.1	Entanglement entropy	30
2.5.2	Entanglement negativity	32
2.5.3	Related quantities	35
2.6	CFT approach to entanglement	37
2.7	Quantum quenches	42
2.7.1	Global quench	43
2.7.2	Local quench	45
2.7.3	Inhomogeneous quenches	46
2.8	Matrix Product States	48
2.9	Density-Matrix Renormalization Group	54
2.9.1	iDMRG	55
2.9.2	DMRG	56
2.9.3	DMRG in the context of MPS	56
2.9.4	tDMRG	60

CONTENTS

3 Magnetization and entanglement ... (Phys. Rev. B 99, 174403 (2019))	63
3.1 Abstract	63
3.2 Model and setup	64
3.3 Magnetization Profiles	66
3.3.1 Generalized hydrodynamics	66
3.3.2 Numerical results	71
3.4 Entropy Profiles	74
3.4.1 XX chain	74
3.4.2 XXZ chain	76
3.5 Boundary Effects	79
3.5.1 XX chain	79
3.5.2 XXZ chain	81
3.6 Fluctuations vs. entropy	83
3.7 Conclusions	85
4 Time evolution of entanglement ... (J. Phys. A: Math. Theor. 53, 205301 (2020))	87
4.1 Abstract	87
4.2 Model and methods	88
4.2.1 Rényi entropy and mutual information	90
4.2.2 Entanglement negativity	91
4.3 Ground state entanglement	94
4.4 Quench from equal fillings	96
4.5 Quench from unequal fillings	99
4.5.1 Homogeneous chain	99
4.5.2 Chain with a defect	101
4.6 Quench in the XXZ chain with a defect	106
4.6.1 Negativity for matrix product states	107
4.6.2 Numerical results	109
4.7 Discussion	112
5 Entanglement spreading after local ... (arXiv:2010.02708 (2020))	115
5.1 Abstract	115
5.2 XXZ chain and low-energy excitations	116
5.3 Entanglement dynamics in the gapless phase	119

5.3.1	Entanglement spreading in the quasiparticle picture	120
5.3.2	Local fermionic excitation	121
5.3.3	Local Majorana excitation	124
5.4	Entanglement after local excitations in CFT	126
5.4.1	Fermionic excitation	129
5.4.2	Majorana excitation	131
5.5	Entanglement dynamics in the gapped phase	134
5.5.1	Magnetization profiles	139
5.6	Summary and discussion	142
6	Summary and conclusions	145
7	Acknowledgements	147
A	Appendix to Phys. Rev. B 99, 174403 (2019)	149
A.1	Perturbative calculation of the edge around ζ_{max}	149
B	Appendix to J. Phys. A: Math. Theor. 53, 205301 (2020)	153
B.1	Correlation matrices for the defect	153
B.2	CFT treatment of the domain wall quench	156
C	Appendix to arXiv:2010.02708 (2020)	161
C.1	Correlation functions of vertex operators	161

CONTENTS

List of Figures

2.1	Depiction of ρ_A in CFT	38
2.2	Three copies of ρ_A sewed together at zero temperature	38
2.3	Graphical depiction of an SVD.	48
2.4	Graphical depiction of $A_{\alpha_{i-1}, \alpha_i}^{\sigma_i}$	50
2.5	Graphical depiction of Eq. (2.8.14).	51
2.6	Contraction of the tensor network for the expectation value of a local operator \hat{O}	52
2.7	Graphical depiction of the DMRG algorithm.	57
2.8	Graphical depiction of $\langle \alpha_{i-1} \sigma_i \alpha_i \hat{H} \alpha'_{i-1} \sigma'_i \alpha'_i \rangle$	59
3.1	Setup of the geometric quench.	65
3.2	Dressed velocity $v(\lambda_*)$ for several values of Δ	68
3.3	Magnetization profiles $\langle S_x^z \rangle$ after the geometric quench as a function of $\zeta = x/t$, for various values of Δ	72
3.4	Edge profiles for $\Delta = -0.8$ and various times t , plotted against $\zeta = x/t$	73
3.5	Entropy profiles after the geometric quench for $t = 50$ and various system sizes.	77
3.6	Entanglement profiles for different values of Δ after the quench.	78
3.7	Comparison of the right edge of the entanglement profile for $\Delta = -0.8$ vs. $\Delta = 0.8$ and various times.	79
3.8	Magnetization and entanglement profiles after reflection of the wavefront from the boundaries.	80
3.9	Magnetization and entanglement profiles for $\Delta = 0.8$ and $\Delta = -0.5$, before and after the reflection of the front from the left boundary.	82

LIST OF FIGURES

3.10	Comparison between the magnetization fluctuations $\mathcal{F}(r)$ and the scaled entanglement entropy $S(r)$	84
4.1	Quench setup.	89
4.2	Comparison of the fits for c_{eff} to the analytical formula and the difference of \mathcal{E}_f and $\frac{1}{2}\mathcal{I}_{1/2}$	95
4.3	Time evolution of the logarithmic negativity \mathcal{E}_f after a quench from equal fillings and comparison of the fitted values of c'_{eff} to the ground-state effective central charge c_{eff}	98
4.4	Logarithmic negativity \mathcal{E}_f and mutual information $\frac{1}{2}\mathcal{I}_{1/2}$ after the domain wall quench in a homogeneous chain.	101
4.5	Entanglement negativity \mathcal{E}_f and mutual information $\frac{1}{2}\mathcal{I}_{1/2}$ after a quench from unequal fillings $n_l = 1$ and $n_r = 0$	102
4.6	Deviations of \mathcal{E}_f and $\frac{1}{2}\mathcal{I}_{1/2}$ from the semiclassical ansatz for $\lambda = 0.8$ and $\lambda = 0.5$	103
4.7	Steady-state negativity and mutual information, as calculated from the correlation matrix.	104
4.8	Entanglement negativity \mathcal{E}_f and mutual information $\frac{1}{2}\mathcal{I}_{1/2}$ after a quench from various unequal fillings.	105
4.9	Graphical representation of ρ_A , the transfer matrix E_1 and its singular value decomposition.	108
4.10	Time evolution of the entanglement negativity \mathcal{E}_s for two adjacent segments across a defect in an XX chain.	111
4.11	Time evolution of the entanglement negativity \mathcal{E}_s for two adjacent segments in an XXZ chain.	112
5.1	Excess entropy after the excitation c_1^\dagger in the gapless regime	123
5.2	Excess entropy after the Majorana excitation in the gapped regime	125
5.3	Entropy growth on the central bond after the Majorana excitation	126
5.4	Time evolution of the excess Rényi entropy in Eq. (5.4.27) after the Majorana excitation	132
5.5	Growth of the Rényi entropy ΔS_2 in CFT and tDMRG calculations	133
5.6	Entanglement growth in the middle of the chain after a domain-wall excitation \tilde{m}_1 in the gapless regime	135
5.7	Scaled levels ν_l obtained from the reduced density matrix eigenvalues λ_l at time $t = 100$ via Eq. (5.5.6) for different Δ	137

LIST OF FIGURES

5.8	Entropy profiles ΔS and ΔS_2 after a domain-wall excitation \tilde{m}_1 . .	138
5.9	Normalized magnetization profiles after a domain-wall excitation \tilde{m}_1 in the gapless regime	141
5.10	Energy difference due to the insertion of local operators m_1 and \tilde{m}_1	143
A.1	Rapidities λ_1 and λ_2 and the corresponding edge magnetization profile.	151

LIST OF FIGURES

Author's publications

This thesis is based upon three publications of the present author:

- **Gruber, M.** & Eisler, V. Magnetization and entanglement after a geometric quench in the XXZ chain. *Phys. Rev. B* **99**, 174403 (2019)
- **Gruber, M.** & Eisler, V. Time evolution of entanglement negativity across a defect. *J. Phys. A: Math. Theor.* **53**, 205301 (2020)
- **Gruber, M.** & Eisler, V. Entanglement spreading after local fermionic excitations in the XXZ chain. arXiv:2010.02708 (2020), submitted to *SciPost Phys.*

Chapter 1

Introduction

In 1935, Einstein, Podolsky and Rosen introduced their famous thought experiment which is now known as the EPR paradox [1]. The thought experiment deals with a pair of particles that has a “spooky” interaction as the measurement of a certain observable of the first particle allows the prediction of the measurement performed on the second, although those two particles are spatially separated. The apparent violation of locality led to the false conclusion that quantum mechanics were not complete. It was Erwin Schrödinger who later understood that these correlations were in fact the characteristic trait of quantum mechanics [2]. He brought up the term “Verschränkung” for it, which translates to entanglement. The two particles from the EPR paradox are nothing else but in an entangled state and can thus not be described without one another. What was back then considered spooky, is now a powerful resource with exciting applications. Quantum entanglement is key to technologies like quantum computation, quantum communication as well as quantum cryptography [3] and of crucial importance in the characterization of quantum many-body physics [4]. While entanglement is a powerful resource in quantum information theory, in quantum many-body physics it is typically connected to an increased computational effort needed to accurately represent the wavefunction.

Suppose that we have a system with an arbitrary bipartition A and B . The physics of subsystem A is fully encoded in the reduced density matrix ρ_A which is obtained by integrating out the remaining degrees of freedom in region B . For a pure, bipartite state, the entanglement can be measured with the von Neumann entropy [5]. The entropy is symmetric with respect to the bipartition and zero for

CHAPTER 1. INTRODUCTION

product states. If the system is in its ground state, the entanglement between A and B then typically follows the so-called area law [6]. The area law states that the entropy scales with the boundary area of the region A . Although also valid in higher dimensions, the area law is especially interesting in one dimension as here the boundary size between two intervals is independent of the interval length. In 1D, the area law was rigorously proven for local and gapped Hamiltonians [7]. Furthermore, it was also proven that the area law follows from an exponential decay of the correlations [8].

The area law is the basis of the success of matrix product states (MPS) [9] and the density-matrix renormalization group (DMRG) [10–12] in the classical simulation of quantum many-body ground states in one dimension. DMRG (see section 2.9 for details) is a variational method that allows very accurate ground state calculations in one-dimensional systems. It is intimately connected to MPS as a ground state obtained via DMRG assumes an MPS form [13, 14]. MPS, by construction, fulfill an area law and are discussed in detail in section 2.8.

The area law might be violated for long-range interactions [15] although it holds true for certain gapped long-range 1D models [16]. However, the area law is most prominently found to be violated for critical (gapless) lattice models [17, 18]. If the system is one-dimensional and at its critical point [19], the correlation length diverges and the system’s low-energy physics can be described by a $1 + 1$ D conformal field theory (CFT). In an infinite, one-dimensional system, one can show that at the critical point, the entanglement entropy of an interval of length ℓ is proportional to $\ln(\ell)$ [20]. In the non-critical regime, but close to the critical point, the entropy scales like $\ln(\xi)$, where ξ is the correlation length [18]. Remarkably, this behaviour of the entanglement entropy at and close to a quantum phase transition is universal. This means that to leading order, the results for various models only differ by the prefactor of the logarithmic growth, related to the central charge.

Until now, we have discussed the entanglement of ground states of one-dimensional systems which is limited by the area law in many cases. Exceptions include critical models in which a logarithmic divergence with the subsystem length ℓ is found. However, the entanglement drastically increases if we bring the system out of equilibrium. One typically observes a rapid growth of entanglement during time evolution which in turn massively restricts the simulability of the system.

The easiest way of studying such nonequilibrium dynamics is a quantum quench

[21]. In a global quench, a global parameter of the Hamiltonian, like a magnetic field, is changed instantaneously. After such a global quench, one finds that the entanglement entropy of an interval increases linearly in time and eventually reaches an extensive value for long times. This was proven within a CFT in [22], where Calabrese and Cardy also gave an intuitive, phenomenological explanation: Due to the high energy of the initial state with respect to the time evolution Hamiltonian, at $t = 0$ entangled quasiparticle pairs are created throughout the system with a certain production rate and then spread out ballistically. If two quasiparticles of a pair are located inside and outside the interval, respectively, they contribute to the entanglement of that interval. This, by construction, leads to a linear entropy increase in time which eventually saturates to an extensive value as both quasiparticles leave the interval. This picture was further developed in [23], where, after identifying the entropy production rate, a quasiparticle interpretation was proven for free-fermion systems, taking into consideration the energy dispersion that yields different quasiparticle velocities.

A more general scenario where the quasiparticle picture is expected to describe the nonequilibrium entanglement dynamics is in integrable systems. The integrability ensures that these quasiparticles have an infinite lifetime. Moreover, an extensive number of conserved quantities exists, which has a strong impact on the relaxation and transport properties after a quench. The dynamics of integrable quantum systems out of equilibrium has recently been a very active field of research [24, 25]. After bringing the state out of equilibrium, the relaxation towards a stationary state during time evolution is observed [26]. In a generic, isolated quantum system this stationary state is expected to be locally described by a Gibbs ensemble. However, integrable systems have an extensive number of conserved quantities. Thus, a local relaxation towards a generalized Gibbs ensemble (GGE) is expected [27, 28]. This GGE maximizes the entropy under the constraint of the non-trivial conserved quantities with the help of Lagrange multipliers which are fixed via the expectation values in the initial state [28].

Eventually, the quasiparticle description of entropy spreading after a global quench for noninteracting chains [23] was generalized to interacting integrable models. In [29], the extensive subsystem entropy at long times was connected to the thermodynamic entropy of a GGE. For shorter times, the entropy growth rate also contains the dressed quasiparticle velocities. For particular quench scenarios, these ingredients may be obtained within the Bethe ansatz framework, allowing accurate

predictions of the steady state entropy [30].

In a simple global quench, both initial state and time evolution Hamiltonian are homogeneous. Another class of quenches is characterized by an inhomogeneous initial state, where two homogeneous half chains with different initial states are joined. These states could correspond to different thermodynamic parameters such as temperature or chemical potential. The recently developed generalized Hydrodynamics (GHD) [31, 32] is a powerful tool to study nonequilibrium dynamics after such inhomogeneous initial states in integrable systems. The theory is based on both hydrodynamic principles as well as the thermodynamic Bethe ansatz (see [33] for a recent review). For long times and large distances from the inhomogeneity, one assumes that a local quasi-stationary state (LQSS) is obtained which is described by a GGE due to the integrability of the system. In this limit, one assumes a description based on fluid cells in which the entropy is locally maximized with respect to all conserved quantities. This means that the hydrodynamic continuity equations must be extended to non-trivial conserved charges. By considering continuity equations for charge and current densities in this LQSS, GHD is able to describe the occupation numbers of the quasiparticles for long times and large distances from the inhomogeneity. Those quasiparticles travel with an effective velocity due to elastic scattering effects.

GHD has been successfully applied to the XXZ model [34–40] as well as to the Hubbard [41] and the Lieb-Liniger model [42]. It was later extended to also capture diffusive corrections to the transport in integrable systems [43–45]. Very lately, some crucial conjectures in the GHD derivation, regarding the expectation values of the current operators in local equilibrium, were proven rigorously [46, 47]. Moreover, by combining GHD with the quasiparticle picture introduced above, the entanglement dynamics after various inhomogeneous quenches were calculated, finding again a linear entropy growth with time [48, 49].

Until now, we have only considered quenches followed by a linear growth of entropy. However, there are other quench scenarios which lead to a weaker, logarithmic increase of entropy. In a local quench, only a local parameter is changed by connecting two, initially separated, half chains in their ground states [50, 51]. The entropy after the connection of two half chains at criticality was found to grow logarithmically in time [50, 51]. Note that although a light-cone spreading with a maximal group velocity is observed, it remains unclear whether a quasiparticle description, analogous to the global quench, exists.

The connection of a completely filled half chain with an empty half chain is called a domain wall quench. This is the simplest case of an initial state that is not translationally invariant and produces a logarithmic entanglement growth in time for free-fermion systems [52, 53]. Another special example of an inhomogeneous initial state is the so-called geometric quench [54, 55] in which a half-filled chain in its ground state is connected to an empty half chain. A geometric quench corresponds to a sudden change of geometry of the system, i.e., the system size is changed. After that, a particle flow from the half-filled half chain into the vacuum of the second half chain, accompanied by a logarithmic increase of entropy, was observed [55]. However, the results obtained in [55] mainly focus on the XX chain, presenting only numerical data for the XXZ chain as GHD techniques were not yet available.

In order to better understand the interacting case, we revisited the geometric quench, applying GHD techniques in the gapless regime of the XXZ chain. The GHD formalism enables us to perfectly capture the magnetization profiles after the quench, finding that they depend qualitatively on the sign of the interaction strength. The numerical simulations were performed via the time-dependent DMRG (tDMRG) algorithm [56, 57]. Furthermore, we proposed a heuristic CFT ansatz for the entropy dynamics which captures the entanglement entropy in the noninteracting case, confirmed by calculations via correlation matrix techniques [58]. Although we do not find any obvious generalization to the interacting case, the numerical entropy profiles are qualitatively similar to the noninteracting case and the profile edges are determined by the front velocities as in the GHD formalism. We conclude our discussion by studying the fluctuations of the subsystem magnetization and their relation to the entanglement. A proportionality between these two quantities was found for ground states of XX [59–62] and XXZ [60] chains, involving the Luttinger parameter. We show that this proportionality between entropy and magnetization fluctuations also holds true in the nonequilibrium dynamics following a geometric quench: We find the same proportionality between the profiles, especially for repulsive interactions, whereas for attractive interactions, strong oscillations of the fluctuations complicate the comparison.

Up to now, we have considered cases where a homogeneous time evolution Hamiltonian is applied. A natural alteration of the setup is to consider an inhomogeneous Hamiltonian where the translational invariance is broken by inserting a hopping defect on the bond connecting two half chains. Such a defect in general destroys

the integrability of the system except for free-fermion chains in which hopping defects were studied in [59, 63–65]. For an unbiased quench across a defect, where the two half chains are initialized in their ground states at half filling, a logarithmic growth of entanglement was observed [64, 66]. The dynamics of the system completely change if a bias is applied by choosing different initial fillings for the two half chains. Due to this bias, a particle current will emerge, causing quasiparticles to be partially transmitted and reflected from the defect and leading to a linear increase of the entropy in time [64]. Although this behaviour reminds of the quasiparticle description after a global quench, the situation here is different as quasiparticles are created continuously in time and only at the defect.

We may now introduce a tripartite setting in which we measure the entanglement between two adjacent intervals $A_{1,2}$ which are located symmetrically around the defect, embedded in the environment B . This setup allows to study the difference in the entanglement behaviour after a global quench and the biased quench across a defect. In the former case, quasiparticle pairs are created throughout the chain and only at $t = 0$. Thus, the quasiparticles will eventually leave the finite intervals $A_{1,2}$, resulting in a decrease of entanglement [67, 68]. In contrast, for a biased quench across the defect, quasiparticles are created continuously at the defect. Hence, after a linear increase for shorter times, the entanglement will saturate and does not decrease again for long times.

Tracing out the environment B in a tripartite setup leads to a reduced density matrix ρ_A in a mixed state. Though, the von-Neumann entropy is only a proper measure of entanglement for bipartite, pure states. The negativity, however, can measure the entanglement of mixed states [69]. The negativity measures how much the spectrum of the partially transposed reduced density matrix $\rho_A^{T_1}$ fails to be positive via the trace norm. In the special case of fermionic Gaussian states, $\rho_A^{T_1}$ can be written as a linear combination of two Gaussian operators [70]. However, one can apply the partial time-reversal instead of the partial transposition which leads to a Gaussian operator [71]. This allows an alternative definition of fermionic negativity [72] which can be evaluated using covariance matrix techniques [73]. The negativity has been considered for global quenches [67, 68], for local quench scenarios [74, 75] as well as for initial states with a density or temperature bias [76–78].

We studied the entanglement negativity across a defect after joining two free-fermion half chains. The negativity is calculated between two adjacent intervals

of length ℓ , symmetrically surrounding the defect. In the ground state, the negativity grows like $\ln(\ell)$ with a prefactor which depends on the defect strength and is termed effective central charge c_{eff} . For an unbiased quench with equal fillings, we find a logarithmic increase in time of the entanglement negativity. The prefactor of the negativity growth is found to be almost the same as for the ground state calculations. In the case of a biased quench across a defect, the ansatz introduced above is applied where quasiparticle pairs are created at the defect. This ansatz accurately describes the negativity which at first increases linearly and then saturates to an extensive value. For different initial fillings other than the domain wall initial state, the generalization of the quasiparticle ansatz is straightforward and the behaviour is qualitatively the same. Finally, we study the unbiased quench for an XXZ chain, as the interacting case is computationally much more demanding [79]. We find an entropy behaviour that is, up to a rescaling of the Fermi velocities, similar to the case of a free-fermion chain.

Interestingly, the negativity was found to be proportional to the $\alpha = 1/2$ Rényi mutual information after a global quench [67]. For the ground state of a free-fermion chain with a defect at the center, we find that the same relation holds true for large interval lengths ℓ . For an unbiased quench with equal fillings, this proportionality still holds true. However, if we consider the biased quench across a defect, the difference between the subleading corrections for the entanglement negativity and the mutual information stays finite in the steady state, even for large interval lengths.

Until now, we have discussed entanglement dynamics following quantum quenches. However, nonequilibrium dynamics can also be induced due to the insertion of local operators. The research on local operator insertions was initiated within a CFT context [80–82]: The initial state is excited from the vacuum of the CFT by the insertion of a local primary operator and it was found that the excess entropy obtains a constant value, depending on the quantum dimension of the local primary. The entropy of a segment is only increased by the linearly propagating excitations when they are passing through said segment. The entanglement spreading after local operator excitations has been studied for fermionic fields [83], descendant fields [84, 85], multiple excitations [86] and for finite temperatures [87] within a CFT whereas only few results on local-operator excitations in integrable spin chains exist. These results only cover free-fermion models like the Ising chain [88], the XX chain [89] as well as XY chains [90, 91]. In contrast to CFT, one here

has to decompose the local excitations into quasiparticles, spreading with different velocities. In XY chains, the excess entropy after a domain wall quench, induced by a local fermionic excitation, was described by a simple probabilistic quasiparticle ansatz [90, 91]. For a bipartition, the density ratio \mathcal{N} counts the quasiparticle excitations that have reached the entangling point. \mathcal{N} can be interpreted as the probability of the initial local excitation reaching this point. The excess entropy due to the quench can be calculated via the binary entropy function involving \mathcal{N} [91].

Up to now, only local-operator excitations in noninteracting spin chains have been considered. We studied the entanglement spreading after the insertion of different local fermionic operators in both the gapless and the antiferromagnetic gapped phase of the XXZ chain. At first, a fermionic creation operator is considered, after which the entanglement is well described for moderate interactions by the quasiparticle ansatz discussed just above, considering only the lowest-lying spinons. Spinons are low-energy excitations above the ground state that follow from the Bethe ansatz [92]. The agreement is good for a moderate interaction strength, for larger interactions, the profiles become more complicated as also higher-energy excitations, in particular particle-hole excitations for attractive interactions, contribute. These excitations have a larger group velocity than spinons and thus determine the edge position of the entanglement profile.

The profiles after a local Majorana excitation show a qualitatively very similar behaviour but the ansatz has to be rescaled to match the profile maxima. In order to understand the difference, we studied the dependence of the Rényi entropies on the anisotropy Δ in a Luttinger liquid theory, which describes the low-energy physics of the XXZ chain. Our CFT results show a good qualitative agreement with the Δ -dependent excess entropy from the tDMRG calculations for short times. For the asymptotic excess entropy however, the Δ -independent result $\ln(2)$ is found after a fermionic creation operator excitation, which is doubled in the case of a Majorana excitation for $\Delta \neq 0$ due to the left-right mixing of the chiral bosonic modes. Finally, we studied a modified Majorana excitation in the gapped phase which excites an antiferromagnetic domain wall. We propose an ansatz for the asymptotic entropy which has a nontrivial, multiplicative factor that depends on the ground state entropy.

This doctoral thesis is structured as follows: Chapter 2 introduces the models and methods applied in this thesis. At first, some basic concepts and the models

considered are introduced. We then discuss the Bethe ansatz framework as well as the GHD formalism. Furthermore, we introduce the entanglement measures Rényi entropy as well as logarithmic negativity and present a CFT approach to calculate them. We then discuss the nonequilibrium entanglement dynamics following different quantum quenches. Finally, we introduce the numerical tools applied throughout the thesis, namely MPS as well as DMRG. In chapter 3, we discuss the magnetization and entanglement dynamics following a geometric quench in the XXZ chain. The entanglement negativity dynamics after quantum quenches across a defect are studied in chapter 4. Finally, in chapter 5, the entanglement spreading after different local fermionic operator insertions is presented. We conclude the thesis with a summary of the presented results in chapter 6.

CHAPTER 1. INTRODUCTION

Chapter 2

Models and Methods

2.1 Basics

This section introduces the basic concepts that are needed throughout the whole thesis. We are going to consider one-dimensional spin-1/2 chains. On each site j of the chain, the operators S^x , S^y and S^z are defined as¹

$$S^x = \frac{1}{2} \begin{pmatrix} 0 & 1 \\ 1 & 0 \end{pmatrix} \quad S^y = \frac{1}{2} \begin{pmatrix} 0 & -i \\ i & 0 \end{pmatrix} \quad S^z = \frac{1}{2} \begin{pmatrix} 1 & 0 \\ 0 & -1 \end{pmatrix}. \quad (2.1.1)$$

The local Hilbert space on each site is then spanned by the two eigenvectors of the S^z operator:

$$\begin{aligned} S^z |\uparrow\rangle &= \frac{1}{2} |\uparrow\rangle \\ S^z |\downarrow\rangle &= -\frac{1}{2} |\downarrow\rangle. \end{aligned} \quad (2.1.2)$$

Thus, the local Hilbert space dimension on each spin-1/2 site is 2. It is convenient to define the ladder operators $S^\pm = S^x \pm iS^y$. Applying the ladder operators on the basis states gives

$$\begin{aligned} S^+ |\uparrow\rangle &= 0, & S^+ |\downarrow\rangle &= |\uparrow\rangle, \\ S^- |\uparrow\rangle &= |\downarrow\rangle, & S^- |\downarrow\rangle &= 0. \end{aligned} \quad (2.1.3)$$

¹In this thesis, we are using the convention $\hbar = 1$.

Basics

The matrices we have just introduced are related to the Pauli matrices as

$$S_j^\alpha = \frac{\sigma_j^\alpha}{2}. \quad (2.1.4)$$

As the local Hilbert space dimension on each site is 2, a spin-1/2 chain of length L has Hilbert space dimension

$$\dim(\mathcal{H}) = 2^L. \quad (2.1.5)$$

The spin on each site $|\sigma_j\rangle$ can either have the value $|\uparrow\rangle$ or $|\downarrow\rangle$. A state defined on the full chain, written in the S^z basis, thus has the form

$$|\sigma_1\rangle \otimes |\sigma_2\rangle \otimes \cdots \otimes |\sigma_L\rangle \equiv |\sigma_1\sigma_2\dots\sigma_L\rangle := |\boldsymbol{\sigma}\rangle. \quad (2.1.6)$$

Eventually, we can write an arbitrary state on the spin chain as a linear combination of the basis vectors

$$|\psi\rangle = \sum_{\boldsymbol{\sigma}} c_{\boldsymbol{\sigma}} |\boldsymbol{\sigma}\rangle, \quad (2.1.7)$$

where the 2^L coefficients $c_{\boldsymbol{\sigma}}$ determine the state. Having defined a state $|\psi\rangle$, the corresponding density matrix is given by

$$\rho = |\psi\rangle \langle\psi|. \quad (2.1.8)$$

The density matrix ρ has only real, non-negative eigenvalues and fulfills

$$\text{Tr}(\rho) = 1. \quad (2.1.9)$$

Usually, one is only interested in an observable supported on a finite subsystem. Let us denote the region of interest by A whereas the rest of the system is $B = \bar{A}$. The reduced density matrix of the subsystem A is then given by

$$\rho_A = \text{Tr}_B(\rho). \quad (2.1.10)$$

The physics of the subsystem A is fully encoded in the reduced density matrix ρ_A . Using ρ_A , one can determine all the correlation functions which are local within A . For an operator which is the product of local operators, $\hat{O} = \prod_j \hat{O}(x_j)$ with $x_j \in A$, the expectation value is given by

$$\langle\psi| \hat{O} |\psi\rangle = \text{Tr}(\rho_A \hat{O}). \quad (2.1.11)$$

2.2 Models

This section introduces the spin chain models considered in this thesis, following the books by Takahashi [92] and Franchini [93]. The XXZ spin chain is an integrable model that describes one-dimensional, magnetic materials with an anisotropy along the z-axis. It is exactly solvable applying Bethe ansatz techniques as discussed in Sec. 2.3. During time evolution, the total magnetization in z-direction is conserved. Furthermore, the flipping of all the spins is a symmetry of the Hamiltonian. In our studies, we are mainly interested in the ground state of the zero-magnetization sector $S^z = 0$. The XXZ Hamiltonian for open boundary conditions is given by

$$\hat{H}_{XXZ} = J \sum_{j=1}^{L-1} (S_j^x S_{j+1}^x + S_j^y S_{j+1}^y + \Delta S_j^z S_{j+1}^z), \quad (2.2.1)$$

where S_j^α are spin-1/2 operators acting on site j and Δ the anisotropy parameter. The coupling parameter J determines the energy scale and is set to $J = 1$. This Hamiltonian can be rewritten in terms of the ladder operators by using

$$S_j^x S_{j+1}^x + S_j^y S_{j+1}^y = \frac{1}{2} (S_j^+ S_{j+1}^- + S_j^- S_{j+1}^+). \quad (2.2.2)$$

The XXZ model is actually equivalent to a chain of spinless fermions with nearest-neighbor interactions of strength Δ , where $\Delta = 0$ corresponds to the free-fermion point. Applying a Jordan-Wigner transformation

$$\sigma_j^+ = \prod_{l=1}^{j-1} (1 - 2c_l^\dagger c_l) c_j^\dagger \quad \sigma_j^- = \prod_{l=1}^{j-1} (1 - 2c_l^\dagger c_l) c_j, \quad (2.2.3)$$

one can bring the Hamiltonian (2.2.1) into the form

$$\hat{H}_{XXZ} = \sum_{j=1}^{L-1} \left[-\frac{1}{2} (c_j^\dagger c_{j+1} + c_{j+1}^\dagger c_j) + \Delta \left(c_j^\dagger c_j - \frac{1}{2} \right) \left(c_{j+1}^\dagger c_{j+1} - \frac{1}{2} \right) \right], \quad (2.2.4)$$

where c_j^\dagger (c_j) are fermionic creation (annihilation) operators, satisfying anticommutation relations $\{c_i, c_j^\dagger\} = \delta_{ij}$.

Models

Δ sets the anisotropy along the z -axis: For $|\Delta| < 1$, a gapless paramagnet is obtained in the ground state. This gapless phase can be described by a Luttinger liquid theory [166]. The ground state has zero magnetization and can be considered a spinon vacuum. From this vacuum, low-energy excitations called spinons can be excited. For $\Delta = 1$, an isotropic ferromagnet with a gapless spectrum is obtained.

The Hamiltonian describes an antiferromagnet along the z -direction for $\Delta > 1$ and a ferromagnet for $\Delta < -1$. Both the ferromagnetic and the antiferromagnetic regime are gapped. In the limit $\Delta \rightarrow -\infty$, the ground state of the XXZ chain in the ferromagnetic regime is given by the fully polarized states

$$|\uparrow\rangle = |\uparrow\uparrow \dots \uparrow\rangle \text{ and } |\downarrow\rangle = |\downarrow\downarrow \dots \downarrow\rangle \quad (2.2.5)$$

as a parallel ordering of neighboring spins is energetically favoured. In contrast, in the antiferromagnetic limit $\Delta \rightarrow \infty$, an anti-parallel ordering is favoured, leading to a linear combination of the so-called Nèel states as ground states

$$|\psi_{\pm}\rangle = \frac{|\uparrow\downarrow\uparrow\downarrow \dots\rangle \pm |\downarrow\uparrow\downarrow\uparrow \dots\rangle}{\sqrt{2}}. \quad (2.2.6)$$

In the antiferromagnetic regime of a finite chain, the ground state shows an Ising-like structure and is almost degenerate with an energy difference decaying exponentially in the system size L . Note that for odd L , the two ground states with $S^z = \pm 1/2$ become exactly degenerate also for finite L . Taking the thermodynamic limit, the two ground states are given by

$$|\psi_{\pm}\rangle = \frac{|\psi_{\uparrow}\rangle \pm |\psi_{\downarrow}\rangle}{\sqrt{2}}, \quad (2.2.7)$$

with $|\psi_{\uparrow}\rangle$ and $|\psi_{\downarrow}\rangle$ being the ground states with spontaneously broken symmetry. The bulk expectation value of the staggered magnetization can be obtained as [94, 95]

$$\langle\psi_{\uparrow}|\sigma_j^z|\psi_{\uparrow}\rangle = -\langle\psi_{\downarrow}|\sigma_j^z|\psi_{\downarrow}\rangle = (-1)^j \prod_{n=1}^{\infty} \tanh^2(n\phi), \quad (2.2.8)$$

using the standard parametrization $\Delta = \cosh(\phi)$. As one can see, in the thermodynamic limit, the XXZ chain in the antiferromagnetic ground state comprises a structure where the expectation value $\langle\sigma_j^z\rangle$ alternates with a Δ -dependent magnetization.

For $\Delta = 0$, one obtains the XX chain. The XX chain and the XXZ chain are both described by a Luttinger liquid theory. The Hamiltonian of the XX chain is given by

$$\hat{H}_{XX} = J \sum_{j=1}^{L-1} (S_j^x S_{j+1}^x + S_j^y S_{j+1}^y) . \quad (2.2.9)$$

We now map the spin-1/2 operators onto spinless fermions c_j by performing a Jordan-Wigner transformation. The resulting Hamiltonian is the $\Delta = 0$ case of Eq. (2.2.4) and represents a hopping chain. For the sake of simplicity, we impose periodic boundary conditions on that hopping chain which allows to diagonalize it via a simple Fourier transform as

$$c_j^\dagger = \frac{1}{\sqrt{L}} \sum_k e^{-iq_k j} c_k^\dagger \quad c_j = \frac{1}{\sqrt{L}} \sum_k e^{iq_k j} c_k , \quad (2.2.10)$$

where $q_k = \frac{2\pi}{L}k$. This eventually leads to the diagonalized form of the XX chain

$$H = \sum_k \omega(k) c_k^\dagger c_k \quad (2.2.11)$$

with the dispersion relation $\omega(k) = -\cos(q_k)$. The ground state is the state with the lowest energy and all the particles are independent of each other. Thus, the ground state is simply given by the state in which all the q_k for which $\omega(q_k)$ is negative are occupied. Thus, all modes in the interval $[-\pi/2, \pi/2]$ are occupied. This interval is called the Fermi sea and $q_F = \pi/2$ is the so-called Fermi wave number.

2.3 Bethe ansatz

This section gives a brief overview of the Bethe ansatz [96] solution of the XXZ chain following [92, 93]. The Bethe ansatz allows us to study both the ground state as well as the excitations of the XXZ chain. We start our discussion with the fully polarized state

$$|\uparrow\rangle = |\uparrow\uparrow \dots \uparrow\rangle. \quad (2.3.1)$$

This state is an eigenstate of the XXZ Hamiltonian in a chain of length L with periodic boundary conditions:

$$H|\uparrow\rangle = E_0|\uparrow\rangle, \quad E_0 = \frac{J\Delta}{4}L. \quad (2.3.2)$$

Starting from the fully polarized state, we are now constructing states by turning certain spins over. If we flip the spin on site n_j , this is denoted as

$$|n_j\rangle = S_{n_j}^- |\uparrow\rangle. \quad (2.3.3)$$

An arbitrary state with R overturned spins can then be written as

$$|\psi_R\rangle = \sum_{\{n_i\}} f(n_1, n_2, \dots, n_R) |n_1, n_2, \dots, n_R\rangle, \quad (2.3.4)$$

where

$$|n_1, n_2, \dots, n_R\rangle = S_{n_1}^- S_{n_2}^- \dots S_{n_R}^- |\uparrow\rangle. \quad (2.3.5)$$

For $f(n_1, n_2, \dots, n_R)$, a superposition of plane waves is taken as

$$f(n_1, n_2, \dots, n_R) = \Omega_R \sum_{\mathcal{P}}^{R!} e^{i \sum_{j=1}^R k_{\mathcal{P}j} n_j + \frac{i}{2} \sum_{j<l}^R \tilde{\Theta}(k_{\mathcal{P}j}, k_{\mathcal{P}l})}, \quad (2.3.6)$$

where Ω_R ist the normalization, \mathcal{P} denotes the permutation of the quasimomenta k_j and $\tilde{\Theta}(k_j, k_l) = \Theta(k_j, k_l) + \pi$. The ansatz $|\psi_R\rangle$ is then inserted into the Schrödinger equation, leading to the eigenvalue equation

$$\begin{aligned} (H - E)\psi = & -\frac{J}{2} \sum_{j=1}^R (1 - \delta_{n_j+1, n_{j+1}}) [f(n_1, \dots, n_j + 1, n_{j+1}, \dots, n_R) + \\ & f(n_1, \dots, n_j, n_{j+1} - 1, \dots, n_R)] + \\ & \left[E_0 - E + J\Delta R - J\Delta \sum_{j=1}^R \delta_{n_j+1, n_{j+1}} \right] f(n_1, n_2, \dots, n_R) = 0. \end{aligned} \quad (2.3.7)$$

Inserting the ansatz Eq. (2.3.6) into Eq. (2.3.7), eventually fixes the scattering phase $\Theta(k_j, k_l)$ as

$$e^{i\Theta(k_j, k_l)} = \frac{e^{i(k_j+k_l)} + 1 - 2\Delta e^{ik_j}}{e^{i(k_j+k_l)} + 1 - 2\Delta e^{ik_l}}. \quad (2.3.8)$$

Imposing periodic boundary conditions gives the quantization relations

$$e^{ik_j L} = \prod_{j \neq l} e^{i\tilde{\Theta}(k_j, k_l)} = (-1)^{R-1} \prod_{j \neq l} \frac{e^{i(k_j+k_l)} + 1 - 2\Delta e^{ik_j}}{e^{i(k_j+k_l)} + 1 - 2\Delta e^{ik_l}}. \quad (2.3.9)$$

Taking the logarithm of Eq. (2.3.9), one finally obtains the Bethe equations as

$$\boxed{k_j L = 2\pi I_j - \sum_{l=1}^R \Theta(k_j, k_l), \quad j = 1, \dots, R}. \quad (2.3.10)$$

Here, the I_j with $j = 1, \dots, R$ are the quantum numbers that determine the state. One now parametrizes the quantization relations with the rapidities and takes the logarithm to end up with modified Bethe equations. The parametrization of the rapidities is chosen in a clever way such that the Bethe equations obtain a form in which they only depend on the difference of rapidities. In the gapped phase this parametrization is given by

$$e^{ik_j} = \pm \frac{\sin(\phi/2(\lambda_j + i))}{\sin(\phi/2(\lambda_j - i))} \quad (2.3.11)$$

where $+$ corresponds to the case $\Delta = \cosh(\phi) > 1$ and $-$ to the case $\Delta = -\cosh(\phi) < 1$. In the gapless regime, we have the parametrization $\Delta = \cos(\gamma)$ and the rapidities are defined by

$$e^{ik_j} = -\frac{\sinh(\gamma/2(\lambda_j + i))}{\sinh(\gamma/2(\lambda_j - i))}. \quad (2.3.12)$$

Both Eq. (2.3.11) and (2.3.12) may lead to complex solutions of the Bethe equations which correspond to bound states. The string hypothesis states that in the thermodynamic limit $L \rightarrow \infty$, those complex solutions can be grouped in strings in which all solutions have the same real part and equidistant imaginary parts, called complexes. A single real solution is a 0-complex, a pair of complex solutions with equidistant imaginary parts is called a 1/2-complex, 2 imaginary and one real

Bethe ansatz

solutions are called 1-complex and so on.

In the ferromagnetic regime $\Delta < -1$, the ground state is given by the fully polarized state

$$|\uparrow\rangle = |\uparrow\uparrow \dots \uparrow\rangle. \quad (2.3.13)$$

It is assumed that each of the solutions of the Bethe equations (2.3.10) belongs to an M -type complex of rapidities

$$\lambda_{M,j} = \lambda_M + i2(M-j)\phi, \quad j = 0, \dots, 2M, \quad (2.3.14)$$

where $\lambda_M \in [-\pi, \pi]$ and arbitrary string lengths are allowed. Each complex constitutes an elementary excitation of a bound state of $2M+1$ magnons. The dispersion relation of such an excitation is then given by

$$\varepsilon_M(p_M) = \frac{\sinh(\phi)}{\sinh((2M+1)\phi)} [\cosh((2M+1)\phi) - \cos(p_M)]. \quad (2.3.15)$$

Note that these excitations are gapped.

In the antiferromagnetic regime $\Delta > 1$, the true ground state has zero magnetization as $R = L/2$ spins have been turned over. In this ground state, all rapidities are real and fill the Fermi sea. The ground-state density $\rho_0(\lambda)$ is given by

$$\rho_0(\lambda) = \frac{K(u)}{2\pi Q} \operatorname{dn} \left(\frac{K(u)\lambda}{Q}, u \right), \quad (2.3.16)$$

where $\operatorname{dn}(\lambda, u)$ is a Jacobian elliptic function. We have used the complete elliptic integral of the first kind

$$K(u) = \int_0^{\pi/2} \frac{dp}{\sqrt{1 - u^2 \sin^2(p)}} \quad (2.3.17)$$

which allows us to define the elliptic modulus u as

$$\frac{\phi}{\pi} = \frac{1}{Q} = \frac{K(\sqrt{1-u^2})}{K(u)}. \quad (2.3.18)$$

For a spinon excitation, two holes are created and $R = L/2 - 1$. Using the transformation as introduced in (2.3.11), one can write the condition (2.3.9) using the rapidities as

$$L\theta_1(\lambda_j, \phi) = 2\pi I_j + \sum_{l=1}^R \theta_2(\lambda_j - \lambda_l, \phi) \quad (2.3.19)$$

which is a different form of the Bethe equations (2.3.10) which now only depends on the difference of rapidities $\lambda_j - \lambda_l$. $\theta_n(\lambda, \phi)$ is defined as

$$\theta_n(\lambda, \phi) = 2 \tan^{-1} \left(\frac{\tan(\phi\lambda/2)}{\tanh(n\phi/2)} \right) + 2\pi \left[\frac{\phi\lambda + \pi}{2\pi} \right]. \quad (2.3.20)$$

Taking the thermodynamic limit and performing a Fourier transform, one eventually obtains the energy difference due to the excitation as

$$\Delta E = \varepsilon_s(q_r) + \varepsilon_s(q_s), \quad (2.3.21)$$

where the spinons have momenta

$$q_r = \frac{2\pi r}{L} = 2\pi \int_{\lambda_r}^{\pi/\phi} \rho_0(\lambda) d\lambda, \quad (2.3.22)$$

where $\phi = \text{acosh}(\Delta)$ and $\rho_0(\lambda)$ is the ground-state density as defined in Eq. (2.3.16). The total momentum of the excitation is given by $q_r + q_s + \pi$. The energy dispersion of such a spinon in the gapped, antiferromagnetic phase is given by

$$\varepsilon_s(q) = \frac{\sinh(\phi)}{\pi} K(u) \sqrt{1 - u^2 \cos^2(q)}. \quad (2.3.23)$$

Finally, we want to consider the paramagnetic, gapless phase $|\Delta| < 1$. In the ground state of the gapless regime, all rapidities λ_j are real, defined on the interval $-\infty < \lambda < \infty$, and fill the Fermi sea. In the thermodynamic limit of Eq. (2.3.10), the rapidity density is defined implicitly by the integral equation

$$\rho(\lambda) + \int_{-\infty}^{\infty} \frac{d\mu}{2\pi} \mathcal{K}(\lambda - \mu) \rho(\mu) = \frac{\theta'_1(\lambda)}{2\pi} \quad (2.3.24)$$

with the differential scattering phase $\mathcal{K}(\lambda) = \theta'_2(\lambda)$ being defined through

$$\theta'_n(\lambda) = \frac{\sin(n\gamma)}{\cosh(\lambda) - \cos(n\gamma)}. \quad (2.3.25)$$

Starting from the ground state, we can now create excitations by removing rapidities. Those low-energy excitations are called spinons and they are created

Bethe ansatz

by removing one rapidity from the ground state which creates two holes. The dispersion relation of a single spinon in the gapless phase is given by

$$\varepsilon_s(q) = \frac{\pi \sin(\gamma)}{2\gamma} \sin(q), \quad (2.3.26)$$

using the standard parametrization $\Delta = \cos(\gamma)$. The total energy difference for a spinon excitation is again given by Eq. (2.3.21) as spinons are always excited in pairs. The total momentum of the excitation is then given by $q_r + q_s$ where $0 \leq q_{r,s} \leq \pi$. The group velocity of each spinon is derived from Eq. (2.3.26) as

$$\frac{d\varepsilon_s(q)}{dq} = \frac{\pi \sin(\gamma)}{2\gamma} \cos(q). \quad (2.3.27)$$

Furthermore, a particle-hole excitation can be created by removing a rapidity from the real axis and placing it on the imaginary axis. Just like the spinon excitation, this is also a low-energy excitation with $S^z = 1$. The dispersion relation of a particle hole excitation is given by

$$\varepsilon_{ph}(q) = \pi \frac{\sin(\gamma)}{\gamma} \left| \sin\left(\frac{q}{2}\right) \right| \sqrt{1 + \cot^2\left(\frac{\pi}{2}\left(\frac{\pi}{\gamma} - 1\right)\right) \sin^2\left(\frac{q}{2}\right)}. \quad (2.3.28)$$

Note that these excitations are only physical for $-1 < \Delta < 0$ and that $0 \leq q \leq 2\pi$ as this is not a composite excitation.

2.3.1 Thermodynamic Bethe ansatz

In this section, we are going to give a brief overview of the Thermodynamic Bethe Ansatz (TBA) in the gapless regime, following [32, 92]. This formalism enables us to study the thermodynamics of the XXZ model.

In the thermodynamic limit, according to the string hypothesis, one obtains

$$\lambda_j \rightarrow \lambda_\alpha^k + i(n_k + 1 - 2a) + i \frac{\pi(1 - v_k)}{2\gamma}. \quad (2.3.29)$$

Here, k sums over the N_s different kinds of excitation species and α indexes the strings of a species. n_k denotes the length of the corresponding string, a sums over

the rapidities of the string and $v_k = \pm 1$ denotes the parity of the string. Those string solutions fulfill the Bethe-Gaudin-Takahashi equations

$$L\theta_j(\lambda_\alpha^j) - \sum_{k=1}^{N_s} \sum_{\beta=1}^{M_k} \Theta_{jk}(\lambda_\alpha^j - \lambda_\beta^k) = 2\pi I_\alpha^j, \quad (2.3.30)$$

where

$$\theta_j = 2v_j \operatorname{atan} \left[(\tan(n_j \gamma / 2))^{-v_j} \tanh(\gamma \lambda / 2) \right] \equiv \theta_j^{v_j}(\lambda) \quad (2.3.31)$$

and

$$\begin{aligned} \Theta_{jk}(\lambda) = & (1 - \delta_{n_j, n_k}) \theta_{|n_j - n_k|}^{v_j v_k}(\lambda) + 2\theta_{|n_j - n_k| + 2}^{v_j v_k}(\lambda) + \dots + \\ & 2\theta_{n_j + n_k - 2}^{v_j v_k}(\lambda) + \theta_{n_j + n_k}^{v_j v_k}(\lambda). \end{aligned} \quad (2.3.32)$$

A given solution of the Bethe equations is determined by the corresponding set of integers I_α^j . In the thermodynamic limit, the rapidities become dense and via the counting functions, one can establish a relation between the I_α^j and the corresponding rapidities λ_α^j . Those rapidities are called occupied, whereas the remaining rapidities $\bar{\lambda}_j$ are called empty. Occupied and empty rapidities correspond to particles and holes. One can then define the so-called root densities

$$\rho_j(\lambda_\alpha^j) = \lim_{L \rightarrow \infty} \frac{1}{L |\lambda_{\alpha+1}^j - \lambda_\alpha^j|} \quad \rho_j^h(\bar{\lambda}_\alpha^j) = \lim_{L \rightarrow \infty} \frac{1}{L |\bar{\lambda}_{\alpha+1}^j - \bar{\lambda}_\alpha^j|} \quad (2.3.33)$$

which describe the particle density $\rho_j(\lambda_\alpha^j)$ and the hole density $\rho_j^h(\bar{\lambda}_\alpha^j)$. In the thermodynamic limit, the Bethe-Gaudin-Takahashi equations can be reformulated as the TBA equations

$$a_j(\lambda) = \sigma_j [\rho_j(\lambda) + \rho_j^h(\lambda)] + \sum_k \int_{-\infty}^{\infty} d\mu T_{jk}(\lambda - \mu) \rho_k(\mu) \quad (2.3.34)$$

where

$$a_j(\lambda) \equiv \frac{1}{2\pi} \frac{d}{d\lambda} \theta_j(\lambda), \quad T_{jk} \equiv \frac{1}{2\pi} \frac{d}{d\lambda} \Theta_{jk}(\lambda). \quad (2.3.35)$$

$\sigma_j = \operatorname{sgn}(q_j)$ is nothing but a sign factor, depending on the v_i . One can show that the number of quasiparticle species is finite when γ is a rational multiple of π . More exactly, at the so-called roots of unity points, one can find the continued fraction representation

$$\gamma = \frac{\pi}{\nu_1 + \frac{1}{\nu_2 + \frac{1}{\nu_3 + \dots}}} \quad (2.3.36)$$

Bethe ansatz

in which case the number of excitation species is given by $N_s = \sum_k \nu_k$. These relations were first introduced by Takahashi and later derived from the normalizability condition for $L \rightarrow \infty$.

The distributions ρ_j are normalized by the total number of particles, leading to

$$\frac{R}{L} = L^{-1} \sum_{\beta,j} 1 \quad (2.3.37)$$

which in the thermodynamic limit $L \rightarrow \infty$ gives

$$\sum_j \int \rho_j(\lambda) n_j d\lambda = \frac{1}{2} - \langle \rho | S^z | \rho \rangle , \quad (2.3.38)$$

where $|\rho\rangle$ is a Bethe ansatz state. Analogously, we obtain [32]

$$\langle \rho | \mathbf{q} | \rho \rangle = \sum_j \int d\lambda q_j(\lambda) \rho_j(\lambda) \quad (2.3.39)$$

where $q_j(\lambda)$ is the single particle eigenvalue of the charge \mathbf{q} , corresponding to a conserved quantity in the XXZ model. Using the TBA formalism just introduced, we can now apply them in the GHD framework discussed in the following subsection. For the sake of simplicity, we will only consider one kind of quasiparticle in the following.

2.4 Generalized Hydrodynamics

This section is an introduction to the concept of generalized hydrodynamics (GHD) which was introduced in [31] and [32]. The introduction of GHD massively improved the understanding of the time evolution of integrable models with inhomogeneities. GHD can be understood as an extension of hydrodynamics to integrable systems with help of the Bethe ansatz in which the dynamics of quasiparticle excitations are described on a hydrodynamic scale. These excitations are moving freely in interacting integrable systems but experience phase shifts when scattering on other quasiparticles. One then makes the assumption that for very large times t and large distances x from the inhomogeneity, a dynamical equilibrium emerges so that the system can be described by a local quasi-stationary state (LQSS). In the case of two homogeneous states being joined at the inhomogeneity, this LQSS is a function of the ray variable $\zeta = \frac{x}{t}$ only. In [31], GHD is introduced by choosing a classical approach starting from the continuity equation of the conserved quantities of the integrable system. In [32], Bethe ansatz solutions are the starting point which are applied to describe the charge carried by the quasiparticles in the LQSS. However, the final result is the same for both approaches.

For an extensive overview of GHD and hydrodynamics, see the review by Doyon [33]. In recent years, a lot of research was done within the field of GHD. This research includes the description of several models including the Lieb-Lininger model [97], soliton gases [42], the Hubbard model [41] and the XXZ chain [34–40]. Further developments include the extension to describe diffusion in integrable systems [43–45] as well as the extension to quantum GHD [98]. Notably, only very recently, Eq. (2.4.21) was proven rigorously in [46, 47]. In [47], Pozsgay derived a generating function for both the charge density and the current operator. The derivation is model-independent and explains the simple relation of the current mean values using transfer matrix methods [99, 100]. For the special case of the XXZ chain, Pozsgay demonstrates the quasi-classical interpretation of the current mean values which are rooted in the dissipationless and factorized scattering in integrable models.

In the approach taken in [32], which is presented in the following, Bertini *et al.* start by considering a conserved charge (Q) and the corresponding density \mathbf{q} . In the case of integrable models, the information spreads linearly from an inhomogeneity because of stable quasiparticle excitations. Eventually, observables can be

described by a stationary state and the expectation value of a density in this state $|\rho\rangle$ reads

$$\langle \rho | \mathbf{q} | \rho \rangle = \int d\lambda q(\lambda) \rho(\lambda), \quad (2.4.1)$$

where $q(\lambda)$ is the single-particle eigenvalue of the charge and $\rho(\lambda)$ is the particle density. Together with the hole density $\rho_h(\lambda)$, they are called “root densities”. Here, we only consider one kind of quasiparticle, in the case of several quasiparticle species, one would have to add a sum over the species k in front of Eq. (2.4.1) and consider eigenvalues q_k and densities ρ_k . Due to the integrability of the system, we will assume that for a given $\zeta = x/t$, the expectation values of observables will be finally described by a local quasi-stationary state (LQSS) of the form ρ_ζ^{LQSS} :

$$\langle O \rangle_{x,t} \equiv \langle \Psi_t | O_x | \Psi_t \rangle = \text{Tr} \left(\rho_\zeta^{LQSS} O_x \right) + o(t^{-\epsilon}). \quad (2.4.2)$$

We are now focusing on one quasiparticle of that LQSS. This quasiparticle contains charge and we denote the charge density carried from \tilde{x} to x during the time interval $[t, t + \delta t]$ as $\Delta_{\tilde{x} \rightarrow x, t}^{\mathbf{q}}$. Using this notation we can write

$$\langle \mathbf{q} \rangle_{x, t + \delta t} - \langle \mathbf{q} \rangle_{x, t} = \int d\tilde{x} \left(\Delta_{\tilde{x} \rightarrow x, t}^{\mathbf{q}} - \Delta_{x \rightarrow \tilde{x}, t}^{\mathbf{q}} \right). \quad (2.4.3)$$

However, for given $\tilde{x} - x$ and t , quasiparticles can only contribute to $\Delta_{\tilde{x} \rightarrow x, t}^{\mathbf{q}}$ if they have the group velocity $v^{gr} = (x - \tilde{x})/\delta t$:

$$\Delta_{\tilde{x} \rightarrow x, t}^{\mathbf{q}} \equiv \int d\lambda \delta(x - \tilde{x} - v^{gr}(\lambda)\delta t) c_{\mathbf{q}}(\lambda|\zeta), \quad (2.4.4)$$

where $c_{\mathbf{q}}(\lambda|\zeta)$ is the charge density which is transported by excitations with rapidity $\in [\lambda, \lambda + d\lambda]$. Plugging Eq. (2.4.4) into Eq. (2.4.3) we arrive at

$$\partial_t \langle \mathbf{q} \rangle_{x, t} = - \int d\lambda \partial_x [v^{gr}(\lambda) c_{\mathbf{q}}(\lambda|\zeta)]. \quad (2.4.5)$$

Combining Eqs. (2.4.1) and (2.4.5) then gives

$$\int d\lambda [q(\lambda) \partial_t \rho(\lambda) + \partial_x (v^{gr}(\lambda) c_{\mathbf{q}}(\lambda|\zeta))] = 0. \quad (2.4.6)$$

However, the charge density is nothing else than

$$c_{\mathbf{q}}(\lambda|\zeta) = q(\lambda)\rho(\lambda) \quad (2.4.7)$$

and after inserting Eq. (2.4.7) into Eq. (2.4.6) we arrive at

$$\int d\lambda q(\lambda) [\partial_t \rho_\zeta(\lambda) + \partial_x (v_\zeta^{gr}(\lambda) \rho_\zeta(\lambda))] = 0. \quad (2.4.8)$$

where we have now explicitly marked the ζ -dependent quantities. As $q(\lambda)$ is independent of ζ , we have obtained a continuity equation for the charge densities and can finally write

$$\boxed{\partial_t \rho_\zeta(\lambda) + \partial_x (v_\zeta^{gr}(\lambda) \rho_\zeta(\lambda)) = 0}, \quad (2.4.9)$$

which can be, using TBA identities, recast in the form

$$[\zeta - v_\zeta^{gr}(\lambda)] \partial_\zeta n_\zeta(\lambda) \rho_\zeta^t(\lambda) = 0. \quad (2.4.10)$$

Here, $n_\zeta(\lambda)$ is the occupation number defined as

$$n_\zeta(\lambda) = \frac{\rho_\zeta(\lambda)}{\rho_\zeta(\lambda) + \rho_\zeta^h(\lambda)} \quad (2.4.11)$$

and $\rho_\zeta^t(\lambda) = \rho_\zeta(\lambda) + \rho_\zeta^h(\lambda)$. If there exists a unique solution of $\zeta - v_\zeta^{gr}(\lambda) = 0$ for any λ , then one can obtain the piecewise constant solution

$$n_\zeta(\lambda) = \Theta(v_\zeta^{gr}(\lambda) - \zeta) n_L(\lambda) + \Theta(\zeta - v_\zeta^{gr}(\lambda)) n_R(\lambda). \quad (2.4.12)$$

We are now going to obtain the very same solution as presented in [31], which we outline in the following. The starting point of our discussion in this classical approach, which was introduced by Castro-Alvaredo *et al.*, is the continuity equation

$$\partial_t q_i(x, t) + \partial_x j_i(x, t) = 0, \quad (2.4.13)$$

where $q_i(x, t)$ is a local density and $j_i(x, t)$ is the local current corresponding to a conserved quantity Q_i of the integrable system with $i \in \{1, 2, \dots, N\}$. The density matrix ρ will be described by a generalized Gibbs ensemble which maximizes the

entropy under the constraint of an extensive number of conserved quantities and has the form

$$\rho = \frac{e^{-\sum_i \beta_i Q_i}}{\text{Tr} (e^{-\sum_i \beta_i Q_i})}, \quad (2.4.14)$$

where the β_i are the potentials corresponding to the Q_i . Depending on the considered system, Q_1 could e.g. be the Hamiltonian H and β_1 the inverse temperature. The vector of β_i is denoted as $\boldsymbol{\beta} = (\beta_1, \beta_2, \dots, \beta_N)$. Taking the Gibbs averages $\langle \dots \rangle_{\boldsymbol{\beta}}$ establishes a connection between the averages and the potentials. We denote the averages as

$$\begin{aligned} \mathbf{q}_i &= \langle q_i \rangle_{\boldsymbol{\beta}(x,t)}, & \mathbf{q}(x,t) &= \langle \mathbf{q} \rangle_{\boldsymbol{\beta}(x,t)} \\ \mathbf{j}_i &= \langle j_i \rangle_{\boldsymbol{\beta}(x,t)}, & \mathbf{j}(x,t) &= \langle \mathbf{j} \rangle_{\boldsymbol{\beta}(x,t)} \end{aligned} \quad (2.4.15)$$

and because of the connection between averages and potentials, the \mathbf{j}_i are also a function of the \mathbf{q}_i :

$$\mathbf{j} = F(\mathbf{q}). \quad (2.4.16)$$

We expect that a hydrodynamic description emerges at large space-time scales. This emergence is based on local entropy maximization only and means that the expectation value of an operator $\langle O(x,t) \rangle$ goes towards $\langle O \rangle_{\boldsymbol{\beta}(x,t)}$. We can now, using Eq. (2.4.13), obtain

$$\partial_t \mathbf{q}(x,t) + \partial_x \mathbf{j}(x,t) = 0. \quad (2.4.17)$$

We denote the one-particle eigenvalue of the conserved charge Q_i as h_i , giving for example the energy $h_1 = e$ for $Q_1 = H$ or the momentum $h_2 = p$ for $Q_2 = P$. Using these h_i , we can denote the average densities as

$$\mathbf{q}_i = \int d\lambda \rho(\lambda) h_i(\lambda). \quad (2.4.18)$$

Applying the Bethe ansatz, one arrives at

$$2\pi \rho_s(\lambda) = p'(\lambda) + \int d\mu \mathcal{K}(\lambda - \mu) \rho(\mu), \quad (2.4.19)$$

where we used the state density defined as $\rho_s(\lambda) = \rho(\lambda) + \rho_h(\lambda)$. $p'(\lambda) = dp(\lambda)/d\lambda$ and $\mathcal{K}(\lambda)$ denotes the differential scattering phase. This transformation can also be inverted, leading to

$$2\pi \rho(\lambda) = n(\lambda) p'^{dr}(\lambda), \quad (2.4.20)$$

where the dressing operation takes into account the scattering between the quasi-particles and is defined as the solution of the integral equation (3.2.5). If we introduce the current spectral density $\rho_c(\lambda)$, we can write, analogously to Eq. (2.4.18),

$$\mathbf{j}_i = \int d\lambda \rho_c(\lambda) h_i(\lambda), \quad (2.4.21)$$

where we define $\rho_c(\lambda)$ via

$$\rho_c(\lambda) = v(\lambda)\rho(\lambda). \quad (2.4.22)$$

Here, $v(\lambda)$ is given by the dressed quasiparticle group velocity

$$v(\lambda) = \frac{e'^{dr}(\lambda)}{p'^{dr}(\lambda)} \quad (2.4.23)$$

which is sometimes also referred to as the effective velocity. The group velocity itself is defined as

$$v^{gr} = \frac{e'(\lambda)}{p'(\lambda)} \quad (2.4.24)$$

and is also connected to the dressed group velocity via

$$v(\lambda) = v^{gr}(\lambda) + \int d\mu \frac{\mathcal{K}(\lambda - \mu)\rho(\mu)}{p'(\lambda)} [v(\mu) - v(\lambda)]. \quad (2.4.25)$$

If we now combine Eqs. (2.4.17), (2.4.18) and (2.4.21) we arrive at

$$\partial_t \rho(\lambda) + \partial_x \rho_c(\lambda) = 0. \quad (2.4.26)$$

However, using the relation between $\rho_c(\lambda)$ and $v(\lambda)$ from Eq. (2.4.22) as well as Eq. (2.4.25), we can finally rewrite Eq. (2.4.26) as

$$\boxed{\partial_t \rho_\zeta(\lambda) + \partial_x (v(\lambda)\rho_\zeta(\lambda)) = 0}. \quad (2.4.27)$$

2.5 Entanglement measures

The phenomenon of entanglement is the essential characteristic of quantum mechanics, the fact that makes it so different from classical physics.

This section introduces the entanglement measures Rényi entropy and logarithmic negativity as well as some related quantities. At first, we are going to discuss the entanglement entropy, a special case of the Rényi entropy. Then we will introduce the entanglement negativity, especially with respect to Gaussian states. Finally, we will briefly mention fluctuations as well as the mutual information, which are both quantities that are related to entanglement.

2.5.1 Entanglement entropy

The role of entanglement in quantum many-body systems is widely studied as in the case of critical chains [17, 101], the XY chain [102] and in free lattice models [58, 103]. Entanglement entropy within quantum field theory and conformal field theory was studied extensively, especially by Calabrese and Cardy [18, 22, 104, 105]. A review of entanglement in many-body physics can be found in [4], a thorough discussion of entanglement measures is given in [106]. The discussion of entanglement entropy in this section follows [5].

Let us begin our discussion with a general, mixed state ρ . This mixed state is defined on the bipartite space $\mathcal{H} = \mathcal{H}_A \otimes \mathcal{H}_{B=\bar{A}}$. This state is now called separable [107] if it can be written as

$$\rho = \sum_j p_j \rho_A^j \otimes \rho_B^j, \quad (2.5.1)$$

where ρ_i^j is a mixed state defined on the respective subspace \mathcal{H}_i and $\sum_j p_j = 1$. If a state is not separable, it is entangled. The entanglement entropy is a measure for the bipartite entanglement in pure states and can be understood with the help of the Schmidt decomposition. If we consider the pure state $\rho = |\psi\rangle\langle\psi|$ with the bipartition A and B , the Schmidt decomposition (which is discussed in more detail in section 2.8) reads

$$|\psi\rangle = \sum_{\alpha=1}^{\min(D_A, D_B)} d_\alpha |A\rangle_\alpha |B\rangle_\alpha. \quad (2.5.2)$$

That relation was obtained from $|\psi\rangle = \sum_{i,j} c_{i,j} |i\rangle_A |j\rangle_B$ via an SVD where $|i\rangle_A$ and $|j\rangle_B$ are basis sets in the respective subsystems A, B with dimensions $D_{A,B}$. A and B are unentangled if there is only one non-vanishing coefficient $d_\alpha = 1$. The singular values d_α can thus be employed to measure the non-separability of the pure state and to quantify the entanglement. Each state which cannot be written as a product state is entangled. To get a quantitative measure of entanglement, the von Neumann entropy was introduced as

$$\boxed{S(\rho_A) = -\text{Tr}(\rho_A \ln(\rho_A))}. \quad (2.5.3)$$

With p_i being the eigenvalues of ρ_A this leads to

$$S(\rho_A) = - \sum_i p_i \ln(p_i), \quad (2.5.4)$$

which is the Shannon entropy of the eigenvalues of the reduced density matrix ρ_A . We can now relate the entanglement entropy between the two subsystems A and B to the Schmidt decomposition of the system. Applying the Schmidt decomposition leads to

$$\rho = \sum_\alpha \sum_\beta d_\alpha d_\beta |A\rangle_{\alpha\beta} \langle A| |B\rangle_{\alpha\beta} \langle B| \quad (2.5.5)$$

which makes it easy to read out the reduced density matrices (cf. Eq. (2.1.10)):

$$\begin{aligned} \rho_A &= \sum_\alpha d_\alpha^2 |A\rangle_{\alpha\alpha} \langle A| \\ \rho_B &= \sum_\alpha d_\alpha^2 |B\rangle_{\alpha\alpha} \langle B|. \end{aligned} \quad (2.5.6)$$

From this notation we can extract the entropies as

$$S(\rho_A) = S(\rho_B) = - \sum_\alpha d_\alpha^2 \ln(d_\alpha^2). \quad (2.5.7)$$

Apparently, $S(\rho_A) = S(\rho_B)$ meaning that the entropy is symmetrical: A is as much entangled with B as B is entangled with A . Thus, we can speak of *the* entanglement entropy between A and B . A and B are maximally entangled when all d_α are the same i.e., $d_\alpha^2 = \frac{1}{D}$ with $D = \min(D_A, D_B)$. This leads to a maximum entanglement of

$$S_{max} = -D \left(\frac{1}{D} \ln \left(\frac{1}{D} \right) \right) = \ln(D). \quad (2.5.8)$$

Entanglement measures

For a product state, there is only one singular value $d = 1$, leading to $S = 0$, so a product state is not entangled. A singlet state is given by

$$|\psi_S\rangle = \frac{1}{\sqrt{2}} (|\uparrow\rangle_A |\downarrow\rangle_B - |\downarrow\rangle_A |\uparrow\rangle_B) \quad (2.5.9)$$

which corresponds to singular values $d_1^2 = d_2^2 = \frac{1}{2}$. Thus, a singlet is a maximally entangled state with $S = \ln(2)$.

The von Neumann entanglement entropy is only a special case of the more general Rényi entropy which for the reduced density matrix ρ_A is defined as

$$S_\alpha(\rho_A) = \frac{1}{1-\alpha} \ln(\text{Tr}(\rho_A^\alpha)). \quad (2.5.10)$$

For integer $\alpha \geq 2$, the Rényi entropies can be measured in cold-atom and ion-trap experiments [108]. For integer α , the entire spectrum of ρ_A can be obtained from the entanglement spectrum of the Rényi entropies [109]. The von Neumann entanglement entropy is obtained from the Rényi entropy in the limit

$$S(\rho_A) = \lim_{\alpha \rightarrow 1} S_\alpha(\rho_A). \quad (2.5.11)$$

The Rényi entropy can be calculated for different setups within a CFT as it can be found in section 2.6 on the CFT approach to entanglement.

2.5.2 Entanglement negativity

This subsection introduces the entanglement negativity following [69, 71]. The entanglement entropy is a useful measure of entanglement for pure states: For a bipartite, pure state, the entanglement between these two partitions can be calculated as discussed above. For mixed states, however, this is not possible as classical and quantum correlations would not be well separated. The mutual information (cf. Eq. (2.5.22)) between those two intervals would also measure both the classical correlations as well as the entanglement and is thus an upper bound on the entanglement between them. Besides other proposed measures (see [5, 106] and references therein), the entanglement negativity, which was first mentioned in [110], was proposed as a computable entanglement measure by Vidal and Werner [69]. The negativity allows to calculate the entanglement between noncomplementary intervals A_1 and A_2 which are embedded in B and $A = A_1 \cup A_2$. The

entanglement negativity is based on the Peres-Horodecki criterion which states that a state ρ_{A_1, A_2} is separable if and only if $\rho_A^{T_1} \geq 0$, i.e., if the partial transpose of the reduced density matrix is positive [5, 107, 111, 112].

$\rho_A^{T_1}$ denotes the partial transpose of ρ_A with respect to A_1 , being defined as

$$\langle i_{A_1}, j_{A_2} | \rho_A^{T_1} | k_{A_1}, l_{A_2} \rangle = \langle k_{A_1}, j_{A_2} | \rho_A | i_{A_1}, l_{A_2} \rangle. \quad (2.5.12)$$

The entanglement negativity is then given by

$$\mathcal{N}(\rho_A) = \frac{\|\rho_A^{T_1}\|_1 - 1}{2}, \quad (2.5.13)$$

where $\|\rho_A^{T_1}\|_1$ denotes the trace norm of $\rho_A^{T_1}$. For an operator O , the trace norm is defined as $\|O\|_1 = \text{Tr}(\sqrt{O^\dagger O})$. If O is Hermitian, the trace norm equals the sum of the absolute values of the eigenvalues of O . The entanglement negativity can thus be interpreted as measuring the extent to which the spectrum of $\rho_A^{T_1}$ contains negative eigenvalues, how much it fails to be positive definite [107]. The entanglement negativity is a non-convex entanglement monotone [113] and vanishes only for unentangled states. The logarithmic negativity

$$\mathcal{E} = \ln \|\rho_A^{T_1}\|_1 \quad (2.5.14)$$

is an entanglement monotone as well but also fulfills additivity as [69]

$$\mathcal{E}(\rho_{A_1} \otimes \rho_{A_2}) = \mathcal{E}(\rho_{A_1}) + \mathcal{E}(\rho_{A_2}). \quad (2.5.15)$$

We are now going to consider Gaussian states and will start with the simpler bosonic case. For bosonic Gaussian states, the partial transpose is the same as the partial time-reversal (TR) [71, 112]. The partial transpose of a bosonic Gaussian state is again Gaussian which allows the calculation of the negativity with the help of covariance matrices [114]. The geometric interpretation of this partial transpose is that it is a mirror reflection in phase space [112]. However, in fermionic systems, the partial transpose and the partial TR in general differ as due to the fermionic anticommutation relations, a minus sign might be acquired. Furthermore, the partial transpose of a fermionic Gaussian state is in general not Gaussian [70]. Yet, one can instead use the partial TR to define a fermionic analog of the negativity as [71]

$$\mathcal{E}_f = \ln \|\rho_A^{R_2}\|_1, \quad (2.5.16)$$

Entanglement measures

where R_2 denotes the partial TR with respect to A_2 . This partial TR of a fermionic density matrix is Gaussian [71] and the fermionic negativity \mathcal{E}_f is indeed a proper measure of entanglement [72].

We are now going to use the fermionic negativity defined in Eq. (2.5.16) as an entanglement measure for fermionic Gaussian states. It is convenient to write the reduced density matrix using Majorana fermions c_m , satisfying the anticommutation relations $\{c_m, c_n\} = 2\delta_{mn}$. With the help of these Majorana fermions, we can expand ρ_A as

$$\rho_A = \sum_{\substack{\kappa, \tau \\ |\kappa| + |\tau| = \text{even}}} w_{\kappa, \tau} c_{2m_1-1}^{\kappa_{2m_1-1}} \cdots c_{2m_{\ell_1}}^{\kappa_{2m_{\ell_1}}} c_{2m'_1-1}^{\tau_{2m'_1-1}} \cdots c_{2m'_{\ell_2}}^{\tau_{2m'_{\ell_2}}}. \quad (2.5.17)$$

Here, the sites of subsystem A_1 are labelled by $\{m_1, \dots, m_{\ell_1}\}$ and those of subsystem A_2 are labelled by $\{m'_1, \dots, m'_{\ell_2}\}$. κ_j with $j = 2m_1 - 1, \dots, 2m_{\ell_1}$ and $\tau_{j'}$ with $j' = 2m'_1 - 1, \dots, 2m'_{\ell_2}$ are bit strings associated with the subsystems A_1 and A_2 , with their norms defined as $|\kappa| = \sum_j \kappa_j$ and $|\tau| = \sum_{j'} \tau_{j'}$, respectively. The bit strings determine which Majorana operators are included as $c_j^0 = \mathbb{1}$ or $c_j^1 = c_j$ and $w_{\kappa, \tau}$ weighs their respective contributions. Note that the overall number of Majorana operators has to be even which reflects the global fermion-number parity symmetry of the state. Using this notation, the partial time reversal R_2 with respect to A_2 acts as [71]

$$\rho_A^{R_2} = O_+ = \sum_{\substack{\kappa, \tau \\ |\kappa| + |\tau| = \text{even}}} w_{\kappa, \tau} i^{|\tau|} c_{2m_1-1}^{\kappa_{2m_1-1}} \cdots c_{2m_{\ell_1}}^{\kappa_{2m_{\ell_1}}} c_{2m'_1-1}^{\tau_{2m'_1-1}} \cdots c_{2m'_{\ell_2}}^{\tau_{2m'_{\ell_2}}}, \quad (2.5.18)$$

where we have introduced the Gaussian operator O_+ that appears also in the result of the standard logarithmic negativity \mathcal{E} . Please note that, in general, O_+ is not a Hermitian operator and its conjugate will be denoted by $O_- = O_+^\dagger$. Using this notation, we can now obtain the fermionic logarithmic negativity as

$$\mathcal{E}_f = \ln \|\rho_A^{R_2}\|_1 = \ln \text{Tr} \sqrt{O_+ O_-} \quad (2.5.19)$$

in which the negativity depends on the product of two Gaussian operators.

It was shown that for free fermions, one can write $\rho_A^{T_2}$ as a linear combination of the two Gaussian operators O_+ and O_- as [70]

$$\rho_A^{T_2} = \frac{1-i}{2} O_+ + \frac{1+i}{2} O_-. \quad (2.5.20)$$

The result in (2.5.16), based on the partial TR, coincides with an upper bound for the entanglement negativity that was presented for Gaussian states as [73]

$$\mathcal{E} \leq \mathcal{E}_f + \ln \sqrt{2}. \quad (2.5.21)$$

The negativity in free-fermion systems was further considered in [115], where this bound of the fermionic negativity was presented and it also was conjectured that the bound might be tighter.

The entanglement between separated blocks in spin chains in the ground state of critical systems was studied in [116], using the spectrum of the partially transposed density matrix obtained via DMRG methods. Similar results were obtained independently in [117]. The approach in [116] was later generalized in [79] to calculate the entanglement negativity in spin chains for arbitrary tripartitions within MPS/DMRG. Further studies investigated the negativity spectrum [118]. Different approaches include the calculation of the partially transposed RDM applying Monte Carlo methods [119, 120].

Finally, we want to mention some results in which the negativity after non-equilibrium dynamics was studied. Two harmonic half chains, initialized at different temperatures and then joined are considered in [76]. In [77], the local quench after joining two half chains at finite temperature was considered, focussing exclusively on adjacent intervals. The analytical formulas presented in [77] agree with the numerical results in the harmonic chain in [76]. Entanglement negativity at finite temperatures has also been studied within CFT [121]. The entanglement negativity for two adjacent and disjoint intervals after a global quench is then studied within the quasiparticle picture and CFT in [68]. The time evolution after joining two critical half chains was calculated in a CFT in [74]. The entanglement negativity within the CFT framework is discussed in section 2.6.

A quasiparticle description for the dynamics of the logarithmic negativity after a quantum quench in integrable systems is given in [67]. Notably, a procedure to measure the entanglement negativity experimentally is proposed in [122]. The recent studies of symmetry resolved entanglement also included studies of the entanglement negativity [75, 123].

2.5.3 Related quantities

This section introduces some further quantities of interest that have been studied and are related to the entanglement measures introduced above. Having intro-

Entanglement measures

duced the Rényi entropy $S_\alpha(\rho_A)$ of a subsystem A , we can also define the Rényi mutual information \mathcal{I}_α between subsystems A_1 and A_2 as [3]

$$\mathcal{I}_\alpha = S_\alpha(\rho_{A_1}) + S_\alpha(\rho_{A_2}) - S_\alpha(\rho_A), \quad (2.5.22)$$

where $A = A_1 \cup A_2$ and the whole system is given by $A \cup B$. The mutual information is symmetric in A_1 and A_2 . For $\alpha = 1$, we get the standard (von Neumann) mutual information which is a measure of both classical and quantum correlations and is thus an upper bound to the entanglement [124]. Although I_1 is not a measure of entanglement, it still fulfills an area law [125] which may be violated for Hamiltonians with long-range interactions [126]. In general, the Rényi mutual information is not even a proper measure as it was found that \mathcal{I}_α might become negative for certain quenches and $\alpha > 2$ [127]. On the other hand, it has been proved that \mathcal{I}_α is always positive in the range $0 < \alpha < 2$ for both fermionic and bosonic Gaussian states [128]. The case $\alpha = 1/2$ is especially interesting as it is related to the logarithmic negativity after a global quench [67].

One more quantity that we are going to consider are the subsystem magnetization fluctuations in a spin chain with a conserved total magnetization. For a subsystem A , the subsystem magnetization fluctuations are defined as

$$\mathcal{F} = \left\langle \left(\sum_{i \in A} S_i^z - \left\langle \sum_{i \in A} S_i^z \right\rangle \right)^2 \right\rangle. \quad (2.5.23)$$

The fluctuations actually share some essential features with the entanglement entropy [59–63]. Namely, at zero temperature, the fluctuations (and all cumulants) are zero for a product state and the fluctuations are symmetric between A and the remainder of the system B . Still, fluctuations are not an entanglement measure. In the ground state of the XXZ chain, a proportionality between the fluctuations and the entropy was reported as [60]

$$\mathcal{F} \simeq K \frac{3}{\pi^2} S + \text{const.}, \quad (2.5.24)$$

where K denotes the Luttinger parameter [166]. The validity of relation (2.5.24) out of equilibrium after a geometric quench in the XXZ chain is discussed in Sec. 3.6.

2.6 CFT approach to entanglement

In order to be able to discuss the entanglement in critical systems as well as after quantum quenches and local operator insertions within the CFT framework, we first introduce the concepts from CFT needed, following the seminal works by Calabrese and Cardy [18, 104] as well as [130, 131]. As introduced in Eq. (2.5.10), the Rényi entropy of a reduced density matrix ρ_A reads

$$S_n(\rho_A) = \frac{1}{1-n} \ln(\text{Tr}(\rho_A^n)) . \quad (2.6.1)$$

We at first consider integer values n and evaluate $\ln(\text{Tr}(\rho_A^n))$ as follows. We will exclusively focus on the 1+1D case. In a quantum field theory, the partition function of the density matrix

$$\rho = \frac{1}{Z} e^{-\beta H} \quad (2.6.2)$$

at finite temperature β is equivalent to a path integral on a cylinder with circumference β . The elements of that density matrix are given by

$$\rho(\{\phi_x\}, \{\phi'_{x'}\}) = \left\langle \prod_x \{\phi_x\} \left| \rho \right| \prod_{x'} \{\phi'_{x'}\} \right\rangle \quad (2.6.3)$$

where the states $\{\phi_x\}$ denote a complete basis in discretized space. This expression can be rewritten as a path integral as

$$\rho(\{\phi_x\}, \{\phi'_{x'}\}) = Z^{-1} \int [d\phi(y, \tau)] \prod_{x'} \delta(\phi(y, 0) - \phi'_{x'}) \prod_x \delta(\phi(y, \beta) - \phi_x) e^{-S_E} , \quad (2.6.4)$$

where S_E denotes the Euclidian action $S_E = \int_0^\beta \mathcal{L} d\tau$ and $Z = \text{Tr}(e^{-\beta H})$. The rows and columns of the reduced density matrix are labelled by the values of the fields at $\tau = 0, \beta$. If we define A as the interval of length ℓ , ranging from u to v , ρ_A then corresponds to a cylinder with a cut along A as depicted in Fig. 2.1.

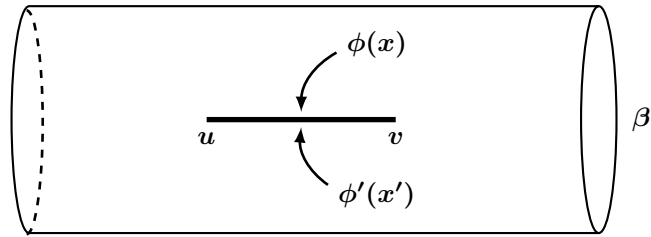


Figure 2.1: Graphical depiction of ρ_A in a CFT. As we have only sewed together in region B , there remains a cut between u and v . The ends of the cuts are called branch points.

Having now ρ_A at hand, the next step is to obtain $\text{Tr}(\rho_A^n)$ for integer n . This problem can be tackled by applying the replica trick which reduces the problem to the task of calculating the partition function of a Riemann surface. Taking n cylinders, we connect them as follows: We label the n copies by $1 \leq j \leq n$ and sew them together at the cuts $x \in A$ such that $\phi_j(x, \tau = 0^-) = \phi_{j+1}(x, \tau = 0^+)$ and the n th copy is then again connected to the first one. If one considers the zero temperature case, this means $\beta \rightarrow \infty$ and thus, ρ_A corresponds to an infinite plane with a cut. $Z_n(A)$ is then given by n planes sewed together at their cuts as it is depicted for $n = 3$ in Fig. 2.2. By doing so, we represent the n -sheeted

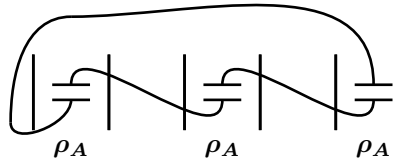


Figure 2.2: Three copies of ρ_A sewed together at zero temperature to obtain $Z_3(A)$ as described in the text.

Riemann surface Σ_n in \mathbb{C}^n as n copies of ϕ on the complex plane \mathbb{C} . Finally, we obtain $\text{Tr}(\rho_A^n)$ as

$$\text{Tr}(\rho_A^n) = \frac{Z_n(A)}{Z^n}, \quad (2.6.5)$$

where the partition function Z is simply obtained by sewing together the complete edges of the cylinder instead of leaving a cut for $x \in A$ as it was done before.

Having evaluated $\text{Tr}(\rho_A^n)$, we can now insert it into Eq. (2.6.1) to obtain the n -Rényi entropy.

Until now, we have considered the entropy of a single interval, ranging from u to v . We now want to generalize this setup to multiple intervals on the n -sheeted Riemann surface, ranging from u_j to v_j . In general, to evaluate such quantities, one can work with branch-point twist fields \mathcal{T}_n and $\bar{\mathcal{T}}_n$ [104, 105, 129]. The partition function on the n -sheeted surface, consisting of n copies which are sewed together along N cuts, can be rewritten as a path integral on the complex plane. This path integral is taken over the Lagrangian density which is found to be a sum of n local densities. The exchange of the n copies is a symmetry of the system and twist fields exist whenever there is a global internal symmetry σ . In our case, the twist field \mathcal{T}_n is associated with the cyclic permutation $\sigma : i \mapsto i + 1 \pmod n$ and $\bar{\mathcal{T}}_n$ corresponds to the inverse permutation. Using these twist fields, an n -sheeted Riemann surface $\Sigma_{n,N}$, on which A consists of N disjoint intervals defined on $[u_j, v_j]$, has the partition function [104, 105]

$$Z_{\Sigma_{n,N}} \propto \langle \mathcal{T}_n(u_1) \bar{\mathcal{T}}_n(v_1) \dots \mathcal{T}_n(u_N) \bar{\mathcal{T}}_n(v_N) \rangle, \quad (2.6.6)$$

where $\mathcal{T}_n(u_j)$ opens slit j and $\bar{\mathcal{T}}_n(v_j)$ closes it. The twist fields are primaries and have scaling dimension

$$\Delta_n = \frac{c}{12} \left(n - \frac{1}{n} \right), \quad (2.6.7)$$

with c being the central charge defining the model. We can now use this formalism to obtain results for the entanglement entropy. The S_n Rényi entropy for a system with N cuts can be calculated from

$$\text{Tr}(\rho_A^n) = \langle \mathcal{T}_n(u_1) \bar{\mathcal{T}}_n(v_1) \dots \mathcal{T}_n(u_N) \bar{\mathcal{T}}_n(v_N) \rangle. \quad (2.6.8)$$

If we consider a single cut ranging from u to v with $\ell = |v - u|$, one obtains a two-point function of primaries, which is universal. Due to conformal symmetry, one obtains the simple result

$$\text{Tr}(\rho_A^n) = \langle \mathcal{T}_n(u) \bar{\mathcal{T}}_n(v) \rangle = \frac{c_n}{|v - u|^{2\Delta_n}}. \quad (2.6.9)$$

Plugging in our results from above, the final result for the Rényi entropy is given by

$$S_n = \frac{c}{6} \left(1 + \frac{1}{n} \right) \log(\ell) + c'_n. \quad (2.6.10)$$

CFT approach to entanglement

which denotes the entropy of a single interval of length ℓ in a critical, infinite chain in its ground state. The result for the von Neumann entropy is simply given for $n = 1$. If the total system is finite with chain length L and periodic boundary conditions are assumed, the partition function is defined on a cylinder with circumference L . After a conformal transformation, one eventually gets

$$S_n = \frac{c}{6} \left(1 + \frac{1}{n} \right) \log \left(\frac{L}{\pi} \sin(\pi\ell/L) \right) + c_n. \quad (2.6.11)$$

Note that for $L \rightarrow \infty$, (2.6.11) becomes (2.6.10) and that (2.6.11) has the symmetry $S_n(\ell) = S_n(L - \ell)$. A discussion of the entanglement entropy after different quantum quenches can be found in Sec. 2.7.

Later, the CFT treatment was also extended to calculating the entanglement negativity. Applying a replica trick, we consider integer powers of n and then distinguish between even and odd n as n_e and n_o . Considering integer n , we get

$$\begin{aligned} \text{Tr} (\rho_A^{T_2})^{n_e} &= \sum_i \lambda_i^{n_e} \\ \text{Tr} (\rho_A^{T_2})^{n_o} &= \sum_i \lambda_i^{n_o}, \end{aligned} \quad (2.6.12)$$

where the λ_i are the eigenvalues of $\rho_A^{T_2}$. The negativity is then given by [130]

$$\mathcal{E} = \lim_{n_e \rightarrow 1} \ln (\text{Tr} (\rho_A^{T_2})^{n_e}) \quad (2.6.13)$$

whereas the limit $n_o \rightarrow 1$ gives the normalization. We already know that $\text{Tr} (\rho_A^n)$ is proportional to the partition function of the n -sheeted Riemann surface which is obtained from a correlation function of twist fields as in Eq. (2.6.8). We now want to calculate the entanglement *between* two intervals A_1 and A_2 with lengths $\ell_1 = |u_1 - v_1|$ and $\ell_2 = |u_2 - v_2|$, respectively. The effect of the partial transpose of A_2 is that the row and column indices in A_2 are exchanged which corresponds to an exchange of twist fields in the correlation function, eventually leading to [130]

$$\text{Tr} ((\rho_A^{T_2})^n) = \langle \mathcal{T}_n(u_1) \bar{\mathcal{T}}_n(v_1) \bar{\mathcal{T}}_n(u_2) \mathcal{T}_n(v_2) \rangle. \quad (2.6.14)$$

Having the twist field correlation functions at hand, we can evaluate them to obtain the entanglement negativity for various setups. The calculations were performed

for both adjacent and disjoint intervals in 1+1D: The negativity of two intervals of lengths ℓ_1 and ℓ_2 in critical systems was studied systematically within CFT in [130, 131]. For two adjacent intervals, the negativity was found to be [130]

$$\mathcal{E} = \frac{c}{4} \ln \frac{\ell_1 \ell_2}{\ell_1 + \ell_2} + \text{const.} \quad (2.6.15)$$

The result for finite systems is obtained straightforwardly by inserting the chord variables. The case of disjoint intervals is much more complicated as the results depend on the full operator content of the CFT. In [131], the entanglement negativity is also calculated for a single interval of length ℓ , leading to

$$\mathcal{E} = \frac{c}{2} \ln(\ell) + 2 \ln c_{1/2}. \quad (2.6.16)$$

This is nothing else than the $S_{1/2}$ Rényi entropy which is equal to the logarithmic negativity for pure states. These CFT techniques have then also been successfully applied onto the critical Ising chain [132].

2.7 Quantum quenches

A crucial question in quantum mechanics is whether the asymptotic state after unitary time evolution of a pure state can be described via statistical ensembles. The simplest setup in which this issue can be studied, both theoretically and experimentally [133–138], is the quantum quench which we are now going to introduce, closely following [139]. In such a quench, an initial state $|\psi_0\rangle$, usually the ground state of a Hamiltonian H_0 , is time-evolved unitarily as

$$|\psi(t)\rangle = e^{-i\hat{H}t} |\psi_0\rangle \quad (2.7.1)$$

with a different Hamiltonian H , inducing non-equilibrium dynamics in the system. However, for a time evolution as in Eq. (2.7.1), the density matrix $\rho(t) = |\psi(t)\rangle \langle\psi(t)|$ never thermalizes. Instead, for a subsystem A , the system can relax *locally* if the limit

$$\lim_{t \rightarrow \infty} \lim_{L \rightarrow \infty} \rho_A(t) = \rho_A(\infty) \quad (2.7.2)$$

exists. It is important to first take the thermodynamic limit and then the infinite time limit. Here, the finite subsystem A can be arbitrarily chosen and the whole infinite system has the property of relaxation to a stationary state, if the limit in Eq. (2.7.2) exists for all possible A [139]. As the Hamiltonian in Eq. (2.7.1) is time-independent, the energy is a conserved quantity and for an arbitrary quantum system, thermalization now means that the stationary state is described by a Gibbs ensemble as

$$\rho_A(\infty) = \text{Tr}_{\bar{A}}(\rho_{\text{Gibbs}}) . \quad (2.7.3)$$

Here, the Gibbs ensemble is defined as

$$\rho_{\text{Gibbs}} = \frac{e^{-\beta\hat{H}}}{Z} \quad (2.7.4)$$

with the partition function $Z = \text{Tr}(e^{-\beta\hat{H}})$. This is expected to happen in generic, isolated quantum systems.

The dynamics after a quench differ for an integrable system. An integrable system has an extensive number of conserved quantities I_n and as these quantities commute with the Hamiltonian, their expectation values are fixed during time evolution. Thus, a relaxation to a generalized Gibbs ensemble (GGE) is expected

for integrable systems [27–29, 140, 141], i.e., the stationary state is described by

$$\rho_{\text{GGE}} = \frac{e^{-\sum_n \lambda_n I_n}}{\text{Tr} (e^{-\sum_n \lambda_n I_n})}. \quad (2.7.5)$$

The relaxation towards a GGE was proposed in [27] which was inspired by experiments with 1D Bose gases [133]. The emergence of a GGE has been shown for observables in integrable systems [28].

In the following subsections, we will discuss the two main categories of quantum quenches, global and local quenches, and then consider different inhomogeneous setups such as the geometric quench [54, 55].

2.7.1 Global quench

In this subsection, the global quench is introduced, following Refs. [22, 29]. In a global quench, the system is modified everywhere in the same way as a global parameter is changed. Global quenches can also be realized experimentally with cold atoms in optical lattices [138]. A physical interpretation of the entanglement entropy after a global quench as given in Eq. (2.7.1) was introduced by Calabrese and Cardy in [22] in the following way: With respect to the time evolution Hamiltonian H , $|\psi_0\rangle$ has a high energy compared to the ground state of H . Thus, the initial state is a source of quasiparticle excitations: When the system is quenched at time $t = 0$, quasiparticle pairs are created throughout the chain and spread out into opposite directions. Each two particles created at the same point are highly entangled. It is assumed that those quasiparticles move classically with a group velocity $v(q)$ and that the maximum velocity is 1. In fact, the maximum velocity with which information can travel in spin chains is limited by the Lieb-Robinson bound [142]. During time evolution, those quasiparticles then travel ballistically, scattering effects are ignored. If, at a certain time, one quasiparticle of the pair has reached a point $x_1 \in A$ and the other one has reached $x_2 \in B$, then A and B are entangled. Note that if both quasiparticles of the pair are located within A or both of them are located within B , then there is no contribution to the entanglement between A and B .

We now assume that the entropy production rate of a quasiparticle pair with momenta p' and p'' is determined by $f(p', p'')$. The entanglement of the interval A

with length ℓ is then given by [22]

$$S_A(t) \approx 2t \int_{-\infty}^0 dp' \int_0^{\infty} dp'' f(p', p'') (v(-p') + v(p'')) \Theta(\ell - (v(-p') + v(p''))t) + 2\ell \int_{-\infty}^0 dp' \int_0^{\infty} dp'' f(p', p'') \Theta((v(-p') + v(p''))t - \ell), \quad (2.7.6)$$

where $\Theta(x)$ denotes the Heaviside function. As we have assumed that $|v(p)| \leq 1$, the second term cannot contribute unless $t > \ell/2$. This means that for short times $t < \ell/2$, the entanglement growth is linear in time. For large times however, the entanglement will only be determined by the second term, obtaining a constant value which is proportional to the interval length ℓ . This is in perfect agreement with the CFT result obtained for an interval of length ℓ in an infinite, critical chain after a global quench which reads [22]

$$S_A(t) \sim \begin{cases} \frac{\pi c t}{6} & \text{if } t < \ell/2 \\ \frac{\pi c \ell}{12} & \text{if } t > \ell/2 \end{cases}, \quad (2.7.7)$$

where c is the central charge of the CFT. Note that also the negativity was calculated via a CFT for global quench scenarios [68].

In [23], the entropy production rate of quasiparticles $f(p', p'')$ was identified for free fermion systems in the thermodynamic limit. Later, this quasiparticle picture was generalized to generic integrable systems by Alba and Calabrese in [29]. It was assumed that the quasiparticle entropy can be obtained from the thermodynamic entropy in the stationary state. Like in [29], we want to start with a simplified and more clear version of Eq. (2.7.6). We assume that there is only one type of quasiparticles with quasimomentum λ , corresponding quasiparticle velocity $v(\lambda)$ and an entropy production rate $s(\lambda)$. For the entropy of an interval of length ℓ after a global quench we then obtain [29]

$$S(t) \sim 2t \int_{2|v|t < \ell} d\lambda v(\lambda) s(\lambda) + \ell \int_{2|v|t > \ell} d\lambda s(\lambda). \quad (2.7.8)$$

Again, we at first observe a linear increase of the entropy with time, followed by a constant entropy proportional to ℓ for long times. For very large times, only the second integral contributes. As discussed at the beginning of section 2.7, the

steady state at long times is expected to be described by a GGE. Thus, the entanglement entropy described by $s(\lambda)$ must be equal to the thermodynamic entropy of the GGE.

In a generic integrable model, there are different species of stable quasiparticle excitations. Due to the integrability, those species have to be treated independently, eventually leading to the conjecture [29]

$$S(t) = \sum_n \left[2t \int_{2|v_n|t < \ell} d\lambda v_n(\lambda) s_n(\lambda) + \ell \int_{2|v_n|t > \ell} d\lambda s_n(\lambda) \right], \quad (2.7.9)$$

where $v_n(\lambda)$ is the velocity of the quasiparticles of type n and $s_n(\lambda)$ their entropy. Remarkably, Eq. (2.7.9) constitutes a simple relation between the thermodynamic entropy and the entanglement entropy for integrable systems in a stationary state after a global quench [29]. $s_n(\lambda)$ is a function of the stationary state densities $\rho_{n,p}^*(\lambda)$ and $\rho_{n,h}^*(\lambda)$ for particles and holes, respectively. Those densities have been obtained for special initial states via Bethe ansatz methods and the integration over all $s_n(\lambda)$ gives an extensive entropy. The ansatz from Eq. (2.7.9) was tested numerically for various initial states of the XXZ chain, finding a very good agreement with the numerical data [30].

2.7.2 Local quench

In contrast, in a local quench, the change of the time evolution Hamiltonian H with respect to H_0 as introduced in Eq. (2.7.1) happens only locally. Initially, one has two half chains in their respective ground states. Then, at time $t = 0$, the two half chains are connected such that the time evolution Hamiltonian is homogeneous. This local quench was considered for a free-fermion chain via correlation matrix techniques and a logarithmic entropy increase in time was found [50, 143]. This setup can also be considered in a CFT, where two half-infinite critical chains are connected and then time-evolved. The entanglement growth after such a local quench is then found to be logarithmic in time as [51]

$$S_n(t) = \frac{c}{6} \left(1 + \frac{1}{n} \right) \log(t) + \text{const.} \quad (2.7.10)$$

This has been generalized in [144] to the case of two half chains of the same length $L/2$ which are connected, followed by a logarithmic entropy increase as

$$S(t) = \frac{c}{3} \log \left| \frac{L}{\pi} \sin \left(\frac{\pi v_F t}{L} \right) \right| + \text{const.} \quad (2.7.11)$$

where v_F is the Fermi velocity. CFT methods were also applied to obtain the negativity after a local quench, which also leads to a logarithmic entanglement increase in time [74].

2.7.3 Inhomogeneous quenches

Another class of quenches has an inhomogeneous initial setup but a homogeneous time evolution Hamiltonian. In a domain wall (DW) quench, two halves of a spin chain which are fully polarized in opposite directions, are joined and then time-evolved with a homogeneous Hamiltonian [43, 145–148]. After such a DW quench, a logarithmic entanglement growth was found in free-fermion chains [52, 53]. In the geometric quench [54, 55], a fully polarized half chain and a half chain in its ground state at zero magnetization are joined, leading to a logarithmic growth of entanglement as well (see [55] and chapter 3 for details).

We can also alter the local quench setup by breaking the translational invariance of the time evolution Hamiltonian. This is done by connecting the two free-fermion half chains via a defect with a hopping λ , where $\lambda = 1$ would correspond to the homogeneous case considered in the previous subsection. Such a local quench across a defect leads to a logarithmic entropy increase [64, 66]. In general, a hopping defect typically breaks the integrability of the system, thus, most results exist for free-fermion chains [63–65]. For the Ising chain [150], a generalization of Eq. (2.7.10) with an effective central charge, depending on the defect strength, was found. Further studies considered a defect connecting two XXZ chains [151] as well as the connection of more complicated defects connecting two noninteracting chains [152, 153].

The entanglement behaviour is completely different, if we consider an inhomogeneous initial setup i.e., if the left and the right chain have a different initial filling and are then connected via a defect. In that case, a linear increase of entanglement is observed [64]. This setup is then described by an ansatz similar to the quasiparticle ansatz introduced above, where now quasiparticles are transmitted

or reflected from the defect. However, in contrast to the global quench, there is a steady production of quasiparticles due to the particle current induced by the unequal fillings and the quasiparticles are only created at the defect.

Let us now sum up the results on quantum quenches from this section. A global quench is usually followed by a linear increase of entropy with time, which can be described instructively in the quasiparticle picture. In the case of a local quench or the geometric quench, a weaker, usually logarithmic, growth of entanglement entropy in time is observed. This is due to the fact that the excess energy of the quench is much higher for the global quench compared to the local quench scenario. A linear increase of entropy can also be observed for a biased quench where two half chains with different fillings are connected via a defect. For further reading we refer to the review articles [21, 24, 26, 154] and references therein.

A different way of exciting the ground state is by inserting a local fermionic operator. Local operator insertions were first studied within a CFT [80–82], based on the CFT approach introduced in section 2.6. Moreover, they have been considered for various setups [87, 89, 90, 155–157]. However, previous works only considered local operator insertions in non-interacting spin chains like the Ising chain [88], the XX chain [89] or the XY chain [90, 91]. The details of our explicit calculation of the excess entropy after certain operator insertions in the interacting XXZ chain can be found in chapter 5.

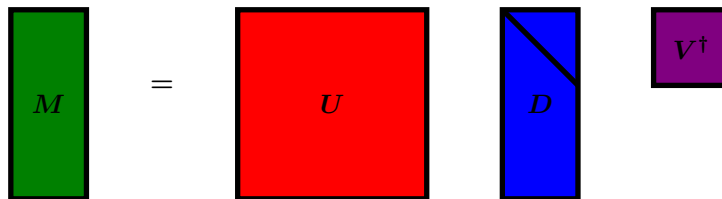


Figure 2.3: Graphical depiction of an SVD. The diagonal line in D depicts the singular values of M .

2.8 Matrix Product States

This section introduces the concept of matrix product states (MPS) and largely follows [12]. At first, we will introduce the idea of a singular value decomposition (SVD) to then construct MPS by subsequently applying SVDs. After that we will shortly discuss matrix product operators (MPOs) and finally see why MPS are especially powerful in 1D.

We start by introducing the SVD. Via an SVD, an arbitrary matrix M of size $D_A \times D_B$ can be decomposed into

$$M = UDV^\dagger, \quad (2.8.1)$$

where the matrices have the following properties:

- U is a matrix of size $D_A \times D_A$ fulfilling $U^\dagger U = \mathbb{1}$.
- D is a diagonal matrix of size $D_A \times D_B$. The non-negative entries of D are the so-called singular values. The number of non-zero singular values is called the (Schmidt) rank r of M . The singular values d_i can be brought into an descending order i.e. $d_1 \geq d_2 \cdots \geq d_r > 0$.
- V^\dagger is a matrix of size $D_B \times D_B$ and fulfills $V^\dagger V = \mathbb{1}$.

The computational cost of an SVD is given by $\mathcal{O}(\max(D_A, D_B)^3)$. A graphical depiction of the SVD can be found in Fig. 2.3. We will first use the SVD to derive the Schmidt decomposition of an arbitrary state. Let us consider a spin chain with a bipartition consisting of regions A and B and the corresponding orthonormal

basis sets $|i\rangle_A$ and $|j\rangle_B$. If the whole system is in a pure state, this state can be written as

$$|\psi\rangle = \sum_{i,j} c_{i,j} |i\rangle_A |j\rangle_B . \quad (2.8.2)$$

We can now consider $c_{i,j}$ as a matrix and perform an SVD on it:

$$c_{i,j} = (UDV^\dagger)_{i,j} . \quad (2.8.3)$$

Writing this equation componentwise with d_i being the singular values and r being the rank of $c_{i,j}$ gives

$$c_{i,j} = \sum_{\alpha=1}^r d_\alpha U_{i\alpha} (V^\dagger)_{\alpha j} . \quad (2.8.4)$$

As U and V are unitary, we can perform the basis transformations $|A\rangle_\alpha = \sum_i U_{i\alpha} |i\rangle_A$ and $|B\rangle_\alpha = \sum_j (V^\dagger)_{\alpha j} |j\rangle_B$ in order to express $|\psi\rangle$ in a new basis:

$$|\psi\rangle = \sum_{\alpha=1}^r d_\alpha |A\rangle_\alpha |B\rangle_\alpha . \quad (2.8.5)$$

This is the so-called Schmidt decomposition of a state $|\psi\rangle$ into two subsystems. This decomposition always exists and from the normalization $\langle\psi|\psi\rangle = 1$ it follows that

$$\sum_{\alpha} d_\alpha^2 = 1 . \quad (2.8.6)$$

We can now use the SVD to decompose an arbitrary quantum state into an MPS. We start from an arbitrary state on a chain with L sites: (cf. Eq. (2.1.7))

$$|\psi\rangle = \sum_{\boldsymbol{\sigma}} c_{\boldsymbol{\sigma}} |\boldsymbol{\sigma}\rangle , \quad (2.8.7)$$

where we have again used the notation $\boldsymbol{\sigma} = \sigma_1 \sigma_2 \dots \sigma_L$. The coefficient vector $c_{\boldsymbol{\sigma}}$ with 2^L elements gets now reshaped into a matrix Ψ of dimension $(2 \times 2^{L-1})$:

$$\Psi_{\sigma_1, (\sigma_2, \dots, \sigma_L)} = c_{\sigma_1 \dots \sigma_L} . \quad (2.8.8)$$

Note that this factor 2 is due to the fact that we focus exclusively on spin-1/2 chains with a local Hilbert space dimension of 2 on each site. Applying an SVD on Ψ gives

$$\Psi_{\sigma_1, (\sigma_2, \dots, \sigma_L)} = \sum_{\alpha_1} U_{\sigma_1, \alpha_1} D_{\alpha_1, \alpha_1} (V^\dagger)_{\alpha_1, (\sigma_2, \dots, \sigma_L)} = \sum_{\alpha_1} U_{\sigma_1, \alpha_1} c_{\alpha_1 \sigma_2, \dots, \sigma_L} . \quad (2.8.9)$$

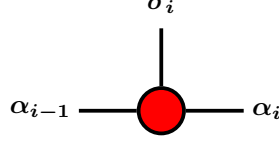


Figure 2.4: Graphical depiction of $A_{\alpha_{i-1}, \alpha_i}^{\sigma_i}$ with the physical spin index σ_i and the link indices α_{i-1} and α_i .

We now decompose U_{σ_1, α_1} into a collection of 2 row vectors A^{σ_1} with entries $A_{\alpha_1}^{\sigma_1} = U_{\sigma_1, \alpha_1}$ and reshape $c_{\alpha_1 \sigma_2, \dots, \sigma_L}$ into a matrix $\Psi_{(\alpha_1 \sigma_2), (\sigma_3, \dots, \sigma_L)}$ and obtain

$$c_{\sigma_1 \dots \sigma_L} = \sum_{\alpha_1} A_{\alpha_1}^{\sigma_1} \Psi_{(\alpha_1 \sigma_2), (\sigma_3, \dots, \sigma_L)}. \quad (2.8.10)$$

Applying another SVD on Ψ gives

$$\begin{aligned} c_{\sigma_1 \dots \sigma_L} &= \sum_{\alpha_1} \sum_{\alpha_2} A_{\alpha_1}^{\sigma_1} U_{(\alpha_1, \sigma_2), \alpha_2} D_{\alpha_2, \alpha_2} (V^\dagger)_{\alpha_2, (\sigma_3, \dots, \sigma_L)} \\ &= \sum_{\alpha_1} \sum_{\alpha_2} A_{\alpha_1}^{\sigma_1} A_{\alpha_1, \alpha_2}^{\sigma_2} \Psi_{(\alpha_2 \sigma_3), \sigma_4, \dots, \sigma_L}. \end{aligned} \quad (2.8.11)$$

Subsequently applying SVDs eventually leads to

$$c_{\boldsymbol{\sigma}} = \sum_{\alpha_1, \dots, \alpha_{L-1}} A_{\alpha_1}^{\sigma_1} A_{\alpha_1, \alpha_2}^{\sigma_2} \dots A_{\alpha_{L-2}, \alpha_{L-1}}^{\sigma_{L-1}} A_{\alpha_{L-1}}^{\sigma_L}. \quad (2.8.12)$$

Using a more compact notation where we omit the α_i indices indicating the matrix multiplications, we end up with $|\psi\rangle$ being represented as an MPS:

$$|\psi\rangle = \sum_{\boldsymbol{\sigma}} A^{\sigma_1} A^{\sigma_2} \dots A^{\sigma_{L-1}} A^{\sigma_L} |\boldsymbol{\sigma}\rangle. \quad (2.8.13)$$

Due to the subsequent application of SVDs and $U^\dagger U = \mathbb{1}$, it follows that

$$\sum_{\sigma_i} (A^{\sigma_i})^\dagger A^{\sigma_i} = \mathbb{1} \quad (2.8.14)$$

which is the definition of left-normalized matrices. An MPS which consists only of left-normalized matrices is called left-canonical. Of course, the decomposition

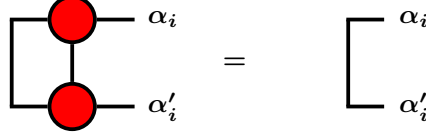


Figure 2.5: Graphical depiction of Eq. (2.8.14). The right-hand side means nothing but $\delta_{\alpha_i, \alpha'_i}$.

of an arbitrary state as it was done above could also be done from the right-hand side starting on site L . If a completely analogous decomposition is done from the right-hand side, one finally obtains an MPS of the form

$$|\psi\rangle = \sum_{\sigma} B^{\sigma_1} B^{\sigma_2} \dots B^{\sigma_{L-1}} B^{\sigma_L} |\sigma\rangle, \quad (2.8.15)$$

where now the B -matrices are right-normalized matrices fulfilling

$$\sum_{\sigma_i} B^{\sigma_i} (B^{\sigma_i})^\dagger = \mathbb{1}. \quad (2.8.16)$$

Analogously, an MPS consisting only of right-normalized matrices is called right-canonical. Using both left- and right-normalized matrices, one can construct a mixed-canonical MPS which is of the form

$$|\psi\rangle = \sum_{\sigma} A^{\sigma_1} \dots A^{\sigma_{i-1}} M^{\sigma_i} B^{\sigma_{i+1}} \dots B^{\sigma_L} |\sigma\rangle, \quad (2.8.17)$$

where there are left-normalized matrices up to site i and right-normalized matrices to the right of i . On the so-called orthogonality center, there is a general matrix M^{σ_i} . Having such a mixed-canonical MPS makes it very easy to calculate the expectation value of a local operator. A local operator, acting on a single site i only, reads

$$\hat{O}^i = \sum_{\sigma_i, \sigma'_i} O^{\sigma_i, \sigma'_i} |\sigma_i\rangle \langle \sigma'_i|. \quad (2.8.18)$$

Due to the mixed-canonical nature of $|\psi\rangle$, all sites left and right to site i can be contracted and the expectation value is simply given by

$$\langle \psi | \hat{O}^i | \psi \rangle = \sum_{\sigma_i, \sigma'_i} O^{\sigma_i, \sigma'_i} \text{Tr} \left(M^{\sigma_i \dagger} M^{\sigma'_i} \right) \quad (2.8.19)$$

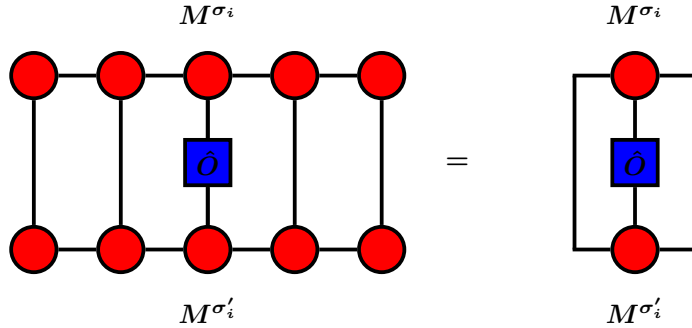


Figure 2.6: Contraction of the tensor network through subsequent contraction from left and right according to Eqs. (2.8.14) and (2.8.16) delivers the expectation value of the local operator \hat{O} from Eq. (2.8.19).

which is depicted graphically in Fig. 2.6. Due to the local Hilbert space dimension 2, one has two matrices M^\uparrow and M^\downarrow on each site where M can e.g. be A or B for a normalized MPS. However, the representation is not unique as we can always replace $M^{\sigma_i} M^{\sigma_{i+1}}$ with $(M^{\sigma_i} X)(X^{-1} M^{\sigma_{i+1}})$. Using the algorithm introduced above, we can in principle describe an arbitrary state with an MPS by subsequently applying SVDs. However, for an arbitrary state, the matrices in the middle of the chain would reach an exponentially large maximum rank of up to $2^{L/2}$. As this would computationally not be feasible, we have to truncate the M -matrices. This is done by discarding small singular values d_i for $i > i_0$. The truncation can either be defined by a threshold ϵ (e.g. 10^{-10}) below which the singular values are discarded or one can set a maximum matrix dimension χ_{\max} beyond which the singular values are discarded. The quality of the approximation is determined by the truncated (or discarded) weight

$$w = 1 - \sum_i^{\chi_{\max}} d_i^2 \quad (2.8.20)$$

which should stay below a defined value. As the singular values are normalized, they have to be re-normalized after truncation as $d_i \mapsto d_i/\sqrt{1-w}$.

The decisive question now is how large the matrices have to be to accurately describe a state. This question is also related to the entanglement entropy of the state. The discarded weight will be small if the singular values decay very quickly. This is true if the entanglement entropy $S_A = -\sum_i d_i^2 \ln(d_i^2)$ (cf. Eq. (2.5.7)) is

small. The maximum entanglement entropy of a reduced density matrix of Hilbert space dimension χ is $S_{\max} = \ln(\chi)$ which means that the matrix size needed can be roughly estimated as

$$\chi_{\max} \approx e^{S_A}. \quad (2.8.21)$$

The simulability of states with an MPS was investigated in [158]. It was found that an at most logarithmic scaling with interval length of the $S_{\alpha < 1}$ Rényi entropy means that the state can be well approximated by an MPS.

Let us now consider ground states in one dimension. Here, the border of a bipartition between A and B is independent of the interval length. Due to the area law [6], which is valid for local and gapped Hamiltonians in 1D [7], the entanglement is then limited by a constant. Thus, ground states of 1D systems with a gapped Hamiltonian can be well approximated by an MPS. Even at criticality, χ_{\max} only grows polynomially with chain length L . The state can be approximated with a small bond dimension, if the eigenvalues of the reduced density matrix decay fast [159]. Indeed, those eigenvalues were found to decay roughly exponentially fast for gapped integrable systems [160, 161]. In two dimensions, the border between subsystems A and B is a line. Thus, the length of the border now depends on the linear subsystem size L which means that the von Neumann entropy is also proportional to L and χ_{\max} grows exponentially as $\chi_{\max} \approx e^L$. As the entanglement scales with the boundary surface area, this relation is called the area law [6]. However, there are states where S_1 fulfills an area law, which still cannot be efficiently approximated by an MPS [158].

Note that the area law is only valid for ground states. Time evolutions, like the global quench discussed in section 2.7.1, can easily lead to exponentially growing bond dimensions in an MPS. In such numerical simulations, the Rényi entropy contains information about the necessary computational effort [158] and therefore limits the feasible simulation time.

The area law in the context of MPS ground states in one dimension will be further discussed in the next section which introduces the ground state search applying the density-matrix renormalization group.

2.9 Density-Matrix Renormalization Group

The density-matrix renormalization group (DMRG) was introduced by Steve White in 1991 [10, 11]. DMRG is based on renormalization group methods and is able to perform extremely accurate ground state calculations for 1D systems [162]. The power of DMRG lies in the fact that, although a general state would need an exponential number of parameters to be exactly described, ground states in one-dimensional systems can be described using relatively few parameters. Those relevant states can be imagined as occupying only a very small corner of the exponentially large Hilbert space of the system. This comes from the fact that the eigenvalues of the reduced density matrix decay exponentially fast. In other words, we assume that there is a reduced state space which can describe the relevant physics. Such a reduced space exists for all short-ranged Hamiltonians in 1D and can be parametrized efficiently using MPS [12]. The connection between DMRG and MPS was found in 1995, when Östlund and Rommer realized that the ground state obtained via DMRG can be written as an MPS [13]. The DMRG algorithm works best for systems with open boundary conditions and, as DMRG is a variational method, can be applied to both fermionic and bosonic systems. Its performance can be improved by exploiting the symmetries of the quantum system.

This section largely follows the exhaustive review by Schollwöck [12]. After a short discussion of ground state search in general, in the following subsections, we are going to first discuss iDMRG and then the related DMRG algorithm for finite systems. After that, we explicitly discuss the implementation of the DMRG algorithm for matrix product states. Finally, we are going to discuss the time-dependent DMRG (tDMRG) algorithm which can be applied to perform unitary time evolutions.

Calculating the ground state energy of a state $|\psi\rangle$ means nothing else but minimizing the functional

$$\frac{\langle\psi|\hat{H}|\psi\rangle}{\langle\psi|\psi\rangle}. \tag{2.9.1}$$

Although it would be rather inefficient, in principal it is possible to obtain the ground state by simply performing an imaginary time evolution. A much more efficient way is via a variational search. To perform this variational search, we want to express an operator (like the Hamiltonian) as a Matrix Product Operator

(MPO). Analogously to an MPS, we will describe an MPO as

$$\hat{O} = \sum_{\boldsymbol{\sigma}, \boldsymbol{\sigma}'} W^{\sigma_1 \sigma'_1} W^{\sigma_2 \sigma'_2} \dots W^{\sigma_L \sigma'_L} |\boldsymbol{\sigma}\rangle \langle \boldsymbol{\sigma}'|, \quad (2.9.2)$$

with $\boldsymbol{\sigma} = \sigma_1 \sigma_2 \dots \sigma_L$. Now having the MPO formulation of an operator at hand, we can discuss the DMRG procedure in detail.

2.9.1 iDMRG

In iDMRG, a chain is subsequently built up by adding sites to eventually obtain the ground state of an infinite system. We start with a very small system consisting of blocks A and B which can e.g. each consist of only one site. We then add a single site to each block, increasing the length of the chain by 2. By adding sites, we also increase the Hilbert space of the whole chain and if we did not truncate, the Hilbert space would blow up exponentially up to 2^L for a spin-1/2 chain. As this is computationally not feasible for large systems, we first choose a maximum bond dimension χ_{\max} for the blocks. For each chain length we now want to find the ground state at the current length and also truncate the newly obtained blocks. After adding two sites to the initial blocks, we obtain the superblock $A \bullet \bullet B$. An arbitrary state of this superblock can be written as

$$|\psi\rangle = \sum_{a_A \sigma_A \sigma_B a_B} \psi_{a_A \sigma_A \sigma_B a_B} |a\rangle_A |\sigma\rangle_A |\sigma\rangle_B |a\rangle_B = \sum_{i_A j_B} \psi_{i_A, j_B} |i\rangle_A |j\rangle_B, \quad (2.9.3)$$

where the right-hand side could be decomposed to a Schmidt decomposition as in Eq. (2.8.5) via an SVD. Using a suitable numerical diagonalization algorithm, we can find the state that minimizes

$$\frac{\langle \psi | \hat{H}_{A \bullet \bullet B} | \psi \rangle}{\langle \psi | \psi \rangle}. \quad (2.9.4)$$

The basis of the new block $A \bullet$ now has dimension $2\chi_{\max}$ where the 2 is coming from the added spin-1/2 site. To truncate the dimension of the newly built block to χ_{\max} again, we calculate the reduced density matrix as

$$\rho_{A \bullet} = \text{Tr}_{\bullet B} (|\psi\rangle \langle \psi|). \quad (2.9.5)$$

The RDM can now be truncated by keeping only the χ_{\max} largest singular values assuring the best possible approximation for the given bond dimension.

2.9.2 DMRG

Now let us turn to the finite size DMRG. Here, the growth of block B works in the same way as described above for iDMRG: A site is added, the ground state of the new block $\bullet B$ is calculated, the reduced density matrix is obtained and the Hilbert space of the new block gets truncated. However, in DMRG, the size of the whole chain does not change as the site added to B is taken from A . This can be done until A only consists of a single site. After that, the direction is reversed and now A grows at the expense of B until B only consists of a single site. This process is called sweeping. One performs sweeps until the energy of the whole system is converged. Fig. 2.7 visualizes the sweeping during DMRG.

Suppose that we knew the exact ground state density matrix $\rho_0 = |\psi_0\rangle\langle\psi_0|$. In that case, the optimal approximation would be to keep the χ_{\max} largest singular values. Thus, the quality of our approximation depends on how quickly the singular values decrease. These reduced density matrix spectra have been studied in certain exactly solved systems [160, 161] and it was found that in general, the eigenvalues decay approximately exponentially fast for ground states of integrable, gapped one-dimensional systems. A fast decay of the eigenvalue spectrum leads to a low entropy. Furthermore, the area law [6] limits the ground state entropy for local, gapped Hamiltonians and thus explains the success of DMRG in 1D. Usually, a χ_{\max} of $\mathcal{O}(100)$ (or even smaller) is sufficient to obtain a discarded weight w smaller than 10^{-10} in the variational ground state search [12].

2.9.3 DMRG in the context of MPS

In this section, we are going to discuss how the DMRG algorithm is actually implemented for a system represented by an MPS. This section will largely follow the PhD thesis by Martin Ganahl [163] as well as the review by Schollwöck [12]. To find the minimum of the energy, we are using the method of Lagrangian multipliers:

$$\langle\psi|\hat{H}|\psi\rangle - \lambda\langle\psi|\psi\rangle. \quad (2.9.6)$$

At first sight, this problem seems very hard as the variables (given by the matrices M^σ) are given as products. However, just like in the DMRG algorithm described above, we can consider only the matrix on site i , M^{σ_i} , while keeping all the other matrices fixed. Now, the minimum in energy can be found with respect to this matrix M^{σ_i} which will lower the energy but certainly not lead to the

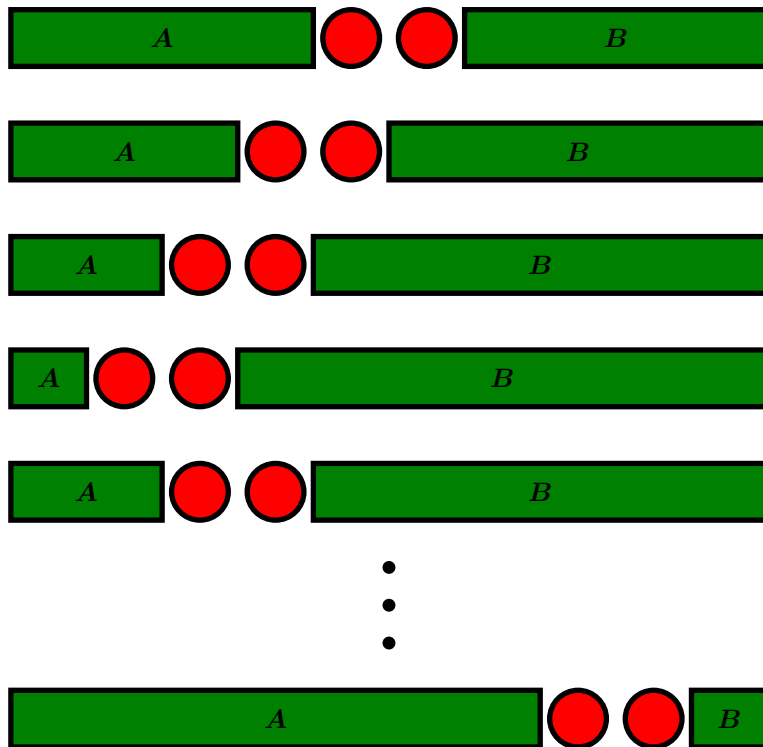


Figure 2.7: Graphical depiction of the sweeps during the DMRG algorithm as described in the text.

Density-Matrix Renormalization Group

global minimum. However, one then moves on to the next site, say $i + 1$, and minimizes the energy with respect to $M^{\sigma_{i+1}}$. In that way, we can iteratively find the ground state by moving through all sites multiple times until the energy has finally converged.

We start with an MPS in the mixed canonical representation, given by

$$|\psi\rangle = \sum_{\sigma} A^{\sigma_1} \dots A^{\sigma_{i-1}} \Psi^{\sigma_i} B^{\sigma_{i+1}} \dots B^{\sigma_L} |\sigma\rangle. \quad (2.9.7)$$

The expectation value of the Hamiltonian \hat{H} in MPS/MPO language leads to a partition of the tensor network where we have parts L and R corresponding to blocks A and B as well as W corresponding to the center site. All the sites left to the central site have been contracted within L and all the sites to the right of the central site have been contracted into R .

$$L_{\beta_{i-1}}^{\alpha_{i-1}, \alpha'_{i-1}} = \left(\sum_{\sigma_1 \sigma'_1} A_{1, \alpha_1}^{\sigma_1 *} W_{1, \beta_1}^{\sigma_1 \sigma'_1} A_{1, \alpha'_1}^{\sigma'_1} \right) \dots \left(\sum_{\sigma_{i-1} \sigma'_{i-1}} A_{\alpha_{i-2}, \alpha_{i-1}}^{\sigma_{i-1} *} W_{\beta_{i-2}, \beta_{i-1}}^{\sigma_{i-1} \sigma'_{i-1}} A_{\alpha'_{i-2}, \alpha'_{i-1}}^{\sigma'_{i-1}} \right)$$

$$R_{\beta_i}^{\alpha_i, \alpha'_i} = \left(\sum_{\sigma_{i+1} \sigma'_{i+1}} B_{\alpha_i, \alpha_{i+1}}^{\sigma_{i+1} *} W_{\beta_i, \beta_{i+1}}^{\sigma_{i+1} \sigma'_{i+1}} B_{\alpha'_i, \alpha'_{i+1}}^{\sigma'_{i+1}} \right) \dots \left(\sum_{\sigma_L \sigma'_L} B_{\alpha_{L-1}, 1}^{\sigma_L *} W_{\beta_{L-1}, 1}^{\sigma_L \sigma'_L} B_{\alpha'_{L-1}, 1}^{\sigma'_L} \right) \quad (2.9.8)$$

This makes it possible to write the matrix elements of \hat{H} as

$$\langle \alpha_{i-1} \sigma_i \alpha_i | \hat{H} | \alpha'_{i-1} \sigma'_i \alpha'_i \rangle = \sum_{\beta_{i-1} \beta_i} L_{\beta_{i-1}}^{\alpha_{i-1}, \alpha'_{i-1}} W_{\beta_{i-1}, \beta_i}^{\sigma_i, \sigma'_i} R_{\beta_i}^{\alpha_i, \alpha'_i} \quad (2.9.9)$$

which is depicted in Fig. 2.8. To now tackle Eq. (2.9.6), we first need the overlap which is given by

$$\langle \psi | \psi \rangle = \sum_{\sigma_i} \Psi_{\alpha_{i-1}, \alpha'_{i-1}}^A M_{\alpha_{i-1}, \alpha_i}^{\sigma_i *} M_{\alpha'_{i-1}, \alpha'_i}^{\sigma_i} \Psi_{\alpha_i, \alpha'_i}^B, \quad (2.9.10)$$

where

$$\Psi_{\alpha_{i-1}, \alpha'_{i-1}}^A = \sum_{\sigma_1 \dots \sigma_{i-1}} (M^{\sigma_{i-1} \dagger} \dots M^{\sigma_1 \dagger} M^{\sigma_1} \dots M^{\sigma_{i-1}})_{\alpha_{i-1}, \alpha'_{i-1}}$$

$$\Psi_{\alpha_i, \alpha'_i}^B = \sum_{\sigma_{i+1} \dots \sigma_L} (M^{\sigma_{i+1}} \dots M^{\sigma_L} M^{\sigma_L \dagger} \dots M^{\sigma_{i+1} \dagger})_{\alpha'_i, \alpha_i}. \quad (2.9.11)$$

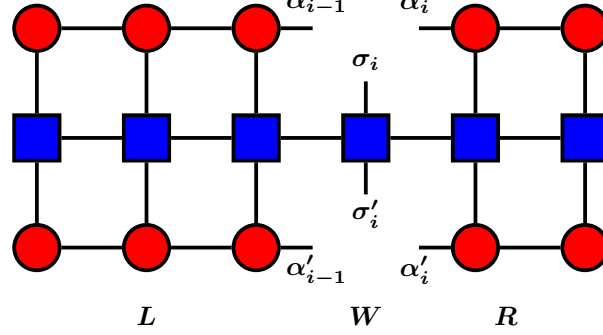


Figure 2.8: Graphical depiction of $\langle \alpha_{i-1} \sigma_i \alpha_i | \hat{H} | \alpha'_{i-1} \sigma'_i \alpha'_i \rangle$ in the context of MPS/MPO. The whole tensor network now consists of the left block L , the right block R and the central block W .

Having \hat{H} in MPO language at hand, we can also write $\langle \psi | \hat{H} | \psi \rangle$ as

$$\langle \psi | \hat{H} | \psi \rangle = \sum_{\sigma_i \sigma'_i} L_{\beta_{i-1}}^{\alpha_{i-1}, \alpha'_{i-1}} W_{\beta_{i-1}, \beta_i}^{\sigma_i, \sigma'_i} R_{\beta_i}^{\alpha_i, \alpha'_i} M_{\alpha_{i-1}, \alpha_i}^{\sigma_i *} M_{\alpha'_{i-1}, \alpha'_i}^{\sigma'_i}. \quad (2.9.12)$$

Plugging those results into Eq. (2.9.6), we obtain

$$\sum_{\sigma_i \sigma'_i} L_{\beta_{i-1}}^{\alpha_{i-1}, \alpha'_{i-1}} W_{\beta_{i-1}, \beta_i}^{\sigma_i, \sigma'_i} R_{\beta_i}^{\alpha_i, \alpha'_i} M_{\alpha_{i-1}, \alpha_i}^{\sigma_i *} M_{\alpha'_{i-1}, \alpha'_i}^{\sigma'_i} - \lambda \sum_{\sigma_i} \Psi_{\alpha_{i-1}, \alpha'_{i-1}}^A M_{\alpha_{i-1}, \alpha_i}^{\sigma_i *} M_{\alpha'_{i-1}, \alpha'_i}^{\sigma_i} \Psi_{\alpha_i, \alpha'_i}^B = 0 \quad (2.9.13)$$

which is an eigenvalue problem that can be solved quite easily as it can be reshaped to a generalized eigenvalue problem of the form

$$Hv - \lambda Nv = 0. \quad (2.9.14)$$

We can now solve this equation and obtain the lowest eigenvalue λ_0 , which is the current ground state energy estimate and $M_{\alpha_{i-1}, \alpha_i}^{\sigma_i}$ is the corresponding matrix on site i . As we are only interested in the lowest eigenvalue, we can apply suitable methods like Lanczos or Jacobi-Davidson algorithms for large sparse matrices. The algorithm basically now works as follows:

Density-Matrix Renormalization Group

- Start from an initial guess for $|\psi\rangle$ that is right-normalized.
- Perform a right sweep: Starting from $i = 1$, move through all sites and solve the eigenproblem for M^{σ_i} . After the optimization, apply an SVD to left-normalize M^{σ_i} into A^{σ_i} . The remainder of the SVD is multiplied onto the right which then serves as the starting point for the optimization of $M^{\sigma_{i+1}}$.
- After having moved until $i = L - 1$, start the left sweep on site $i = L$: Again solve the eigenvalue problem on each site. But now, after the optimization, one right-normalizes M^{σ_i} into B^{σ_i} and multiplies the remainder of the SVD onto the left. This will then be the starting guess for the next site.
- Repeat right and left sweeps until the energy of the system has converged.

2.9.4 tDMRG

Starting from an arbitrary state $|\psi(t = 0)\rangle$, tDMRG is a powerful tool to time-evolve the state unitarily as

$$|\psi(t)\rangle = e^{-i\hat{H}t} |\psi(t = 0)\rangle . \quad (2.9.15)$$

By simply exchanging the expression in the exponential function, one can perform an imaginary time evolution as

$$|\psi_\beta\rangle = e^{-\beta\hat{H}} |\psi_0\rangle \quad (2.9.16)$$

which can be used to obtain the ground state of a system. The method which we are now going to introduce works for both real and imaginary time evolution.

The time-evolution via time-evolving block decimation (TEBD) was first introduced by Vidal [164]. Soon afterwards, the time-dependent density-matrix renormalization group (tDMRG) was introduced [56, 57]. The differences between those methods are very subtle and both of them are based on MPS. A review on time-evolution methods for MPS can be found in [165]. In the present thesis, we applied tDMRG for all time evolutions.

To perform a time evolution, we first have to perform a Trotter decomposition. We are assuming that our Hamiltonian has nearest-neighbor interactions only, i.e., $\hat{H} = \sum_i \hat{h}_i$ where each \hat{h}_i acts on sites i and $i + 1$ only. This is e.g. true for the

XXZ Hamiltonian (2.2.1). We have to discretize the time evolution in timesteps δt such that $t = N\delta t$ which leads to a first-order Trotter decomposition:

$$e^{-i\hat{H}\delta t} = e^{-i\hat{h}_1\delta t} e^{-i\hat{h}_2\delta t} \dots e^{-i\hat{h}_{L-1}\delta t} + \mathcal{O}((\delta t)^2). \quad (2.9.17)$$

The error comes from the fact that \hat{h}_i and \hat{h}_{i+1} in general do not commute. However, the time evolutions on all even (odd) bonds commute with each other and can therefore be carried out simultaneously. This leads to the following time evolution:

$$|\psi(t + \delta t)\rangle = e^{-i\hat{H}_{\text{even}}\delta t} e^{-i\hat{H}_{\text{odd}}\delta t} |\psi(t)\rangle. \quad (2.9.18)$$

However, this can be simply improved by performing a second-order Trotter decomposition as

$$e^{-i\hat{H}\delta t} = e^{-i\hat{H}_{\text{odd}}\delta t/2} e^{-i\hat{H}_{\text{even}}\delta t} e^{-i\hat{H}_{\text{odd}}\delta t/2} + \mathcal{O}((\delta t)^3). \quad (2.9.19)$$

As we have now defined a way of performing the time evolution on all sites, for the rest of the discussion it is sufficient to only consider the time evolution on sites $i + 1$ and $i + 2$ for one timestep performed by applying $e^{-i\hat{h}_{i+1}\delta t}$. The matrix elements of the time evolution operator are denoted as

$$U^{\sigma_{i+1}\sigma_{i+2}, \sigma'_{i+1}\sigma'_{i+2}} = \langle \sigma_{i+1}\sigma_{i+2} | e^{-i\hat{h}_{i+1}\delta t} | \sigma'_{i+1}\sigma'_{i+2} \rangle. \quad (2.9.20)$$

This operator can now be applied on the mixed canonical state

$$|\psi\rangle = \sum_{\boldsymbol{\sigma}} A^{\sigma_1} \dots A^{\sigma_i} \Psi^{\sigma_{i+1}\sigma_{i+2}} B^{\sigma_{i+3}} \dots B^{\sigma_L} |\boldsymbol{\sigma}\rangle \quad (2.9.21)$$

which turns $\Psi^{\sigma_{i+1}\sigma_{i+2}}$ into

$$\Phi^{\sigma_{i+1}\sigma_{i+2}} = \sum_{\sigma'_{i+1}\sigma'_{i+2}} U^{\sigma_{i+1}\sigma_{i+2}, \sigma'_{i+1}\sigma'_{i+2}} \Psi^{\sigma_{i+1}\sigma_{i+2}}. \quad (2.9.22)$$

As we have now successfully applied $e^{-i\hat{h}_{i+1}\delta t}$, we now want to move on with $e^{-i\hat{h}_{i+3}\delta t}$. However, before we can do so, we have to bring the state $|\phi\rangle = e^{-i\hat{h}_{i+1}\delta t} |\psi\rangle$ into the form

$$|\phi\rangle = \sum_{\boldsymbol{\sigma}} A^{\sigma_1} \dots A^{\sigma_{i+2}} \Phi^{\sigma_{i+3}\sigma_{i+4}} B^{\sigma_{i+5}} \dots B^{\sigma_L} |\boldsymbol{\sigma}\rangle \quad (2.9.23)$$

Density-Matrix Renormalization Group

on which we can then apply $e^{-i\hat{h}_{i+3}\delta t}$. This is again done by performing SVDs: At first, $A^{\sigma_{i+1}}$ is extracted from the left of $\Phi^{\sigma_{i+1}\sigma_{i+2}}$ and then, $B^{\sigma_{i+3}}$ is multiplied from the right to obtain $\Phi^{\sigma_{i+2}\sigma_{i+3}}$. Similarly, we again perform an SVD, split of $A^{\sigma_{i+2}}$ from the left and multiply $B^{\sigma_{i+4}}$ from the right to end up with Eq. (2.9.23). In that way, we can perform the local time-evolution steps throughout the whole chain.

Chapter 3

Magnetization and entanglement after a geometric quench in the XXZ chain (Phys. Rev. B 99, 174403 (2019))

In this chapter we present our findings from Ref. [149], which is one of the main publications of the author. In the following, the abstract and the sections II. - VII. of the paper, which contain the used methods, the obtained results as well as the conclusions, are completely included in sections 3.1 - 3.7 of the present thesis. The appendix was also taken from the paper and can be found in A.1.

The paper was written to equal parts by the author of this thesis and Viktor Eisler. All the calculations in the paper, except for the analytical XX chain results in 3.4.1 and 3.5.1 and the perturbation results in A.1, were performed by the author of this thesis. Both authors contributed equally to the interpretation of the results.

3.1 Abstract

We investigate the dynamics of the XXZ spin chain after a geometric quench, which is realized by connecting two half chains prepared in their ground states with zero and maximum magnetizations, respectively. The profiles of magnetization after the subsequent time evolution are studied numerically by density-matrix

renormalization group methods, and a comparison to the predictions of generalized hydrodynamics yields a very good agreement. We also calculate the profiles of entanglement entropy and propose an ansatz for the noninteracting XX case, based on arguments from conformal field theory. In the general interacting case, the propagation of the entropy front is studied numerically both before and after the reflection from the chain boundaries. Finally, our results for the magnetization fluctuations indicate a leading order proportionality relation to the entanglement entropy.

3.2 Model and setup

We consider the XXZ spin chain that is given by the Hamiltonian

$$H = J \sum_{j=1}^{L-1} (S_j^x S_{j+1}^x + S_j^y S_{j+1}^y + \Delta S_j^z S_{j+1}^z) \quad (3.2.1)$$

where S_j^α are spin-1/2 operators acting on site j , J is the coupling, and Δ the anisotropy parameter. We set $J = 1$ and consider open boundary conditions on a chain of length L . The XXZ model is equivalent to a chain of spinless fermions with nearest-neighbor interactions of strength Δ , with $\Delta = 0$ corresponding to the free-fermion point.

The protocol of the geometric quench is illustrated in Fig. 3.1. Initially, the chain is split into two halves and the left-hand side is initialized in the ground state $|GS\rangle$ of an XXZ chain of length $L/2$. On the other hand, the right half chain is prepared in the fully polarized state $|\downarrow\downarrow\downarrow\dots\rangle$, or the vacuum state in the fermionic language. Subsequently, the two half-chains are joined together at $t = 0$ and the system is allowed to evolve unitarily,

$$|\psi(t)\rangle = e^{-iHt} |GS\rangle \otimes |\downarrow\downarrow\downarrow\dots\rangle \quad (3.2.2)$$

governed by the Hamiltonian in Eq. (3.2.1). In other words, we would like to study how the ground state prepared on a half chain expands into vacuum after an instantaneous change of geometry (i.e., the size of the chain), hence the term geometric quench. We are primarily interested in the magnetization $\langle S_j^z \rangle \equiv \langle \psi(t) | S_j^z | \psi(t) \rangle$ and the entanglement profile, as measured by the entanglement entropy between two segments A and B , as depicted in Fig. 3.1.

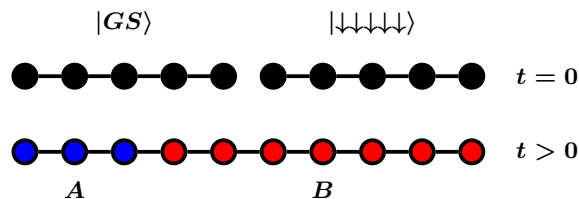


Figure 3.1: Setup of the geometric quench.

The ground state of the XXZ chain can be constructed with the help of the Bethe ansatz [92, 93]. Here we will focus on the regime $|\Delta| < 1$ in which the ground state is a gapless Luttinger liquid [166], and we use the standard parametrization $\Delta = \cos(\gamma)$. The quasiparticle excitations of the XXZ chain are created upon the vacuum state $|\downarrow\downarrow\downarrow\dots\rangle$ and are labeled by their rapidity λ . They satisfy appropriate quantization conditions, as given by the roots of the Bethe equations. In particular, the ground state involves only magnons with real λ , but in general the solutions admit a family of string excitations [92], corresponding to roots parallel to the imaginary axis. In the thermodynamic limit $L \rightarrow \infty$, and in the zero-magnetization sector, the roots on the real axis become continuous and their density $\rho(\lambda)$ satisfies the linear integral equation

$$\rho(\lambda) + \int_{-\infty}^{\infty} \frac{d\mu}{2\pi} \mathcal{K}(\lambda - \mu) \rho(\mu) = \frac{p'(\lambda)}{2\pi}. \quad (3.2.3)$$

Note that the right-hand side of Eq. (3.2.3) contains the derivative of the bare momentum $p'(\lambda) = \theta'_1(\lambda)$, while the integral on the left is due to elastic scattering between quasiparticles, with the kernel $\mathcal{K}(\lambda) = \theta'_2(\lambda)$ being the differential scattering phase. Both of them are given via

$$\theta'_n(\lambda) = \frac{\sin(n\gamma)}{\cosh(\lambda) - \cos(n\gamma)}, \quad n = 1, 2. \quad (3.2.4)$$

In fact, Eq. (3.2.3) is just a simple example of the so-called dressing operation, where a certain function of the rapidity gets modified by the presence of the other quasiparticles. The dressed version f^{dr} of a bare function f is defined as the solution of

$$f^{dr}(\lambda) + \int_{-\infty}^{\infty} \frac{d\mu}{2\pi} \mathcal{K}(\lambda - \mu) n(\mu) f^{dr}(\mu) = f(\lambda), \quad (3.2.5)$$

which is a Fredholm-type integral equation and can be solved numerically [167]. Here, $n(\mu)$ is the occupation function, i.e., the ratio of the particle density (occupied rapidities) and the total root density, including the density of holes (unoccupied rapidities). However, since the XXZ ground state does not contain holes, one has $n(\mu) \equiv 1$. Hence, the root density is just proportional to the derivative of the dressed momentum, $2\pi\rho(\lambda) = p'^{dr}(\lambda)$. Another important quantity we shall need is the dressed quasiparticle energy $e^{dr}(\lambda)$, which follows from (3.2.5), with the bare energy given by

$$e(\lambda) = \frac{-\sin^2(\gamma)}{\cosh(\lambda) - \cos(\gamma)}. \quad (3.2.6)$$

On the numerical side, we carry out density-matrix renormalization group (DMRG) calculations [12], using the ITensor C++ library [168]. The ground-state search is performed by applying DMRG on the left half chain, whereas the vacuum state on the right half chain has a trivial matrix product state representation. After the quench, the time evolution is done by applying tDMRG with a time step of $\delta t = 0.05$, a truncated weight of 10^{-10} , and a maximum bond dimension of $\chi_{max} = 1200$.

3.3 Magnetization Profiles

We start our study of the geometric quench with a discussion of the magnetization profiles. Before presenting our numerical results, we shall introduce an efficient method that has been developed recently for the study of transport in integrable systems.

3.3.1 Generalized hydrodynamics

The understanding of time evolution in integrable models due to initial inhomogeneities has recently come to a breakthrough by the development of generalized hydrodynamics [31, 32]. The idea of GHD is to give an effective description of the dynamics and the underlying state at a hydrodynamic scale. Indeed, in interacting integrable models the quasiparticle excitations are moving freely, experiencing only phase shifts due to the scattering on other quasiparticles. One then assumes that, for large times t and large distances x from the inhomogeneity, a dynamical

equilibrium emerges, and the system is described by a local quasi-stationary state (LQSS).

For the class of initial states, where the inhomogeneity is solely due to the junction of two, otherwise homogeneous states without any inherent length scale, the LQSS depends only on the ray variable $\zeta = \frac{x}{t}$. Assuming that there is only one type of quasiparticles involved (such as for the geometric quench), specifying the LQSS amounts to finding the particle density $\rho_\zeta(\lambda)$ that varies along the rays. The kinetic theory of quasiparticles eventually leads to the continuity equation [31, 32]

$$\partial_t \rho_\zeta(\lambda) + \partial_x (v(\lambda) \rho_\zeta(\lambda)) = 0, \quad (3.3.1)$$

where the velocity $v(\lambda)$ is given by the dressed quasiparticle group velocity

$$v(\lambda) = \frac{e^{dr}(\lambda)}{p^{dr}(\lambda)}. \quad (3.3.2)$$

The GHD equation (3.3.1) could be interpreted as an infinite set of continuity equations for each λ , corresponding to the infinite set of conserved charges that are present for integrable models. Despite its apparent simplicity, one should stress that the solution of (3.3.1) is, in general, nontrivial since the dressed velocity (3.3.2) itself depends on the quasiparticle density. Indeed, the dressing operation (3.2.5) contains information about the full occupation function $n_\zeta(\lambda)$, and thus Eq. (3.3.1) has to be solved self-consistently. However, if the densities depend only on the ray variable ζ , the GHD equation could be shown to simplify to [31, 32]

$$(\zeta - v(\lambda)) \partial_\zeta n_\zeta(\lambda) = 0, \quad (3.3.3)$$

which has the piecewise continuous solution

$$n_\zeta(\lambda) = \Theta(v(\lambda) - \zeta) n_L(\lambda) + \Theta(\zeta - v(\lambda)) n_R(\lambda), \quad (3.3.4)$$

where Θ is the Heaviside step function and $n_{L/R}(\lambda)$ is the initial occupation on the left/right half chain.

The solution (3.3.4) has a clear physical interpretation, namely that the information on the initial occupations gets transported by the quasiparticles. Along a given ray $\zeta > 0$ on the right-hand side of the chain, only the quasiparticles emitted from the left half chain become visible that have sufficient velocity $v(\lambda) > \zeta$ to arrive there. Similarly, for $\zeta < 0$ the quasiparticles are emitted from the right half

Magnetization Profiles

chain and propagate to the left. Thus, for the simple initial states considered here, solving the GHD equation boils down to determining the solution to $v(\lambda) = \zeta$, where the dressing of the velocity is calculated with respect to the occupation function in (3.3.4).

The situation further simplifies for the geometric quench, since the ground-state occupation is given by $n_L(\lambda) = 1$, whereas for the vacuum, one trivially has $n_R(\lambda) = 0$. We shall first assume that the dressed velocity is a monotonically increasing function with a unique solution $v(\lambda_*) = \zeta$ for each ζ and hence

$$n_\zeta(\lambda) = \Theta(\lambda - \lambda_*). \quad (3.3.5)$$

One has thus the condition that the function

$$v(\lambda_*) = \frac{e'^{dr}(\lambda_*)}{p'^{dr}(\lambda_*)} \quad (3.3.6)$$

has to be monotonically increasing, when the dressing is evaluated with the occupation in (3.3.5); i.e., the integrals in (3.2.5) are carried out over $[\lambda_*, \infty)$. The velocity (3.3.6) can be evaluated numerically and the result is shown in Fig. 3.2 for various Δ . One can see clearly, that our assumption is satisfied only for attractive interactions $\Delta < 0$, whereas for the repulsive case $\Delta > 0$ the velocity $v(\lambda_*)$ develops a maximum.

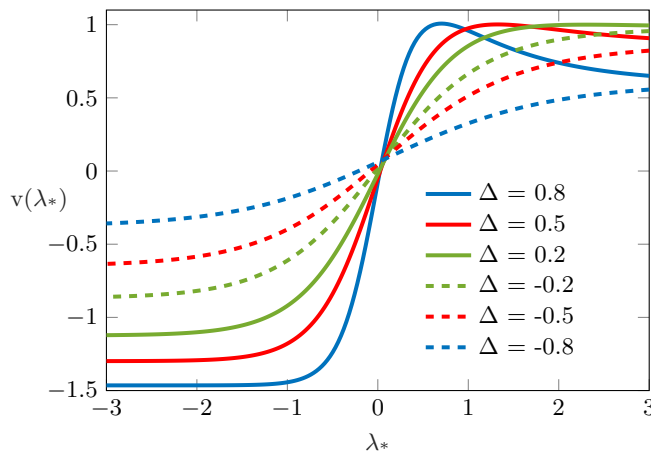


Figure 3.2: Dressed velocity $v(\lambda_*)$ corresponding to the occupation function in Eq. (3.3.5), for several values of Δ .

The above discrepancy can be understood as follows. For $\Delta < 0$, the maximum velocity occurs for $\lambda_* \rightarrow \infty$, which gives the expansion velocity of the front into vacuum. Note that in this limit the occupation (3.3.5) vanishes completely, and thus the group velocity is given by its bare (undressed) value

$$v_0(\lambda) = \frac{e'(\lambda)}{p'(\lambda)} = \frac{\sin(\gamma) \sinh(\lambda)}{\cosh(\lambda) - \cos(\gamma)}. \quad (3.3.7)$$

In particular, one has

$$v_0(\lambda \rightarrow \infty) = \sin(\gamma), \quad (3.3.8)$$

which turns out to be the real maximum for $\Delta < 0$. However, for $\Delta > 0$, the equation $v'_0(\tilde{\lambda}) = 0$ has a nontrivial solution with

$$\cosh(\tilde{\lambda}) = \frac{1}{\Delta}. \quad (3.3.9)$$

The maximum velocity thus occurs at a finite value of the rapidity, and one obtains $v_0(\tilde{\lambda}) = 1$, independently of Δ . Consequently, the ansatz for the occupation function has to be modified as

$$n_\zeta(\lambda) = \Theta(\lambda - \lambda_1)\Theta(\lambda_2 - \lambda), \quad (3.3.10)$$

where the velocities must satisfy

$$v(\lambda_1) = v(\lambda_2) = \zeta. \quad (3.3.11)$$

Note that the rapidities $\lambda_1 < \tilde{\lambda} < \lambda_2$ are located on different sides of the maximum and can be found iteratively.

Interestingly, the GHD solution for the geometric quench yields different vacuum expansion velocities, with the rightmost ray given by $\zeta_{max} = 1$ and $\zeta_{max} = \sin(\gamma)$ for positive and negative values of Δ , respectively. Note, however, that by decreasing ζ , the solution λ_2 of (3.3.11) eventually goes to infinity, and thus the ansatz (3.3.10) actually goes over to (3.3.5) with $\lambda_1 \rightarrow \lambda_*$. In particular, one finds that the minimum of the dressed velocity occurs for $\lambda_* \rightarrow -\infty$ (see Fig. 3.2), where (3.3.5) simply corresponds to the ground-state occupation. Therefore, the leftmost ray is given via the spinon velocity [93]

$$\zeta_{min} = -v_s = -\frac{\pi \sin(\gamma)}{2\gamma}. \quad (3.3.12)$$

Magnetization Profiles

Finally, in order to obtain the magnetization profile, one needs the particle density $\rho_\zeta(\lambda)$. This is given explicitly by

$$\rho_\zeta(\lambda) = n_\zeta(\lambda) \frac{p'^{dr}(\lambda)}{2\pi}, \quad (3.3.13)$$

where the dressing is calculated with an occupation $n_\zeta(\lambda)$ that corresponds to either (3.3.5) or (3.3.10). In turn, the magnetization is given by

$$\langle S^z \rangle = -\frac{1}{2} + \int \rho_\zeta(\lambda) d\lambda. \quad (3.3.14)$$

Although in general the GHD ansatz requires a numerical solution of the integral equations for the dressing, there is one particular regime for which an approximate analytical result can be given. Namely, for $\Delta > 0$ the magnetization profile around the $\zeta_{max} = 1$ edge can be obtained to leading order via a perturbative solution, with the details of the calculation presented in the Appendix. Indeed, the edge regime $\zeta \rightarrow 1$ corresponds to occupied rapidities in the interval $[\lambda_1, \lambda_2]$, where $\lambda_{1,2} = \tilde{\lambda} \mp \epsilon$ and we assume $\epsilon \ll 1$. The perturbative solution of Eq. (3.3.11) then gives to lowest order

$$\epsilon(\zeta) = \sqrt{2(1-\zeta)} \tan(\gamma). \quad (3.3.15)$$

Moreover, the profile can also be approximated by noting that the integral in (3.3.14) is taken over a very short interval around $\tilde{\lambda}$ and the effect of dressing in (3.3.13) can be neglected. This yields

$$\langle S^z \rangle \approx -\frac{1}{2} + \frac{1}{\pi} p'(\tilde{\lambda}) \epsilon(\zeta) = -\frac{1}{2} + \frac{1}{\pi} \sqrt{2(1-\zeta)} \quad (3.3.16)$$

and thus one has a leading square-root singularity of the edge profile, which is independent of Δ . Interestingly, the very same behavior was found for the edge profile in the XXZ chain with a magnetic field gradient [169].

To conclude this section, one should remark that the analytical form of the entire profile can be found explicitly for the noninteracting XX chain [55]. There, instead of rapidities, one can simply work with momentum modes, and the velocities $v(q) = \sin q$ are given by the derivative of the dispersion, independently of the occupation function. The magnetization along the ray ζ then follows from the number of modes that satisfy $v(q) > \zeta$. In general, $v(q) = \zeta$ has two solutions for $|\zeta| < 1$, given by $q_\pm = \pi/2 \pm \arccos \zeta$. Note, however, that the initial state

on the left-hand side is the half-filled ground state and thus $|q| \leq \pi/2$ must be satisfied. Hence, the modes that contribute lie in the interval $[q_-, \pi/2]$ and the magnetization reads

$$\langle S^z \rangle = -\frac{1}{2} + \mathcal{N}(\zeta), \quad \mathcal{N}(\zeta) = \frac{1}{2\pi} \arccos \zeta. \quad (3.3.17)$$

3.3.2 Numerical results

We now present our numerical results from DMRG calculations and compare them to the $\langle S^z \rangle$ profiles as obtained from (3.3.14) by solving the GHD equations. In Fig. 3.3 the magnetization profiles are reported for a system with $L = 200$ sites and for a fixed time $t = 64$ after the quench. Instead of the lattice site $j = 1, \dots, L$, we introduce the (half-integer) distance $x = j - (L + 1)/2$ from the junction of the half chains to index the sites, and plot the data $\langle S_x^z \rangle$ against the ray variable $\zeta = x/t$. For all the anisotropies presented, one generally observes a very good agreement between the DMRG data and the GHD solution. There are, however, some extra features that should be discussed.

First, for $\Delta > 0$, the right edge of the front indeed lies at $\zeta_{max} = 1$, as predicted by GHD, and the ansatz (3.3.10) for the occupation provides, up to oscillations, a very good description of the edge regime. However, although the approximate solution in Eq. (3.3.16), shown by the green dashed lines in Fig. 3.3, seems to capture the leading behavior of the edge, its applicability is restricted to a rather small neighborhood of $\zeta = 1$. As further discussed in the Appendix, this is due to the fact that the solution (3.3.15), which gives the interval of occupied rapidities, actually fails to satisfy $\epsilon \ll 1$, unless $1 - \zeta$ is chosen to be extremely small. In particular, ϵ diverges for $\Delta = 0$ and the approximation improves as $\Delta \rightarrow 1$.

On the other hand, for $\Delta < 0$, the GHD edge is given by $\zeta_{max} = \sin(\gamma)$, whereas the density can be clearly seen to extend beyond this value up to $\zeta \approx 1$. Moreover, the GHD profile shows a qualitatively different behavior around ζ_{max} , where the square-root singularity seems to be replaced with a linear profile. In fact, this is very reminiscent of the case of the domain-wall initial state $|\uparrow\uparrow\uparrow \dots\rangle \otimes |\downarrow\downarrow\downarrow \dots\rangle$, where the analytical GHD profile can be obtained [37] and the edge behavior has recently been investigated in detail [170, 171]. In particular, the tail has been interpreted as a dilute regime of quasiparticles, where the interactions renormalize to zero and the edge $\zeta = 1$ corresponds to the free magnon velocity [171].

To have a better overview of the situation for the geometric quench, we show in

Magnetization Profiles

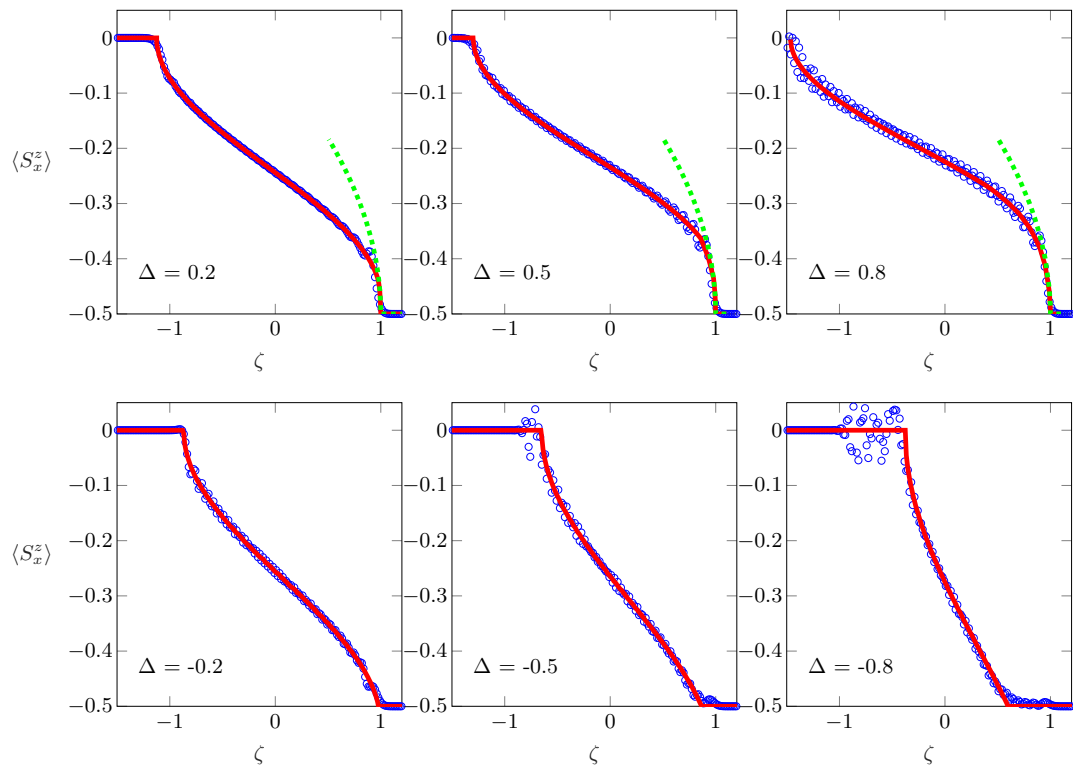


Figure 3.3: Magnetization profiles $\langle S_x^z \rangle$ after the geometric quench as a function of $\zeta = x/t$, for various values of Δ . The symbols (blue) are the results of DMRG calculations, whereas the solid lines (red) are obtained from the numerical solution of the GHD ansatz. For $\Delta > 0$ the approximation near the edge, Eq. (3.3.16), is shown by dashed lines (green).

Fig. 3.4 the magnified edge region for $\Delta = -0.8$ and various times t . One can see a slow decrease of the scaled profiles in the regime $\zeta_{max} < \zeta < 1$, suggesting that the tail should indeed contain only a finite number of particles that could escape from the bulk of the front region. We expect that, when plotted against ζ , the tail should vanish in the $t \rightarrow \infty$ limit, as the escaped density becomes smeared out in an infinitely large region. Note, however, that the results of Ref. [171] for the domain-wall quench are also compatible with a logarithmic increase in time of the overall number of particles in the tail regime. A detailed analysis of the tail would require much more numerical effort and is beyond the scope of the present

paper.

One should also comment on the left edge of the profile, i.e., the front region that connects to the ground state outside the light cone. As pointed out before, the GHD ansatz suggests that the left edge should extend with the spinon velocity, i.e., the speed of the excitations above the zero-magnetization background. This seems to be in perfect accordance with the numerical data for $\Delta > 0$. In the attractive ($\Delta < 0$) case, however, one observes very strong oscillations beyond the GHD edge $\zeta < \zeta_{min}$. We believe that, similarly to the right edge, this feature is due to a small number of particles that escape from the attractive bulk of the front. Note also, that the GHD edge seems to have a square-root behavior for all values of Δ . However, a perturbative treatment is more complicated in this case, since one has to consider the perturbation around the completely filled ground state, instead of the vacuum.

Finally, it is interesting to note that in the limit $\Delta \rightarrow -1$ one has $\zeta_{min} = \zeta_{max} = 0$, and thus the bulk of the front region vanishes completely. This is a clear signal of subballistic transport in the regime $\Delta \leq -1$. On the other hand, the limit $\Delta \rightarrow 1$ shows no singular features, suggesting that the $\Delta > 1$ regime is smoothly connected and the ballistic nature of the dynamics is preserved. These expectations seem to be confirmed by our DMRG numerics.

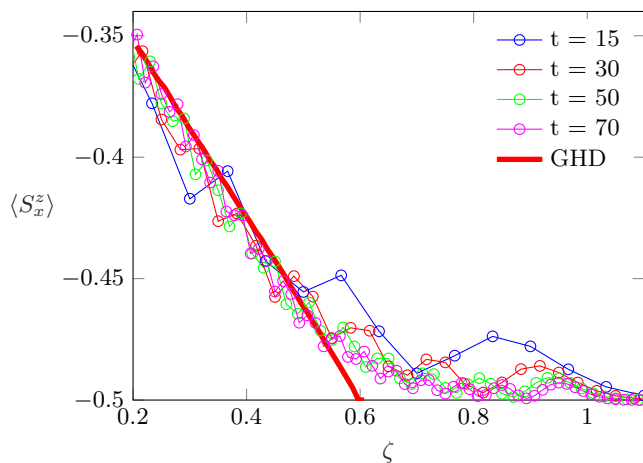


Figure 3.4: Edge profiles for $\Delta = -0.8$ and various times t , plotted against $\zeta = x/t$. The GHD solution is shown by the red solid line.

3.4 Entropy Profiles

The front dynamics can be further characterized by calculating the entanglement entropy $S = -\text{Tr} \rho_A \ln \rho_A$ for a given bipartition of the chain (see Fig. 3.1), where ρ_A is the corresponding reduced density matrix. The entanglement profile is obtained at a fixed time t by varying the boundary between the subsystems $A = [1, L/2 + r]$ and $B = [L/2 + r + 1, L]$. In particular, $r = 0$ corresponds to a bipartition across the initial cut, the case that was already considered in Ref. [55].

As opposed to the magnetization, the entanglement profile is more complicated to be captured within the hydrodynamic approach. Indeed, although there has been much progress in understanding the entropy evolution in terms of the quasiparticle picture [29, 30], these results are restricted to quench scenarios in which the growth is linear in time. In contrast, it has already been observed in [55] that the geometric quench induces a logarithmic entropy growth for $r = 0$, which is also a characteristic of local quench protocols [50, 51, 143, 144].

We first consider the noninteracting ($\Delta = 0$) case where, invoking results from CFT and with some heuristic arguments, we are able to provide an ansatz for the full entanglement profile.

3.4.1 XX chain

To find a quantitative description of the entropy profile, there are some features to be noted about the structure of the hydrodynamic state described above Eq. (3.3.17). First, the fermionic density $\mathcal{N}(\zeta)$ is exactly one-half of the corresponding one for a domain-wall initial state [172, 173], where the occupied modes $[q_-, q_+]$ are not restricted below the Fermi level $q_F = \pi/2$. Hence, the LQSS after the geometric quench is reminiscent of that of the domain-wall problem, but differs by the presence of a sharp Fermi edge. We thus argue that the entropy can be obtained as a sum of two contributions, due to the spatially varying occupation and to the Fermi-edge singularity, respectively.

The contribution from the Fermi edge can be identified by recalling the results for the local quench, where two half-filled semi-infinite chains are joined together [51]. Indeed, since the initial filling is unbiased, the time evolution is entirely due to the presence of two Fermi edges at momenta $q_F = \pm\pi/2$. The resulting entropy

profile can be obtained via CFT [51] and reads

$$S_{loc} = \frac{1}{6} \ln(t^2 - r^2), \quad (3.4.1)$$

where we have ignored the nonuniversal constant that is independent of both t and r . This result can also be generalized to finite-size chains by substituting the corresponding chord variables [144]

$$t \rightarrow \frac{L}{\pi} \sin\left(\frac{\pi t}{L}\right), \quad r \rightarrow \frac{L}{\pi} \sin\left(\frac{\pi r}{L}\right). \quad (3.4.2)$$

It is important to stress that the result (3.4.1) and (3.4.2) gives the entropy profile resulting from two Fermi edges, whereas we need only the contribution from $q_F = \pi/2$, i.e. from the right-moving wave front. Thus, using trigonometric identities we rewrite

$$S_{loc} = \frac{1}{6} \ln \left[\frac{L}{\pi} \sin\left(\frac{\pi(t-r)}{L}\right) \frac{L}{\pi} \sin\left(\frac{\pi(t+r)}{L}\right) \right], \quad (3.4.3)$$

which has exactly the desired additive form, with the arguments $t \mp r$ corresponding to the Fermi edges $q_F = \pm\pi/2$, respectively.

The second piece of contribution we have to identify is due to the space-dependent occupation. As we have already remarked, this should be closely related to the domain-wall problem, where the entropy profile is also known explicitly [52]. In fact, the solution can be found via a curved-space CFT approach [53], by identifying the underlying curved metric [174] and mapping it conformally onto a flat one on the upper half plane. The result can be cast in the form

$$S_{dw} = \frac{1}{6} \ln(\mathcal{L} \sin q_F(r/t)), \quad (3.4.4)$$

where the conformal length is given by

$$\mathcal{L} = t \left[1 - \left(\frac{r}{t}\right)^2 \right]. \quad (3.4.5)$$

Note that (3.4.4) contains a nonuniversal part with $\sin q_F(r/t)$ being the spatially varying Fermi velocity, where $q_F(x) = \arccos(x)$. This term plays the role of a cutoff renormalization in the CFT picture.

We now give a heuristic argument on how to modify the expression in (3.4.4) in order to get the result for the geometric quench. As already pointed out, the fermionic density for the geometric quench is exactly the half of that in the domain-wall case, by restricting to the modes with $q \in [q_-, \pi/2]$. Due to the particle-hole symmetry of the problem, one could also have worked with the modes $q \in [\pi/2, q_+]$ and arrive at the same result. Thus, assuming that the universal entropy contribution of the domain-wall problem could, in some way, be written as a sum over modes, this symmetry argument implies that the universal contribution to the geometric quench should be $\frac{1}{12} \ln \mathcal{L}$. Moreover, one should also take into account the halved density when considering the nonuniversal piece, where for the geometric quench one has $q_F(x) = \pi \mathcal{N}(x) = \arccos(x)/2$, such that

$$\frac{1}{6} \ln(\sin q_F(r/t)) = \frac{1}{12} \left[\ln \left(1 - \frac{r}{t} \right) - \ln 2 \right]. \quad (3.4.6)$$

Finally, collecting the different contributions, one arrives at the result

$$S_g = \frac{1}{6} \ln \left[\frac{L}{\pi} \sin \left(\frac{\pi(t-r)}{L} \right) \right] + \frac{1}{12} \ln [(t-r)(1-(r/t)^2)] + k, \quad (3.4.7)$$

where $|r| < t$ and k is a nonuniversal constant. In particular, setting $r = 0$ one recovers the ansatz put forward in [55]. To test the result (3.4.7), we calculated the entropy profiles for free-fermion chains using standard correlation matrix techniques [58]. Figure 3.5 shows the result for a fixed time $t = 50$ and for various chain sizes, compared to the ansatz (3.4.7) shown by solid lines. One sees a very good agreement with the numerical data. The only free parameter is the constant, which was fixed at $k \approx 0.44$ by fitting the ansatz to one of the data sets. We also carried out calculations for a larger time $t = 100$ (not shown) with similarly good agreement, confirming the validity of the result in Eq. (3.4.7).

3.4.2 XXZ chain

We continue with the numerical study of the entanglement profile for the XXZ chain. In Fig. 3.6 the results of DMRG calculations for a chain with $L = 200$ are shown. The snapshots of the profiles are plotted for various times, and the Δ values considered are the same as for the magnetization in Fig. 3.3. At $t = 0$ (blue curve)

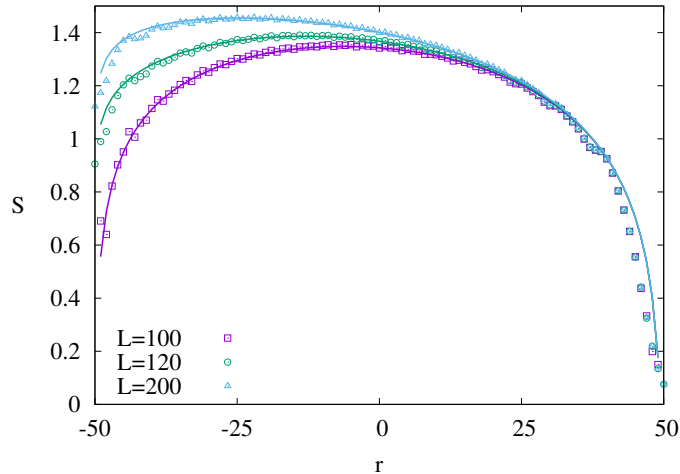


Figure 3.5: Entropy profiles after the geometric quench for $t = 50$ and various system sizes. The solid lines correspond to the ansatz S_g in Eq. (3.4.7). Only the front region $|r| < t$ is shown.

the entanglement entropy is trivially vanishing for a cut across the right half chain, whereas the profile on the left is given by the well-known CFT formula for the ground state [18]. After the quench, the entanglement spreads in both directions and a profile qualitatively similar to the XX case emerges. However, one expects that the left and right edges of the front are given by $r = \zeta_{min}t$ and $r = \zeta_{max}t$, respectively, as indicated by the dashed lines in Fig. 3.6. While for $\Delta > 0$ this seems to hold perfectly, for $\Delta < 0$ one observes, similarly to the magnetization profiles, a tail reaching beyond the GHD edges on both sides, increasing for large negative values of Δ .

It is instructive to have a closer look at the right tail of the front expanding into the vacuum. As already discussed in the previous section, the tail behavior is reminiscent of the domain-wall quench in which, however, the dynamics is invariant under the change of sign in Δ . To emphasize the difference for the geometric quench, in Fig. 3.7 we compare the edge entropy profiles between $\Delta = 0.8$ and $\Delta = -0.8$. While in the repulsive case the profile has a sharp edge with an abrupt increase, for the attractive one the free edge remains soft until reaching the GHD edge, where the slope becomes steep. The profile between the soft and hard edges develops a steplike structure, as can be seen for larger times in Fig. 3.7. In fact,

Entropy Profiles

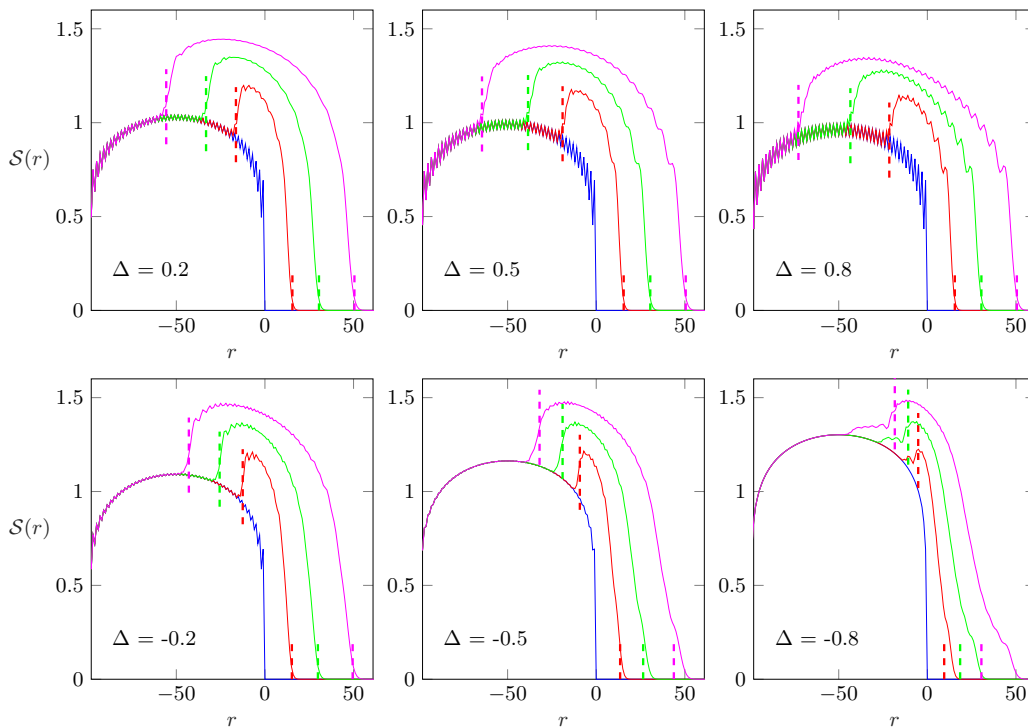


Figure 3.6: Entanglement profiles for different values of Δ at times $t = 0$ (blue), $t = 15$ (red), $t = 30$ (green) and $t = 50$ (magenta) after the quench. The GHD edges $r = \zeta_{min}t$ and $r = \zeta_{max}t$ are marked by vertical dashed lines.

beyond the left edge the profile develops a qualitatively similar tail, which can already be seen in Fig. 3.6 without magnifying the region.

Regarding the bulk profile, it is tempting to find a generalization to the ansatz in (3.4.7). In fact, the CFT result (3.4.3) for the local quench can be applied to the XXZ case by explicitly including the spinon velocity, i.e., substituting $t \rightarrow v_s t$, which we have verified by DMRG calculations. On the other hand, however, the other constituent of the ansatz originates from the domain-wall quench, where the result (3.4.4) is specific to free fermions. Hence, despite the qualitatively similar behavior of the profiles, the XXZ case can not simply be related to the XX result (3.4.7) by rescaling with the front velocities.

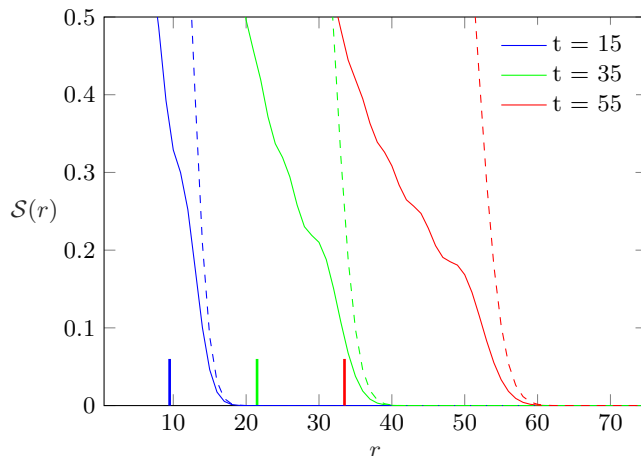


Figure 3.7: Comparison of the right edge of the entanglement profile for $\Delta = -0.8$ (solid lines) vs. $\Delta = 0.8$ (dashed lines) and various times. The GHD edges $r = \zeta_{max}t$ for $\Delta = -0.8$ are indicated by vertical lines.

3.5 Boundary Effects

So far we have only considered situations in which the propagating front does not reach the boundaries of the chain. Since the formulation of GHD genuinely involves the thermodynamic limit, it is interesting to ask what happens when finite-size effects play a dominant role, i.e., when reflections of the wave front occur.

3.5.1 XX chain

We start again by considering the XX chain for which, due to the complete independence of the quasiparticle velocities from the mode occupations, the hydrodynamic picture remains applicable even after reflections from the boundaries take place. Indeed, determining the magnetization requires only a proper bookkeeping of the contributions from the reflected particles. Considering a fixed site with $x > 0$ on the right-hand side of the chain, the result (3.3.17) remains true for times $t < L - x$, i.e., until the reflected particles with maximal velocity $v_{max} = 1$ arrive there. For larger times one simply adds the contribution of the reflected

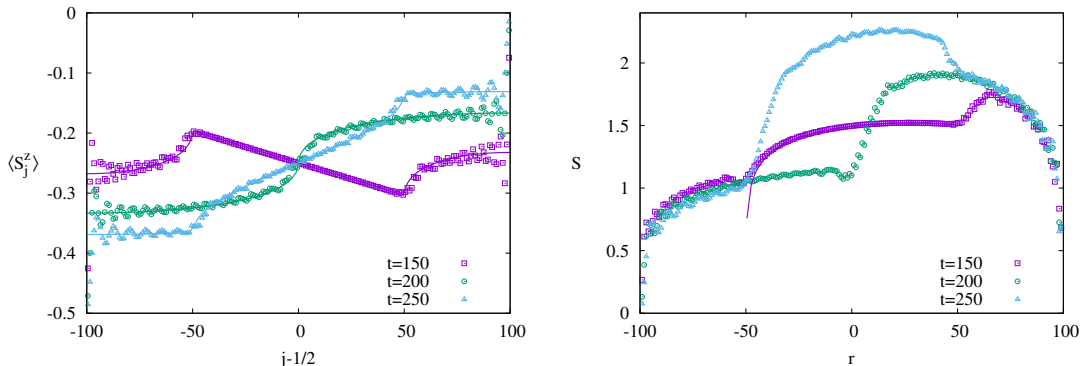


Figure 3.8: Magnetization (left) and entanglement (right) profiles after reflection of the wavefront from the boundaries. The solid lines show the results (3.3.17), (3.5.1) and (3.5.2) for the magnetization and (3.4.7) for the entropy, respectively.

density

$$\langle S_x^z \rangle = -\frac{1}{2} + \mathcal{N}\left(\frac{x}{t}\right) + \mathcal{N}\left(\frac{L-x}{t}\right), \quad (3.5.1)$$

where $L-x < t < L+x$. This last requirement ensures, that only reflections from the right end of the chain could take place.

For even larger times, one has to take into account the reflections from the left boundary. To this end one should first note, that the left-moving particles could be considered as *holes* penetrating the originally zero-magnetization background. This also follows directly from the exact symmetry relation $\langle S_{-x}^z \rangle = -1/2 - \langle S_x^z \rangle$, which can be used to obtain the magnetization on the left-hand side of the chain. Hence, for times $t > L+x$, the contribution of the reflected holes should appear as

$$\langle S_x^z \rangle = -\frac{1}{2} + \mathcal{N}\left(\frac{x}{t}\right) + \mathcal{N}\left(\frac{L-x}{t}\right) - \mathcal{N}\left(\frac{L+x}{t}\right). \quad (3.5.2)$$

The above result is then valid for times $L+x < t < 2L-x$, i.e., until the fastest holes arrive at site x after a double reflection from both left and right boundaries. Clearly, this pattern could be continued to arbitrary times after multiple reflections, always adding the fermionic density with the proper sign and argument.

The results (3.3.17), (3.5.1), and (3.5.2) are compared to exact numerical free-fermion calculations on the left of Fig. 3.8. One observes that, apart from oscillations, the average magnetization is well described by the semiclassical formulas.

The oscillations are rather strong around the boundaries and one expects that, after many reflections, the profile becomes increasingly noisy. On the right of Fig. 3.8 we also plotted the corresponding entanglement profiles. As one can see, the result in (3.4.7) remains valid for that part of the profile which is not yet reached by the reflected wavefront. Interestingly, after each reflection one has a steady increase of entanglement, which was already pointed out in [55] for $r = 0$. Unfortunately, however, a quantitative understanding of the profile is still beyond our reach.

3.5.2 XXZ chain

In contrast to the XX case, it is far from trivial how the hydrodynamic approach could be extended to include reflected quasiparticles in the interacting case. Here we try to understand only some simple qualitative features of the dynamics after reflection, focusing on the front that propagates on the left-hand side of the system. In order to avoid interference with the reflection of the right-propagating front, for this simulation we considered a chain of size $L = L_1 + L_2$, composed initially of two unequal pieces $L_1 = 40$ (ground state) and $L_2 = 80$ (vacuum).

Our results for both the magnetization and entropy profiles are shown in Fig. 3.9 for two different anisotropies, with the colors corresponding to different evolution times. The dashed lines indicate the calculated front positions, assuming that the speed of propagation after reflection is still given by the spinon velocity v_s . The blue curves correspond to times $t = L_1/v_s$, i.e., when the front is just supposed to reach the boundary, which is indeed what we observe in Fig. 3.9. In contrast, after reflection there is a clear mismatch between the calculated and the actual edge locations: the front slows down for $\Delta > 0$ and speeds up for $\Delta < 0$, the effect becoming more apparent for larger times. The change of speed is due to the fact that the reflected front no longer propagates in a zero-magnetization background, but rather in a nontrivial one left behind by the primary front. Since this background is inhomogeneous, we expect that the speed of the reflected front will actually change in time, which is supported by our numerical data. A more detailed analysis is, however, difficult due to the ambiguity in defining the edge of the reflected front, with its location getting washed out by superimposed oscillations. Regarding the entropy evolution, one should comment on the previous observations made in Ref. [55], where the following ansatz for the entropy across the junction

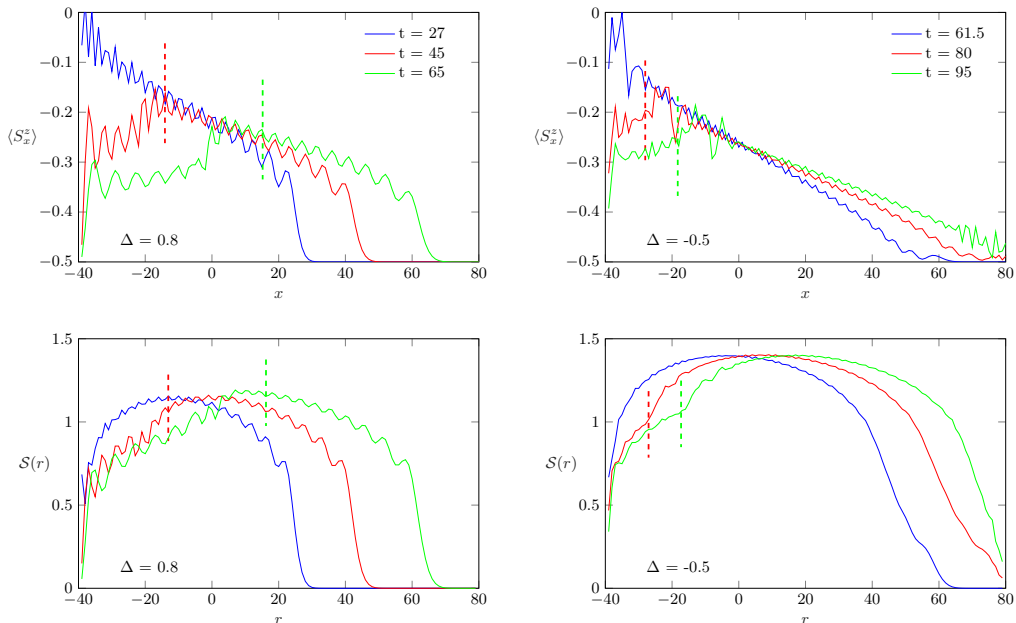


Figure 3.9: Magnetization (top) and entanglement (bottom) profiles for $\Delta = 0.8$ (left) and $\Delta = -0.5$ (right), just before (blue) and after the reflection (red, green) of the front from the left boundary of the chain. The data are plotted against the distance from the junction. The dashed lines indicate the edge positions corresponding to a reflected front with constant speed v_s .

$r = 0$ for times $t \ll 2L_2$ was put forward

$$S(r = 0) = \frac{1}{6} \ln \left[\sqrt{v_e t} \frac{2L_1}{\pi} \sin \left(\frac{\pi v_e t}{2L_1} \right) \right] + \text{const.} \quad (3.5.3)$$

Note that this is nothing else but the XX result (3.4.7) for $r = 0$ and $L = 2L_1$, after a rescaling $t \rightarrow v_e t$, where the parameter v_e was interpreted as an entanglement spreading rate. Indeed, $t = 2L_1/v_e$ should correspond to the roundtrip time of the entanglement front and the speed v_e was obtained by fitting the ansatz (3.5.3) to the data, with the result $v_e < v_s$ for $\Delta = 0.5$ and $v_e \gtrsim v_s$ for $\Delta = -0.5$ (see Fig. 12 of Ref. [55]). This is in perfect accordance with our observations in Fig. 3.9. However, instead of being an entanglement spreading rate, the correct interpretation of v_e is due to the modified quasiparticle velocity in the inhomogeneous background. Indeed, the very same effect appears also in the magnetization

profile. Remarkably, even though the front velocity appears to be time dependent after reflection, the simple ansatz (3.5.3) was found to give a rather good description of the entropy for $t < 2L_1/v_e$, with v_e being the average round-trip velocity.

3.6 Fluctuations vs. entropy

To conclude our studies of the geometric quench, we shall consider yet another physical quantity, namely the profile of the magnetization fluctuations. Since the XXZ dynamics conserves the overall magnetization, the fluctuations are clearly vanishing for the full chain. However, considering only a segment A (see Fig. 3.1), the subsystem fluctuations can be defined as

$$\mathcal{F} = \left\langle \left(\sum_{i \in A} S_i^z - \left\langle \sum_{i \in A} S_i^z \right\rangle \right)^2 \right\rangle, \quad (3.6.1)$$

where the expectation values are taken with respect to the time-evolved state (3.2.2). Note that in the fermion language, \mathcal{F} is equivalent to the variance of the particle number in A .

For free-fermion systems, the study of fluctuations is motivated by an exact relation between the ground-state entanglement entropy and the particle number statistics [59], reproducing the entropy as a cumulant series [61, 62]. The scaling of the variance has thus been extensively studied in the ground state of the XX chain [63, 175] as well as out of equilibrium for the simple domain-wall initial state [173, 176]. In all of the above-mentioned cases one finds that, to leading order, the entropy is simply proportional to the variance, whereas the higher-order cumulants give only subleading contributions.

Although the cumulant series relation between entropy and fluctuations is deeply rooted in the free-fermion nature of the state, there are some known extensions to interacting systems. In particular, for critical ground states described by a Luttinger liquid, the fluctuations were also found to be proportional to the entropy [60]

$$\mathcal{F} \simeq K \frac{3}{\pi^2} S + \text{const.} \quad (3.6.2)$$

Here K denotes the Luttinger parameter, while the constant is non universal. The relation (3.6.2) has been checked explicitly for the XXZ ground state [60], where

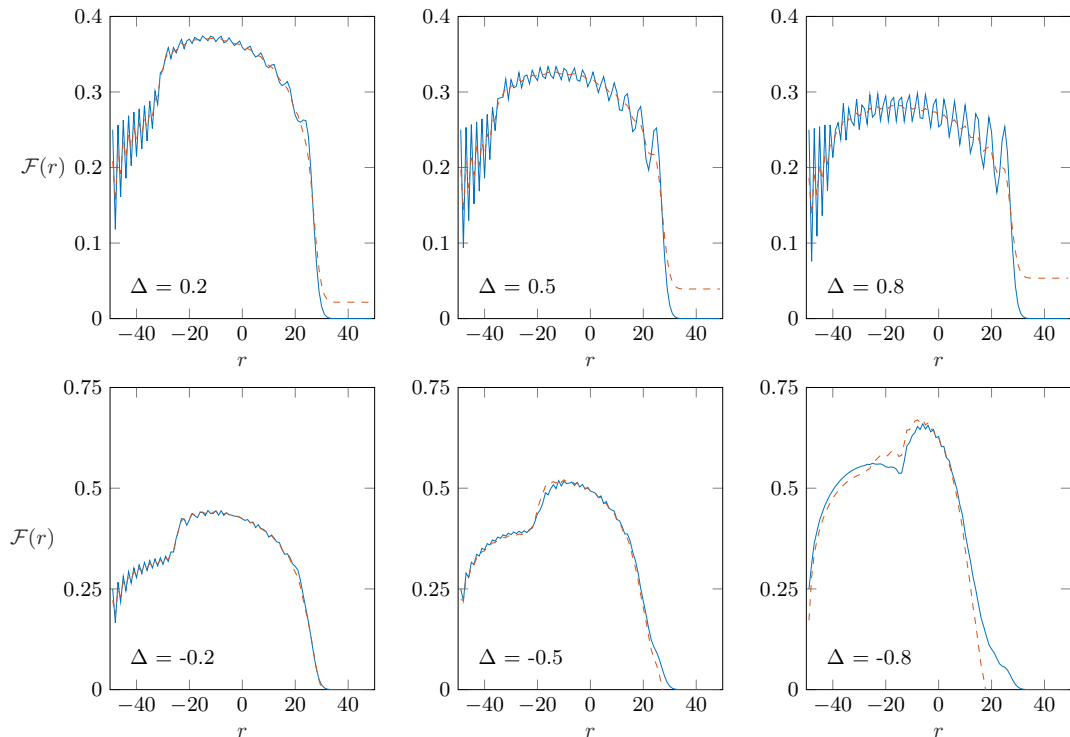


Figure 3.10: Comparison between the magnetization fluctuations $\mathcal{F}(r)$ (blue) and the scaled entanglement entropy $S(r)$ (red), according to Eq. (3.6.2), for a system of $L = 100$ and at $t = 30$.

the Luttinger parameter is known from the Bethe ansatz solution

$$K = \frac{1}{2} \left(1 - \frac{\text{acos}(\Delta)}{\pi} \right)^{-1}. \quad (3.6.3)$$

However, to the best of our knowledge, no such relation has been established in an out-of-equilibrium context so far.

Our goal here is to study the fluctuations after the geometric quench, which can also be rewritten as a sum over correlation functions

$$\mathcal{F} = \sum_{i,j \in A} [\langle S_i^z S_j^z \rangle - \langle S_i^z \rangle \langle S_j^z \rangle]. \quad (3.6.4)$$

Although these objects are straightforward to evaluate via DMRG, one needs the full matrix of correlators within the subsystem. This makes the computation somewhat more demanding; thus the simulations are now performed on a smaller chain with $L = 100$ sites. The fluctuation profile $\mathcal{F}(r)$ is measured at time $t = 30$, and is shown by the blue lines in Fig. 3.10 for a set of interaction parameters Δ . The front region is clearly visible and qualitatively similar to the entropy profiles. In order to test the relation (3.6.2) between entropy and fluctuations, we have fitted the constant for the region of the profile that corresponds to the ground state (i.e., outside the light cone). This was done by first smoothing out the oscillations in the data and then minimizing the difference between the corresponding profiles $\mathcal{F}(r)$ and $\mathcal{S}(r)$. With the fitted constant, one can now compare the profiles in the entire front region by plotting the ansatz (3.6.2), shown by the red dashed lines in Fig. 3.10, together with $\mathcal{F}(r)$. Quite remarkably, the two profiles show a good agreement also within the front region, up to the superimposed oscillations. The collapse is particularly good for moderate values of Δ , while for larger negative values the curves start to differ increasingly (for large $\Delta > 0$ the oscillations dominate the profile and the comparison is difficult).

The fact that Eq. (3.6.2) seems to give a decent approximation also in the far-from-equilibrium front region is rather intriguing, since the Luttinger parameter K in Eq. (3.6.3) is calculated for the ground state. To have a better understanding of this result, one should try to analyze the behavior of correlation functions in (3.6.4), which we leave for further studies.

3.7 Conclusions

We have investigated the time evolution after a geometric quench in the XXZ chain and showed that the magnetization profiles are nicely captured by generalized hydrodynamics. While the entanglement profile is harder to describe within the hydrodynamic picture, we were able to put forward an ansatz for the noninteracting case that shows a very good agreement with the DMRG data.

In order to arrive at our ansatz (3.4.7), we had to apply some heuristic arguments, expressing the entropy production in the geometric quench as a kind of mixture of local and domain-wall quenches. It would be desirable to put this result on firm ground, e.g., by a direct CFT treatment along the lines of Ref. [174], identifying the curved-space metric corresponding to the inhomogeneous time-evolved state.

Conclusions

This might also allow for a generalization to initial states with arbitrary fillings on both sides. Ideally, however, one would like to cast the entropy as a sum over contributions from the different quasimomenta, analogously to what has been found for global quenches [29], which would enable us to solve the interacting problem as well. Whether such a representation is possible in situations with a logarithmic entropy growth is still unclear.

Another interesting aspect is the physics of the edge, which was shown [177–181] to display a universal Tracy-Widom scaling [182] for free fermions. Clearly, the situation is more complicated in the interacting case, since one has a splitting between the GHD edge and the free edge. Recent studies for the domain-wall quench hint towards the possibility that the free tail is characterized by a Tracy-Widom-like $t^{1/3}$ length scale [170], while the GHD edge seems to spread diffusively as $t^{1/2}$ [171]. We believe that the vacuum edge of the geometric quench may belong to the same type of edge universality as observed for the domain wall. Additionally, however, one has another edge appearing in our problem that connects to the ground-state region and might display a different type of behavior. A detailed study of these edge phenomena requires much more numerical effort and is left for future studies.

Finally, it would be illuminating to understand how the presence of boundaries could be reconciled with the theory of generalized hydrodynamics. One feature we observed is that the edge velocity becomes time dependent after reflection, due to propagation in a nontrivial inhomogeneous background. Whether a quantitative description of the reflected front is possible along the lines of GHD is an interesting question to be addressed.

Acknowledgments

We thank J. Viti and J.-M. Stéphan for a fruitful discussion. The authors acknowledge funding from the Austrian Science Fund (FWF) through Project No. P30616-N36.

Chapter 4

Time evolution of entanglement negativity across a defect (J. Phys. A: Math. Theor. 53, 205301 (2020))

In this chapter we present our findings from Ref. [183], which is one of the main publications of the author. In the following, the abstract and the sections 2. - 7. of the paper, which contain the used methods, the obtained results as well as the conclusions, are completely included in sections 4.1 - 4.7 of the present thesis. The appendices A and B were also taken from the paper and can be found in B.1 and B.2, respectively.

The paper was first drafted by the author of this thesis and later substantially edited equally by him and Viktor Eisler. All the calculations in the paper, except for the CFT calculations in B.2, were performed by the author of this thesis. Both authors contributed equally to the interpretation of the results.

4.1 Abstract

We consider a quench in a free-fermion chain by joining two homogeneous half chains via a defect. The time evolution of the entanglement negativity is studied between adjacent segments surrounding the defect. In case of equal initial fillings,

the negativity grows logarithmically in time and essentially equals one-half of the Rényi mutual information with index $\alpha = 1/2$ in the limit of large segments. In sharp contrast, in the biased case one finds a linear increase followed by the saturation at an extensive value for both quantities, which is due to the backscattering from the defect and can be reproduced in a quasiparticle picture. Furthermore, a closer inspection of the subleading corrections reveals that the negativity and the mutual information have a small but finite difference in the steady state. Finally, we also study a similar quench in the XXZ spin chain via density-matrix renormalization group methods and compare the results for the negativity to the fermionic case.

4.2 Model and methods

We consider a chain of noninteracting fermions with a single hopping defect, described by the Hamiltonian

$$\hat{H} = \hat{H}_l + \hat{H}_r - \frac{\lambda}{2} \left(f_0^\dagger f_1 + f_1^\dagger f_0 \right), \quad (4.2.1)$$

where the hopping amplitude λ characterizes the defect in the middle of the chain, while the homogeneous half-chains on the left/right hand side of the defect are given by

$$\hat{H}_l = -\frac{1}{2} \sum_{j=-L+1}^{-1} \left(f_j^\dagger f_{j+1} + f_{j+1}^\dagger f_j \right), \quad \hat{H}_r = -\frac{1}{2} \sum_{j=1}^{L-1} \left(f_j^\dagger f_{j+1} + f_{j+1}^\dagger f_j \right). \quad (4.2.2)$$

The full chain has $2L$ sites and the fermionic annihilation (creation) operators f_j (f_j^\dagger) with $j = -L + 1, \dots, L$ satisfy the canonical anticommutation relation $\{f_i, f_j^\dagger\} = \delta_{ij}$. The defect $\lambda \leq 1$ is assumed to be weaker than the tunneling in the leads \hat{H}_l and \hat{H}_r .

In the following sections we shall either consider the ground state or the time evolution generated by (4.2.1). In the latter case, the chain is initially split in two halves and our quench protocol is depicted in Fig. 4.1. Here the initial state $|\psi_\sigma\rangle$ of the left/right part ($\sigma = l, r$) is given by the respective ground state of $\hat{H}_\sigma - \mu_\sigma \sum_{j \in \sigma} f_j^\dagger f_j$, where the chemical potential μ_σ sets the filling n_σ of the corresponding half-chain. In particular, one sets $\mu_l = \mu_r = 0$ to initialize both

chains in their half-filled ground states $n_l = n_r = 1/2$, whereas the choice $\mu_l = 1$ and $\mu_r = -1$ corresponds to the step-like density $n_l = 1$ and $n_r = 0$ (also known as the domain wall initial state). In either case, the two halves are then coupled via a defect, depicted by the dashed bond in Fig. 4.1, and the resulting unitary time evolution is given by

$$|\psi(t)\rangle = e^{-i\hat{H}t} |\psi_l\rangle \otimes |\psi_r\rangle . \quad (4.2.3)$$

We are primarily interested in the buildup of entanglement in the time-evolved state $|\psi(t)\rangle$, between two segments A_1 and A_2 as shown by the colored sites in Fig. 4.1. We restrict ourselves to the case of adjacent segments of equal lengths ℓ , located symmetrically around the defect. The bipartite case of $\ell = L$ ($B = \emptyset$) was studied in Ref. [64], where the entanglement in the pure state $\rho = |\psi(t)\rangle \langle \psi(t)|$ is simply measured by the Rényi entropies between the two halves. In general, however, one has to first extract the reduced density matrix $\rho_A = \text{Tr}_B(\rho)$ of the subsystem $A = A_1 \cup A_2$ by tracing out over the environment B . This leaves us with a mixed state where the entanglement is much harder to be quantified and requires a proper measure.

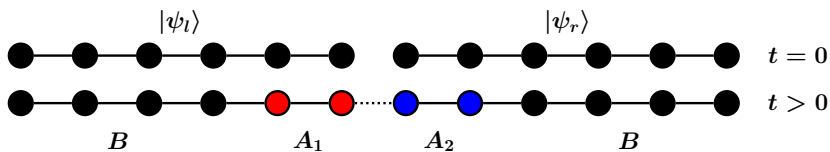


Figure 4.1: Quench setup.

Before introducing this measure, one should remark that the time-evolved state (4.2.3) is Gaussian and thus fully characterized by its correlation matrix $C_{mn}(t) = \langle \psi(t) | f_m^\dagger f_n | \psi(t) \rangle$. Indeed, since we are dealing with free fermions, the Hamiltonian (4.2.1) can be written in the quadratic form

$$\hat{H} = \sum_{m,n} H_{m,n} f_m^\dagger f_n , \quad (4.2.4)$$

which defines the elements $H_{m,n}$ of the hopping matrix H . Then the time evolution of the correlation matrix can simply be obtained as

$$C(t) = e^{iHt} C(0) e^{-iHt} . \quad (4.2.5)$$

The initial correlation matrix of the decoupled system at $t = 0$ has a block-diagonal form

$$C(0) = \begin{pmatrix} C_l & 0 \\ 0 & C_r \end{pmatrix}, \quad (4.2.6)$$

where C_σ is the ground-state correlation matrix at filling n_σ , with matrix elements given by [184]

$$(C_\sigma)_{m,n} = \frac{1}{2(L+1)} \left[\frac{\sin(q_{F,\sigma}(m-n))}{\sin\left(\frac{\pi}{2(L+1)}(m-n)\right)} - \frac{\sin(q_{F,\sigma}(m+n))}{\sin\left(\frac{\pi}{2(L+1)}(m+n)\right)} \right], \quad (4.2.7)$$

and the Fermi wavenumber is defined as

$$q_{F,\sigma} = \frac{\pi(n_\sigma L + 1/2)}{L+1}. \quad (4.2.8)$$

In particular, half-filling $n_\sigma = 1/2$ corresponds to a Fermi momentum $q_{F,\sigma} = \pi/2$, whereas for the step initial condition ($n_l = 1, n_r = 0$) the correlations simplify to $(C_l)_{m,n} = \delta_{m,n}$ and $(C_r)_{m,n} = 0$.

4.2.1 Rényi entropy and mutual information

For the pure state $\rho = |\psi(t)\rangle \langle\psi(t)|$, the reduced density matrix of the segment A_1 is given by $\rho_{A_1} = \text{Tr}_{B \cup A_2}(\rho)$. The Rényi entropy between the segment A_1 and the rest of the system is defined as

$$S_\alpha(\rho_{A_1}) = \frac{1}{1-\alpha} \ln \text{Tr}(\rho_{A_1}^\alpha), \quad (4.2.9)$$

with the von Neumann entropy corresponding to the limit $\alpha = 1$. Note, however, that these measures do not give information about the entanglement between A_1 and A_2 . To gain some insight about the latter, one could consider the Rényi mutual information defined by the combination of subsystem entropies

$$\mathcal{I}_\alpha = S_\alpha(\rho_{A_1}) + S_\alpha(\rho_{A_2}) - S_\alpha(\rho_A). \quad (4.2.10)$$

The standard (von Neumann) mutual information with $\alpha = 1$ is known to be a measure of total (classical and quantum) correlations and is thus an upper bound to the entanglement [124]. Unfortunately, however, for generic α it is not even a

proper measure. Indeed, it was demonstrated that \mathcal{I}_α may become negative for $\alpha > 2$ after a certain quench [127]. On the other hand, it has been proved that \mathcal{I}_α is always positive in the range $0 < \alpha < 2$ for both fermionic and bosonic Gaussian states [128]. Furthermore, recently it was pointed out that the particular case $\alpha = 1/2$ is intimately related to a proper entanglement measure, the logarithmic negativity (see below), after a global quench [67]. Thus our focus will be exclusively on the case $\alpha = 1/2$.

The Rényi mutual information (4.2.10) is a simple combination of bipartite entropies in the pure Gaussian state ρ and is thus uniquely determined by the correlation matrix (4.2.5). In particular, for the segment A_1 one has

$$S_\alpha(\rho_{A_1}) = \frac{1}{1-\alpha} \sum_j \ln [\zeta_j^\alpha + (1-\zeta_j)^\alpha], \quad (4.2.11)$$

where ζ_j are the eigenvalues of the *reduced* correlation matrix $C_{A_1}(t)$, with indices restricted to the segment $m, n \in A_1$. Similar expressions hold for the other terms in the mutual information (4.2.10), where the eigenvalues of the respective reduced correlation matrices $C_{A_2}(t)$ and $C_A(t)$ must be used.

4.2.2 Entanglement negativity

The logarithmic negativity is a versatile measure of entanglement [69]. Its definition relies on the partial transpose of the density matrix, which may have negative eigenvalues only if the system is entangled [107]. For *bosonic* systems, the effect of the partial transpose is well known to be identical to a partial time reversal [112]. However, for *fermionic* systems this is not any more the case. Indeed, in contrast to partial time reversal [71], the partial transpose in general does not lead to a Gaussian operator [70]. However, it has been proved that the definition based on partial time reversal also yields a proper measure of entanglement [72]. Therefore, we shall adopt here the fermionic version of the logarithmic negativity, since it is directly amenable to correlation-matrix techniques.

In order to define the fermionic negativity, it is more convenient to work in the Majorana operator basis

$$c_{2j-1} = f_j + f_j^\dagger, \quad c_{2j} = i(f_j - f_j^\dagger), \quad (4.2.12)$$

satisfying the anticommutation relations $\{c_m, c_n\} = 2\delta_{mn}$. We can now expand the reduced density matrix ρ_A supported on the segment $A = A_1 \cup A_2$ encompassing

Model and methods

the defect (see Fig. 4.1) as

$$\rho_A = \sum_{\substack{\kappa, \tau \\ |\kappa| + |\tau| = \text{even}}} w_{\kappa, \tau} c_{-2\ell+1}^{\kappa_1} \cdots c_0^{\kappa_{2\ell}} c_1^{\tau_1} \cdots c_{2\ell}^{\tau_{2\ell}}. \quad (4.2.13)$$

Here κ_j and τ_j with $j = 1, \dots, 2\ell$ are bit strings associated to the subspaces A_1 and A_2 , with their norms defined as $|\kappa| = \sum_j \kappa_j$ and $|\tau| = \sum_j \tau_j$, respectively. The bit strings indicate whether a Majorana operator is included or not, $c_j^0 = \mathbb{1}$ or $c_j^1 = c_j$, with the weight of the corresponding term in the expansion given by $w_{\kappa, \tau}$. Importantly, the sum is restricted to terms, where the overall number of Majorana operators is even, reflecting the global fermion-number parity symmetry of the state.

The partial time reversal R_2 with respect to A_2 acts as [71]

$$\rho_A^{R_2} = O_+ = \sum_{\substack{\kappa, \tau \\ |\kappa| + |\tau| = \text{even}}} w_{\kappa, \tau} i^{|\tau|} c_{-2\ell+1}^{\kappa_1} \cdots c_0^{\kappa_{2\ell}} c_1^{\tau_1} \cdots c_{2\ell}^{\tau_{2\ell}}, \quad (4.2.14)$$

where we have introduced the shorthand notation O_+ which will be useful also for the definition of the partial transpose. Note that, in general, O_+ is not a Hermitian operator and its conjugate will be denoted by $O_- = O_+^\dagger$. The fermionic logarithmic negativity is then defined as

$$\mathcal{E}_f = \ln \|\rho_A^{R_2}\|_1 = \ln \text{Tr} \sqrt{O_+ O_-}. \quad (4.2.15)$$

Our goal is now to calculate \mathcal{E}_f via the Majorana covariance matrix

$$\Gamma_{mn} = \frac{1}{2} \text{Tr} (\rho [c_m, c_n]), \quad (4.2.16)$$

where ρ is the density matrix obtained from the pure state (4.2.3) as before. Since the dynamics conserves the fermion number, the covariance matrix Γ is completely determined by $C(t)$ obtained from (4.2.5). Using the definition (4.2.12), it is easy to show that the following relations hold

$$\Gamma_{2j-1, 2l} = -\Gamma_{2j, 2l-1} = i (2 \text{Re}(C_{jl}(t)) - \delta_{jl}), \quad \Gamma_{2j-1, 2l-1} = \Gamma_{2j, 2l} = 2i \text{Im}(C_{jl}(t)). \quad (4.2.17)$$

Note that we have suppressed the explicit t -dependence of the Γ matrix for notational simplicity. Due to the Gaussianity of the state, the reduced density matrix

ρ_A is characterized by the reduced covariance matrix Γ_A . Moreover, one can show that O_{\pm} are both Gaussian operators, with corresponding covariance matrix elements

$$(\Gamma_{\pm})_{mn} = \frac{1}{2} \text{Tr} (O_{\pm}[c_m, c_n]), \quad (4.2.18)$$

that can be written in the block form [70, 185]

$$\Gamma_{\pm} = \begin{pmatrix} \Gamma_{A_1 A_1} & \pm i \Gamma_{A_1 A_2} \\ \pm i \Gamma_{A_2 A_1} & -\Gamma_{A_2 A_2} \end{pmatrix}, \quad (4.2.19)$$

where the block indices A_1 and A_2 denote the corresponding submatrices of Γ_A . Clearly, evaluating the entanglement negativity in (4.2.15) boils down to an exercise of multiplying Gaussian operators and taking their trace. This has been carried out in Ref. [73] by introducing the auxiliary density matrix

$$\rho_{\times} = \frac{O_+ O_-}{\text{Tr} (O_+ O_-)}, \quad (4.2.20)$$

which is a normalized Gaussian state with a real spectrum. Using the multiplication rules of Gaussian states, one can show that the corresponding covariance matrix can be written as [73]

$$\Gamma_{\times} \simeq \left(\frac{\mathbb{1} + \Gamma_A^2}{2} \right)^{-1} \begin{pmatrix} \Gamma_{A_1 A_1} & 0 \\ 0 & -\Gamma_{A_2 A_2} \end{pmatrix}, \quad (4.2.21)$$

where \simeq denotes equality up to a similarity transformation. Indeed, it turns out that the result for \mathcal{E}_f depends only on the spectra $\{\pm \nu_j^{\times}\}$ of Γ_{\times} as well as that $\{\pm \nu_j\}$ of Γ_A , where $j = 1, \dots, 2\ell$ and the eigenvalues come in pairs due to the antisymmetry of the covariance matrix. The traces appearing in \mathcal{E}_f can then be evaluated as

$$\begin{aligned} \text{Tr} (O_+ O_-) &= \text{Tr} (\rho_A^2) = \prod_{j=1}^{2\ell} \frac{1 + \nu_j^2}{2}, \\ \text{Tr} (\rho_{\times}^{1/2}) &= \prod_{j=1}^{2\ell} \left[\left(\frac{1 + \nu_j^{\times}}{2} \right)^{1/2} + \left(\frac{1 - \nu_j^{\times}}{2} \right)^{1/2} \right]. \end{aligned} \quad (4.2.22)$$

Ground state entanglement

Finally, using the formula (4.2.9) for the Rényi entropies, the logarithmic negativity can be put in the suggestive form

$$\mathcal{E}_f = \frac{1}{2} [S_{1/2}(\rho_\times) - S_2(\rho_A)]. \quad (4.2.23)$$

We have thus obtained \mathcal{E}_f as a combination of Rényi entropies of the reduced density matrix ρ_A and the auxiliary density matrix ρ_\times , which in turn can be evaluated using the trace formulas (4.2.22). Note that, since the covariance matrix Γ_\times is equivalent to the one in (4.2.21) which depends only on the matrix elements of Γ_A , the negativity is uniquely determined by the fermionic correlation matrix via (4.2.17). It is instructive to check the limit when ρ_A corresponds to a pure state, such that $\Gamma_A^2 = \mathbb{1}$ and one has trivially $S_2(\rho_A) = 0$. Furthermore, from (4.2.21) one observes that Γ_\times becomes block diagonal and thus $S_{1/2}(\rho_\times) = S_{1/2}(\rho_{A_1}) + S_{1/2}(\rho_{A_2})$. Substituting into (4.2.23) and using the symmetry property $S_{1/2}(\rho_{A_1}) = S_{1/2}(\rho_{A_2})$ of the Rényi entropy, one obtains the well known relation $\mathcal{E}_f = S_{1/2}(\rho_{A_1})$.

4.3 Ground state entanglement

Although the main focus of our work is the time evolution of the entanglement across a defect, it turns out to be very useful to have a look at the ground-state entanglement first. Namely, we shall consider here the ground state of the chain (4.2.1) and calculate the entanglement negativity for the same geometry as for the quench shown in Fig. 4.1, i.e. for two equal segments surrounding the defect. In fact, in the bipartite case when the segment is taken to be the half-chain ($B = \emptyset$), it has been shown that the entanglement entropies in the ground state and after the quench are very closely related [64, 186].

The defect problem for the entanglement was first studied in Ref. [187] where a single interval neighbouring the defect was considered in an infinite chain. The logarithmic scaling of the entropy was found to persist, albeit with a prefactor (dubbed as effective central charge) that varies continuously with the defect strength. Importantly, the contributions to the entanglement from the two boundaries of the interval were found to be additive. An analytical expression for the defect contribution was later derived in [188] by considering the half-chain entropy for $\alpha = 1$, and further exact results for various other α were obtained in [189].

We shall now argue that the effective central charge for $\alpha = 1/2$ will govern also the scaling of the entanglement negativity. Obviously, for the bipartite case

this follows immediately from the relation $\mathcal{E}_f = S_{1/2}(\rho_{A_1}) = \frac{1}{2} \mathcal{I}_{1/2}$. However, even in the generic tripartite case, one expects that the negativity should only be sensitive to the defect contribution. Indeed, \mathcal{E}_f measures the entanglement between the segments A_1 and A_2 and should not care about the contribution of the homogeneous boundaries between A and B . Now, this is exactly the contribution contained in $S_{1/2}(\rho_A)$, which is subtracted in the mutual information. Indeed, as shown in [190], in the limit of $\ell \gg 1$, the Rényi entropy of an interval containing the defect in the middle is just given by the homogeneous result. Therefore, in complete analogy to [67], we assume by a continuity argument that the relation $\mathcal{E}_f \simeq \frac{1}{2} \mathcal{I}_{1/2}$ should hold in the tripartite case as well. Note that the factor $1/2$ just compensates the double counting of the defect contribution.

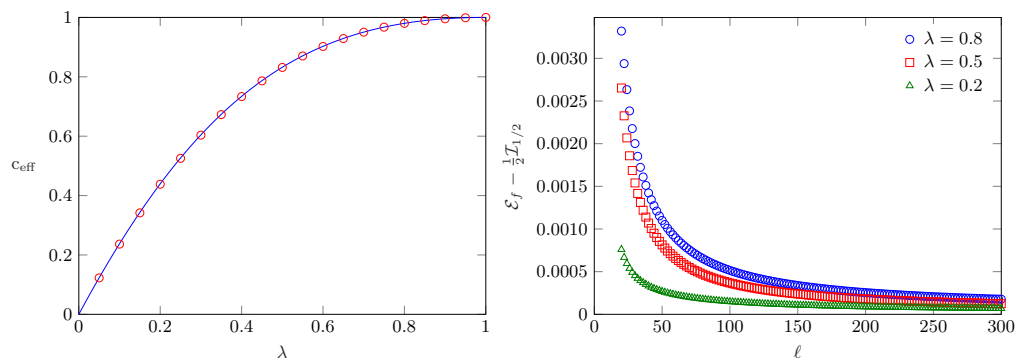


Figure 4.2: Left: comparison of the fits for c_{eff} (circles) according to Eq. (4.3.3), to the analytical formula (4.3.2) (line). Right: difference of \mathcal{E}_f and $\frac{1}{2} \mathcal{I}_{1/2}$ as a function of ℓ for different coupling strengths λ .

One can now use the results for the $\alpha = 1/2$ Rényi entropy to put forward the ansatz for the negativity

$$\mathcal{E}_f \simeq \frac{1}{2} \mathcal{I}_{1/2} = \frac{c_{\text{eff}}}{4} \ln(\ell) + \text{const}, \quad (4.3.1)$$

where the effective central charge reads [189]

$$c_{\text{eff}} = \frac{4}{\pi^2} \text{asin}(s)(\pi - \text{asin}(s)), \quad s = \frac{2}{\lambda + \lambda^{-1}}. \quad (4.3.2)$$

Here s is the transmission amplitude of the defect at the Fermi level $q_F = \pi/2$, i.e. the square root of the transmission coefficient $s = \sqrt{T_{q_F}}$, see (4.5.3). Note that

c_{eff} is given by a smooth function that varies between zero and one, which are the limiting cases of decoupled ($\lambda = 0$) and homogeneous ($\lambda = 1$) chains.

To test our ansatz in (4.3.1), we carried out numerical calculations using the methods of Sec. 4.2, where $C(t)$ has to be replaced by the ground-state correlation matrix. This can be evaluated directly in the thermodynamical limit $L \rightarrow \infty$ [187], with the formulas summarized in Appendix B.1. For a fixed value of λ , we find indeed a logarithmic growth of \mathcal{E}_f with the segment size, which can be fitted to

$$\mathcal{E}_f = \frac{c_{\text{eff}}}{4} \ln(\ell) + a + \frac{b}{\ell}, \quad (4.3.3)$$

in the range up to $\ell = 300$ and including also subleading corrections. A comparison of the fits for c_{eff} obtained from Eq. (4.3.3) and the analytic prediction (4.3.2) is shown on the left of Fig. 4.2, with a perfect agreement. Furthermore, we also compared the logarithmic negativity and the mutual information directly, with their difference shown on the right of Fig. 4.2. One can clearly see that the difference decreases with increasing ℓ , which confirms the assumption $\mathcal{E}_f \simeq \frac{1}{2} \mathcal{I}_{1/2}$ up to subleading corrections that seem to vanish in the $\ell \rightarrow \infty$ limit.

4.4 Quench from equal fillings

After having investigated the ground-state problem, we now move to the quench scenario depicted in Fig. 4.1. First we consider equal fillings, restricting ourselves to the case of half-filled chains $n_l = n_r = 1/2$. For a homogeneous chain ($\lambda = 1$), the time evolution of the entanglement entropy after such a local quench has been calculated for hopping chains [50] as well as within CFT [51, 144]. Moreover, CFT calculations could even be extended to the treatment of the negativity after the quench, using the techniques introduced in [130, 131]. For symmetric intervals in an infinite chain $L \rightarrow \infty$ and $t < \ell$, one obtains the result [74]

$$\mathcal{E}_f = \frac{c}{4} \ln \left(\frac{t^2 + \epsilon^2 \ell - t}{\epsilon^2} \frac{\ell + t}{\ell + t} \right) + \text{const}, \quad (4.4.1)$$

where ϵ is a short-distance cutoff, ubiquitous in CFT calculations. Remarkably, the exact same result can be found for the Rényi mutual information $\frac{1}{2} \mathcal{I}_{1/2}$ in the limit of adjacent intervals, based on the results of Ref. [191], where only the case $\alpha = 1$ was considered but the generalization to $\alpha = 1/2$ is trivial. It should

be stressed that both CFT results contain, in general, a contribution from a non-universal function which, however, is expected to vanish for the Dirac fermion theory we are interested in, and is thus not included in (4.4.1). The characteristic feature of (4.4.1) is an early logarithmic growth for $t \ll \ell$ which then levels off into a plateau, followed by a sharp decrease around $t \rightarrow \ell$. For $t > \ell$, i.e. after the front created by the quench travels through the segment, the negativity assumes its ground-state value $\mathcal{E}_f = c/4 \ln \ell + \text{const}$.

On the other hand, for local quenches across a defect, another interesting result was found for the time evolution of the Rényi entropy of a half-chain, $\ell = L$. Namely, for a hopping chain with a defect, it turns out that the growth of the entropy is logarithmic and governed by the exact same effective central charge as found for the ground-state entanglement [64, 66]. The result was later generalized to arbitrary CFTs with a conformal defect [186]. In particular, for $\alpha = 1/2$ and in the limit $t \ll L$, one finds for the hopping chain

$$S_{1/2}(\rho_{A_1}) = \frac{c_{\text{eff}}}{2} \ln(t) + \text{const}, \quad (4.4.2)$$

where c_{eff} is given by (4.3.2). Note that in the homogeneous case $c_{\text{eff}} = 1$, and thus taking the limit $\ell \rightarrow \infty$, $t \gg \epsilon$ and setting $c = 1$ in (4.4.1) exactly reproduces (4.4.2), as it should.

We now consider the negativity in the tripartite setup of Fig. 4.1. Similarly to the ground-state case in Sec. 4.3, we argue that the relation $\mathcal{E}_f \simeq \frac{1}{2} \mathcal{I}_{1/2}$ should hold also for the local quench across a defect. However, apart from the homogeneous case $\lambda = 1$, we are not aware of any calculations (neither lattice, nor CFT), which would generalize the formula (4.4.2) on the Rényi entropy for an interval $\ell < L$ that is not the half-chain. Nevertheless, it is reasonable to expect that, until the front reaches the boundary $t < \ell$, the entropy of the composite interval $S_{1/2}(\rho_A)$ actually remains constant. Then, by combining the results (4.4.1) and (4.4.2), we propose the following simple ansatz

$$\mathcal{E}_f = \frac{c'_{\text{eff}}}{4} \ln \left(t^2 \frac{\ell - t}{\ell + t} \right) + \text{const}. \quad (4.4.3)$$

Note that one has only two fitting parameters, namely the prefactor c'_{eff} as well as the constant. Clearly, for the limiting cases $\lambda = 0$ and $\lambda = 1$, one has to have $c'_{\text{eff}} = 0$ and $c'_{\text{eff}} = c = 1$, respectively.

For intermediate values of λ , we have determined c'_{eff} by fitting the ansatz (4.4.3) to the numerically calculated \mathcal{E}_f curves for a fixed interval length $\ell = 50$. The

Quench from equal fillings

results are shown in Fig. 4.3. On the left of the figure the numerical data is shown together with the ansatz (4.4.3). On the right hand side we plot the obtained values of c'_{eff} as a function of λ , compared to the equilibrium effective central charge c_{eff} . One can clearly see that the two functions behave very similarly and one has $c'_{\text{eff}} \approx c_{\text{eff}}$. Indeed, for larger values of λ the agreement is almost perfect, however the deviation increases for smaller defect strengths. This is also obvious from the left of Fig. 4.3, where the data for $\lambda = 0.2$ shows already some larger discrepancy compared to the fit function.

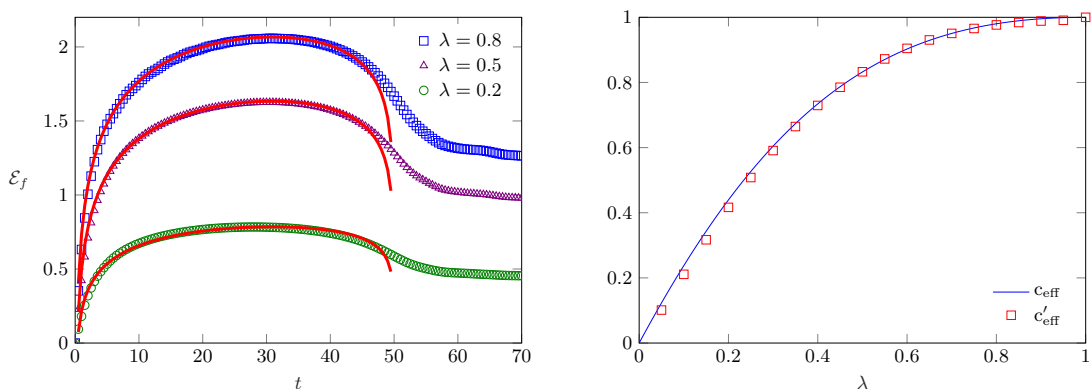


Figure 4.3: Left: time evolution of the logarithmic negativity \mathcal{E}_f after a quench from equal fillings, for $\ell = 50$ and $2L = 600$. The red solid lines show the ansatz (4.4.3) the data is fitted to. Right: comparison of the fitted values of c'_{eff} to the ground-state effective central charge c_{eff} from (4.3.2)

Although the mismatch of the data might be due to finite-size effects, we observe essentially the same behaviour for larger $\ell = 75$. This rather suggests that the simplistic ansatz (4.4.3) is probably not the exact leading functional form of \mathcal{E}_f . In fact, we have also tried a more complicated three-parameter ansatz, assigning two different prefactors to the logarithmic terms with arguments t and $(\ell - t)/(\ell + t)$. Unfortunately, however, the fits turn out to be very unstable against changing the fitting interval, making the results unreliable. Thus we conclude that, without some additional insights (e.g. from CFT calculations) on the structure of \mathcal{E}_f , extracting the proper time-dependence from numerical calculations is a very hard task.

We have also compared the behaviour of \mathcal{E}_f and $\frac{1}{2} \mathcal{I}_{1/2}$ directly. One finds that

the curves almost exactly overlap until roughly $t \approx \ell$, with no visible deviations. Around $t = \ell$ there is only a slight deviation between the two functions, which, however diminishes again for $t \gg \ell$. Indeed, both quantities are expected to converge towards their ground-state values asymptotically, where the deviation was already found to be tiny, see Fig. 4.2. Therefore, for better visibility of the data, we have not included $\frac{1}{2} \mathcal{Z}_{1/2}$ in the left of Fig. 4.3.

4.5 Quench from unequal fillings

We now study initial states with unequal fillings, where the behaviour of the entanglement negativity turns out to be qualitatively different from the unbiased case discussed above. In most of our calculations we shall actually consider the maximally biased case, $n_l = 1$ and $n_r = 0$, while at the end of the section we show that the generalization to arbitrary fillings is straightforward. Similarly to the unbiased case, we first discuss the negativity evolution for a homogeneous chain ($\lambda = 1$), where results can also be obtained via CFT techniques.

4.5.1 Homogeneous chain

This case is also known as the domain-wall quench, due to the form of the initial state in the spin-chain equivalent of the hopping model. Here one can work directly in the thermodynamic limit, $L \rightarrow \infty$, where the correlation matrix is known exactly and has the simple form [177]

$$C_{mn}(t) = \frac{i^{n-m} t}{2(m-n)} [J_{m-1}(t)J_n(t) - J_m(t)J_{n-1}(t)], \quad (4.5.1)$$

where $J_m(t)$ is the Bessel function of order m . Remarkably, the correlation matrix for the domain-wall quench is unitarily equivalent to the one in a static ground-state problem, namely a hopping chain with a linear chemical potential [146], with the time t playing the role of the characteristic length scale of the potential. This can actually be shown to be a particular example of a more general mapping, known as emergent eigenstate solution [192]. Consequently, the entanglement properties in the dynamical and static problems are identical.

The entanglement entropy for a biased hopping chain was studied in [52, 55, 146, 149] between two parts of the chain, with the cut located somewhere along the

emerging front. The growth was found to be logarithmic, however with a different prefactor as for the local (unbiased) quench. The analytical understanding of the results for $n_l = 1$ and $n_r = 0$ came afterwards, when the method of curved-space CFT was developed [53]. The basic idea is that certain inhomogeneous free-fermion problems can be treated by first mapping the problem to a CFT in a curved background metric. The entanglement entropies can be calculated by applying standard replica-trick methods [104] for the curved-space Dirac fermion theory (see also [193] for recent results on inhomogeneous Luttinger liquids). This makes it possible to extract the entropy analytically for a half-chain, or even generalize the calculations to a finite segment within the front region [53]. The mutual information $\frac{1}{2} \mathcal{I}_{1/2}$ in our setup can be obtained immediately from the latter result.

Furthermore, it is possible to combine the curved-space technique with the CFT approach to the negativity [130, 131]. The calculation is straightforward but somewhat lengthy, thus we present it in Appendix B.2. As a result, we obtain for both the negativity and the mutual information

$$\mathcal{E}_f = \frac{1}{2} \mathcal{I}_{1/2} = \frac{1}{4} \ln [t f(\ell/t)] + c_1, \quad f(\xi) = \begin{cases} 1 & t < \ell \\ \frac{(1-\sqrt{1-\xi^2})^2}{\xi^3} & t > \ell \end{cases} \quad (4.5.2)$$

Note that, apart from an explicit factor of t which gives the logarithmic growth of the negativity, (4.5.2) depends only on a scaling function of the variable $\xi = \ell/t$. It should be stressed that the calculation in Appendix B.2 refers only to $\xi < 1$, as the curved-space CFT is able to describe only the front region with nontrivial fermionic density. However, the $\xi > 1$ result can be obtained by using continuity and some simple arguments. Indeed, for $\ell > t$, the segments include parts of the chain outside the front, where the density is either zero or one. Clearly, these pieces do not contribute to the entanglement at all, which is thus given by the result for $\ell = t$, i.e. by the limit $\xi \rightarrow 1$. The CFT results in (4.5.2) are compared to our numerical calculations in Fig. 4.4 with a very good agreement. The constant $c_1 \approx 0.646$ has been obtained by fitting the data for \mathcal{E}_f in the regime $t < \ell$. The only visible deviations are around $t = \ell$, i.e. when the boundaries of the segments are close to the edges of the front. Indeed, the front is known to have a nontrivial scaling behaviour around the edge [177, 178, 181], characterized by the scale $t^{1/3}$, which is not resolved by the CFT treatment. Nevertheless, when plotted against $t/\ell = \xi^{-1}$ and after subtracting $1/4 \ln(t)$, the lattice data for increasing ℓ converge

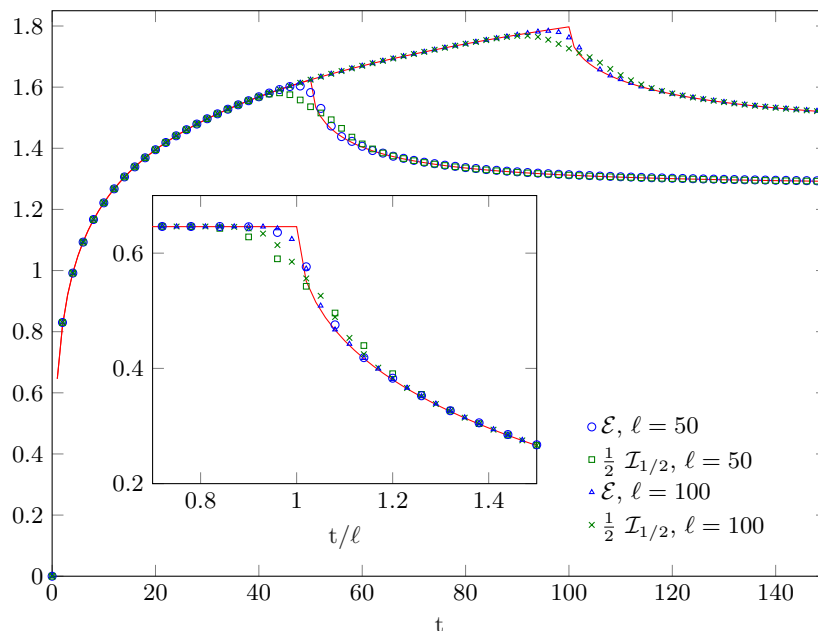


Figure 4.4: Logarithmic negativity \mathcal{E}_f and mutual information $\frac{1}{2} \mathcal{I}_{1/2}$ after the domain wall quench in a homogeneous chain ($\lambda = 1$), compared to the CFT prediction (4.5.2) (red solid lines) for two different segment sizes. The inset shows the scaled data around $t = \ell$, after subtracting $\frac{1}{4} \ln(t)$.

smoothly towards the CFT result as shown in the inset of Fig. 4.4. Note also that the $t \rightarrow \infty$ behaviour can be obtained by expanding $f(\xi) \approx \xi/4$ for $\xi \rightarrow 0$, such that the steady state is characterized by $\mathcal{E}_f = 1/4 \ln \ell + \text{const}$.

4.5.2 Chain with a defect

The time evolution of entanglement across a defect turns out to be qualitatively different [64]. Indeed, an imperfect transmission between the half-chains gives rise to scattering, i.e. the single-particle modes are partially transmitted and reflected with probabilities T_q and $R_q = 1 - T_q$, respectively. For a weak hopping defect parametrized by $\lambda = e^{-\nu}$, the transmission coefficient is given by

$$T_q = \frac{\sin^2(q)}{\cosh^2(\nu) - \cos^2(q)}. \quad (4.5.3)$$

Quench from unequal fillings

The transmitted and reflected particles become entangled in the wavefunction, and the contribution of such a pair in the $\alpha = 1/2$ Rényi entropy is $s_{1/2}(T_q)$, where

$$s_{1/2}(x) = 2 \ln(x^{1/2} + (1-x)^{1/2}) \quad (4.5.4)$$

is the density of the Rényi entropy, c.f. Eq. (4.2.11). Now, due to the density bias in the initial state, there is a constant influx of particles and consequently a steady generation of entanglement at the defect. For a half-chain, $\ell = L$, at maximum bias and in the limit $L \rightarrow \infty$, this was found to give, to leading order, a linear growth of entanglement [64]

$$S_{1/2}(\rho_{A_1}) = t \int_0^\pi \frac{dq}{2\pi} v_q s_{1/2}(T_q), \quad (4.5.5)$$

where $v_q = \sin(q)$ is the single-particle group velocity and the integral is taken over all modes with $v_q > 0$.

This simple semiclassical picture of entanglement production, based on the propagation of entangled pairs of quasiparticles, bears a strong similarity to global quenches [22, 29]. One should stress, however, that here the pairs are created

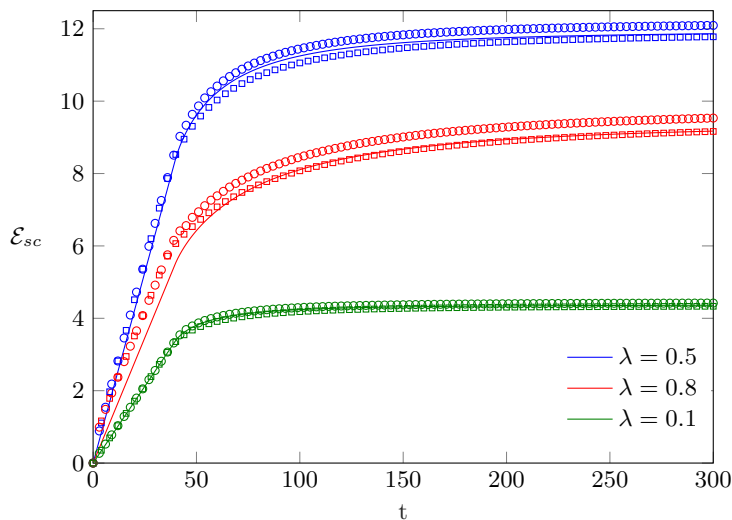


Figure 4.5: Entanglement negativity \mathcal{E}_f (circles) and mutual information $\frac{1}{2} \mathcal{I}_{1/2}$ (squares) after a quench from unequal fillings $n_l = 1$ and $n_r = 0$, compared to the semiclassical ansatz (4.5.6) (lines) for $\ell = 40$ and different values of λ .

solely at the defect site but steadily in time, in contrast to a global quench where pairs are created only at $t = 0$ but homogeneously along the chain. Nevertheless, the continuity argument $\mathcal{E}_f \simeq \frac{1}{2} \mathcal{I}_{1/2}$ can be applied the very same way as for the global quench [67]. Indeed, due to the strictly local production of entanglement at the common boundary of the segments, the only effect of their finite size is to cut off the growth of the negativity once the distance travelled by a given mode $v_q t$ exceeds the segment size ℓ . This leads to the semiclassical expression

$$\mathcal{E}_{sc} = \int_0^\pi \frac{dq}{2\pi} \min(v_q t, \ell) s_{1/2}(T_q). \quad (4.5.6)$$

To test the validity of our ansatz \mathcal{E}_{sc} , in Fig. 4.5 we plot the integrals (4.5.6) for various λ and compare them to the numerical data for \mathcal{E}_f and $\frac{1}{2} \mathcal{I}_{1/2}$ obtained for a chain of length $2L = 500$ from the correlation-matrix method. One can see that the semiclassical picture provides a rather good description of the data to leading order, there are, however, still some sizeable corrections which tend to diminish for smaller values of λ . The quantities \mathcal{E}_f and $\frac{1}{2} \mathcal{I}_{1/2}$ perfectly overlap in the regime $t < \ell$ of linear growth, where the result is identical to the one for the half-chain (4.5.5), as there is no contribution to the entanglement from the outer boundaries of the segments. Interestingly, however, there is a clearly visible splitting for $t > \ell$, after the front has traversed the segments.

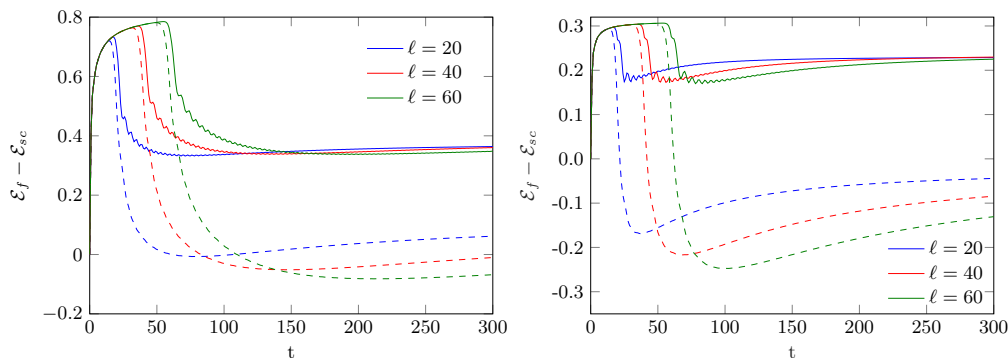


Figure 4.6: Deviations of \mathcal{E}_f (solid lines) and $\frac{1}{2} \mathcal{I}_{1/2}$ (dashed lines) from the semiclassical ansatz (4.5.6) for $\lambda = 0.8$ (left) and $\lambda = 0.5$ (right) and various segment sizes ℓ .

Quench from unequal fillings

In order to better understand the corrections beyond the semiclassical picture, in Fig. 4.6 we have subtracted \mathcal{E}_{sc} from the data, shown for the two larger values of λ and several segment sizes. Similarly to \mathcal{E}_{sc} , the deviation also shows different behaviour in the regimes $t < \ell$ and $t > \ell$. Until roughly $t \approx \ell$, one observes a steady growth which becomes slower for larger defect strengths. A closer inspection shows that this subleading growth is actually slower than logarithmic for all the values $\lambda \neq 1$ we have checked. When the front crosses the segment boundary, one has a sharp drop in all of the curves, which is then followed again by a very slow increase. Note that the splitting of the \mathcal{E}_f and $\frac{1}{2}\mathcal{I}_{1/2}$ curves is even more apparent in Fig. 4.6. However, due to the very slow variation of the data, it is hard to draw a firm conclusion about the asymptotic behaviour, despite the relatively large times considered in the calculations.

The steady state after the quench across the defect can actually be captured directly. Indeed, the elements of the correlation matrix in (4.2.5) have a well defined limit [194]

$$\tilde{C}_{m,n} = \lim_{t \rightarrow \infty} \lim_{N \rightarrow \infty} C_{m,n}(t), \quad (4.5.7)$$

with the explicit formulas collected in Appendix B.1. These can be used to evaluate the subleading scaling of the steady-state negativity and mutual information,

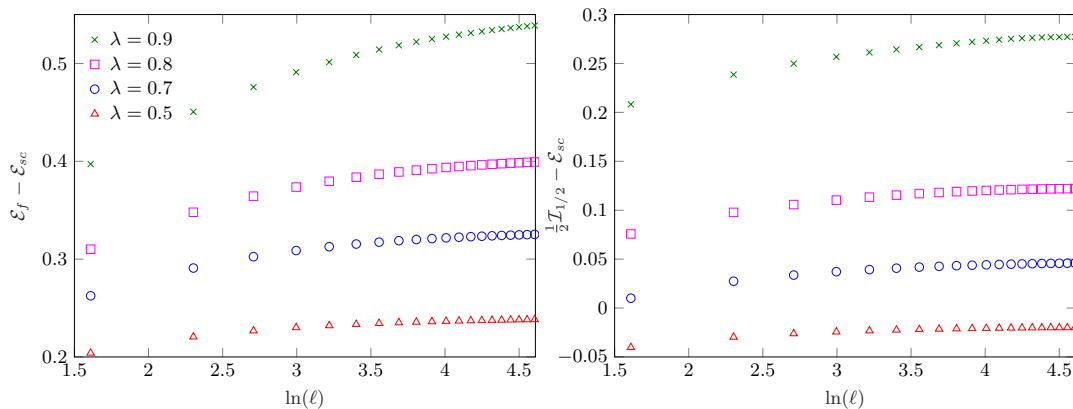


Figure 4.7: Steady-state negativity (left) and mutual information (right), as calculated from the correlation matrix (4.5.7) after subtracting the extensive semiclassical contribution (4.5.6). The data is plotted against $\ln(\ell)$ for various defect strengths λ . Note the different vertical scales.

i.e. after subtracting the extensive contribution $\lim_{t \rightarrow \infty} \mathcal{E}_{sc}$ that follows from the semiclassical description (4.5.6). The results are shown in Fig. 4.7, with both the data for \mathcal{E}_f (left) as well as $\frac{1}{2} \mathcal{I}_{1/2}$ (right) plotted against $\ln(\ell)$. Rather clearly, the subleading terms in the steady state are different for the two quantities and the scaling in ℓ is slower than logarithmic. This is also supported by the form of the steady-state correlation matrix (B.1.10) on a given side of the defect, which is a Toeplitz matrix with a symbol given by T_q for $q > 0$ and zero otherwise. While this yields immediately the extensive part of the negativity (4.5.6), one has also $T_q \rightarrow 0$ for $q \rightarrow 0$ and thus no jump singularity is present. Nevertheless, the symbol is still nonanalytic and shows a very sharp increase around $q = 0$ as $\lambda \rightarrow 1$. Thus a weaker than logarithmic growth of the subleading term, although unlikely from the numerics, cannot be excluded.

Finally, we briefly consider the case of arbitrary fillings with $n_l > n_r$. The straightforward generalization of the semiclassical ansatz reads

$$\mathcal{E}_{sc} = \int_{q_{F,r}}^{q_{F,l}} \frac{dq}{2\pi} \min(v_q t, \ell) s_{1/2}(T_q), \quad (4.5.8)$$

where the integral is carried out only between the Fermi wavenumbers $q_{F,\sigma} = \pi n_\sigma$. In other words, one has to consider only the contributions from the uncompensated

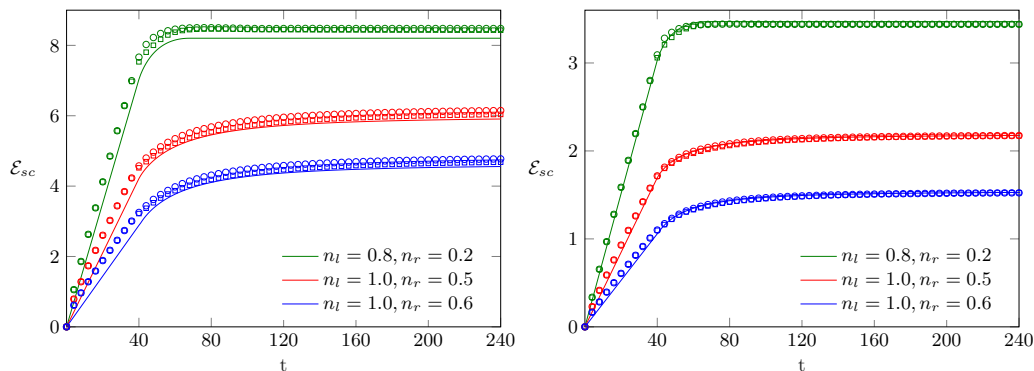


Figure 4.8: Entanglement negativity \mathcal{E}_f (circles) and mutual information $\frac{1}{2} \mathcal{I}_{1/2}$ (squares) after a quench from various unequal fillings, compared to the semiclassical ansatz (4.5.8) (lines) for $\ell = 40$ and $\lambda = 0.5$ (left) resp. $\lambda = 0.1$ (right).

fermionic modes, that can propagate from the left to the right half-chain. The resulting curves are shown in Fig. 4.8, for two different λ and various fillings, together with the numerically calculated \mathcal{E}_f and $\frac{1}{2}\mathcal{I}_{1/2}$ in a chain of size $2L = 500$. As expected, the plots are very similar to the one in Fig. 4.5, with the deviations from the semiclassical prediction decreasing for smaller λ . Due to the similar qualitative behaviour, a detailed analysis of the subleading terms is not presented for this case.

4.6 Quench in the XXZ chain with a defect

Finally we are considering a quench in the XXZ spin chain, given by the Hamiltonian

$$\hat{H}_{XXZ} = \sum_{j=-L+1}^{L-1} [J_j (S_j^x S_{j+1}^x + S_j^y S_{j+1}^y) + \Delta S_j^z S_{j+1}^z], \quad (4.6.1)$$

where S_j^α are spin-1/2 operators, Δ is the anisotropy parameter, and the XX-coupling is given by

$$J_j = \begin{cases} 1 & \text{if } j \neq 0, \\ \lambda \Theta(t) & \text{if } j = 0. \end{cases} \quad (4.6.2)$$

Here $\Theta(t)$ is the Heaviside step function, in other words, the quench consists of simply joining two decoupled XXZ half-chains at time $t = 0$. Applying a Jordan-Wigner transformation, the Hamiltonian (4.6.1) can be mapped into a chain of interacting fermions and the setup becomes exactly the same as the one depicted in Fig. 4.1 for free fermions without a density bias.

However, it turns out that the negativity depends on the choice of basis and is not equivalent in the fermion or spin representation. Indeed, using spin variables, one has to apply the conventional definition of the logarithmic negativity via the partial transpose of the density matrix [69]

$$\mathcal{E}_s = \ln \|\rho_A^{T_2}\|_1. \quad (4.6.3)$$

Here the partial transpose is taken with respect to subsystem A_2 , defined by its matrix elements as

$$\langle e_i^{(1)}, e_j^{(2)} | \rho_A^{T_2} | e_k^{(1)}, e_l^{(2)} \rangle = \langle e_i^{(1)}, e_l^{(2)} | \rho_A | e_k^{(1)}, e_j^{(2)} \rangle, \quad (4.6.4)$$

where $|e_i^{(1)}\rangle$ and $|e_j^{(2)}\rangle$ denote orthonormal bases on the Hilbert spaces pertaining to segments A_1 and A_2 .

Clearly, since we are now faced with a non-Gaussian problem, we have to compute the negativity \mathcal{E}_s via density-matrix renormalization group (DMRG) [10–12] methods. In particular, the time evolution $|\psi(t)\rangle = e^{-i\hat{H}_{XXZ}t} |\psi(0)\rangle$ after the quench is first performed with time-dependent DMRG (tDMRG) simulations [56, 57], which give access to the reduced density matrix ρ_A in a matrix product state (MPS) representation [168]. The partial transpose and the corresponding logarithmic negativity can then be calculated using the method of Ref. [79], which is briefly reviewed in the following subsection.

4.6.1 Negativity for matrix product states

Let us consider the time-evolved state after the quench $|\psi(t)\rangle = e^{-i\hat{H}_{XXZ}t} |\psi(0)\rangle$ and its MPS representation

$$|\psi(t)\rangle = \sum_{\sigma_1 \dots \sigma_{2L}} T_{\nu_1}^{\sigma_1} T_{\nu_1 \nu_2}^{\sigma_2} \dots T_{\nu_{2L-1}}^{\sigma_{2L}} |\sigma_1 \dots \sigma_{2L}\rangle, \quad (4.6.5)$$

where $T_{\nu_{i-1} \nu_i}^{\sigma_i}$ denotes the tensor on site i with bond indices ν_{i-1} and ν_i and the physical index $\sigma_i = 0, 1$. In Eq. (4.6.5) and all the following equations, we assume summation over all repeated bond indices ν_i implicitly, and indicate only summations over the physical indices for better readability.

Our goal is to calculate the negativity for the geometry depicted in Fig. 4.1, i.e. between two adjacent segments A_1 and A_2 with $A = A_1 \cup A_2$. The main step is to construct the reduced density matrix ρ_A , which is shown graphically on the left of Fig. 4.9, after tracing out over the environment B . The squares in different colors depict the tensors belonging to either subsystems A_1 or A_2 , c.f. Fig. 4.1. One can now introduce new basis states in the Hilbert spaces of the two intervals A_1 and A_2 as

$$|w_{\nu_{1l}, \nu_{1r}}^{(1)}\rangle = \sum_{\{\sigma_i\}} \prod_{i \in A_1} T_{\nu_{i-1} \nu_i}^{\sigma_i} |\sigma_i\rangle, \quad |w_{\nu_{2l}, \nu_{2r}}^{(2)}\rangle = \sum_{\{\sigma_i\}} \prod_{i \in A_2} T_{\nu_{i-1} \nu_i}^{\sigma_i} |\sigma_i\rangle, \quad (4.6.6)$$

where the index pairs ν_{1l}, ν_{1r} and ν_{2l}, ν_{2r} indicate the uncontracted left- and right-most bond indices for each block. Using these basis states, we can eventually write

the reduced density matrix as

$$\rho_A = \delta_{\nu_{1l}, \nu'_{1l}} \delta_{\nu_{2r}, \nu'_{2r}} \delta_{\nu_{1r}, \nu_{2l}} \delta_{\nu'_{1r}, \nu'_{2l}} |w_{\nu_{1l}, \nu_{1r}}^{(1)}\rangle \langle w_{\nu'_{1l}, \nu'_{1r}}^{(1)}| \otimes |w_{\nu_{2l}, \nu_{2r}}^{(2)}\rangle \langle w_{\nu'_{2l}, \nu'_{2r}}^{(2)}|, \quad (4.6.7)$$

where the delta functions carry out the contractions of the remaining bond indices, as visualized in the left of Fig. 4.9.

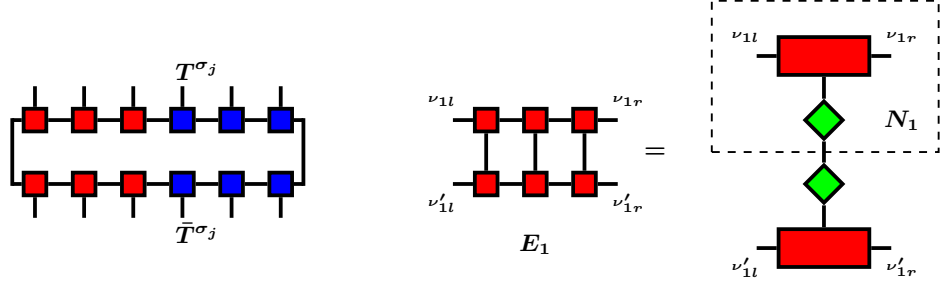


Figure 4.9: Graphical representation of the reduced density matrix ρ_A (left), the transfer matrix E_1 corresponding to the segment A_1 (middle), and its singular value decomposition (right). The boxes represent tensors with the contractions indicated by the links between them.

The representation (4.6.7) yields a decomposition of ρ_A on the two subspaces corresponding to A_1 and A_2 . However, the main problem is that the choice of basis in (4.6.6) is not orthogonal. Indeed, the overlaps between these states are given by the so-called transfer matrices

$$\langle w_{\nu_{1l}, \nu_{1r}}^{(1)} | w_{\nu'_{1l}, \nu'_{1r}}^{(1)} \rangle = [E_1]_{\nu'_{1l}, \nu'_{1r}}^{\nu_{1l}, \nu_{1r}}, \quad \langle w_{\nu_{2l}, \nu_{2r}}^{(2)} | w_{\nu'_{2l}, \nu'_{2r}}^{(2)} \rangle = [E_2]_{\nu'_{2l}, \nu'_{2r}}^{\nu_{2l}, \nu_{2r}}, \quad (4.6.8)$$

that are obtained by contracting all the tensors with their complex conjugates via their physical indices within the respective segment

$$[E_1]_{\nu'_{1l}, \nu'_{1r}}^{\nu_{1l}, \nu_{1r}} = \prod_{i \in A_1} \sum_{\sigma_i} T_{\nu_{i-1} \nu_i}^{\sigma_i} \bar{T}_{\nu'_{i-1} \nu'_i}^{\sigma_i}, \quad [E_2]_{\nu'_{2l}, \nu'_{2r}}^{\nu_{2l}, \nu_{2r}} = \prod_{i \in A_2} \sum_{\sigma_i} T_{\nu_{i-1} \nu_i}^{\sigma_i} \bar{T}_{\nu'_{i-1} \nu'_i}^{\sigma_i}. \quad (4.6.9)$$

These objects are thus four-index tensors, corresponding to the uncontracted left- and rightmost bond indices, see the middle panel of Fig. 4.9 for a graphical representation of E_1 .

In order to obtain an orthogonal basis, one has to perform a singular value decomposition (SVD) of the transfer matrices $E_1 = U_1 D_1 V_1^\dagger$ and $E_2 = U_2 D_2 V_2^\dagger$. This amounts to introducing a basis change via

$$|w_{\nu_{1l}, \nu_{1r}}^{(1)}\rangle = \sum_m [N_1]_{\nu_{1l}, \nu_{1r}}^m |v_m^{(1)}\rangle, \quad |w_{\nu_{2l}, \nu_{2r}}^{(2)}\rangle = \sum_n [N_2]_{\nu_{2l}, \nu_{2r}}^n |v_n^{(2)}\rangle, \quad (4.6.10)$$

where $N_1 = U_1 D_1^{1/2}$ and $N_2 = U_2 D_2^{1/2}$, and the new indices m and n correspond to the singular values contained in the diagonal matrices D_1 and D_2 . The pictorial representation of the SVD for E_1 is shown on the right of Fig. 4.9, where $D_1^{1/2}$ is depicted by the green rhombi. Inserting (4.6.10) into (4.6.7), one immediately obtains the matrix elements of the reduced density matrix

$$[\rho_A]_{n, n'}^{m, m'} = [N_1]_{\nu_{1l}, \nu_{2l}}^m [\bar{N}_1]_{\nu_{1l}, \nu_{2l}}^{m'} [N_2]_{\nu_{2l}, \nu_{2r}}^n [\bar{N}_2]_{\nu_{2l}, \nu_{2r}}^{n'} \quad (4.6.11)$$

expressed in the orthogonal bases $|v_m^{(1)}\rangle$ and $|v_n^{(2)}\rangle$. Note that (4.6.11) is now exactly in the form required to carry out the partial transposition according to (4.6.4). Indeed, the index pairs m, m' and n, n' correspond to the intervals A_1 and A_2 , respectively. Therefore, the matrix elements of $\rho_A^{T_2}$ can simply be obtained by exchanging n and n' . Finally, the logarithmic negativity \mathcal{E}_s in Eq. 4.6.3 can be calculated via an explicit diagonalization of $\rho_A^{T_2}$.

Regarding the computational effort, one has to stress that the cost of constructing the transfer matrices in (4.6.9) scales as $\mathcal{O}(\chi_{max}^6)$ with the maximum bond dimension χ_{max} of the MPS. This, however, grows with the time evolution where we set the requirement $\epsilon \sim 10^{-8} - 10^{-9}$ for the truncated weight. For a feasible computation of the transfer matrices, we truncated back the bond dimension to $\chi_{max} = 300$. The range of each index m, m' as well as n, n' in the representation (4.6.11) is then bounded by χ_{max}^2 , which is still too large for a tractable calculation. However, since the singular values of E_1 and E_2 decay rapidly, one can apply a truncation after the SVD which we set to $\chi'_{max} = 80$. All in all, the evaluation of entanglement negativity is computationally much more demanding than that of the entropy, severely limiting the attainable segment sizes and simulation times in our numerics.

4.6.2 Numerical results

The methods outlined in the previous subsection are now used to evaluate the time evolution of the logarithmic negativity across a defect in the XXZ chain. We focus

exclusively on the unbiased case, as the bias induces a much more rapid growth of entanglement, which makes the DMRG calculations very demanding. We first present the results for the XX chain, which is just the special case of $\Delta = 0$ in (4.6.1). Note that, even though the XX chain with a defect is exactly mapped into the fermionic Hamiltonian in Eq. (4.2.1) via a Jordan-Wigner transformation, the negativity \mathcal{E}_s calculated for the spin chain in (4.6.3) is not equivalent to the fermionic one \mathcal{E}_f defined in (4.2.15). Indeed, it has been shown in [70] that the partial transposition in the spin basis yields a linear combination of two fermionic Gaussian operators

$$\rho_A^{T_2} = \frac{1-i}{2}O_+ + \frac{1+i}{2}O_-, \quad (4.6.12)$$

where $O_+ = \rho_A^{R_2}$ is the operator obtained in (4.2.14) by partial time reversal of the fermionic degrees of freedom and $O_- = O_+^\dagger$. Since in general the operators O_+ and O_- do not commute, one has no access to the spectrum of $\rho_A^{T_2}$ and hence to \mathcal{E}_s via simple covariance-matrix techniques. Nevertheless, the spin-chain negativity can be shown to be upper-bounded by the fermionic one as [73, 115]

$$\mathcal{E}_s \leq \mathcal{E}_f + \ln \sqrt{2}. \quad (4.6.13)$$

The time evolution of \mathcal{E}_s obtained from tDMRG simulations are shown by the full symbols in Fig. 4.10 for various defect strengths λ . The results are compared to the fermionic negativity \mathcal{E}_f , shown by the empty symbols, and indicate that the upper bound in (4.6.13) actually holds even without the additional constant, i.e. one has $\mathcal{E}_s \leq \mathcal{E}_f$. The two quantities have a very similar qualitative behaviour, with their difference diminishing with decreasing λ . Unfortunately, however, the simulation times as well as the size of the segments are severely limited in the tDMRG simulations due to the increasing entanglement and bond dimension during time evolution, especially for higher values of λ . This makes a quantitative analysis of the discrepancy between \mathcal{E}_s and \mathcal{E}_f rather complicated. We also performed analogous tDMRG simulations for the XXZ chain with the anisotropy parameter $0 < \Delta < 1$. The fermionic analogue of this setting corresponds to an interacting problem and thus not amenable to Gaussian techniques. We first considered the homogeneous case $\lambda = 1$, where the post-quench Hamiltonian is integrable and its low-energy behaviour is described by a Luttinger liquid. In particular, the spreading of excitations created above the ground state is given by the spinon

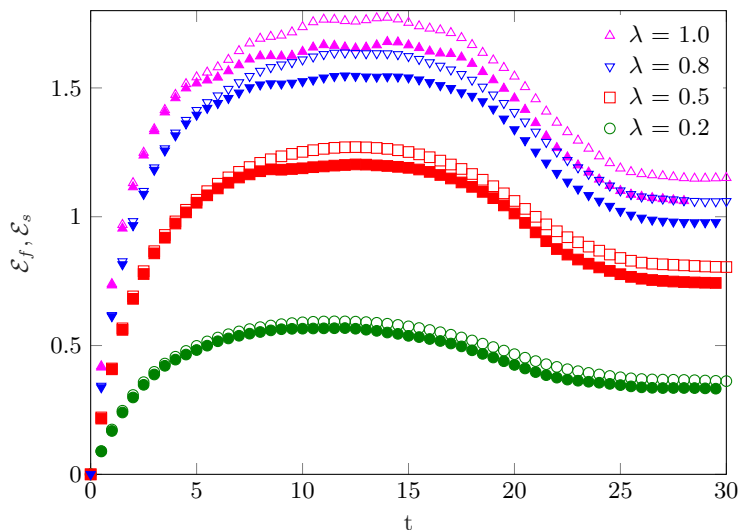


Figure 4.10: Time evolution of the entanglement negativity \mathcal{E}_s (full symbols) for two adjacent segments of size $\ell = 20$ across a defect of various strengths λ in an XX chain with $2L = 100$. The data for the fermionic negativity \mathcal{E}_f (empty symbols) in the analogous quench of the hopping chain with a defect is shown for comparison.

velocity [93]

$$v_s = \frac{\pi \sqrt{1 - \Delta^2}}{2 \arccos(\Delta)}. \quad (4.6.14)$$

This strongly suggests that the main difference with respect to the homogeneous XX quench is due to the change in the Fermi velocity. On the left of Fig. 4.11 we have thus plotted the logarithmic negativity \mathcal{E}_s calculated for various Δ against the variable $v_s t$, which indeed leads to a nice data collapse.

The situation for $\lambda \neq 1$ is more complicated, as the presence of the defect breaks the integrability of the model. The time evolution of the negativity is shown on the right of Fig. 4.11 for various defect strengths λ and fixed $\Delta = 0.5$, for a segment size $\ell = 20$. Qualitatively, one observes a very similar behaviour as for the XX chain in Fig. 4.10. However, in previous studies of the half-chain entropy in Ref. [151] it was observed that the entropy growth is actually suppressed for repulsive interactions $\Delta > 0$, corresponding to an effective central charge that goes to zero in the limit of large chain sizes. This is actually the same mechanism

Discussion

that was found for the ground-state entropy of the XXZ chain with a defect [195], and is the manifestation of a Kane-Fisher type renormalization behaviour [196]. Therefore it is reasonable to expect that the entanglement negativity would show a similar behaviour in the limit of large ℓ . Unfortunately, however, the segment sizes required to test such a crossover are well beyond the limitations of our simulations.

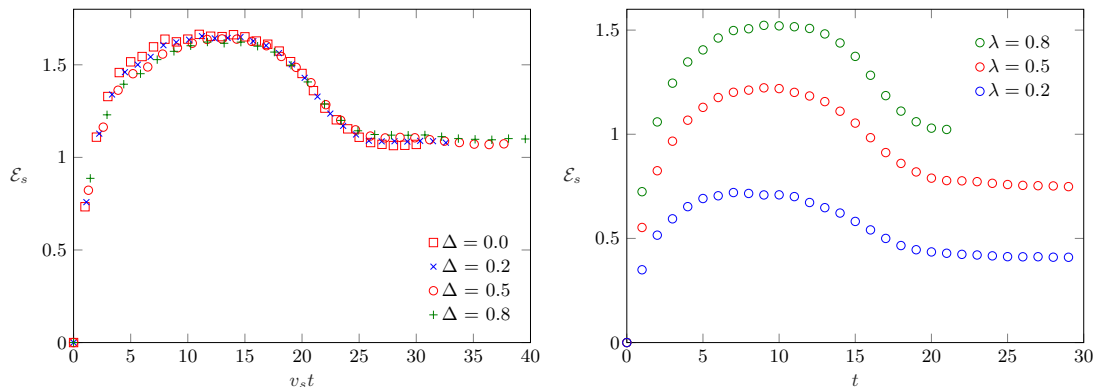


Figure 4.11: Time evolution of the entanglement negativity \mathcal{E}_s for two adjacent segments of size $\ell = 20$ in an XXZ chain with $2L = 100$. Left: homogeneous quench ($\lambda = 1$) for different anisotropies Δ . Right: quench across a defect of different strengths λ and $\Delta = 0.5$.

4.7 Discussion

We have studied entanglement in a hopping chain with a defect, focusing on the fermionic version of the logarithmic negativity \mathcal{E}_f between two segments neighbouring the defect, and its relation to the Rényi mutual information $\frac{1}{2} \mathcal{I}_{1/2}$. In the ground state of the chain, the negativity scales logarithmically with an effective central charge c_{eff} , and the difference $\mathcal{E}_f - \frac{1}{2} \mathcal{I}_{1/2}$ goes to zero for increasing segment sizes. For a quench across the defect, starting from disconnected half-chains both at half filling, the growth of the negativity is logarithmic in time and the prefactor seems to be well approximated by c_{eff} . When the quench is performed from biased fillings, the entanglement growth becomes linear, followed by a saturation at an extensive value, which is due to backscattering from the defect and can be understood in a semiclassical picture. Although the ansatz (4.5.6) gives a very

good leading order description of both \mathcal{E}_f and $\frac{1}{2}\mathcal{I}_{1/2}$, the subleading corrections behave differently and their difference in the steady state remains finite even for large segment sizes. We have also calculated the standard logarithmic negativity \mathcal{E}_s via DMRG methods in the XXZ spin chain after a (unbiased) quench across a defect. In the noninteracting XX case, closely related to the fermionic chain, we found that the spin-chain negativity is upper bounded by the fermionic one, $\mathcal{E}_s \leq \mathcal{E}_f$. In the general XXZ case, the results for \mathcal{E}_s look qualitatively similar to the XX case for the small segment sizes attainable.

While the entanglement growth in the biased case has a very clear physical interpretation, the result for equal fillings is harder to grasp and would require some insight from CFT calculations. In fact, for the bipartite case of a half-chain, the CFT representation of the density matrix after the quench can be transformed into the one for the ground state by an appropriate conformal mapping [186]. Unfortunately, however, this transformation works only for the half-chain and it is unclear whether a generalization to our geometry exists.

It is important to stress that, although the semiclassical picture for unequal fillings is analogous to the one for a global quench [67], the qualitative behaviour of the negativity is completely different. Indeed, in the latter case the quasiparticles are created only at $t = 0$, and thus the pairs that contribute to the entanglement growth eventually leave the segments. This implies that the negativity will decrease again for large times, decaying towards zero. In contrast, in our case there is a constant production of entangled pairs at the defect, and thus the negativity keeps growing until it eventually saturates at an extensive value. Furthermore, while for the global quench the deviation between \mathcal{E}_f and $\frac{1}{2}\mathcal{I}_{1/2}$ seems to vanish for increasing ℓ , for the defect we observe a finite difference between the two quantities. Understanding the origin of this discrepancy requires further investigations.

Finally, it would be interesting to extend these investigations to disjoint segments. In particular, it would be illuminating to see how the disagreement between the fermionic and XX chain negativities changes with separation. One expects the discrepancy to become larger, as the partial transpose is a sum of four fermionic Gaussian operators already in the ground state [197]. While the extension of both the fermionic as well as the spin-chain calculations are, in principle, straightforward, the computational effort of the DMRG calculations are much more demanding and are thus left for future studies.

Acknowledgments

We thank D. Bauernfeind, F. Maislinger and Z. Zimborás for useful discussions. The authors acknowledge funding from the Austrian Science Fund (FWF) through Project No. P30616-N36.

Chapter 5

Entanglement spreading after local fermionic excitations in the XXZ chain (arXiv:2010.02708 (2020))

In this chapter we present our findings from Ref. [198], which is one of the main publications of the author. In the following, the abstract and the sections II. - VI. of the paper, which contain the used methods, the obtained results as well as the conclusions, are completely included in sections 5.1 - 5.6 of the present thesis. The appendix was also taken from the paper and can be found in C.1.

The paper was first drafted by the author of this thesis and later substantially edited equally by him and Viktor Eisler. All numerical calculations were performed by the author of this thesis. Both authors equally performed the CFT calculations and contributed equally to the interpretation of the results.

5.1 Abstract

We study the spreading of entanglement produced by the time evolution of a local fermionic excitation created above the ground state of the XXZ chain. The resulting entropy profiles are investigated via density-matrix renormalization group calculations, and compared to a quasiparticle ansatz. In particular, we assume that the entanglement is dominantly carried by spinon excitations traveling at different velocities, and the entropy profile is reproduced by a probabilistic ex-

pression involving the density fraction of the spinons reaching the subsystem. The ansatz works well in the gapless phase for moderate values of the XXZ anisotropy, eventually deteriorating as other types of quasiparticle excitations gain spectral weight. Furthermore, if the initial state is excited by a local Majorana fermion, we observe a nontrivial rescaling of the entropy profiles. This effect is further investigated in a conformal field theory framework, carrying out calculations for the Luttinger liquid theory. Finally, we also consider excitations creating an antiferromagnetic domain wall in the gapped phase of the chain, and find again a modified quasiparticle ansatz with a multiplicative factor.

5.2 XXZ chain and low-energy excitations

We consider an XXZ chain of length L with open boundary conditions that is given by the Hamiltonian

$$H = J \sum_{j=-L/2+1}^{L/2-1} (S_j^x S_{j+1}^x + S_j^y S_{j+1}^y + \Delta S_j^z S_{j+1}^z), \quad (5.2.1)$$

where $S_j^\alpha = \sigma_j^\alpha/2$ are spin-1/2 operators acting on site j , and Δ is the anisotropy. The energy scale is set by the coupling J which we fix at $J = 1$. The XXZ Hamiltonian (5.2.1) conserves the total magnetization S^z in z -direction and we will be interested in its ground state in the zero-magnetization sector $S^z = 0$. Equivalently, the XXZ spin chain can be rewritten in terms of spinless fermions by performing a Jordan-Wigner transformation, which brings (5.2.1) into the form

$$H = \sum_{j=-L/2+1}^{L/2-1} \left[\frac{1}{2}(c_j^\dagger c_{j+1} + c_{j+1}^\dagger c_j) + \Delta \left(c_j^\dagger c_j - \frac{1}{2} \right) \left(c_{j+1}^\dagger c_{j+1} - \frac{1}{2} \right) \right], \quad (5.2.2)$$

where c_j^\dagger (c_j) are fermionic creation (annihilation) operators, satisfying anticommutation relations $\{c_i, c_j^\dagger\} = \delta_{ij}$. One then has a half-filled fermionic hopping chain with nearest-neighbour interactions of strength Δ . For $|\Delta| \leq 1$ the system is in a critical phase with gapless excitations above the ground state, whereas a gap opens for $|\Delta| > 1$. The case $\Delta = 1$ corresponds to the isotropic Heisenberg antiferromagnet.

In the following we give a short and non-technical introduction to the construction of the ground state and low-lying excited states of the XXZ chain. To keep the discussion simple, we shall rather consider a periodic chain, and focus on the behaviour in the thermodynamic limit $L \rightarrow \infty$. The exact eigenstates of the XXZ chain can be found from Bethe ansatz [92, 93]. These are constructed as a superposition of plane waves, the so-called magnons, labeled by their rapidities λ_i which provide a convenient parametrization of the quasimomenta. The allowed values of the rapidities follow from the Bethe equations, with real solutions corresponding to spin-wave like states. Complex solutions organize themselves into strings and correspond to bound states.

For $|\Delta| < 1$ the half-filled ground state is obtained by occupying all the allowed vacancies of the $L/2$ real rapidities, thus forming a tightly packed Fermi sea. Low-energy excitations in the $S^z = 1$ sector are called spinons and are created by removing a rapidity. This creates two holes in the Fermi sea, with all the remaining rapidities moving slightly with respect to their ground-state values, and the energy difference can be calculated from this back-flow effect. In the thermodynamic limit, the result can be found analytically and written directly in terms of the quasimomenta q_1 and q_2 of the two spinons as [92]

$$\Delta E = \varepsilon_s(q_1) + \varepsilon_s(q_2), \quad (5.2.3)$$

where the spinon dispersion relation in the gapless regime with $\Delta = \cos(\gamma)$ is given by

$$\varepsilon_s(q) = \frac{\pi \sin(\gamma)}{2} \frac{\sin(q)}{\gamma}. \quad (5.2.4)$$

Note that spinons are always excited in pairs, with the individual momenta confined to $0 \leq q_{1,2} \leq \pi$. The total momentum is then given by $q_1 + q_2$, and due to the additivity of (5.2.3) one actually has a band of excitation energies. In particular, the lower edge of the two-spinon band is obtained by setting $q_2 = 0$ or $q_2 = \pi$, and thus simply corresponds to shifting the dispersion in (5.2.4) for $q > \pi$. The group velocity of the spinons can be directly obtained from the derivative of the dispersion

$$v_s(q) = \frac{d\varepsilon_s(q)}{dq} = \frac{\pi \sin(\gamma)}{2} \frac{\cos(q)}{\gamma}. \quad (5.2.5)$$

Further low-energy excitations with $S^z = 1$ can be created by removing a single rapidity from the real axis and placing it onto the $\text{Im } \lambda = \pi$ axis. The energy of

this particle-hole excitation can be obtained, similarly to the spinon case, from the back-flow equations of the rapidities and yields the dispersion [92]

$$\varepsilon_{ph}(q) = \pi \frac{\sin(\gamma)}{\gamma} \left| \sin\left(\frac{q}{2}\right) \right| \sqrt{1 + \cot^2\left(\frac{\pi}{2}\left(\frac{\pi}{\gamma} - 1\right)\right) \sin^2\left(\frac{q}{2}\right)}. \quad (5.2.6)$$

However, in contrast to spinons, particle-hole excitations are not composite objects and their momentum range is thus $0 \leq q < 2\pi$. Note that these spin-wave like excitations are only physical for $-1 < \Delta < 0$, i.e. in case of attractive interactions. For low momenta $q \rightarrow 0$, the dispersion relation Eq. (5.2.6) approaches the one for spinons in Eq. (5.2.4). The group velocities of particle-hole excitations are obtained by taking the derivative of $\varepsilon_{ph}(q)$. Interestingly, it was found that the maximum particle-hole velocity can exceed the maximum spinon velocity only if the anisotropy satisfies $\Delta < \Delta^* \approx -0.3$, which was demonstrated in a particular quench protocol [199].

Finally, we consider the gapped phase where we focus exclusively on the antiferromagnetic regime $\Delta > 1$, with the standard parametrization $\Delta = \cosh \phi$. For even L the ground state has $S^z = 0$ and is again given by $L/2$ magnons with real rapidities. However, the allowed number of vacancies is now $L/2 + 1$, which allows to construct a slightly shifted Fermi sea. In the Ising limit $\Delta \rightarrow \infty$, this yields an exact twofold degenerate ground state, given by the linear combinations of the two Néel states

$$|\psi_{\pm}\rangle = \frac{|\uparrow\downarrow\uparrow\downarrow\dots\rangle \pm |\downarrow\uparrow\downarrow\uparrow\dots\rangle}{\sqrt{2}}. \quad (5.2.7)$$

For finite Δ , the two states $|\psi_{\pm}\rangle$ constructed this way are only quasi-degenerate, with an energy difference decaying exponentially in the system size L . Considering the thermodynamic limit one can write

$$|\psi_{\pm}\rangle = \frac{|\psi_{\uparrow}\rangle \pm |\psi_{\downarrow}\rangle}{\sqrt{2}}, \quad (5.2.8)$$

where $|\psi_{\uparrow}\rangle$ and $|\psi_{\downarrow}\rangle$ correspond to ground states with spontaneously broken symmetry, displaying antiferromagnetic ordering. In fact, the bulk expectation value of the staggered magnetization can be calculated analytically as [94, 95]

$$\langle\psi_{\uparrow}|\sigma_j^z|\psi_{\uparrow}\rangle = -\langle\psi_{\downarrow}|\sigma_j^z|\psi_{\downarrow}\rangle = (-1)^j \prod_{n=1}^{\infty} \tanh^2(n\phi). \quad (5.2.9)$$

The low-lying excitations in the gapped phase are given again by spinons, by creating two holes in the Fermi sea. The excitation energy is still given by Eq. (5.2.3), with the dispersion in the gapped phase obtained as [92]

$$\varepsilon_s(q) = \frac{\sinh(\phi)}{\pi} K(u) \sqrt{1 - u^2 \cos^2(q)}, \quad (5.2.10)$$

where the complete elliptic integral of the first kind reads

$$K(u) = \int_0^{\pi/2} \frac{dp}{\sqrt{1 - u^2 \sin^2(p)}} \quad (5.2.11)$$

and the elliptic modulus u satisfies

$$\phi = \pi \frac{K(\sqrt{1 - u^2})}{K(u)}. \quad (5.2.12)$$

The spinon velocity is obtained from the derivative of (5.2.10) and reads

$$v_s(q) = \frac{\sinh(\phi)}{\pi} K(u) \frac{u^2 \sin(q) \cos(q)}{\sqrt{1 - u^2 \cos^2(q)}}. \quad (5.2.13)$$

5.3 Entanglement dynamics in the gapless phase

The goal of this section is to study the entanglement dynamics after a particular class of excitations. Namely, we first initialize the chain in its gapless ground state $|\psi_0\rangle$, which is then excited by an operator that is strictly local in terms of the creation/annihilation operators c_j^\dagger and c_j appearing in the fermionic representation (5.2.2) of the XXZ chain. The system is then let evolve freely and we are interested in the emerging entanglement pattern in the time-evolved state $|\psi(t)\rangle$. For a bipartition into a subsystem A and the rest of the chain B , this is characterized by the von Neumann entropy

$$S(t) = -\text{Tr} [\rho_A(t) \ln \rho_A(t)], \quad (5.3.1)$$

with the reduced density matrix $\rho_A(t) = \text{Tr}_B \rho(t)$ and $\rho(t) = |\psi(t)\rangle \langle \psi(t)|$. In particular, we consider the bipartition $A = [-L/2 + 1, r]$ and $B = [r + 1, L/2]$ and study the entropy profiles

$$\Delta S = S(t) - S(0) \quad (5.3.2)$$

along the chain by varying r , where $r = 0$ corresponds to the half-chain. Note that by subtracting the ground-state entropy $S(0)$, we aim to extract information about the excess entanglement created by a local excitation.

In the following subsections we first introduce an intuitive picture for the description of the entanglement spreading in terms of the low-lying quasiparticle excitations introduced in Sec. 5.2. We then proceed to the numerical study of the entanglement profiles after exciting the ground state with a fermionic creation operator, and compare the results to our quasiparticle ansatz. In the last part we consider an excitation created by a local Majorana fermion operator.

5.3.1 Entanglement spreading in the quasiparticle picture

Let us consider an excitation above the ground state of the XXZ chain by acting with a fermion creation operator c_j^\dagger . To capture the dynamics, one would have to first decompose the initial local excited state in the eigenbasis of the Hamiltonian. As discussed in the previous section, these eigenstates are described by quasiparticles parametrized by their rapidities or quasimomenta. The entanglement properties of various eigenstates in the XXZ chain were studied before in [155, 156], whereas a systematic CFT treatment of low-energy excitations was introduced in [200, 201]. In the framework of free quantum field theory, a surprisingly simple result on quasiparticle excitations was recently found in [202, 203]. Namely, the excess entanglement measured from the ground state was found to be completely independent of the quasiparticle momenta, depending only on the ratio p of the subsystem and full chain lengths. Moreover, for quasiparticles described by a single momentum, the excess entropy is given by a binary formula $\Delta S = -p \ln p - (1-p) \ln(1-p)$, which allows for a simple probabilistic interpretation. Indeed, the ratio p is just the probability of finding the quasiparticle within the subsystem.

Motivated by these results, we now put forward a simple ansatz for the spreading of entanglement after the local excitation. Under time evolution, the quasiparticles involved in the decomposition of the initial state spread out with their corresponding group velocities. However, our main assumption is that their contribution to entanglement is still independent of the momentum. Furthermore, we shall also assume that the dominant part of the entanglement is carried by the lowest-lying spinon modes, and that a spatially localized excitation translates to a homogeneous distribution of the momenta in the initial state. Under these assumptions

we expect that the entanglement profile at time $t \gg 1$ and distance $r \gg 1$ from the excitation, in the space-time scaling limit $\zeta = r/t$ fixed, is determined exclusively via

$$\mathcal{N} = \int_0^\pi \frac{dq}{\pi} \Theta(v_s(q) - \zeta), \quad (5.3.3)$$

where $\Theta(x)$ is the Heaviside step function and $v_s(q)$ is the spinon velocity. In fact, this is nothing else but the fraction of the spinon modes with sufficient velocity to arrive at the subsystem. The simple probabilistic interpretation of the entanglement then leads to the binary entropy formula for the profile

$$\Delta S = -\mathcal{N} \ln(\mathcal{N}) - (1 - \mathcal{N}) \ln(1 - \mathcal{N}). \quad (5.3.4)$$

In particular, for the gapless case considered here, inserting the expression (5.2.5) of the spinon velocity into (5.3.3), the spinon fraction can immediately be found as

$$\mathcal{N} = \frac{1}{\pi} \arccos\left(\frac{\zeta}{v}\right), \quad (5.3.5)$$

where $v = v_s(0)$ denotes the maximal spinon velocity.

In summary, our simplistic ansatz (5.3.4) provides an interpretation of the excess entropy based on the dispersive dynamics of the quasiparticle modes, where \mathcal{N} is the fraction of the initially localized excitation that arrives at the subsystem. In fact, the very same ansatz has recently been suggested for the description of entanglement spreading after local fermionic excitations in the XY chain, finding an excellent agreement with numerics [91]. Note, however, that the XY chain is equivalent to a free-fermion model and thus all the single-particle modes can exactly be included in \mathcal{N} . In contrast, for the interacting XXZ chain, restricting ourselves to the spinon modes should necessarily introduce some limitations to the quasiparticle ansatz, as demonstrated in the following subsection.

5.3.2 Local fermionic excitation

We continue with the numerical study of the excitation produced by the fermionic creation operator c_j^\dagger . The fermion operators are related to the spin variables via the Jordan-Wigner transformation

$$c_j^\dagger = \left(\prod_{l=-L/2+1}^{j-1} \sigma_l^z \right) \sigma_j^+, \quad c_j = \left(\prod_{l=-L/2+1}^{j-1} \sigma_l^z \right) \sigma_j^-, \quad (5.3.6)$$

where σ_j^α are the Pauli matrices and $\sigma_j^\pm = (\sigma_j^x \pm i\sigma_j^y) / 2$. For simplicity, we shall only consider the case where the excitation is created by c_1^\dagger in the middle of the chain. The time-evolved state after the excitation is then given by

$$|\psi(t)\rangle = N^{-1/2} e^{-iHt} c_1^\dagger |\psi_0\rangle, \quad (5.3.7)$$

where $|\psi_0\rangle$ is the ground state and the normalization is given by

$$N = \langle \psi_0 | c_1 c_1^\dagger | \psi_0 \rangle = 1/2 \quad (5.3.8)$$

as the ground state is half filled. The time evolution is actually implemented via time-dependent DMRG (tDMRG) [56, 57] in the spin-representation of the XXZ chain, by first carrying out the ground-state search and applying the string operator (5.3.6) onto the MPS representation of $|\psi_0\rangle$. The calculations were performed using the ITensor C++ library [168] and a truncated weight of 10^{-9} .

The results of our simulations are shown in Fig. 5.1 for various interaction strengths Δ . The different symbols correspond to snapshots of the entropy profile ΔS at different times, plotted against the scaled distance $\zeta = r/t$. The quasiparticle ansatz (5.3.4) computed using the spinon fraction (5.3.5) is shown by the red solid lines. For moderate values of $|\Delta|$, one observes a very good agreement with the numerical profiles.

Systematic deviations from (5.3.4) also occur for larger Δ , especially in the attractive regime. Indeed, for $\Delta = -0.5$ one already observes that the edges of the profile obtained from numerics fall slightly outside of the spinon edge, whereas the bulk profile still shows a good agreement. For $\Delta = -0.8$ the mismatch becomes more drastic both in the bulk and around the edges, signaling the breakdown of the naive spinon ansatz. Clearly, for strong attractive interactions the local excited state should have significant overlaps with other quasiparticle excitations of the XXZ chain. In fact, as discussed in Sec. 5.2, in this regime the maximum velocity of particle-hole excitations exceeds the spinon velocity and matches perfectly the edges of the profile, as indicated by the black dashed lines in Fig. 5.1.

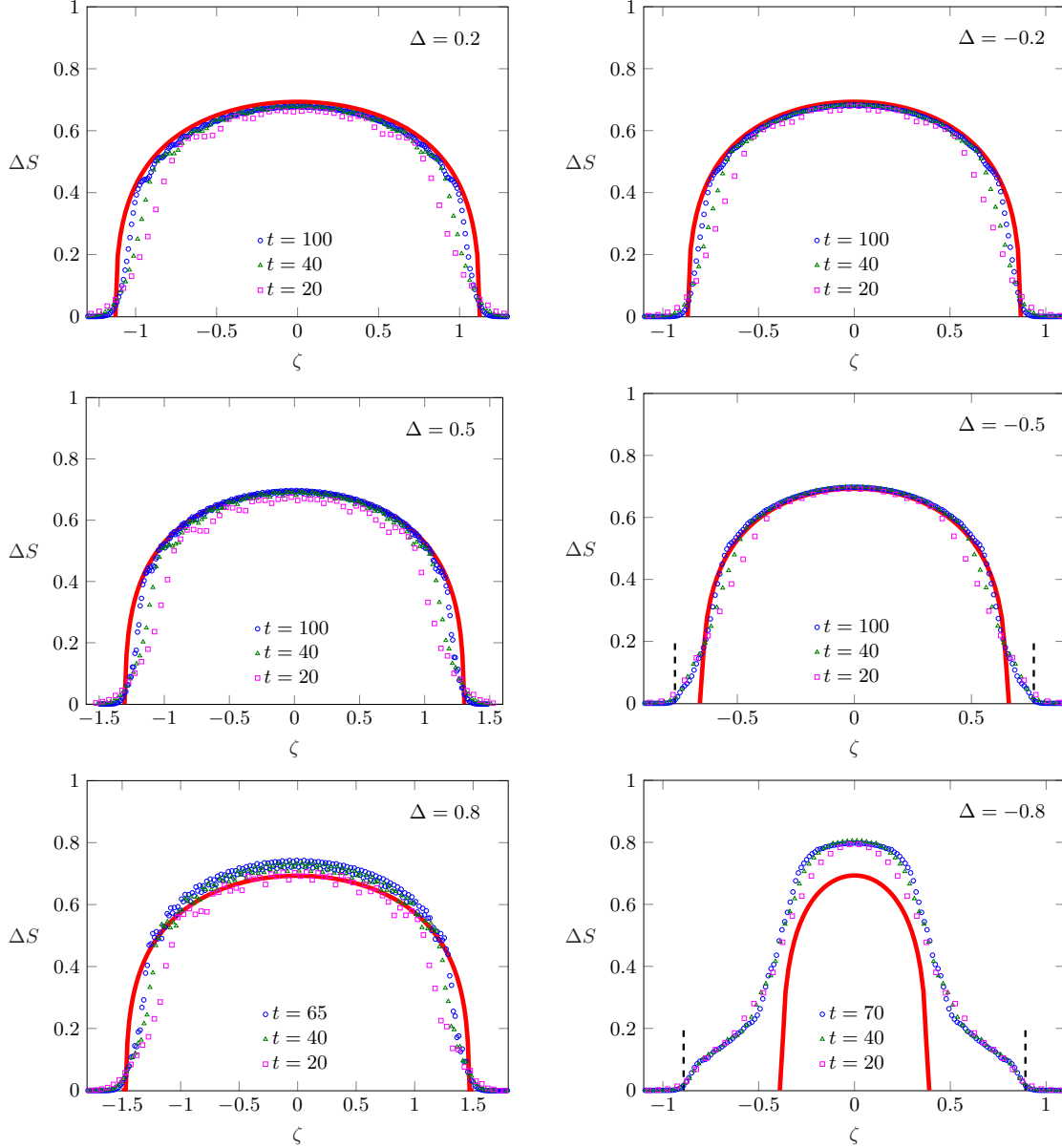


Figure 5.1: Excess entropy profiles ΔS obtained from tDMRG simulations at different times (symbols), after the excitation c_1^\dagger in a chain of length $L = 300$. The scaled profiles are plotted against $\zeta = r/t$ and compared to the quasiparticle ansatz (red lines) in Eq. (5.3.4). The dashed black lines denote the maximum velocity of the particle-hole excitations, derived from Eq. (5.2.6).

Hence, the entropy spreading should be determined by the coexistence of the spinon and particle-hole excitations, allowing to reach values beyond $\ln(2)$. Presumably, improving the ansatz (5.3.4) would require the knowledge of the overlaps with the different families of quasiparticles. Finally, it should be noted that, even though the edge locations of the profile seem to be captured, significant deviations in the bulk also occur for large repulsive interactions (see $\Delta = 0.8$ in Fig. 5.1), which might be due to bound-state contributions.

5.3.3 Local Majorana excitation

As a second example, we are going to consider local Majorana excitations, given in terms of the spin variables via

$$m_{2j-1} = \left(\prod_{l=-L/2+1}^{j-1} \sigma_l^z \right) \sigma_j^x, \quad m_{2j} = \left(\prod_{l=-L/2+1}^{j-1} \sigma_l^z \right) \sigma_j^y, \quad (5.3.9)$$

and satisfying the anticommutation relations $\{m_k, m_l\} = 2\delta_{kl}$. Majorana operators are Hermitian and related to the fermion creation/annihilation operators as $m_{2j-1} = c_j + c_j^\dagger$ and $m_{2j} = i(c_j - c_j^\dagger)$. Focusing again on an excitation m_1 in the middle of the chain, the time-evolved state is now given by

$$|\psi(t)\rangle = e^{-iHt} m_1 |\psi_0\rangle. \quad (5.3.10)$$

The entanglement profiles ΔS obtained from tDMRG simulations of (5.3.10) are depicted in Fig. 5.2 for four different values of Δ . To visualize the spreading of the profile, we now plot the unscaled data against the location of the subsystem boundary. For $\Delta = 0$, the profile looks similar to that of the corresponding c_1^\dagger excitation and is indeed perfectly reproduced by the quasiparticle ansatz (5.3.4). However, in the interacting case $\Delta \neq 0$, one observes a marked difference when compared to the corresponding panels in Fig. 5.1. Namely, the profiles in Fig. 5.2 clearly exceed the value $\ln(2)$, indicated by the dashed horizontal lines, which is the maximum of the ansatz (5.3.4). Nevertheless, we observe that the profiles after the m_1 excitations can be well described by a simple rescaling of the spinon ansatz (5.3.4), as shown by the solid lines in Fig. 5.2. The constant factor multiplying the ansatz is chosen such that the maxima of the profiles at $r = 0$ are correctly reproduced.

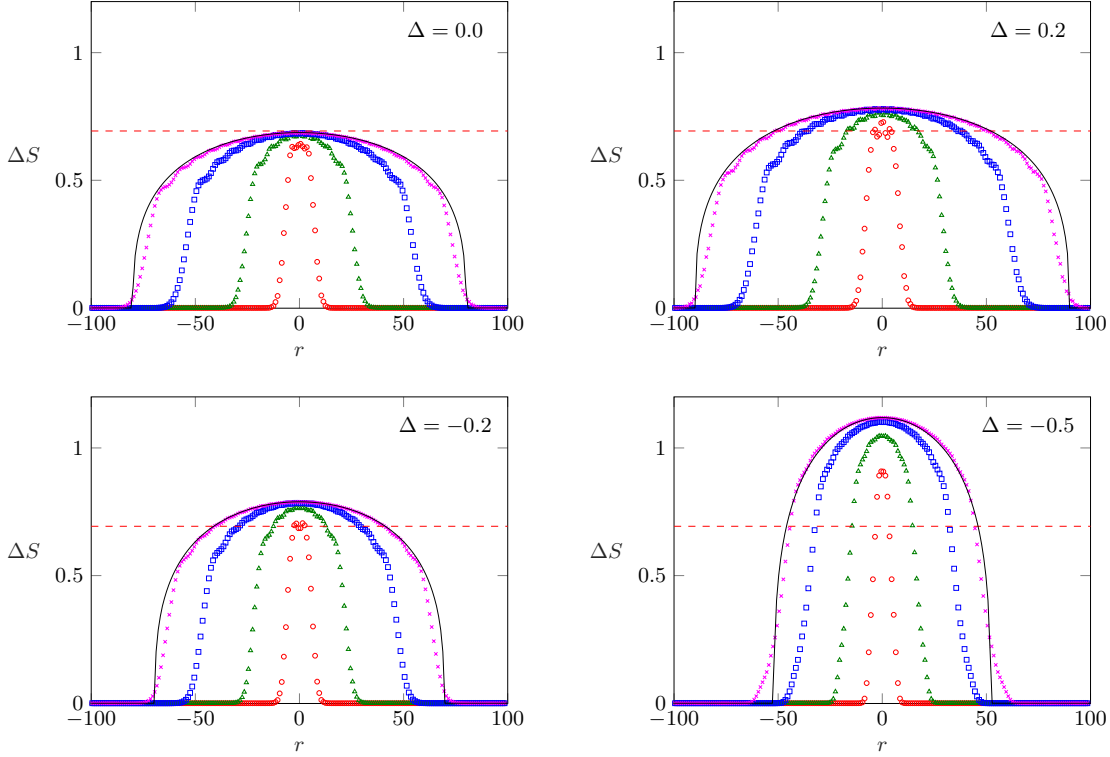


Figure 5.2: Excess entropy profiles ΔS as a function of r at times $t = 10, 30, 60, 80$ (red, green, blue, magenta) after the Majorana excitation m_1 for four different values of Δ and $L = 200$. The red dashed lines indicate the value $\ln(2)$. The black solid lines show the spinon ansatz Eq. (5.3.4) for $t = 80$, multiplied by a constant to match the maxima of the profiles.

To better understand the behaviour of the maxima, on the left of Fig. 5.3 we plot the time evolution of the excess entropy ΔS in the middle of the chain ($r = 0$) with $L = 200$ and for various Δ . One observes that the asymptotic value of the excess entropy grows with increasing $|\Delta|$, approaching its maximum very slowly in time. In fact, for even larger times the entropy starts to decrease again as one approaches $vt \approx L$, when the fastest spinons leave the subsystem after a reflection from the chain end. This is demonstrated on the right of Fig. 5.3 by repeating the calculations for a smaller chain with $L = 50$. The emergence of a plateau is clearly visible, which then immediately repeats itself for $vt > L$ due to the symmetry of the geometry, with the spinons reflected from the other end of the

chain entering the subsystem again. However, the question why the height of the plateau depends on the interaction strength Δ can only be answered via a more involved CFT analysis of the problem, which is presented in the next section.

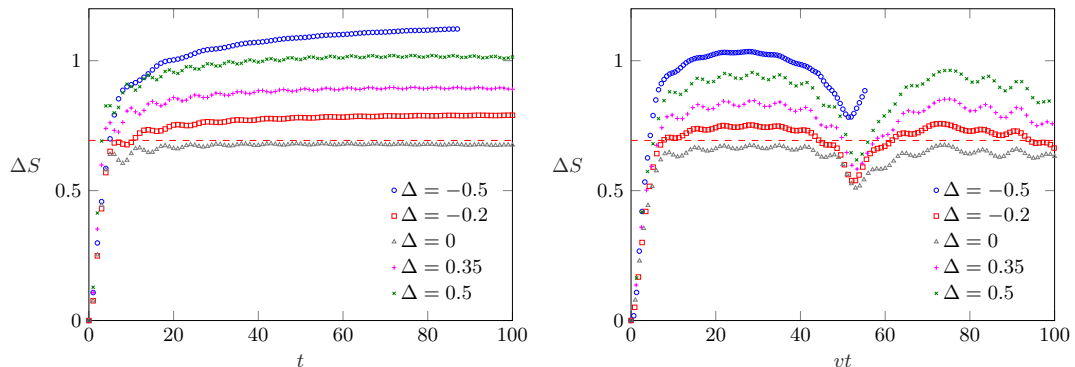


Figure 5.3: Left: Entropy growth in the middle of the chain $r = 0$, after the Majorana excitation m_1 for different values of Δ and $L = 200$. The red dashed line indicates the value $\ln(2)$. Right: ΔS for a smaller chain with $L = 50$ against the scaled time vt for the same Δ values.

5.4 Entanglement after local excitations in CFT

The low-energy physics of the gapless XXZ chain can be captured within quantum field theory via the bosonization procedure [204]. Using the fermionic representation (5.2.2) of the chain, one introduces the Heisenberg operators $c(x, \tau) = e^{\tau H} c_x e^{-\tau H}$, where x is the spatial coordinate along the chain and we introduced the imaginary time $\tau = it$. Linearizing the dispersion around the Fermi points, one can approximate

$$c(x, \tau) \simeq e^{ik_F x} \psi(x, \tau) + e^{-ik_F x} \bar{\psi}(x, \tau), \quad (5.4.1)$$

where $\psi(x, \tau)$ and $\bar{\psi}(x, \tau)$ are the right and left-moving components of a fermion field. The phase factors with the Fermi momentum, where $k_F = \pi/2$ for a half-filled chain, are included to ensure that the chiral fermions are described by slowly varying fields. Introducing the complex coordinates $w = v\tau - ix$ and $\bar{w} = v\tau + ix$, where v denotes the Fermi velocity, they can be written in a bosonized form [204]

$$\psi(w) = \frac{1}{\sqrt{2\pi}} e^{-i\sqrt{4\pi}\varphi(w)}, \quad \bar{\psi}(\bar{w}) = \frac{1}{\sqrt{2\pi}} e^{i\sqrt{4\pi}\bar{\varphi}(\bar{w})}, \quad (5.4.2)$$

where $\varphi(w)$ and $\bar{\varphi}(\bar{w})$ are the chiral boson fields. In terms of the new bosonic variables

$$\phi = \varphi + \bar{\varphi}, \quad \theta = \varphi - \bar{\varphi}, \quad (5.4.3)$$

one can show that the bosonized form of the XXZ chain (5.2.2) is described by the Luttinger liquid Hamiltonian [166]

$$H_{LL} = \frac{v}{2} \int dx [K(\partial_x \theta)^2 + K^{-1}(\partial_x \phi)^2]. \quad (5.4.4)$$

Apart from the velocity v , the Hamiltonian (5.4.4) is characterized by the Luttinger parameter K . Both of them can be fixed from the exact Bethe ansatz solution as

$$v = \frac{\pi \sin(\gamma)}{2\gamma}, \quad K = \frac{1}{2} \left(1 - \frac{\gamma}{\pi}\right)^{-1}, \quad (5.4.5)$$

with the usual parametrization $\Delta = \cos(\gamma)$. Note that $v = v_s(0)$ is just the maximum of the spinon velocity (5.2.5).

In CFT language, the Luttinger liquid corresponds to a free compact boson field theory. In order to study entanglement evolution after local operator excitations, we shall thus use the framework developed for a generic CFT [80, 82]. In the following we summarize the main steps of the procedure. Let us consider the state

$$|\psi\rangle = N^{-1/2} \mathcal{O}(-d) |0\rangle \quad (5.4.6)$$

excited from the CFT vacuum $|0\rangle$ by insertion of the local operator $\mathcal{O}(-d)$, where N accounts for the normalization of the state. For the sake of generality, we consider the situation where the excitation is inserted at a distance d measured from the center of the chain. After time evolution, the density matrix reads

$$\rho(t) = N^{-1} e^{-iHt} e^{-\epsilon H} \mathcal{O}(-d) |0\rangle \langle 0| \mathcal{O}^\dagger(-d) e^{-\epsilon H} e^{iHt}, \quad (5.4.7)$$

where ϵ is a UV regularization that is required for the state to be normalizable. Working in a Heisenberg picture, the time evolution can be absorbed into the operators, and the state can be represented as

$$\rho(t) = \frac{\mathcal{O}(w_2, \bar{w}_2) |0\rangle \langle 0| \mathcal{O}^\dagger(w_1, \bar{w}_1)}{\langle \mathcal{O}^\dagger(w_1, \bar{w}_1) \mathcal{O}(w_2, \bar{w}_2) \rangle}, \quad (5.4.8)$$

where the complex coordinates of the operator insertions are given by

$$\begin{aligned} w_1 &= -i(vt - d) + \epsilon, & \bar{w}_1 &= -i(vt + d) + \epsilon, \\ w_2 &= -i(vt - d) - \epsilon, & \bar{w}_2 &= -i(vt + d) - \epsilon. \end{aligned} \quad (5.4.9)$$

It should be stressed that the \bar{w}_j coordinates are actually not the complex conjugates of w_j , as we are assuming $\tau = it$ to be real, such that we can work with Euclidean spacetime.

With the expression (5.4.8) at hand, one can proceed to construct the path-integral representation of the reduced density matrix, by opening a cut at $\tau = 0$ along the spatial coordinates of the subsystem A . The Rényi entropy

$$S_n(t) = \frac{1}{1-n} \ln \text{Tr} [\rho_A^n(t)] \quad (5.4.10)$$

for integer n can then be obtained by applying the replica trick [104], i.e. sewing together n copies of the path integrals cyclically along the cuts. In turn, one can express the excess Rényi entropy $\Delta S_n = S_n(t) - S_n(0)$ via correlation functions of the local operator as [80, 82]

$$\Delta S_n = \frac{1}{1-n} \log \left[\frac{\langle \mathcal{O}^\dagger(w_1, \bar{w}_1) \mathcal{O}(w_2, \bar{w}_2) \dots \mathcal{O}(w_{2n}, \bar{w}_{2n}) \rangle_{\Sigma_n}}{\langle \mathcal{O}^\dagger(w_1, \bar{w}_1) \mathcal{O}(w_2, \bar{w}_2) \rangle_{\Sigma_1}^n} \right], \quad (5.4.11)$$

where Σ_n denotes the n -sheeted Riemann surface, with w_1, \dots, w_{2n} and $\bar{w}_1, \dots, \bar{w}_{2n}$ being the replica coordinates of the insertion points (5.4.9).

Although the expression (5.4.11) for the excess Rényi entropy is very general, the calculation of $2n$ -point functions on the complicated Riemann surface Σ_n may become rather involved. However, if the subsystem A is given by a single interval $0 \leq x \leq \ell$ in an infinite chain, the geometry can be simplified by the conformal transformation

$$z = \left(\frac{w}{w + i\ell} \right)^{1/n}, \quad \bar{z} = \left(\frac{\bar{w}}{\bar{w} - i\ell} \right)^{1/n}, \quad (5.4.12)$$

which maps the n -sheeted surface onto a single Riemann sheet. This transformation leads to the holomorphic coordinates of the operator insertions

$$z_{2j-1} = e^{2\pi ij/n} \left(\frac{d - vt - i\epsilon}{\ell + d - vt - i\epsilon} \right)^{1/n}, \quad z_{2j} = e^{2\pi ij/n} \left(\frac{d - vt + i\epsilon}{\ell + d - vt + i\epsilon} \right)^{1/n}, \quad (5.4.13)$$

while the anti-holomorphic ones are given by

$$\bar{z}_{2j-1} = e^{-2\pi i j/n} \left(\frac{d+vt+i\epsilon}{\ell+d+vt+i\epsilon} \right)^{1/n}, \quad \bar{z}_{2j} = e^{-2\pi i j/n} \left(\frac{d+vt-i\epsilon}{\ell+d+vt-i\epsilon} \right)^{1/n}. \quad (5.4.14)$$

Furthermore, if the local operators are primary fields of the CFT with respective conformal dimensions $h_{\mathcal{O}}$ and $\bar{h}_{\mathcal{O}}$, the $2n$ -point function transforms as

$$\left\langle \prod_{j=1}^n \mathcal{O}^\dagger(w_{2j-1}, \bar{w}_{2j-1}) \mathcal{O}(w_{2j}, \bar{w}_{2j}) \right\rangle_{\Sigma_n} = \prod_{i=1}^{2n} \left(\frac{dw}{dz} \right)_{z_i}^{-h_{\mathcal{O}}} \left(\frac{d\bar{w}}{d\bar{z}} \right)_{\bar{z}_i}^{-\bar{h}_{\mathcal{O}}} \times \left\langle \prod_{j=1}^n \mathcal{O}^\dagger(z_{2j-1}, \bar{z}_{2j-1}) \mathcal{O}(z_{2j}, \bar{z}_{2j}) \right\rangle_{\Sigma_1}. \quad (5.4.15)$$

In the end, one is left with a problem of calculating $2n$ -point functions on the complex plane. For the sake of simplicity, in the following we shall only consider the case $n = 2$, and apply the procedure outlined above to the Luttinger liquid theory, with the local excitations considered in section 5.3.

5.4.1 Fermionic excitation

We start with the fermion creation operator, which after bosonization (5.4.2) corresponds to the field insertion

$$\mathcal{O}_f(w, \bar{w}) = e^{ik_F d} e^{i\sqrt{4\pi}\varphi(w)} + e^{-ik_F d} e^{-i\sqrt{4\pi}\bar{\varphi}(\bar{w})}, \quad (5.4.16)$$

where we omitted normalization factors that cancel in the expression (5.4.11). Clearly, $\mathcal{O}_f(w, \bar{w})$ is not itself a primary operator but rather a linear combination of two. Hence, the calculation of the four-point function that appears in ΔS_2 involves a number of terms with primaries, each of which can be mapped from Σ_2 to the complex plane using the transformation rule (5.4.15). The calculation of these correlation functions can be facilitated by first performing a canonical transformation

$$\theta' = \sqrt{K}\theta, \quad \phi' = \frac{1}{\sqrt{K}}\phi. \quad (5.4.17)$$

which absorbs the Luttinger parameter K in the Hamiltonian (5.4.4). However, since the variables θ and ϕ are actually linear combinations (5.4.3) of the chiral

bosons, the change of variables corresponds to the Bogoliubov transformation

$$\varphi = \cosh(\xi)\varphi' + \sinh(\xi)\bar{\varphi}' \quad \bar{\varphi} = \sinh(\xi)\varphi' + \cosh(\xi)\bar{\varphi}', \quad (5.4.18)$$

where $K = e^{2\xi}$. Thus, the transformation of the Luttinger liquid Hamiltonian induces a left-right mixing of the chiral bosonic modes. In the following we shall use the shorthand notations $c = \cosh(\xi)$ and $s = \sinh(\xi)$.

Clearly, our task now boils down to evaluate correlation functions of vertex operators

$$V_{\alpha,\beta}(z, \bar{z}) = e^{i\sqrt{4\pi}\alpha\varphi'(z) + i\sqrt{4\pi}\beta\bar{\varphi}'(\bar{z})} \quad (5.4.19)$$

on the complex plane with respect to the Luttinger liquid theory scaled to the free-fermion point. The n -point function of vertex operators is then well known and given by [205]

$$\left\langle \prod_{j=1}^n V_{\alpha_i, \beta_i}(z_i, \bar{z}_i) \right\rangle = \prod_{i < j} (z_i - z_j)^{\alpha_i \alpha_j} (\bar{z}_i - \bar{z}_j)^{\beta_i \beta_j}, \quad (5.4.20)$$

where the neutrality conditions

$$\sum_{i=1}^n \alpha_i = 0, \quad \sum_{i=1}^n \beta_i = 0 \quad (5.4.21)$$

must be satisfied, otherwise the correlator vanishes. In particular, considering the two-point function one immediately sees that the vertex operator (5.4.19) is a primary with scaling dimensions $h = \alpha^2/2$ and $\bar{h} = \beta^2/2$.

With all the ingredients at hand, performing the calculation for ΔS_2 is a straightforward but cumbersome exercise, and we refer to Appendix C.1 for the main details. It turns out that the result depends only on the cross-ratios

$$\eta = \frac{z_{12}z_{34}}{z_{13}z_{24}}, \quad \bar{\eta} = \frac{\bar{z}_{12}\bar{z}_{34}}{\bar{z}_{13}\bar{z}_{24}} \quad (5.4.22)$$

of the holomorphic and anti-holomorphic coordinates (5.4.13) and (5.4.14), where $z_{ij} = z_i - z_j$ and $\bar{z}_{ij} = \bar{z}_i - \bar{z}_j$, respectively. In terms of the cross-ratios, the final result reads

$$\Delta S_2 = -\ln \left(\frac{1 + |\eta|^{(c+s)^2} + |1 - \eta|^{(c+s)^2}}{2} \right). \quad (5.4.23)$$

It is important to stress that the notation $|\eta|$ should be understood as $(\eta\bar{\eta})^{1/2}$, since the two cross ratios are not conjugate variables. In particular, in the limit $\epsilon \rightarrow 0$ of the regularization, one has the behaviour [80, 82]

$$\lim_{\epsilon \rightarrow 0} \eta = \begin{cases} 0 & \text{if } 0 < vt < d \text{ or } vt > d + \ell \\ 1 & \text{if } d < vt < d + \ell \end{cases}, \quad \lim_{\epsilon \rightarrow 0} \bar{\eta} = 0. \quad (5.4.24)$$

This yields the following limit for the Rényi entropy

$$\lim_{\epsilon \rightarrow 0} \Delta S_2 = \begin{cases} 0 & \text{if } 0 < vt < d \text{ and } vt > d + \ell \\ \ln(2) & \text{if } d < vt < d + \ell \end{cases}. \quad (5.4.25)$$

The result has a very simple interpretation. Namely, our excitation is an equal superposition of a left- and right-moving fermion, and the entanglement is changed by $\ln(2)$ only when the right-moving excitation is located within the interval. In fact, this is exactly the same picture that lies behind the quasiparticle ansatz (5.3.4), without the dispersion of the wavefront. Interestingly, apart from the presence of the spinon velocity v , the limiting result (5.4.25) is independent of the anisotropy Δ . The only effect of the left-right boson mixing appears in the exponents of the cross-ratios in (5.4.23), which simply determines how the sharp step-function for ΔS_2 is rounded off for finite UV regularizations. In fact, this result is very similar to the one obtained for a non-chiral EPR-primary excitation in Ref. [82, 84]. Moreover, this is also a simple generalization of the result in Ref. [89], where the superposition of purely holomorphic and anti-holomorphic primaries was considered.

5.4.2 Majorana excitation

We move on to consider the Majorana excitation

$$\mathcal{O}_m(w, \bar{w}) = \mathcal{O}_f(w, \bar{w}) + \mathcal{O}_f^\dagger(w, \bar{w}). \quad (5.4.26)$$

The calculation of ΔS_2 follows the exact same procedure as for $\mathcal{O}_f(w, \bar{w})$, however, one has now an even larger number of terms to consider. The main steps are again outlined in Appendix C.1, which lead to the result

$$\Delta S_2 = -\ln\left(\frac{2A + B + C}{8}\right), \quad (5.4.27)$$

where the terms in the logarithm are given by

$$A = |1 - \eta|^{(c+s)^2} + |1 - \eta|^{(c-s)^2} + |\eta|^{(c+s)^2} + |\eta|^{(c-s)^2} \quad (5.4.28)$$

$$B = 2 + \eta^{2c^2} \bar{\eta}^{2s^2} + \eta^{2s^2} \bar{\eta}^{2c^2} + (1 - \eta)^{2c^2} (1 - \bar{\eta})^{2s^2} + (1 - \eta)^{2s^2} (1 - \bar{\eta})^{2c^2} \quad (5.4.29)$$

$$C = \left[|\eta|^{(c+s)^2} |1 - \eta|^{(c-s)^2} + |\eta|^{(c-s)^2} |1 - \eta|^{(c+s)^2} \right] (Z + \bar{Z}) \quad (5.4.30)$$

and a new variable is introduced as

$$Z = \frac{z_1 \bar{z}_2 (1 - z_1^2) (1 - z_2^2)}{\bar{z}_1 z_2 (1 - z_1^2) (1 - \bar{z}_2^2)}. \quad (5.4.31)$$

The result is thus rather involved and cannot be written as a function of the cross-ratios alone. However, in the limit $\epsilon \rightarrow 0$, the factors in A , B , and C can trivially be evaluated using (5.4.24), as well as using $Z \rightarrow 1$ and $\bar{Z} \rightarrow 1$. For the case $\Delta \neq 0$, this leads to the following simple result

$$\lim_{\epsilon \rightarrow 0} \Delta S_2 = \begin{cases} 0 & \text{if } 0 < vt < d \text{ and } vt > d + \ell \\ 2 \ln(2) & \text{if } d < vt < d + \ell \end{cases}. \quad (5.4.32)$$

In sharp contrast, for $\Delta = 0$, where $c = 1$ and $s = 0$, one recovers the result (5.4.25). Hence, one arrives at the rather surprising result that the excess entropy is doubled in case of interactions, which must be a consequence of the left-right boson mixing.

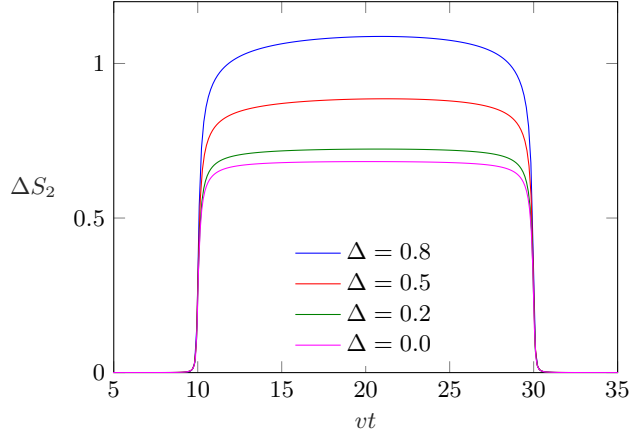


Figure 5.4: Time evolution of the excess Rényi entropy in Eq. (5.4.27) after the Majorana excitation with $\ell = 20$, $d = 10$ and $\epsilon = 0.1$.

Obviously, for finite values of the regularization ϵ , this transition should take place continuously, rather than giving an abrupt jump. The behaviour of ΔS_2 for $\epsilon = 0.1$ is shown in Fig. 5.4 for an interval of length $\ell = 20$ at a distance $d = 10$ from the excitation. One can clearly see the development of a plateau for times $d < vt < d + \ell$, the height of which increases monotonously with Δ . Nevertheless, even for the largest value $\Delta = 0.8$, the expected maximum of $2 \ln(2)$ is by far not reached. The very slow convergence towards the $\epsilon \rightarrow 0$ (or, equivalently, $t \rightarrow \infty$) limit can be understood by looking at the structure of the terms appearing in (5.4.27). In fact, for smaller values of $|\Delta|$, the slowest converging pieces are given by $\eta^{2c^2} \bar{\eta}^{2s^2}$ as well as $(1 - \eta)^{2s^2} (1 - \bar{\eta})^{2c^2}$ in the expression (5.4.29) of B , due to the large-time behaviour $\bar{\eta} \approx 1 - \eta \approx (\epsilon/2vt)^2$ for $d \ll vt \ll \ell + d$. Hence, the apparent nontrivial values of the plateau in Fig. 5.4 is a consequence of the very slow decay $(\epsilon/vt)^{4s^2}$, where the exponent for e.g. $\Delta = 0.5$ is given by $4s^2 \approx 0.08$. Clearly, observing convergence towards $\Delta S_2 \rightarrow 2 \ln(2)$ would require enormous time scales as well as interval lengths.

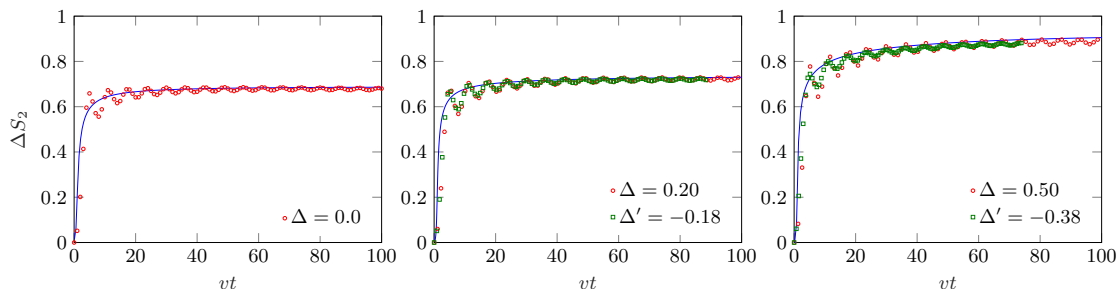


Figure 5.5: Growth of the Rényi entropy ΔS_2 for pairs of conjugate interaction parameters Δ and Δ' (red and green symbols) for a chain of length $L = 200$. The blue solid lines show the CFT result Eq. (5.4.27) with $\ell = 200$ and $d = 1$. The regularization $\epsilon = 0.55, 0.40, 0.35$ (from left to right) was tuned to obtain the best match with the tDMRG data.

Despite the different geometry considered for the CFT calculations, we expect that the result (5.4.27) should also give quantitative predictions for the finite XXZ chain in a certain regime. First of all, for the half-chain bipartition where the excitation is applied directly at the boundary, the role of the dispersion should not play an important role, as all the excitations can immediately enter the subsystem.

Furthermore, one could argue that the finite chain effectively corresponds to an interval of size $\ell = L$, which is the distance the quasiparticles have to cover before leaving the subsystem after reflection from the chain end. Clearly, the exact form of the plateau will not be the same in the two cases, but one expects the CFT results to be applicable in a regime $vt \ll L$. Finally, there is a highly nontrivial symmetry $s \rightarrow -s$ displayed by all the terms (5.4.28)-(5.4.30) in the expression of ΔS_2 , corresponding to a change of the Luttinger parameter $K \rightarrow 1/K$, which is expected to be observed also in the lattice calculations. Note that since $K = 1$ corresponds to the free-fermion point $\Delta = 0$, the symmetry relates interaction strengths of different sign.

In Fig. 5.5 we show a comparison of ΔS_2 obtained from tDMRG calculations for a XXZ chain with $L = 200$ divided in the middle, to the CFT result (5.4.27) shown by the blue solid lines. For the latter we have set $\ell = L$ and $d = 1$ as discussed above, whereas the regularization ϵ was set by hand in order to achieve the best agreement with the numerical data. One indeed observes that the CFT result gives, up to oscillations, a good quantitative description of the XXZ numerics. Furthermore, for each $\Delta \neq 0$, we also performed the calculation for the conjugate Δ' corresponding to $K' = 1/K$, leading to a remarkably good collapse of the curves.

5.5 Entanglement dynamics in the gapped phase

The CFT studies of the previous section give a rather good qualitative description of the entanglement spreading in the critical phase of the XXZ chain. To obtain a complete picture, in this section we shall study the dynamics in the gapped antiferromagnetic phase. For a physically motivated setting, we choose one of the symmetry-broken ground states $|\psi_\uparrow\rangle$ from Eq. (5.2.8), with a nonvanishing staggered magnetization (5.2.9). We now consider local Majorana operators, defined in terms of the spin variables as

$$\tilde{m}_{2j-1} = \left(\prod_{l=-L/2+1}^{j-1} \sigma_l^x \right) \sigma_j^z, \quad \tilde{m}_{2j} = \left(\prod_{l=-L/2+1}^{j-1} \sigma_l^x \right) \sigma_j^y. \quad (5.5.1)$$

Note that these operators differ from the ones in (5.3.9) discussed in the gapless phase by an interchange of the x and z spin components, but they also obey

Majorana fermion statistics with anticommutation relations $\{\tilde{m}_k, \tilde{m}_l\} = 2\delta_{kl}$. We focus on the case of a domain wall created by \tilde{m}_1 in the center of the chain, which is then time evolved by the XXZ Hamiltonian (5.2.1)

$$|\psi(t)\rangle = e^{-iHt} \tilde{m}_1 |\psi_\uparrow\rangle . \quad (5.5.2)$$

Note that, in order to find the proper symmetry-broken ground state, in the DMRG simulation we add to the Hamiltonian a small staggered field in the z -direction, which is then decreased towards zero during the sweeps.

First we have a look at the entropy growth ΔS for the half-chain $r = 0$ as a function of time, shown on the left of Fig. 5.6 for several values of the anisotropy $\Delta > 1$. One observes a clear saturation of the excess entropy for large times, which is reached very quickly for large values of Δ . The asymptotic value of ΔS decreases with Δ and always exceeds $\ln(2)$. Remarkably, as shown on the right of Fig. 5.6, we find that the asymptotic excess entropy is well described by the formula $\Delta S = S(0) + \ln(2)$, where $S(0)$ is the ground-state entropy of the half-chain in the symmetry-broken state. Repeating the calculation for the excess Rényi entropy ΔS_2 , we find the exact same relation with $S_2(0)$.

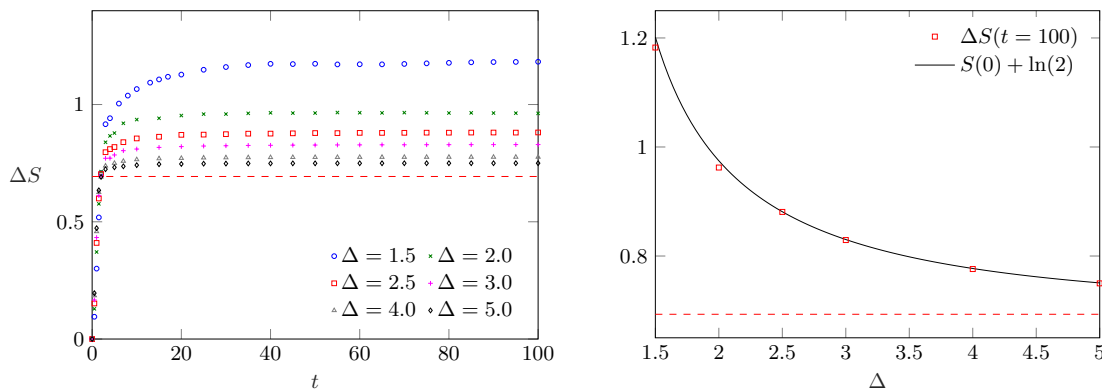


Figure 5.6: Left: Entanglement growth in the middle of the chain after a domain-wall excitation \tilde{m}_1 for different values of $\Delta > 1$ and $L = 400$. Right: ΔS at $t = 100$ compared to $S(0) + \ln(2)$ from Eq. (5.5.4). The red dashed line denotes $\ln(2)$. Note the different vertical scales.

To gain a deeper understanding of the above relation, one should invoke the exact results for the reduced density matrix of the half-chain, which can be found

with the corner transfer matrix (CTM) method as [160]

$$\rho_A = \frac{e^{-H_{CTM}}}{\text{Tr}(e^{-H_{CTM}})}, \quad H_{CTM} = \sum_{j=0}^{\infty} \epsilon_j n_j, \quad (5.5.3)$$

where the single-particle eigenvalues are given by $\epsilon_j = 2j\phi$ with $\phi = \text{acosh}(\Delta)$, and $n_j = 0, 1$ denotes fermionic occupation numbers. In other words, the entanglement Hamiltonian H_{CTM} of the ground state is characterized by an equispaced single-particle entanglement spectrum. Strictly speaking, this result applies to a half-infinite chain, but in practice it holds also for finite chains of length much larger than the correlation length. Note also, that the result (5.5.3) applies for the symmetric ground state, whereas for the symmetry-broken state the term $j = 0$ is missing from the sum. In that case, the von Neumann and Rényi entropies can be simply expressed as [206]

$$S(0) = \sum_{j=1}^{\infty} \left[\log(1 + e^{-2j\phi}) + \frac{2j\phi}{1 + e^{2j\phi}} \right], \quad (5.5.4)$$

as well as

$$S_n(0) = \frac{1}{1-n} \left[\sum_{j=1}^{\infty} \log(1 + e^{-2nj\phi}) - n \sum_{j=1}^{\infty} \log(1 + e^{-2j\phi}) \right]. \quad (5.5.5)$$

It is easy to see that the inclusion of the term $j = 0$ with $\epsilon_0 = 0$ simply yields an extra $\ln(2)$ contribution to the entropies. This change alone, however, would not explain our findings for the asymptotic excess entropy in Fig. 5.6, which seems to indicate that $S(t) \approx 2S(0) + \ln(2)$ for $t \gg 1$. Indeed, in order to obtain such a formula, one would have to add a double degeneracy for each ϵ_j with $j \neq 0$. Let us now discuss how such a degeneracy is reflected in the eigenvalues λ_l of the reduced density matrix. In fact, it is more convenient to introduce the scaled quantity

$$\nu_l = -\frac{1}{\phi} \ln \left(\frac{\lambda_l}{\lambda_0} \right), \quad (5.5.6)$$

where λ_0 denotes the maximal eigenvalue. For the initial symmetry-broken ground state, ν_l are independent of Δ and can only assume even integer values, with occasional multiplicities due to different integer partitions. The lowest lying λ_l

yield $\nu_l = 0, 2, 4, 6, 6, \dots$, i.e. the first degeneracy appears as $6 = 2 + 4$. The inclusion of the $\epsilon_0 = 0$ term simply gives an overall double degeneracy of the levels λ_l . The doubling of the ϵ_j for $j \neq 0$ further increases the degeneracies. Altogether, the combined effect would lead to the multiplicities $(2, 4, 6)$ for $\nu_l = 0, 2, 4$.

To check these predictions, in Fig. 5.7 we have plotted the 12 lowest lying ν_l calculated from the reduced density matrix eigenvalues, as obtained from tDMRG simulations after time evolving the state (5.5.2) to $t = 100$. One can see that the ν_l lie indeed rather close to the expected even integer values, approximately reproducing the expected multiplicity structure. Interestingly, the largest deviation around $\nu_l = 4$ is found for $\Delta = 5$, where one actually finds the best agreement with the entropy formula, see Fig. 5.6. In fact, however, the contribution of these eigenvalues to the entropy is already negligible. Note that the situation for larger values of ν_l is much less clear, as they correspond to very small eigenvalues λ_l which are already seriously affected by tDMRG truncation errors.

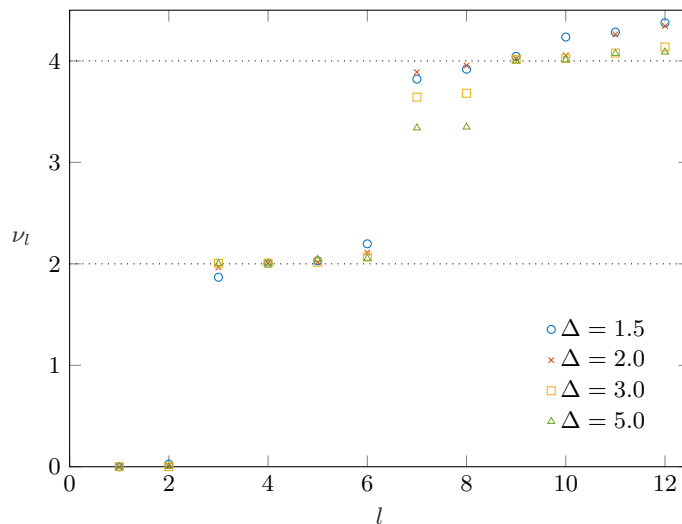


Figure 5.7: Scaled levels ν_l obtained from the reduced density matrix eigenvalues λ_l at time $t = 100$ via Eq. (5.5.6) for different Δ .

Although we find a nontrivial asymptotic behaviour of the half-chain entanglement, we expect that the full profile should still be described, up to a multiplicative factor, by the quasiparticle ansatz introduced in section 5.3.1, similarly to the Majorana excitation in the gapless phase in Fig. 5.2. Therefore, we put forward

the ansatz

$$\Delta S = \left(1 + \frac{S(0)}{\ln 2}\right) [-\mathcal{N} \ln(\mathcal{N}) - (1 - \mathcal{N}) \ln(1 - \mathcal{N})], \quad (5.5.7)$$

and for the excess Rényi entropy we propose

$$\Delta S_n = \left(1 + \frac{S_n(0)}{\ln 2}\right) \frac{1}{1 - n} \ln [\mathcal{N}^n + (1 - \mathcal{N})^n]. \quad (5.5.8)$$

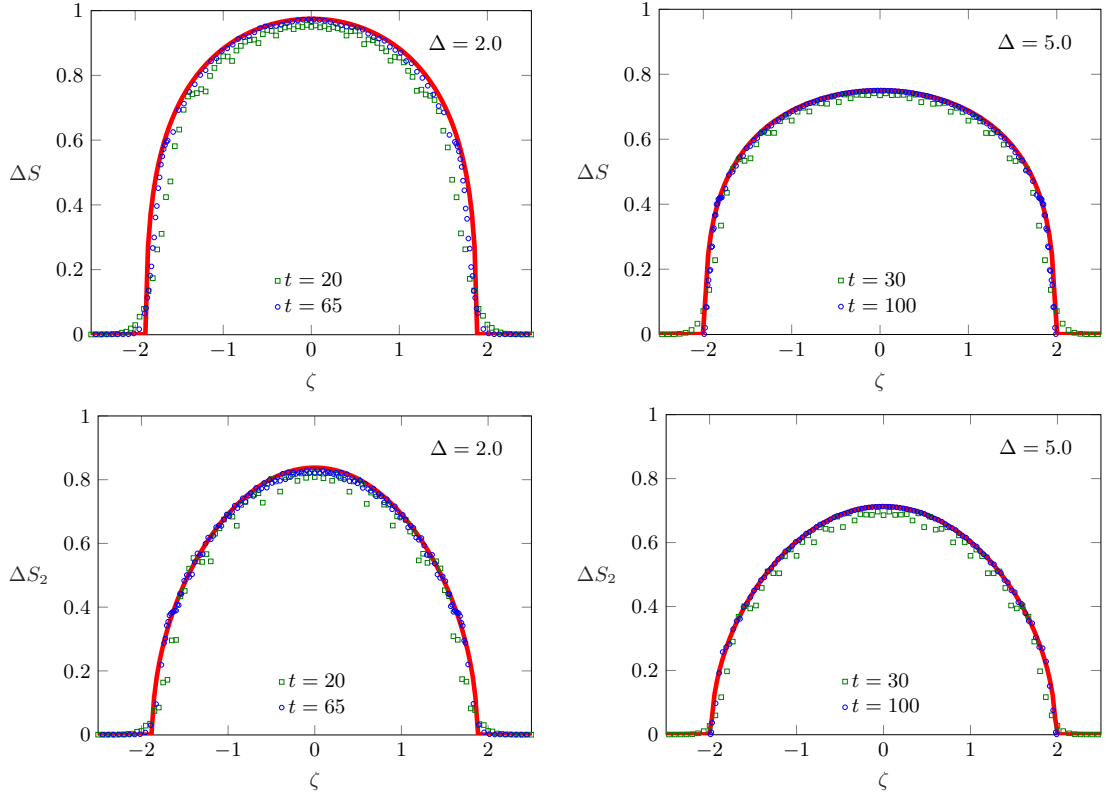


Figure 5.8: Entropy profiles ΔS (top) and ΔS_2 (bottom) after a domain-wall excitation \tilde{m}_1 for two different values of Δ and $L = 400$. The solid lines show the ansatz Eq. (5.5.7) for the von Neumann, as well as Eq. (5.5.8) for the $n = 2$ Rényi excess entropy.

The quasiparticle fraction \mathcal{N} must now be evaluated via (5.3.3) by using the spinon velocities (5.2.13) in the gapped phase. Note that the binary entropy functions are multiplied by a factor to reproduce our findings for the half-chain, where $\mathcal{N} = 1/2$. The results of our numerical calculations for the profiles ΔS and ΔS_2 , plotted against the scaling variable $\zeta = r/t$, are shown in Fig. 5.8. The solid lines show the respective ansatz (5.5.7) and (5.5.8), which give a very good description of the data for both Δ values shown. In fact, we checked that the profiles are nicely reproduced even for $\Delta = 1.5$, which already corresponds to a relatively large correlation length.

5.5.1 Magnetization profiles

To conclude this section, we also investigate the spreading of the magnetization profiles for the antiferromagnetic domain wall excited by \tilde{m}_1 . This setting was studied previously with a focus on the edge behaviour of the profile [207]. In order to remove the dependence on the ground-state value (5.2.9) of the staggered magnetization, we consider the normalized profile

$$\mathcal{M}_j(t) = \frac{\langle \psi(t) | \sigma_j^z | \psi(t) \rangle}{\langle \psi_\uparrow | \sigma_j^z | \psi_\uparrow \rangle}, \quad (5.5.9)$$

which then varies between $-1 \leq \mathcal{M}_j(t) \leq 1$ along the chain. We are mainly interested in the quasiparticle description of the time-evolved profile. In fact, a very similar problem was studied for a ferromagnetic domain wall in the XY chain [91], by first expanding the excited state in the single-particle basis of the Hamiltonian, which can then be time evolved trivially.

Here we assume that the dominant weight for our simple domain wall is carried by single-spinon excitations $|q\rangle$. Strictly speaking, this is only possible if one considers antiperiodic or open boundary conditions on the spins, since for a periodic chain spinons are created in pairs (i.e. one actually has a pair of domain walls). The time evolved state can then be written as

$$|\psi(t)\rangle \simeq \sum_q e^{-it\varepsilon_s(q)} c(q) |q\rangle, \quad (5.5.10)$$

where $\varepsilon_s(q)$ is the spinon dispersion (5.2.10), while $c(q)$ are the overlaps of the domain-wall excitation with the single-spinon states. Note that the momentum of

a single spinon satisfies $0 \leq q \leq \pi$, however, the total momentum of spinons above the quasidegenerate ground state is shifted by π . Since the domain wall is created by a strictly local fermionic operator, we assume that in the thermodynamic limit $|c(q)|$ becomes a constant in momentum space, i.e. $c(q) = e^{i\alpha(q)}/\sqrt{N}$ is just a phase factor normalized by the number N of spinon states. Using this in (5.5.10), one obtains for the profile

$$\mathcal{M}_j(t) = \frac{1}{N} \sum_p \sum_q e^{-it(\varepsilon_s(q) - \varepsilon_s(p))} e^{i(\alpha(q) - \alpha(p))} \frac{\langle p | \sigma_j^z | q \rangle}{\langle \psi_\uparrow | \sigma_j^z | \psi_\uparrow \rangle}. \quad (5.5.11)$$

Clearly, the main difficulty of calculating (5.5.11) is due to the form factors $\langle p | \sigma_j^z | q \rangle$. For the transverse Ising and XY chains, such form factors are known explicitly [208, 209] and were used to obtain a double integral representation of the magnetization profile [88, 91]. The hydrodynamic limit can then be obtained from the stationary-phase analysis of the integrals. Moreover, there exists a number of form factor results for the XXZ chain as well (see e.g. [210, 211]), which were used in numerical studies of the magnetization profile after a spin-flip excitation [212]. Unfortunately, however, the expressions are typically rather involved or not in a representation that could be useful for our purposes. In fact, we are not aware of any results where the required single-spinon matrix elements are evaluated as a function of the spinon rapidity or momentum.

Nevertheless, based on the known results, we give a handwaving argument about how the main structure of the form factor should look like. Most importantly, we assume that it becomes singular for $p \rightarrow q$ and can be written as

$$\lim_{p \rightarrow q} \frac{\langle p | \sigma_j^z | q \rangle}{\langle \psi_\uparrow | \sigma_j^z | \psi_\uparrow \rangle} \simeq \frac{i}{N} e^{i(q-p)j} \frac{\mathcal{F}(q)}{p - q}. \quad (5.5.12)$$

Here the only j -dependence is in the exponential factor that follows from the action of the translation operator, and the function $\mathcal{F}(q)$ denotes the slowly varying part of the form factor around its pole. The factor $1/N$ is required for a proper thermodynamic limit of (5.5.11). Converting the sums into integrals, one can proceed with the stationary phase analysis similarly to the XY case [91], by expanding the phases around $Q = q - p = 0$. Using a resolution of the pole and the definition of the step function

$$\frac{1}{Q} = i\pi\delta(Q) + \lim_{\epsilon \rightarrow 0} \frac{1}{Q + i\epsilon}, \quad \Theta(x) = -\lim_{\epsilon \rightarrow 0} \int_{-\infty}^{\infty} \frac{dQ}{2\pi i} \frac{e^{-iQx}}{Q + i\epsilon}, \quad (5.5.13)$$

one arrives at the following simple expression for the profile

$$\mathcal{M}_j(t) = 1 - 2\tilde{\mathcal{N}}, \quad \tilde{\mathcal{N}} = \int_0^\pi \frac{dq}{\pi} \Theta(v_s(q)t - j) \mathcal{F}(q). \quad (5.5.14)$$

Note that the proper normalization of the profile for $t = 0$ requires to have

$$\int_0^\pi \frac{dq}{\pi} \mathcal{F}(q) = 1. \quad (5.5.15)$$

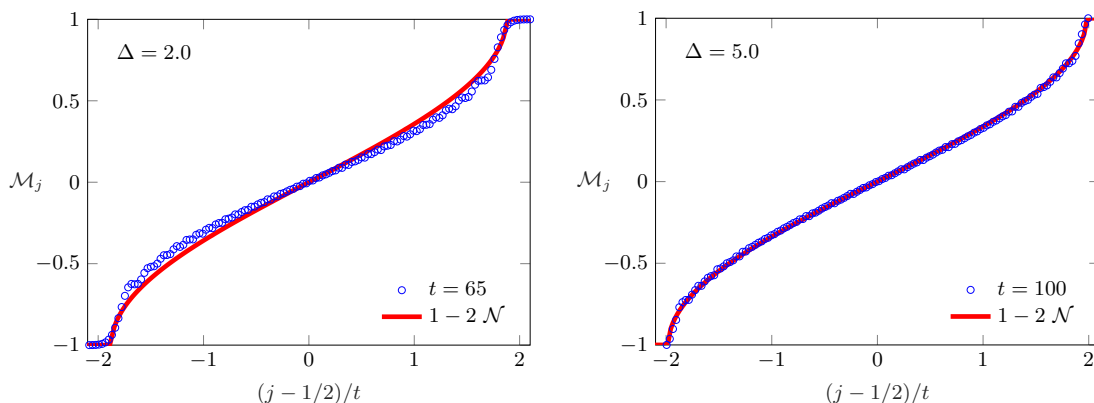


Figure 5.9: Normalized magnetization profiles $\mathcal{M}_j(t)$ obtained from tDMRG calculations for $\Delta = 2.0$ (left) and $\Delta = 5.0$ (right) after a domain-wall excitation \tilde{m}_1 in a chain of length $L = 400$. The solid lines show the ansatz $1 - 2\mathcal{N}$, with the spinon fraction Eq. (5.3.3) calculated from the velocities in Eq. (5.2.13).

The result (5.5.14) is nothing else but the quasiparticle interpretation of the magnetization profile in the hydrodynamic limit. Indeed, the initial sharp domain wall is carried away by spinons of different momenta q and velocities $v_s(q)$, where $\mathcal{F}(q)$ gives the corresponding weight. Unfortunately, without an explicit analytical result on the form factor, one has to make a guess on the weight function. The simplest assumption is $\mathcal{F}(q) \equiv 1$, which indeed holds true for the XY chain form factors [91]. With this simple choice one actually has $\tilde{\mathcal{N}} = \mathcal{N}$, that is we recover the spinon fraction introduced in (5.3.3) for the description of the entropy profile. In Fig. 5.9 we show the comparison of this simple ansatz to the tDMRG data, with a rather good agreement for a large $\Delta = 5$. For $\Delta = 2$, however, one can already

see the deviations from our simple ansatz, which fails completely for even smaller anisotropies. Thus, in sharp contrast to the case of the entanglement entropies, the spinon contributions to the magnetization cannot be taken to be equal, except for close to the Ising limit.

5.6 Summary and discussion

We studied the entanglement spreading in the XXZ chain after excitations that are strictly local in terms of the fermion operators. In the gapless phase we found that the time evolution after a fermion creation operator yields an entropy profile that can be well described by a probabilistic quasiparticle ansatz for not too large Δ , assuming equal contributions from low-lying spinon excitations. On the other hand, for a local Majorana excitation we observe that the quasiparticle ansatz holds only up to a multiplicative factor, determined by the excess entropy at the operator insertion point. This is in agreement with our CFT calculations, which suggest that the excess entropy exceeds $\ln(2)$ for any $\Delta \neq 0$, with a very slow convergence towards the asymptotic value $2\ln(2)$. In the symmetry-broken gapped phase we considered a different Majorana excitation, creating an antiferromagnetic domain wall. For the entropy profile we find again a nontrivial prefactor, whereas our simple ansatz for the magnetization, assuming equal contributions from the spinons, holds only in the Ising limit $\Delta \rightarrow \infty$.

The main limitation of our quasiparticle ansatz (5.3.4) is that it includes only the low-lying spinons. It is natural to ask how well such an assumption actually holds for our local excitations in the different regimes. A simple way to quantify the spectral weight of the spinons in the gapless regime is via the energy difference $\langle \Delta E \rangle = \langle \psi_0 | (m_1 H m_1 - H) | \psi_0 \rangle$ of the Majorana excitation (equal to that of c_1^\dagger by particle-hole symmetry) measured from the ground state, whereas in the gapped case we replace $m_1 \rightarrow \tilde{m}_1$. Our assumption in both regimes was that one can practically work with single-spinon states, whose energies above the ground state are given by the corresponding dispersions $\varepsilon_s(q)$ in (5.2.4) and (5.2.10), respectively. This yields the simple formula for the energy difference

$$\langle \Delta E \rangle = \int_0^\pi \varepsilon_s(q) \frac{dq}{\pi}. \quad (5.6.1)$$

To test the validity of our assumption, in Fig. 5.10 we compare the energy difference obtained from DMRG to the formula (5.6.1) in both gapless and gapped

phases. As expected, the result at the free-fermion point $\Delta = 0$ is exactly reproduced, while the error remains relatively small in the regime $|\Delta| \lesssim 0.5$. However, not surprisingly, the overall behaviour of $\langle \Delta E \rangle$ is not properly captured by the naive ansatz (5.6.1), especially for $\Delta \rightarrow -1$, which is exactly what we observed for the entropy profiles in Fig. 5.1. On the other hand, in the gapped phase shown on the right of Fig. 5.10, one has a qualitatively good description in the entire regime, with the error decreasing for $\Delta \gg 1$. This explains why we had a much better overall description of the entropy profiles for $\Delta > 1$ via the quasiparticle ansatz (5.5.7).

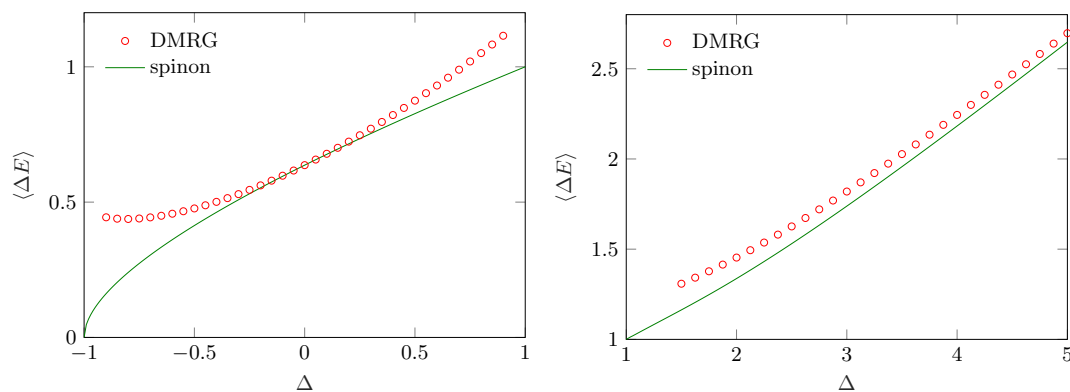


Figure 5.10: Energy difference due to the insertion of local operator m_1 in the gapless (left) and \tilde{m}_1 in the gapped (right) regime. DMRG results (symbols) for $L = 400$ are compared to the spinon ansatz (lines) in Eq. (5.6.1). Note the different vertical scales.

Another feature that is not completely understood is the multiplicative factor of the spinon ansatz appearing for Majorana excitations. In the gapless phase this could be accounted for the mixing of the chiral boson modes and yields a factor 2 in the limit $t \rightarrow \infty$ for any $\Delta \neq 0$. The exceptional behaviour of the XX chain can actually be also understood directly, using a duality transformation [213–216] that relates it to two independent and critical transverse Ising chains. Furthermore, as shown in [88], the Majorana excitation on the XX chain transforms under the dual map into a Majorana excitation acting only on a *single* Ising chain. Hence, the asymptotic excess entropy is given by $\ln(2)$ and there is no doubling in this case. On the other hand, in the gapped phase the prefactor in (5.5.7) seems to

Summary and discussion

be nontrivially related to the ground-state entanglement entropy. Note that a similar observation was reported after a local quench in the non-critical transverse Ising chain [143], where the entanglement plateau was also found to be related to the ground-state value. A deeper understanding of these effects requires further studies.

Finally, let us comment about the case where the locality of the excitation is not imposed in the fermionic but rather in the spin picture. In other words, instead of the c_j^\dagger excitation one could consider the spin operator σ_j^+ by dropping the Jordan-Wigner string in (5.3.6). According to our tDMRG calculations carried out for this case, the entropy profiles change completely, becoming more flat in the center with a maximum that stays way below $\ln(2)$. In short, the fermionic nature of the local excitations turns out to be essential for the applicability of the quasiparticle description.

Acknowledgments

The authors acknowledge funding from the Austrian Science Fund (FWF) through Project No. P30616-N36.

Chapter 6

Summary and conclusions

In this thesis, we have studied the nonequilibrium dynamics following inhomogeneous quantum quenches and local operator insertions. We mainly focused on the Rényi entropy profiles as well as the logarithmic negativity spreading in inhomogeneous setups.

In chapter 3, we have studied the nonequilibrium dynamics following a geometric quench in an XXZ chain. In the noninteracting (XX) case, we are able to describe the entanglement with a heuristic CFT ansatz. Applying GHD, we are able to describe the magnetization profiles after the quench in the gapless regime of the XXZ chain. For the interacting case, we can understand the entanglement profiles only qualitatively by identifying front edge positions. However, we show that a proportionality between the subsystem magnetization fluctuations and the entropy, originally established in equilibrium, also holds true after the geometric quench.

In chapter 4, we have studied the negativity across defects after connecting two free-fermion half chains. As the logarithmic negativity allows to measure the entanglement of mixed states, we are able to quantify the entanglement between adjacent, noncomplementary intervals which encompass the defect. For an unbiased quench with equal initial fillings, we find a logarithmic increase of entanglement across the defect. For the biased quench with a defect, we present a quasiparticle ansatz, leading to a linear increase of entanglement, followed by a saturation. Here, the quasiparticles are produced continuously in time at the defect. Moreover, we also present numerical tDMRG results for the XXZ chain, finding a qualitatively similar behaviour after the unbiased quench. Finally, we

studied the relation between the negativity and the $\alpha = 1/2$ Rényi mutual information. A proportionality that is valid for the ground state of an XX chain with a defect, is found to also hold true in the case of an unbiased quench with equal initial fillings for large interval lengths ℓ . However, in the case of a biased quench across a defect, the proportionality turns out to be no longer valid.

In chapter 5, we have studied the excess entropy due to the insertion of local fermionic operators in the XXZ chain. In the gapless phase, the entropy profiles after a fermionic creation operator insertion are well described by a probabilistic quasiparticle ansatz which only considers low-energy spinon excitations. The same ansatz holds true for a local Majorana excitation if the entropy profile maximum is rescaled. We understand this Δ -dependent scaling of the profiles within a Luttinger liquid theory. After a modified Majorana excitation in the gapped phase, a quasiparticle ansatz for asymptotic entropy profiles, that depends on the ground state entropy, is presented. The respective low-energy approximations just described work well near the free-fermion point in the gapless phase and in the limit of large Δ in the antiferromagnetic gapped phase.

Chapter 7

Acknowledgements

First of all, I would like to thank my supervisor, Viktor Eisler. The last three years have been a real pleasure and I really enjoyed working on such interesting topics. Thank you for giving me this opportunity, for always having an open ear and an open door and for patiently answering my very many questions.

I would also like to thank Hans Gerd Evertz who accepted all the administrative duties of being the official supervisor for the last three years.

Thank you Daniel Bauernfeind and Florian Maislinger for being such great roommates. Thank you for the numerous enlightening talks, both on and off topic, for the *Stricherlliste* and for the after work beers.

I would also like to thank all the (also former) colleagues at the institute for the pleasant and collegial working atmosphere. I would like to especially thank Markus Aichhorn, Gerhard Dorn, Delia Fugger, Johannes Graspeuntner, Gernot Kraberger, Markus Richter, Franz Rohrhofer, Michael Rumetshofer, Hermann Schnait, Irakli Titvinidze, Robert Triebel and Wolfgang von der Linden.

Furthermore, thanks to Andreas Hirczy for keeping all the computers running and Brigitte Schwarz for keeping the administration running.

I would very much like to thank my parents. Thank you for your ongoing support in every possible way, for your ongoing interest in my work and most of all for your unconditional love.

Without you, none of this would have been possible.

Finally, I would like to thank you, Nana. Thank you for each and every wonderful day together, for making me laugh and above all for your love.

CHAPTER 7. ACKNOWLEDGEMENTS

Appendix A

Appendix to Phys. Rev. B 99, 174403 (2019)

A.1 Perturbative calculation of the edge around ζ_{max}

As discussed in the main text, for $\Delta > 0$ the GHD solution around the rightmost ray $\zeta_{max} = 1$ is given by the occupation function (3.3.10) by solving (3.3.11). We assume that, sufficiently close to the GHD edge, the interval $[\lambda_1, \lambda_2]$ of occupied rapidities remains small, i.e., $|\lambda_{1,2} - \tilde{\lambda}| \ll 1$, with $\tilde{\lambda}$ given by (3.3.9). For such an occupation, the dressing of a function f can be considered as a perturbation around its bare value

$$f^{dr}(\lambda) \approx f(\lambda) + \delta f(\lambda). \quad (\text{A.1.1})$$

Inserting into the dressing equation (3.2.5) one obtains

$$f(\lambda) + \delta f(\lambda) + \int_{\lambda_1}^{\lambda_2} \frac{d\mu}{2\pi} \mathcal{K}(\lambda - \mu) [f(\mu) + \delta f(\mu)] = f(\lambda). \quad (\text{A.1.2})$$

To extract the leading order in the perturbation series, we neglect the term δf within the integral and expand all the functions to first order in $\nu = \lambda - \mu$, which leaves us with

$$\delta f(\lambda) + \int_{\lambda-\lambda_2}^{\lambda-\lambda_1} \frac{d\nu}{2\pi} (\mathcal{K}(0) + \nu \mathcal{K}'(0)) (f(\lambda) - \nu f'(\lambda)) = 0. \quad (\text{A.1.3})$$

Setting $\lambda_1 = \tilde{\lambda} - \epsilon_1$, $\lambda_2 = \tilde{\lambda} + \epsilon_2$ and carrying out the integrals, we finally arrive at

$$2\pi \delta f(\lambda) = -\mathcal{K}(0)f(\lambda)(\epsilon_1 + \epsilon_2) - [\mathcal{K}'(0)f(\lambda) - \mathcal{K}(0)f'(\lambda)] \times \quad (\text{A.1.4})$$

$$\frac{\epsilon_1^2 - \epsilon_2^2 + 2(\lambda - \tilde{\lambda})(\epsilon_1 + \epsilon_2)}{2} + \mathcal{O}(\epsilon^3). \quad (\text{A.1.5})$$

With this result at hand, we can now calculate from Eq. (3.3.2) the dressed velocity

$$v \approx \frac{e' + \delta e'}{p' + \delta p'} \approx \frac{e'}{p'} \left[1 + \frac{\delta e'}{e'} - \frac{\delta p'}{p'} + \left(\frac{\delta p'}{p'} \right)^2 - \left(\frac{\delta e'}{e'} \right) \left(\frac{\delta p'}{p'} \right) \right], \quad (\text{A.1.6})$$

where we have dropped the arguments λ . Applying (A.1.5) for both $\delta e'$ and $\delta p'$ and keeping only up to quadratic terms in $\epsilon_{1,2}$, one has

$$v \approx v_0 \left[1 + \frac{\mathcal{K}(0)}{2\pi} \left(\frac{e''}{e'} - \frac{p''}{p'} \right) \frac{\epsilon_1^2 - \epsilon_2^2 + 2(\lambda - \tilde{\lambda})(\epsilon_1 + \epsilon_2)}{2} \right], \quad (\text{A.1.7})$$

where v_0 is the bare velocity; see Eq. (3.3.7). The correction to the bare velocity depends on the ratios of second and first derivatives of the energy and momentum. Since the factor multiplying them is already quadratic in $\epsilon_{1,2}$, it is enough to evaluate the ratios at $\lambda = \tilde{\lambda}$. Interestingly, however, a simple calculation leads to the result

$$\left. \frac{e''}{e'} \right|_{\lambda=\tilde{\lambda}} = \left. \frac{p''}{p'} \right|_{\lambda=\tilde{\lambda}}. \quad (\text{A.1.8})$$

Hence, to leading order, the velocity around the edge is just given by its bare value, with corrections $\mathcal{O}(\epsilon^3)$. The rapidities $\lambda_{1,2}$ then follow from the condition $v_0(\lambda_1) = v_0(\lambda_2) = \zeta$. Expanding the bare velocity around $\tilde{\lambda}$ gives

$$v_0(\tilde{\lambda} \pm \epsilon) \approx v_0(\tilde{\lambda}) \pm \epsilon v_0'(\tilde{\lambda}) + \frac{\epsilon^2}{2} v_0''(\tilde{\lambda}). \quad (\text{A.1.9})$$

However, as discussed in the main text, $\tilde{\lambda}$ is exactly the maximum of the bare velocity, $v_0'(\tilde{\lambda}) = 0$, with its value given by $v_0(\tilde{\lambda}) = 1$. Furthermore, the second derivative can be calculated as $v_0''(\tilde{\lambda}) = -\cot^2(\gamma)$ and thus we get

$$v_0(\tilde{\lambda} \pm \epsilon) = 1 - \frac{\epsilon^2}{2} \cot^2(\gamma) = \zeta. \quad (\text{A.1.10})$$

Solving for ϵ then leads to the result

$$\epsilon = \sqrt{2(1 - \zeta)} \tan(\gamma), \quad (\text{A.1.11})$$

reported in Eq. (3.3.15) of the main text.

It should be stressed that for the perturbation theory to work, the condition $\epsilon \ll 1$ must be satisfied. From (A.1.11) one can see that this becomes problematic, as the interaction strength is decreased. Indeed, for $\Delta \rightarrow 0$ ($\gamma \rightarrow \pi/2$) one has $\epsilon \rightarrow \infty$; i.e., the solution diverges. The reason is that for very small interactions, the bare velocity develops only a very tiny maximum around extremely high rapidities $\tilde{\lambda} \gg 1$, thus deteriorating the quality of the approximation. In particular, at the free-fermion point $\Delta = 0$ the approximation fails completely, which can also be seen by expanding the analytical result (3.3.17) for the magnetization profile around $\zeta = 1$. This gives to leading order

$$\langle S^z \rangle \approx -\frac{1}{2} + \frac{1}{2\pi} \sqrt{2(1 - \zeta)}, \quad (\text{A.1.12})$$

where the coefficient of the square root is off by a factor of 2 with respect to the approximation (3.3.16). Moreover, even considering a larger value $\Delta = 0.8$ and requiring $\epsilon < 0.1$, one has from (A.1.11) the condition $\zeta > 0.99$. This explains why the approximate profile deviates essentially immediately from the GHD solution in Fig. 3.3.

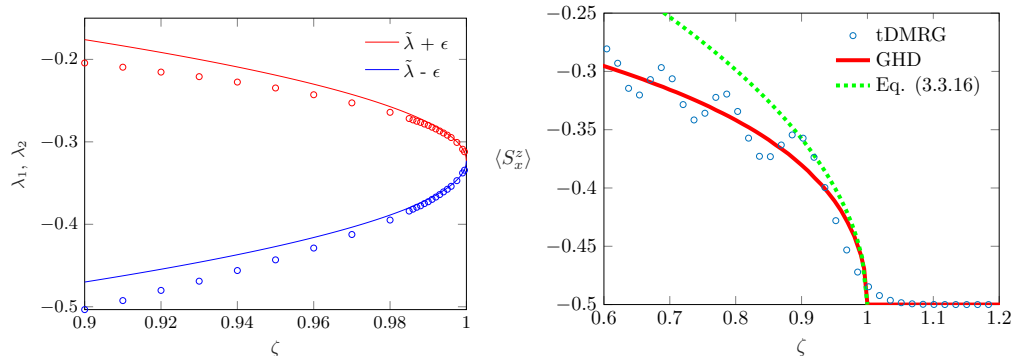


Figure A.1: Left: rapidities λ_1 (blue circles) and λ_2 (red circles) as obtained from the iterative numerical solution of Eq. (3.3.11) for $\Delta = 0.95$. The approximate solutions are shown by solid lines, see Eq. (A.1.11), with a good agreement near $\zeta = 1$. Right: corresponding edge magnetization profile and its approximation.

On the other hand, one expects that the edge approximation should perform much better for $\Delta \rightarrow 1$, i.e., around the isotropic Heisenberg point. This is indeed what we observe by comparing it to the numerical solutions λ_1 and λ_2 of the GHD ansatz (3.3.11). This is shown in the left panel of Fig. A.1 for $\Delta = 0.95$, where the approximation appears to be rather good around the edge but deviates as one moves farther away. In the right panel of Fig. A.1 we also show the edge profile for the magnetization, comparing the GHD solution to the approximation (3.3.16) and to the tDMRG data for $L = 200$ and $t = 60$.

Appendix B

Appendix to J. Phys. A: Math. Theor. 53, 205301 (2020)

B.1 Correlation matrices for the defect

We collect here the integral formulas for the correlation matrix elements $\langle c_m^\dagger c_n \rangle$ in the thermodynamic limit $L \rightarrow \infty$ of the hopping chain (4.2.1), with a single weak hopping defect parametrized by $\lambda = e^{-\nu}$. We consider both the ground state of the chain as well as the NESS after time evolution from a domain wall. The former has been considered in Ref. [187] while in the latter case the results were obtained in Ref. [194]. In each case the result depends on whether the lattice sites are chosen on the same (left or right) or opposite sides of the defect, i.e. the correlation matrix has a block form. We shall only consider matrix elements with $m \leq n$, since the others follow from hermiticity.

In the ground state of an infinite chain, the matrix elements read

$$C_{m,n} = \begin{cases} C_0(n-m) - C_1(n+m) & \text{if } m, n \geq 1 \\ C_0(n-m) - C_1(2-n-m) & \text{if } m, n \leq 0 \\ C_2(n-m) & \text{if } m \leq 0, n \geq 1 \end{cases} \quad (\text{B.1.1})$$

where the different contributions depend only on the difference $r = n - m$ and sum $s = n + m$ of the indices. The first translationally invariant piece is given by

$$C_0(r) = \frac{\sin\left(\frac{\pi}{2}r\right)}{\pi r}, \quad (\text{B.1.2})$$

Correlation matrices for the defect

which is just the homogeneous result. The extra contributions on the same side of the defect were obtained in [187] and read

$$C_1(s) = \frac{\text{sh } \nu}{2} (e^\nu I_s - e^{-\nu} I_{s-2}), \quad (\text{B.1.3})$$

where

$$I_s = \int_0^{\pi/2} \frac{dq}{\pi} \frac{\cos qs}{\text{sh}^2 \nu + \sin^2 q}. \quad (\text{B.1.4})$$

Interestingly, one observes that the contributions $C_1(2k) = 0$ vanish completely for even $s = 2k$, which follows from the property $e^\nu I_{2k} = e^{-\nu} I_{2k-2}$ of the integrals defined above. Finally, the matrix elements on opposite sides of the defect are given by

$$C_2(r) = \frac{\text{ch } \nu}{2} I_r - \frac{e^\nu}{4} I_{r+2} - \frac{e^{-\nu}}{4} I_{r-2}. \quad (\text{B.1.5})$$

Using the property found above, it is easy to see that also these contributions vanish for $r = 2k$. Thus the correlation matrix has a checkerboard structure as in the homogeneous case.

In the limit $\nu = 0$ one has trivially $C_1(s) = 0$, whereas for the offdiagonal block one finds

$$\begin{aligned} C_2(r) &= \int_0^{\pi/2} \frac{dq}{2\pi} \frac{\cos qr - [\cos q(r-2) + \cos q(r+2)]}{\sin^2 q} / 2 \\ &= \int_0^{\pi/2} \frac{dq}{\pi} \cos qr = C_0(r), \end{aligned} \quad (\text{B.1.6})$$

i.e. one recovers the results for the homogeneous chain. In the opposite limit $\nu \rightarrow \infty$ of a vanishing defect coupling, one finds $C_1(s) = C_0(s)$ which is the result for a half-infinite chain. On the other hand, $C_2(r) = 0$ as it should for two decoupled half-chains.

Now we consider the correlation matrix elements $\tilde{C}_{m,n}$ for the NESS, which emerges in the $t \rightarrow \infty$ limit of time evolution from a domain wall initial state. The results were obtained in [194] by solving the problem for a finite system size and time and then considering the limits $L \rightarrow \infty$ and $t \rightarrow \infty$ via contour integration tricks. In order to bring the formulas for the matrix elements in a transparent form, it is useful to introduce the transmission and reflection coefficients

$$T_q = \frac{\sin^2 q}{\text{sh}^2 \nu + \sin^2 q}, \quad R_q = \frac{\text{sh}^2 \nu}{\text{sh}^2 \nu + \sin^2 q}, \quad (\text{B.1.7})$$

as well as the auxiliary integral expressions

$$\tilde{I}_r = \int_0^\pi \frac{dq}{2\pi} \frac{i \sin qr}{\text{sh}^2 \nu + \sin^2 q}. \quad (\text{B.1.8})$$

Analogously to (B.1.1), the matrix elements can be written down by a separation of cases

$$\tilde{C}_{m,n} = \begin{cases} \tilde{C}_0(n-m) & \text{if } m, n \geq 1 \\ \delta_{m,n} - \tilde{C}_0(m-n) & \text{if } m, n \leq 0 \\ \tilde{C}_2(n-m) + \tilde{C}_3(n+m) & \text{if } m \leq 0, n \geq 1 \end{cases} \quad (\text{B.1.9})$$

The correlations are thus translationally invariant if both sites are located on the same side. They can be written in a very instructive form

$$\tilde{C}_0(r) = \int_0^\pi \frac{dq}{2\pi} T_q e^{iqr}. \quad (\text{B.1.10})$$

Indeed, this can be interpreted as a correlation matrix where the occupation function is given by the transmission probability for all the modes with positive velocities. Note that the correlations on the left/right hand side are now related by the symmetry property $\tilde{C}_{m,n} = \delta_{m,n} - \tilde{C}_{1-m,1-n}$. If the sites are located on opposite sides, the correlations are given via the expressions

$$\tilde{C}_2(r) = \frac{\text{ch } \nu}{2} \tilde{I}_r - \frac{e^\nu}{4} \tilde{I}_{r+2} - \frac{e^{-\nu}}{4} \tilde{I}_{r-2} \quad (\text{B.1.11})$$

and

$$\tilde{C}_3(s) = i \int_0^\pi \frac{dq}{2\pi} \sqrt{T_q R_q} e^{iq(s-1)}. \quad (\text{B.1.12})$$

The limiting cases are also straightforward to obtain. For $\nu = 0$ we have $T_q \equiv 1$ and $R_q \equiv 0$ such that

$$\tilde{C}_0(r) = \frac{1}{2} \delta_{r,0} + i \int_0^\pi \frac{dq}{2\pi} \sin qr, \quad (\text{B.1.13})$$

which is exactly the NESS result for the homogeneous chain. For the offdiagonal block one obtains $C_3(s) = 0$ as well as

$$\tilde{C}_2(r) = i \int_0^\pi \frac{dq}{4\pi} \frac{\sin qr - [\sin q(r-2) + \sin q(r+2)]/2}{\sin^2 q} = i \int_0^\pi \frac{dq}{2\pi} \sin qr, \quad (\text{B.1.14})$$

i.e. the full matrix becomes translationally invariant, as it should. In the opposite limit $\nu \rightarrow \infty$ one has $T_q \equiv 0$ and $R_q \equiv 1$, and thus $\tilde{C}_0(r) = \tilde{C}_2(r) = \tilde{C}_3(s) = 0$. One then simply recovers the initial $t = 0$ form of the correlation matrix since the transmission vanishes between the two half-chains.

B.2 CFT treatment of the domain wall quench

In this appendix we present the CFT calculation of the mutual information and entanglement negativity for a domain wall initial state time evolved with a homogeneous hopping chain. The key insight to the problem was provided in Ref. [53], where it was shown that the inhomogeneous time-evolved state can be mapped onto a CFT with a curved background metric. This metric was first obtained in [174] where the imaginary-time evolution of the domain wall initial state was considered. Alternatively, one could use the exact mapping from the domain-wall melting to a ground-state problem with a linear potential [146, 192]. Here we will follow the latter route.

Let us consider a free-fermion chain with a slowly varying linear potential, with the corresponding length scale given by t . The ground state of this chain is unitarily equivalent to the time-evolved state starting from a domain wall [146]. For $t \gg 1$ one can apply a local density approximation (LDA), i.e. one assumes that the ground state around position x is locally equivalent to a homogeneous ground state, corresponding to the dispersion $\omega_q = -\cos q + x/t$. The spatially varying Fermi momentum and velocity are then given by, respectively,

$$q_F(x) = \arccos(x/t), \quad v_F(x) = \sin q_F(x) = \sqrt{1 - (x/t)^2}. \quad (\text{B.2.1})$$

The LDA yields a description where the state can be *locally* described via a 2D massless Dirac fermion field theory. The crucial finding of Ref. [53] is that one can define a *globally* valid Dirac theory, living in a curved background metric, where the changing of the Fermi velocity can be absorbed by introducing the coordinate transformation

$$z = \int_0^x \frac{dx'}{v_F(x')} + iy = t \arcsin \frac{x}{t} + iy. \quad (\text{B.2.2})$$

The curved metric is then given by $ds^2 = e^{2\sigma(x)} dzd\bar{z}$, where the Weyl factor has to be chosen as $e^{\sigma(x)} = v_F(x)$ in order to reproduce the local fermion propagators.

Once the proper metric and field theory have been identified, the calculation of the entropy can be performed by applying the replica trick and the corresponding twist-field formalism [104]. Namely, the Rényi entropy S_n can be obtained by calculating expectation values of twist fields \mathcal{T}_n and $\bar{\mathcal{T}}_n$ inserted at the spatial boundaries (and imaginary time $y = 0$) of the subsystem at hand. Here we focus on an interval $A_1 = [x_1, x_2]$ such that

$$\text{Tr}(\rho_{A_1}^n) = \epsilon(x_1)^{\Delta_n} \epsilon(x_2)^{\Delta_n} \langle \mathcal{T}_n(x_1) \bar{\mathcal{T}}_n(x_2) \rangle, \quad (\text{B.2.3})$$

where the scaling dimension of the twist fields is given by

$$\Delta_n = \frac{c}{12} \left(n - \frac{1}{n} \right), \quad (\text{B.2.4})$$

with the central charge being $c = 1$ for the Dirac theory. Note that we have explicitly included a UV cutoff $\epsilon(x)$ in (B.2.3) which, in contrast to homogeneous systems, carries a spatial dependence and thus cannot be ignored. Indeed, since the only relevant microscopic energy scale on the lattice is given by the Fermi velocity, the cutoff must be chosen as $\epsilon(x) = \epsilon_0 v_F^{-1}(x)$, where ϵ_0 is a dimensionless constant.

In order to evaluate the expectation value in (B.2.3), one should point out that, due to the change of coordinates in (B.2.2), the curved-space field theory lives on the infinite strip $[-\frac{\pi}{2}t, \frac{\pi}{2}t] \times \mathbb{R}$. Therefore, one has to first map the theory onto the upper half plane by the conformal transformation $g(z) = e^{i(z/t + \pi/2)}$. The twist-field two-point function can then be written as

$$\langle \mathcal{T}_n(x_1) \bar{\mathcal{T}}_n(x_2) \rangle = \left(e^{-\sigma(x_1)} \left| \frac{dg(z_1)}{dz_1} \right| \right)^{\Delta_n} \left(e^{-\sigma(x_2)} \left| \frac{dg(z_2)}{dz_2} \right| \right)^{\Delta_n} \times \langle \mathcal{T}_n(g(z_1)) \bar{\mathcal{T}}_n(g(z_2)) \rangle_{\text{UHP}}. \quad (\text{B.2.5})$$

In the above expression we simply used the transformation properties of the twist fields under the Weyl transformation (i.e. changing to the curved-space coordinates) as well as the mapping $g(z)$. The remaining step is to evaluate the two-point function on the upper half plane which, using the method of images, can be written as a four-point function on the full plane. Up to multiplicative constants, one obtains for the Dirac theory [53]

$$\langle \mathcal{T}_n(g(z_1)) \bar{\mathcal{T}}_n(g(z_2)) \rangle_{\text{UHP}} = [\text{Im } g(z_1) \text{Im } g(z_2) \eta_{1,2}]^{-\Delta_n}, \quad (\text{B.2.6})$$

$$\eta_{1,2} = \frac{|g(z_1) - g(z_2)|^2}{|g(z_1) - g^*(z_2)|^2}. \quad (\text{B.2.7})$$

CFT treatment of the domain wall quench

It should be noted that, for a generic CFT, the result is more complicated and is multiplied by a non-universal function $\mathcal{F}(\eta_{1,2})$ of the four-point ratio $\eta_{1,2}$, see e.g. [105]. For the Dirac theory, however, one has $\mathcal{F} \equiv 1$ [217].

We are now ready to calculate the Rényi mutual information (4.2.9) between two adjacent intervals $A_1 = [x_1, x_2]$ and $A_2 = [x_2, x_3]$. Putting everything together, one arrives at the result

$$\mathcal{I}_n = \frac{1+n}{6n} \ln \left[\epsilon^{-1}(x_2) e^{\sigma(x_2)} \left| \frac{dg(z_2)}{dz_2} \right|^{-1} \text{Im} g(z_2) \left(\frac{\eta_{1,2} \eta_{2,3}}{\eta_{1,3}} \right)^{1/2} \right]. \quad (\text{B.2.8})$$

The calculation for the logarithmic negativity follows a similar procedure, but is slightly more involved. In the replica approach it can be written as [130, 131]

$$\mathcal{E} = \lim_{n_e \rightarrow 1} \ln \text{Tr}(\rho_A^{T_2})^{n_e}, \quad (\text{B.2.9})$$

where the calculation has to be carried out for an even n_e number of replicas and then taking the limit $n_e \rightarrow 1$. Indeed, the limit $n_o \rightarrow 1$ from an odd number of copies would give the log of the trace (which is trivially zero) instead of the trace norm. Furthermore, the effect of the partial transpose is to interchange the twist operators \mathcal{T}_n and $\bar{\mathcal{T}}_n$ located at the ends of the segment A_2 over which the transpose is taken. We will restrict ourselves to adjacent intervals $A_1 = [x_1, x_2]$ and $A_2 = [x_2, x_3]$, such that the trace can be written as the three-point function

$$\text{Tr}(\rho_A^{T_2})^n = \prod_{i=1}^3 \epsilon(x_i)^{\Delta(i)} \langle \mathcal{T}_n(x_1) \bar{\mathcal{T}}_n^2(x_2) \mathcal{T}_n(x_3) \rangle. \quad (\text{B.2.10})$$

where the scaling dimensions are given by

$$\Delta_{(1)} = \Delta_{(3)} = \Delta_n, \quad \Delta_{(2)} = \begin{cases} \Delta_{n_o} & n = n_o, \\ 2\Delta_{n_e/2} & n = n_e. \end{cases} \quad (\text{B.2.11})$$

Clearly, the scaling dimension $\Delta_{(2)}$ corresponding to the composite field $\bar{\mathcal{T}}_n^2$ shows a strong parity dependence.

To calculate the twist-field expectation value, one uses again the transformation properties

$$\begin{aligned} \langle \mathcal{T}_n(x_1) \bar{\mathcal{T}}_n^2(x_2) \mathcal{T}_n(x_3) \rangle &= \prod_{i=1}^3 \left(e^{-\sigma(x_i)} \left| \frac{dg(z_i)}{dz_i} \right| \right)^{\Delta(i)} \times \\ &\langle \mathcal{T}_n(g(z_1)) \bar{\mathcal{T}}_n^2(g(z_2)) \mathcal{T}_n(g(z_3)) \rangle_{\text{UHP}}. \end{aligned} \quad (\text{B.2.12})$$

The last step is to evaluate the three-point function on the upper half plane, which has already been considered in [74]. For the Dirac theory one has

$$\langle \mathcal{T}_n(g(z_1)) \bar{\mathcal{T}}_n^2(g(z_2)) \mathcal{T}_n(g(z_3)) \rangle_{\text{UHP}} = \prod_{i=1}^3 [\text{Im } g(z_i)]^{-\Delta(i)} \left[\eta_{1,2}^{\Delta(2)} \eta_{2,3}^{\Delta(2)} \eta_{1,3}^{\Delta(1)+\Delta(3)-\Delta(2)} \right]^{-1/2}, \quad (\text{B.2.13})$$

where the four-point ratios are defined as

$$\eta_{i,j} = \frac{|g(z_i) - g(z_j)|^2}{|g(z_i) - g^*(z_j)|^2}. \quad (\text{B.2.14})$$

Note that here we assumed that the non-universal function $\mathcal{F}(\{\eta_{i,j}\})$, which could depend on the full operator content for a generic CFT, becomes again trivial for the Dirac theory [217]. Finally, since $\Delta_1 = 0$ from (B.2.4), the only nontrivial scaling dimension from (B.2.11) that survives the replica limit (B.2.9) is $\lim_{n_e \rightarrow 1} \Delta_{(2)} = 2\Delta_{1/2} = -1/4$. In turn, the entanglement negativity can be written as

$$\mathcal{E} = \frac{1}{4} \ln \left[\epsilon^{-1}(x_2) e^{\sigma(x_2)} \left| \frac{dg(z_2)}{dz_2} \right|^{-1} \text{Im } g(z_2) \left(\frac{\eta_{1,2} \eta_{2,3}}{\eta_{1,3}} \right)^{1/2} \right]. \quad (\text{B.2.15})$$

Comparing (B.2.15) to (B.2.8), one finds immediately $\mathcal{E} = \frac{1}{2} \mathcal{I}_{1/2}$. Note, however, that the result of the CFT calculation is valid only up to a nonuniversal additive constant. Nevertheless, one can use a continuity argument to make sure that this constant is the same for both quantities. Namely, if one considers a *bipartite* situation where A is the full system, then one has exactly $\mathcal{E} = \frac{1}{2} \mathcal{I}_{1/2}$. Therefore the equality should be valid, up to subleading terms, for arbitrary adjacent segments. Finally, it should be stressed that the calculation was carried out in complete generality for free-fermion systems that have an underlying curved-space CFT. In the last step we apply the result to our specific example of the linear potential. Introducing the scaling variables $\xi_i = x_i/t$, the various factors appearing in the argument of (B.2.15) read

$$\epsilon^{-1}(x_2) = e^{\sigma(x_2)} = \text{Im } g(z_2) = \sqrt{1 - \xi_2^2}, \quad \left| \frac{dg(z_2)}{dz_2} \right|^{-1} = t, \quad (\text{B.2.16})$$

whereas the square-root of the four-point ratios can be evaluated as

$$(\eta_{i,j})^{1/2} = \frac{1 - \xi_i \xi_j - \sqrt{(1 - \xi_i^2)(1 - \xi_j^2)}}{|\xi_i - \xi_j|}. \quad (\text{B.2.17})$$

CFT treatment of the domain wall quench

In particular, for the symmetric arrangement of the segments considered in the main text, $\xi_3 = -\xi_1 = \xi = \ell/t$ and $\xi_2 = 0$, the ratios further simplify to

$$(\eta_{1,2})^{1/2} = (\eta_{2,3})^{1/2} = \frac{1 - \sqrt{1 - \xi^2}}{\xi}, \quad (\eta_{1,3})^{1/2} = \xi, \quad (\text{B.2.18})$$

and plugging into (B.2.15) yields the result in (4.5.2).

Appendix C

Appendix to arXiv:2010.02708 (2020)

C.1 Correlation functions of vertex operators

In the following we give the main steps of the calculation of the excess Rényi entropy ΔS_2 , obtained via the ratio (5.4.11) of four-point and two-point functions. As in the main text, we consider two different local operators, the one corresponding to the fermion creation

$$\mathcal{O}_f = e^{ik_F d} \psi^\dagger + e^{-ik_F d} \bar{\psi}^\dagger, \quad (\text{C.1.1})$$

as well as the Hermitian Majorana excitation

$$\mathcal{O}_m = e^{ik_F d} \psi^\dagger + e^{-ik_F d} \bar{\psi}^\dagger + e^{-ik_F d} \psi + e^{ik_F d} \bar{\psi}. \quad (\text{C.1.2})$$

They are composed of chiral fermion fields which, after the Bogoliubov transformation (5.4.18), can be written as vertex operators (5.4.19) involving chiral boson fields. The holomorphic and anti-holomorphic components of the vertex operators are summarized in the table below, where $c = \cosh(\xi)$ and $s = \sinh(\xi)$.

We start by evaluating the two point function in the denominator of (5.4.11). Using the fact that vertex operators are primaries with conformal dimensions $h = \alpha^2/2$ and $\bar{h} = \beta^2/2$, one immediately obtains the nonvanishing two-point functions on the plane as

$$\begin{aligned} \langle \psi(w_1, \bar{w}_1) \psi^\dagger(w_2, \bar{w}_2) \rangle &\propto (w_1 - w_2)^{-c^2} (\bar{w}_1 - \bar{w}_2)^{-s^2}, \\ \langle \bar{\psi}(w_1, \bar{w}_1) \bar{\psi}^\dagger(w_2, \bar{w}_2) \rangle &\propto (w_1 - w_2)^{-s^2} (\bar{w}_1 - \bar{w}_2)^{-c^2}. \end{aligned} \quad (\text{C.1.3})$$

Correlation functions of vertex operators

	ψ	ψ^\dagger	$\bar{\psi}$	$\bar{\psi}^\dagger$
α	$-c$	c	s	$-s$
β	$-s$	s	c	$-c$

Table C.1: Parameters of the vertex operators (5.4.19) for the fermionic fields

From (5.4.9) we have $w_1 - w_2 = \bar{w}_1 - \bar{w}_2 = 2\epsilon$, thus we obtain for the two-point functions

$$\langle \mathcal{O}_f^\dagger(w_1, \bar{w}_1) \mathcal{O}_f(w_2, \bar{w}_2) \rangle = 2(2\epsilon)^{-(c^2+s^2)}, \quad \langle \mathcal{O}_m^\dagger(w_1, \bar{w}_1) \mathcal{O}_m(w_2, \bar{w}_2) \rangle = 4(2\epsilon)^{-(c^2+s^2)}. \quad (\text{C.1.4})$$

Let us now move to the four-point function on the Riemann surface Σ_2 . This is a sum of many terms, from which the nonvanishing contributions allowed by the neutrality conditions (5.4.21) are given by

$$\langle \psi\psi^\dagger\bar{\psi}\bar{\psi}^\dagger \rangle, \quad \langle \bar{\psi}\bar{\psi}^\dagger\psi\psi^\dagger \rangle, \quad \langle \bar{\psi}\psi^\dagger\psi\bar{\psi}^\dagger \rangle, \quad \langle \psi\bar{\psi}^\dagger\bar{\psi}\psi^\dagger \rangle, \quad \langle \psi\psi^\dagger\psi\psi^\dagger \rangle, \quad \langle \bar{\psi}\bar{\psi}^\dagger\bar{\psi}\bar{\psi}^\dagger \rangle. \quad (\text{C.1.5})$$

We first analyze the Jacobian of the transformation (5.4.15) from $\Sigma_2 \rightarrow \Sigma_1$. The derivatives of the mapping are given by

$$\frac{dw}{dz} = i\ell \frac{nz^{n-1}}{(1-z^n)^2}, \quad \frac{d\bar{w}}{d\bar{z}} = -i\ell \frac{n\bar{z}^{n-1}}{(1-\bar{z}^n)^2}. \quad (\text{C.1.6})$$

Introducing the variable

$$\chi = \frac{(1-z_1^2)^2(1-z_2^2)^2}{4z_1z_2}, \quad (\text{C.1.7})$$

one obtains for the first four contributions in (C.1.5)

$$\ell^{-2(c^2+s^2)} \chi^{c^2/2} \bar{\chi}^{s^2/2} \chi^{s^2/2} \bar{\chi}^{c^2/2} = \ell^{-2(c^2+s^2)} |\chi|^{c^2+s^2}, \quad (\text{C.1.8})$$

whereas for the last two contributions we have, respectively

$$\ell^{-2(c^2+s^2)} \chi^{c^2} \bar{\chi}^{s^2}, \quad \ell^{-2(c^2+s^2)} \chi^{s^2} \bar{\chi}^{c^2}. \quad (\text{C.1.9})$$

Note that there is an extra sign factor $(-i)^{c^2} (i)^{s^2} (i)^{s^2} (-i)^{c^2} = (-i)^{2(c^2-s^2)} = -1$ which multiplies the first two Jacobian.

The next step is to evaluate the vertex four-point functions. Using (5.4.20) this reads for the first term in (C.1.5)

$$z_{12}^{-c^2} z_{34}^{-s^2} z_{13}^{-cs} z_{24}^{-cs} z_{14}^{cs} z_{23}^{cs} \bar{z}_{12}^{-s^2} \bar{z}_{34}^{-c^2} \bar{z}_{13}^{-cs} \bar{z}_{24}^{-cs} \bar{z}_{14}^{cs} \bar{z}_{23}^{cs} = (-1) |1-\eta|^{2cs} |\eta|^{-(c^2+s^2)} |z_{13} z_{24}|^{-(c^2+s^2)} \quad (\text{C.1.10})$$

Note that we have used the property $z_{34} = -z_{12}$. It is easy to check that one obtains the very same factor from the second term. Similarly, using $z_{23} = z_{14}$, one can check that the third and fourth terms deliver

$$z_{12}^{cs} z_{34}^{cs} z_{13}^{-cs} z_{24}^{-cs} z_{14}^{-c^2} z_{23}^{-s^2} \bar{z}_{12}^{cs} \bar{z}_{34}^{cs} \bar{z}_{13}^{-cs} \bar{z}_{24}^{-cs} \bar{z}_{14}^{-s^2} \bar{z}_{23}^{-c^2} = |\eta|^{2cs} |1-\eta|^{-(c^2+s^2)} |z_{13} z_{24}|^{-(c^2+s^2)}. \quad (\text{C.1.11})$$

For the fifth term one has

$$[\eta(1-\eta)]^{-c^2} (z_{13} z_{24})^{-c^2} [\bar{\eta}(1-\bar{\eta})]^{-s^2} (\bar{z}_{13} \bar{z}_{24})^{-s^2}, \quad (\text{C.1.12})$$

and the last term follows by interchanging c and s above.

In order to obtain an expression in terms of the cross-ratios, one can rewrite (C.1.7) as

$$\chi = \left(\frac{\ell}{2\epsilon} \right)^2 \eta(1-\eta) z_{13} z_{24}. \quad (\text{C.1.13})$$

Putting everything together, one arrives at the four-point function

$$2(2\epsilon)^{-2(c^2+s^2)} \left[|\eta|^{(c+s)^2} + |1-\eta|^{(c+s)^2} + 1 \right]. \quad (\text{C.1.14})$$

Evaluating the four-point function for the Majorana excitation (C.1.2) is more cumbersome, since one has a large number of terms to consider. There are, however, some simple rules and symmetry arguments which make the task easier. First of all, one should clearly always have the same number of creation and annihilation operators, for the neutrality conditions (5.4.21) of the vertex correlation functions to be satisfied. This already drastically reduces the number of terms to consider. The remaining ones can be collected into families, some of them given by (C.1.5). Let us consider the family generated by the first term in (C.1.5), by allowing permutations of the left- and right-moving operators separately (i.e. interchanging the first or last two operators). If only the first or last two are interchanged, the vertex correlator (C.1.10) is modified by replacing

$$|1-\eta|^{2cs} \rightarrow |1-\eta|^{-2cs}, \quad (\text{C.1.15})$$

Correlation functions of vertex operators

whereas the correlator remains the same if both of them are interchanged. The next family is generated by the second term in (C.1.5), which is actually related to the first one by Hermitian conjugation. Hence this just gives a factor of two. The same argument holds for the next two families, where interchanging only one pair modifies the correlator in (C.1.11) as

$$|\eta|^{2cs} \rightarrow |\eta|^{-2cs}. \quad (\text{C.1.16})$$

Finally, the single interchange in the fifth family leads to

$$(1 - \eta)^{-c^2} \rightarrow (1 - \eta)^{c^2}, \quad (1 - \bar{\eta})^{-s^2} \rightarrow (1 - \bar{\eta})^{s^2}, \quad (\text{C.1.17})$$

whereas the last family follows by interchanging c and s above.

There are, however, two additional families appearing where the left- and right-moving particles are intertwined. They are given by the representative correlators

$$\langle \psi \bar{\psi}^\dagger \psi^\dagger \bar{\psi} \rangle, \quad \langle \bar{\psi} \psi^\dagger \bar{\psi}^\dagger \psi \rangle. \quad (\text{C.1.18})$$

Defining the variable

$$\sigma = \frac{(1 - z_1^2)^2 (1 - \bar{z}_2^2)^2}{4z_1 \bar{z}_2}, \quad (\text{C.1.19})$$

the corresponding Jacobians contain the factors $\sigma^{c^2} \bar{\sigma}^{s^2}$ and $\sigma^{s^2} \bar{\sigma}^{c^2}$, respectively. Furthermore, the vertex correlation functions yield

$$|\eta|^{\pm 2cs} |1 - \eta|^{\mp 2cs} (z_{13} \bar{z}_{24})^{-c^2} (\bar{z}_{13} z_{24})^{-s^2}, \quad |\eta|^{\pm 2cs} |1 - \eta|^{\mp 2cs} (z_{13} \bar{z}_{24})^{-s^2} (\bar{z}_{13} z_{24})^{-c^2}, \quad (\text{C.1.20})$$

and each term comes with a double multiplicity. Collecting all the terms, the four-point function takes the form

$$2 (2\epsilon)^{-2(c^2+s^2)} (2A + B + C), \quad (\text{C.1.21})$$

where the factors A , B and C are reported in (5.4.28)-(5.4.30).

Bibliography

1. Einstein, A., Podolsky, B. & Rosen, N. Can Quantum-Mechanical Description of Physical Reality Be Considered Complete? *Phys. Rev.* **47**, 777–780. <https://doi.org/10.1103/PhysRev.47.777> (1935) (cit. on p. 3).
2. Schrödinger, E. Discussion of Probability Relations between Separated Systems. *Mathematical Proceedings of the Cambridge Philosophical Society* **31**, 555–563. <https://doi.org/10.1017/S0305004100013554> (1935) (cit. on p. 3).
3. Nielsen, M. A. & Chuang, I. L. *Quantum Computation and Quantum Information* (Cambridge University Press, Cambridge, UK, 2010) (cit. on pp. 3, 36).
4. Calabrese, P., Cardy, J. & Doyon, B. Entanglement entropy in extended quantum systems. *J. Phys. A: Math. Theor.* **42**, 500301. <https://doi.org/10.1088/1751-8121/42/50/500301> (2009) (cit. on pp. 3, 30).
5. Amico, L., Fazio, R., Osterloh, A. & Vedral, V. Entanglement in many-body systems. *Rev. Mod. Phys.* **80**, 517–576. <https://doi.org/10.1103/RevModPhys.80.517> (2008) (cit. on pp. 3, 30, 32, 33).
6. Eisert, J., Cramer, M. & Plenio, M. B. Area laws for the entanglement entropy. *Rev. Mod. Phys.* **82**. <https://doi.org/10.1103/RevModPhys.82.277> (2010) (cit. on pp. 4, 53, 56).
7. Hastings, M. B. An area law for one-dimensional quantum systems. *J. Stat. Mech.* **2007**, P08024. <https://doi.org/10.1088/1742-5468/2007/08/p08024> (2007) (cit. on pp. 4, 53).
8. Brandão, F. & Horodecki, M. An area law for entanglement from exponential decay of correlations. *Nature Phys* **9**, 721–726. <https://doi.org/10.1038/nphys2747> (2013) (cit. on p. 4).

BIBLIOGRAPHY

9. Cirac, I., Perez-Garcia, D., Schuch, N. & Verstraete, F. *Matrix Product States and Projected Entangled Pair States: Concepts, Symmetries, and Theorems* 2020. arXiv: 2011.12127 (cit. on p. 4).
10. White, S. R. Density matrix formulation for quantum renormalization groups. *Phys. Rev. Lett.* **69**, 2863–2866. <https://doi.org/10.1103/PhysRevLett.69.2863> (1992) (cit. on pp. 4, 54, 107).
11. White, S. R. Density-matrix algorithms for quantum renormalization groups. *Phys. Rev. B* **48**, 10345–10356. <https://doi.org/10.1103/PhysRevB.48.10345> (1993) (cit. on pp. 4, 54, 107).
12. Schollwöck, U. The density-matrix renormalization group in the age of matrix product states. *Ann. Phys.* **326**, 96–192. <https://doi.org/10.1016/j.aop.2010.09.012> (2011) (cit. on pp. 4, 48, 54, 56, 66, 107).
13. Östlund, S. & Rommer, S. Thermodynamic Limit of Density Matrix Renormalization. *Phys. Rev. Lett.* **75**, 3537–3540. <https://doi.org/10.1103/PhysRevLett.75.3537> (1995) (cit. on pp. 4, 54).
14. Dukelsky, J., A Martin-Delgado, M., Nishino, T. & Sierra, G. Equivalence of the variational matrix product method and the density matrix renormalization group applied to spin chains. *EPL* **43**, 457–462. <https://doi.org/10.1209/epl/i1998-00381-x> (1998) (cit. on p. 4).
15. Eisert, J. & Osborne, T. J. General Entanglement Scaling Laws from Time Evolution. *Phys. Rev. Lett.* **97**, 150404. <https://doi.org/10.1103/PhysRevLett.97.150404> (2006) (cit. on p. 4).
16. Kuwahara, T. & Saito, K. Area law of noncritical ground states in 1D long-range interacting systems. *Nat Commun* **11**, 4478. <https://doi.org/10.1038/s41467-020-18055-x> (2020) (cit. on p. 4).
17. Vidal, G., Latorre, J. I., Rico, E. & Kitaev, A. Entanglement in Quantum Critical Phenomena. *Phys. Rev. Lett.* **90**, 227902. <https://doi.org/10.1103/PhysRevLett.90.227902> (2003) (cit. on pp. 4, 30).
18. Calabrese, P. & Cardy, J. L. Entanglement entropy and quantum field theory. *J. Stat. Mech.* **2004**, P06002. <https://doi.org/10.1088/1742-5468/2004/06/p06002> (2004) (cit. on pp. 4, 30, 37, 77).
19. Sachdev, S. *Quantum Phase Transitions* (Cambridge University Press, New York, 1999) (cit. on p. 4).

-
20. Holzhey, C., Larsen, F. & Wilczek, F. Geometric and renormalized entropy in conformal field theory. *Nucl. Phys. B* **424**, 443–467. [https://doi.org/10.1016/0550-3213\(94\)90402-2](https://doi.org/10.1016/0550-3213(94)90402-2) (1994) (cit. on p. 4).
 21. Essler, F. H. L. & Fagotti, M. Quench dynamics and relaxation in isolated integrable quantum spin chains. *J. Stat. Mech.* **2016**, 064002. <https://doi.org/10.1088/1742-5468/2016/06/064002> (2016) (cit. on pp. 5, 47).
 22. Calabrese, P. & Cardy, J. L. Evolution of entanglement entropy in one-dimensional systems. *J. Stat. Mech.* **2005**, P04010. <https://doi.org/10.1088/1742-5468/2005/04/p04010> (2005) (cit. on pp. 5, 30, 43, 44, 102).
 23. Fagotti, M. & Calabrese, P. Evolution of entanglement entropy following a quantum quench: Analytic results for the XY chain in a transverse magnetic field. *Phys. Rev. A* **78**, 010306. <https://doi.org/10.1103/PhysRevA.78.010306> (2008) (cit. on pp. 5, 44).
 24. Calabrese, P., Essler, F. H. L. & Mussardo, G. Introduction to ‘Quantum Integrability in Out of Equilibrium Systems’. *J. Stat. Mech.* **2016**, 064001. <https://doi.org/10.1088/1742-5468/2016/06/064001> (2016) (cit. on pp. 5, 47).
 25. Gogolin, C. & Eisert, J. Equilibration, thermalisation, and the emergence of statistical mechanics in closed quantum systems. *Rep. Prog. Phys.* **79**, 056001. <https://doi.org/10.1088/0034-4885/79/5/056001> (2016) (cit. on p. 5).
 26. Vasseur, R. & Moore, J. E. Nonequilibrium quantum dynamics and transport: from integrability to many-body localization. *J. Stat. Mech.* **2016**, 064010. <https://doi.org/10.1088/1742-5468/2016/06/064010> (2016) (cit. on pp. 5, 47).
 27. Rigol, M., Dunjko, V., Yurovsky, V. & Olshanii, M. Relaxation in a Completely Integrable Many-Body Quantum System: An Ab Initio Study of the Dynamics of the Highly Excited States of 1D Lattice Hard-Core Bosons. *Phys. Rev. Lett.* **98**, 050405. <https://doi.org/10.1103/PhysRevLett.98.050405> (2007) (cit. on pp. 5, 43).
 28. Vidmar, L. & Rigol, M. Generalized Gibbs ensemble in integrable lattice models. *J. Stat. Mech.* **2016**, 064007. <https://doi.org/10.1088/1742-5468/2016/06/064007> (2016) (cit. on pp. 5, 43).

BIBLIOGRAPHY

29. Alba, V. & Calabrese, P. Entanglement and thermodynamics after a quantum quench in integrable systems. *Proc. Natl. Acad. Sci.* **114**, 7947. <https://doi.org/10.1073/pnas.1703516114> (2017) (cit. on pp. 5, 43–45, 74, 86, 102).
30. Alba, V. & Calabrese, P. Entanglement dynamics after quantum quenches in generic integrable systems. *SciPost Phys.* **4**, 017. <https://doi.org/10.21468/SciPostPhys.4.3.017> (2018) (cit. on pp. 6, 45, 74).
31. Castro-Alvaredo, O. A., Doyon, B. & Yoshimura, T. Emergent Hydrodynamics in Integrable Quantum Systems Out of Equilibrium. *Phys. Rev. X* **6**, 041065. <https://doi.org/10.1103/PhysRevX.6.041065> (2016) (cit. on pp. 6, 25, 27, 66, 67).
32. Bertini, B., Collura, M., De Nardis, J. & Fagotti, M. Transport in Out-of-Equilibrium *XXZ* Chains: Exact Profiles of Charges and Currents. *Phys. Rev. Lett.* **117**, 207201. <https://doi.org/10.1103/PhysRevLett.117.207201> (2016) (cit. on pp. 6, 22, 24, 25, 66, 67).
33. Doyon, B. Lecture Notes On Generalised Hydrodynamics. *SciPost Phys. Lect. Notes*, 18. <https://doi.org/10.21468/SciPostPhysLectNotes.18> (2020) (cit. on pp. 6, 25).
34. Piroli, L., De Nardis, J., Collura, M., Bertini, B. & Fagotti, M. Transport in out-of-equilibrium *XXZ* chains: Nonballistic behavior and correlation functions. *Phys. Rev. B* **96**, 115124. <https://doi.org/10.1103/PhysRevB.96.115124> (2017) (cit. on pp. 6, 25).
35. Ilievski, E. & De Nardis, J. Microscopic Origin of Ideal Conductivity in Integrable Quantum Models. *Phys. Rev. Lett.* **119**, 020602. <https://doi.org/10.1103/PhysRevLett.119.020602> (2017) (cit. on pp. 6, 25).
36. Bulchandani, V. B., Vasseur, R., Karrasch, C. & Moore, J. E. Bethe-Boltzmann hydrodynamics and spin transport in the *XXZ* chain. *Phys. Rev. B* **97**, 045407. <https://doi.org/10.1103/PhysRevB.97.045407> (2018) (cit. on pp. 6, 25).
37. Collura, M., De Luca, A. & Viti, J. Analytic solution of the domain-wall nonequilibrium stationary state. *Phys. Rev. B* **97**, 081111(R). <https://doi.org/10.1103/PhysRevB.97.081111> (2018) (cit. on pp. 6, 25, 71).

38. Gopalakrishnan, S., Huse, D. A., Khemani, V. & Vasseur, R. Hydrodynamics of operator spreading and quasiparticle diffusion in interacting integrable systems. *Phys. Rev. B* **98**, 220303. <https://doi.org/10.1103/PhysRevB.98.220303> (2018) (cit. on pp. 6, 25).
39. Bastianello, A., Alba, V. & Caux, J.-S. Generalized Hydrodynamics with Space-Time Inhomogeneous Interactions. *Phys. Rev. Lett.* **123**, 130602. <https://doi.org/10.1103/PhysRevLett.123.130602> (2019) (cit. on pp. 6, 25).
40. Alba, V. Towards a generalized hydrodynamics description of Rényi entropies in integrable systems. *Phys. Rev. B* **99**, 045150. <https://doi.org/10.1103/PhysRevB.99.045150> (2019) (cit. on pp. 6, 25).
41. Ilievski, E. & De Nardis, J. Ballistic transport in the one-dimensional Hubbard model: The hydrodynamic approach. *Phys. Rev. B* **96**, 081118. <https://doi.org/10.1103/PhysRevB.96.081118> (2017) (cit. on pp. 6, 25).
42. Doyon, B., Yoshimura, T. & Caux, J.-S. Soliton Gases and Generalized Hydrodynamics. *Phys. Rev. Lett.* **120**, 045301. <https://doi.org/10.1103/PhysRevLett.120.045301> (2018) (cit. on pp. 6, 25).
43. Ljubotina, M., Žnidarič, M. & Prosen, T. Spin diffusion from an inhomogeneous quench in an integrable system. *Nat Commun* **8**, 16117. <https://doi.org/10.1038/ncomms16117> (2017) (cit. on pp. 6, 25, 46).
44. De Nardis, J., Bernard, D. & Doyon, B. Hydrodynamic Diffusion in Integrable Systems. *Phys. Rev. Lett.* **121**, 160603. <https://doi.org/10.1103/PhysRevLett.121.160603> (2018) (cit. on pp. 6, 25).
45. Nardis, J. D., Bernard, D. & Doyon, B. Diffusion in generalized hydrodynamics and quasiparticle scattering. *SciPost Phys.* **6**, 49. <https://doi.org/10.21468/SciPostPhys.6.4.049> (2019) (cit. on pp. 6, 25).
46. Borsi, M., Pozsgay, B. & Pristiyák, L. Current Operators in Bethe Ansatz and Generalized Hydrodynamics: An Exact Quantum-Classical Correspondence. *Phys. Rev. X* **10**, 011054. <https://doi.org/10.1103/PhysRevX.10.011054> (2020) (cit. on pp. 6, 25).
47. Pozsgay, B. Algebraic Construction of Current Operators in Integrable Spin Chains. *Phys. Rev. Lett.* **125**, 070602. <https://doi.org/10.1103/PhysRevLett.125.070602> (2020) (cit. on pp. 6, 25).

BIBLIOGRAPHY

48. Bertini, B., Fagotti, M., Piroli, L. & Calabrese, P. Entanglement evolution and generalised hydrodynamics: noninteracting systems. *J. Phys. A: Math. Theor.* **51**, 39LT01. <https://doi.org/10.1088/1751-8121/aad82e> (2018) (cit. on p. 6).
49. Alba, V., Bertini, B. & Fagotti, M. Entanglement evolution and generalised hydrodynamics: interacting integrable systems. *SciPost Phys.* **7**, 5. <https://doi.org/10.21468/SciPostPhys.7.1.005> (2019) (cit. on p. 6).
50. Eisler, V. & Peschel, I. Evolution of entanglement after a local quench. *J. Stat. Mech.* **2007**, P06005. <https://doi.org/10.1088/1742-5468/2007/06/P06005> (2007) (cit. on pp. 6, 45, 74, 96).
51. Calabrese, P. & Cardy, J. Entanglement and correlation functions following a local quench: a conformal field theory approach. *J. Stat. Mech.* **2007**, P10004. <https://doi.org/10.1088/1742-5468/2007/10/p10004> (2007) (cit. on pp. 6, 45, 74, 75, 96).
52. Eisler, V. & Peschel, I. Surface and bulk entanglement in free-fermion chains. *J. Stat. Mech.* **2014**, P04005. <https://doi.org/10.1088/1742-5468/2014/04/p04005> (2014) (cit. on pp. 7, 46, 75, 99).
53. Dubail, J., Stéphan, J.-M., Viti, J. & Calabrese, P. Conformal Field Theory for Inhomogeneous One-dimensional Quantum Systems: the Example of Non-Interacting Fermi Gases. *SciPost Phys.* **2**, 002. <https://doi.org/10.21468/SciPostPhys.2.1.002> (2017) (cit. on pp. 7, 46, 75, 100, 156, 157).
54. Mossel, J., Palacios, G. & Caux, J.-S. Geometric quenches in quantum integrable systems. *J. Stat. Mech.* **2010**, L09001. <https://doi.org/10.1088/1742-5468/2010/09/109001> (2010) (cit. on pp. 7, 43, 46).
55. Alba, V. & Heidrich-Meisner, F. Entanglement spreading after a geometric quench in quantum spin chains. *Phys. Rev. B* **90**, 075144. <https://doi.org/10.1103/PhysRevB.90.075144> (2014) (cit. on pp. 7, 43, 46, 70, 74, 76, 81, 82, 99).
56. White, S. R. & Feiguin, A. E. Real-Time Evolution Using the Density Matrix Renormalization Group. *Phys. Rev. Lett.* **93**, 076401. <https://doi.org/10.1103/PhysRevLett.93.076401> (2004) (cit. on pp. 7, 60, 107, 122).

-
57. Daley, A. J., Kollath, C., Schollwöck, U. & Vidal, G. Time-dependent density-matrix renormalization-group using adaptive effective Hilbert spaces. *J. Stat. Mech.* **2004**, P04005. <https://doi.org/10.1088/1742-5468/2004/04/p04005> (2004) (cit. on pp. 7, 60, 107, 122).
 58. Peschel, I. & Eisler, V. Reduced density matrices and entanglement entropy in free lattice models. *J. Phys. A: Math. Theor.* **42**, 504003. <https://doi.org/10.1088/1751-8113/42/50/504003> (2009) (cit. on pp. 7, 30, 76).
 59. Klich, I. & Levitov, L. Quantum Noise as an Entanglement Meter. *Phys. Rev. Lett.* **102**, 100502. <https://doi.org/10.1103/PhysRevLett.102.100502> (2009) (cit. on pp. 7, 8, 36, 83).
 60. Song, H. F., Rachel, S. & Le Hur, K. General relation between entanglement and fluctuations in one dimension. *Phys. Rev. B* **82**, 012405. <https://doi.org/10.1103/PhysRevB.82.012405> (2010) (cit. on pp. 7, 36, 83).
 61. Song, H. F., Flindt, C., Rachel, S., Klich, I. & Le Hur, K. Entanglement entropy from charge statistics: Exact relations for noninteracting many-body systems. *Phys. Rev. B* **83**, 161408(R). <https://doi.org/10.1103/PhysRevB.83.161408> (2011) (cit. on pp. 7, 36, 83).
 62. Calabrese, P., Mintchev, M. & Vicari, E. Exact relations between particle fluctuations and entanglement in Fermi gases. *EPL* **98**, 20003. <https://doi.org/10.1209/0295-5075/98/20003> (2012) (cit. on pp. 7, 36, 83).
 63. Song, H. F., Rachel, S., Flindt, C., Klich, I., Laflorencie, N. & Le Hur, K. Bipartite fluctuations as a probe of many-body entanglement. *Phys. Rev. B* **85**, 035409. <https://doi.org/10.1103/PhysRevB.85.035409> (2012) (cit. on pp. 8, 36, 46, 83).
 64. Eisler, V. & Peschel, I. On entanglement evolution across defects in critical chains. *EPL* **99**, 20001. <https://doi.org/10.1209/0295-5075/99/20001> (2012) (cit. on pp. 8, 46, 89, 94, 97, 101, 102).
 65. Gamayun, O., Lychkovskiy, O. & Caux, J.-S. Fredholm determinants, full counting statistics and Loschmidt echo for domain wall profiles in one-dimensional free fermionic chains. *SciPost Phys.* **8**. <https://doi.org/10.21468/SciPostPhys.8.3.036> (2020) (cit. on pp. 8, 46).

BIBLIOGRAPHY

66. Thomas, K. H. & Flindt, C. Entanglement entropy in dynamic quantum-coherent conductors. *Phys. Rev. B* **91**, 125406. <https://doi.org/10.1103/PhysRevB.91.125406> (2015) (cit. on pp. 8, 46, 97).
67. Alba, V. & Calabrese, P. Quantum information dynamics in multipartite integrable systems. *EPL* **126**, 60001. <https://doi.org/10.1209/0295-5075/126/60001> (2019) (cit. on pp. 8, 9, 35, 36, 91, 95, 103, 113).
68. Coser, A., Tonni, E. & Calabrese, P. Entanglement negativity after a global quantum quench. *J. Stat. Mech.* **2014**, P12017. <https://doi.org/10.1088/1742-5468/2014/12/p12017> (2014) (cit. on pp. 8, 35, 44).
69. Vidal, G. & Werner, R. F. Computable measure of entanglement. *Phys. Rev. A* **65**, 032314. <https://doi.org/10.1103/PhysRevA.65.032314> (2002) (cit. on pp. 8, 32, 33, 91, 106).
70. Eisler, V. & Zimborás, Z. On the partial transpose of fermionic Gaussian states. *New J. Phys.* **17**, 053048. <https://doi.org/10.1088/1367-2630/17/5/053048> (2015) (cit. on pp. 8, 33, 34, 91, 93, 110).
71. Shapourian, H., Shiozaki, K. & Ryu, S. Partial time-reversal transformation and entanglement negativity in fermionic systems. *Phys. Rev. B* **95**, 165101. <https://doi.org/10.1103/PhysRevB.95.165101> (2017) (cit. on pp. 8, 32–34, 91, 92).
72. Shapourian, H. & Ryu, S. Entanglement negativity of fermions: Monotonicity, separability criterion, and classification of few-mode states. *Phys. Rev. A* **99**, 022310. <https://doi.org/10.1103/PhysRevA.99.022310> (2019) (cit. on pp. 8, 34, 91).
73. Eisert, J., Eisler, V. & Zimborás, Z. Entanglement negativity bounds for fermionic Gaussian states. *Phys. Rev. B* **97**, 165123. <https://doi.org/10.1103/PhysRevB.97.165123> (2018) (cit. on pp. 8, 35, 93, 110).
74. Wen, X., Chang, P.-Y. & Ryu, S. Entanglement negativity after a local quantum quench in conformal field theories. *Phys. Rev. B* **92**, 075109. <https://doi.org/10.1103/PhysRevB.92.075109> (2015) (cit. on pp. 8, 35, 46, 96, 159).
75. Feldman, N. & Goldstein, M. Dynamics of charge-resolved entanglement after a local quench. *Phys. Rev. B* **100**, 235146. <https://doi.org/10.1103/PhysRevB.100.235146> (2019) (cit. on pp. 8, 35).

-
76. Eisler, V. & Zimborás, Z. Entanglement negativity in the harmonic chain out of equilibrium. *New J. Phys.* **16**, 123020. <https://doi.org/10.1088/1367-2630/16/12/123020> (2014) (cit. on pp. 8, 35).
 77. Hoogeveen, M. & Doyon, B. Entanglement negativity and entropy in non-equilibrium conformal field theory. *Nucl. Phys. B* **898**, 78–112. <https://doi.org/10.1016/j.nuclphysb.2015.06.021> (2015) (cit. on pp. 8, 35).
 78. Gullans, M. J. & Huse, D. A. Entanglement Structure of Current-Driven Diffusive Fermion Systems. *Phys. Rev. X* **9**, 021007. <https://doi.org/10.1103/PhysRevX.9.021007> (2019) (cit. on p. 8).
 79. Ruggiero, P., Alba, V. & Calabrese, P. Entanglement negativity in random spin chains. *Phys. Rev. B* **94**, 035152. <https://doi.org/10.1103/PhysRevB.94.035152> (2016) (cit. on pp. 9, 35, 107).
 80. Nozaki, M., Numasawa, T. & Takayanagi, T. Quantum Entanglement of Local Operators in Conformal Field Theories. *Phys. Rev. Lett.* **112**, 111602. <https://doi.org/10.1103/PhysRevLett.112.111602> (2014) (cit. on pp. 9, 47, 127, 128, 131).
 81. Nozaki, M. Notes on quantum entanglement of local operators. *J. High Energy Phys.* **2014**, 147. [https://doi.org/10.1007/JHEP10\(2014\)147](https://doi.org/10.1007/JHEP10(2014)147) (2014) (cit. on pp. 9, 47).
 82. He, S., Numasawa, T., Takayanagi, T. & Watanabe, K. Quantum dimension as entanglement entropy in two dimensional conformal field theories. *Phys. Rev. D* **90**, 041701. <https://doi.org/10.1103/PhysRevD.90.041701> (2014) (cit. on pp. 9, 47, 127, 128, 131).
 83. Nozaki, M., Numasawa, T. & Matsuura, S. Quantum entanglement of fermionic local operators. *J. High Energy Phys.* **2016**, 150. [https://doi.org/10.1007/JHEP02\(2016\)150](https://doi.org/10.1007/JHEP02(2016)150) (2016) (cit. on p. 9).
 84. Caputa, P. & Veliz-Osorio, A. Entanglement constant for conformal families. *Phys. Rev. D* **92**, 065010. <https://doi.org/10.1103/PhysRevD.92.065010> (2015) (cit. on pp. 9, 131).
 85. Chen, B., Gui, W., He, S. & Wu, J.-q. Entanglement entropy for descendent local operators in 2D CFTs. *J. High Energy Phys.* **2015**, 173. [https://doi.org/10.1007/JHEP10\(2015\)173](https://doi.org/10.1007/JHEP10(2015)173) (2015) (cit. on p. 9).

BIBLIOGRAPHY

86. Guo, W., He, S. & Luo, Z. Entanglement entropy in (1+1)D CFTs with multiple local excitations. *J. High Energy Phys.* **2018**, 154. [https://doi.org/10.1007/JHEP05\(2018\)154](https://doi.org/10.1007/JHEP05(2018)154) (2018) (cit. on p. 9).
87. Caputa, P., Simón, J., Štikonas, A. & Takayanagi, T. Quantum entanglement of localized excited states at finite temperature. *J. High Energy Phys.* **2015**, 102. [https://doi.org/10.1007/JHEP01\(2015\)102](https://doi.org/10.1007/JHEP01(2015)102) (2015) (cit. on pp. 9, 47).
88. Eisler, V., Maislinger, F. & Evertz, H. G. Universal front propagation in the quantum Ising chain with domain-wall initial states. *SciPost Phys.* **1**, 014. <https://doi.org/10.21468/SciPostPhys.1.2.014> (2016) (cit. on pp. 9, 47, 140, 143).
89. Zhang, J. & Calabrese, P. Subsystem distance after a local operator quench. *J. High Energ. Phys.* **56**. [https://doi.org/10.1007/JHEP02\(2020\)056](https://doi.org/10.1007/JHEP02(2020)056) (2020) (cit. on pp. 9, 47, 131).
90. Eisler, V. & Maislinger, F. Hydrodynamical phase transition for domain-wall melting in the XY chain. *Phys. Rev. B* **98**, 161117. <https://doi.org/10.1103/PhysRevB.98.161117> (16 2018) (cit. on pp. 9, 10, 47).
91. Eisler, V. & Maislinger, F. Front dynamics in the XY chain after local excitations. *SciPost Phys.* **8**, 37. <https://doi.org/10.21468/SciPostPhys.8.3.037> (2020) (cit. on pp. 9, 10, 47, 121, 139–141).
92. Takahashi, M. *Thermodynamics of One-Dimensional Solvable Models* (Cambridge University Press, Cambridge, UK, 1999) (cit. on pp. 10, 15, 18, 22, 65, 117–119).
93. Franchini, F. *An Introduction to Integrable Techniques for One-Dimensional Quantum Systems* Lecture Notes in Physics Vol. 940 (Springer, Berlin, 2017) (cit. on pp. 15, 18, 65, 69, 111, 117).
94. Baxter, R. Spontaneous staggered polarization of the F-model. *J. Stat. Phys.* **9**, 145. <https://doi.org/10.1007/BF01016845> (1973) (cit. on pp. 16, 118).
95. Izergin, A., Kitanine, N., Maillet, J. & Terras, V. Spontaneous magnetization of the XXZ Heisenberg spin-1/2 chain. *Nucl. Phys. B* **554**, 679–696. [https://doi.org/10.1016/S0550-3213\(99\)00273-4](https://doi.org/10.1016/S0550-3213(99)00273-4) (1999) (cit. on pp. 16, 118).

-
96. Bethe, H. Zur Theorie der Metalle. *Z. Physik* **71**, 205–226. <https://doi.org/10.1007/BF01341708> (1931) (cit. on p. 18).
 97. Doyon, B., Dubail, J., Konik, R. & Yoshimura, T. Large-Scale Description of Interacting One-Dimensional Bose Gases: Generalized Hydrodynamics Supersedes Conventional Hydrodynamics. *Phys. Rev. Lett.* **119**, 195301. <https://doi.org/10.1103/PhysRevLett.119.195301> (2017) (cit. on p. 25).
 98. Ruggiero, P., Calabrese, P., Doyon, B. & Dubail, J. Quantum Generalized Hydrodynamics. *Phys. Rev. Lett.* **124**, 140603. <https://doi.org/10.1103/PhysRevLett.124.140603> (2020) (cit. on p. 25).
 99. Korepin, V., Bogoliubov, N. & Izergin, A. *Quantum inverse scattering method and correlation functions* (Cambridge University Press, 1993) (cit. on p. 25).
 100. Faddeev, L. Instructive history of the quantum inverse scattering method. *Acta Appl Math* **39**, 69–84. https://doi.org/10.1007/978-94-011-0017-5_3 (1995) (cit. on p. 25).
 101. Korepin, V. E. Universality of Entropy Scaling in One Dimensional Gapless Models. *Phys. Rev. Lett.* **92**, 096402. <https://doi.org/10.1103/PhysRevLett.92.096402> (2004) (cit. on p. 30).
 102. Peschel, I. On the entanglement entropy for an XY spin chain. *J. Stat. Mech.* **2004**, P12005. <https://doi.org/10.1088/1742-5468/2004/12/p12005> (2004) (cit. on p. 30).
 103. Calabrese, P., Mintchev, M. & Vicari, E. Entanglement Entropy of One-Dimensional Gases. *Phys. Rev. Lett.* **107**, 020601. <https://doi.org/10.1103/PhysRevLett.107.020601> (2011) (cit. on p. 30).
 104. Calabrese, P. & Cardy, J. Entanglement entropy and conformal field theory. *J. Phys. A: Math. Theor.* **42**, 504005. <https://doi.org/10.1088/1751-8113/42/50/504005> (2009) (cit. on pp. 30, 37, 39, 100, 128, 157).
 105. Calabrese, P., Cardy, J. & Tonni, E. Entanglement entropy of two disjoint intervals in conformal field theory. *J. Stat. Mech.* **2009**, P11001. <https://doi.org/10.1088/1742-5468/2009/11/p11001> (2009) (cit. on pp. 30, 39, 158).
 106. Plenio, M. B. & Virmani, S. An Introduction to Entanglement Measures. *Quantum Info. Comput.* **7**, 1–51 (2007) (cit. on pp. 30, 32).

BIBLIOGRAPHY

107. Peres, A. Separability Criterion for Density Matrices. *Phys. Rev. Lett.* **77**, 1413–1415. <https://doi.org/10.1103/PhysRevLett.77.1413> (1996) (cit. on pp. 30, 33, 91).
108. Brydges, T., Elben, A., Jurcevic, P., Vermersch, B., Maier, C., Lanyon, B. P., Zoller, P., Blatt, R. & Roos, C. F. Probing Rényi entanglement entropy via randomized measurements. *Science* **364**, 260–263. <https://doi.org/10.1126/science.aau4963> (2019) (cit. on p. 32).
109. Calabrese, P. & Lefevre, A. Entanglement spectrum in one-dimensional systems. *Phys. Rev. A* **78**, 032329. <https://doi.org/10.1103/PhysRevA.78.032329> (2008) (cit. on p. 32).
110. Zyczkowski, K., Horodecki, P., Sanpera, A. & Lewenstein, M. Volume of the set of separable states. *Phys. Rev. A* **58**, 883–892. <https://doi.org/10.1103/PhysRevA.58.883> (1998) (cit. on p. 32).
111. Horodecki, M., Horodecki, P. & Horodecki, R. Separability of mixed states: necessary and sufficient conditions. *Physics Letters A* **223**, 1–8. [https://doi.org/10.1016/S0375-9601\(96\)00706-2](https://doi.org/10.1016/S0375-9601(96)00706-2) (1996) (cit. on p. 33).
112. Simon, R. Peres-Horodecki Separability Criterion for Continuous Variable Systems. *Phys. Rev. Lett.* **84**, 2726. <https://doi.org/10.1103/PhysRevLett.84.2726> (2000) (cit. on pp. 33, 91).
113. Plenio, M. B. Logarithmic Negativity: A Full Entanglement Monotone That is not Convex. *Phys. Rev. Lett.* **95**, 090503. <https://doi.org/10.1103/PhysRevLett.95.090503> (2005) (cit. on p. 33).
114. Audenaert, K., Eisert, J., Plenio, M. B. & Werner, R. F. Entanglement properties of the harmonic chain. *Phys. Rev. A* **66**, 042327. <https://doi.org/10.1103/PhysRevA.66.042327> (2002) (cit. on p. 33).
115. Herzog, C. P. & Wang, Y. Estimation for entanglement negativity of free fermions. *J. Stat. Mech.* **2016**, 073102. <https://doi.org/10.1088/1742-5468/2016/07/073102> (2016) (cit. on pp. 35, 110).
116. Wichterich, H., Molina-Vilaplana, J. & Bose, S. Scaling of entanglement between separated blocks in spin chains at criticality. *Phys. Rev. A* **80**, 010304. <https://doi.org/10.1103/PhysRevA.80.010304> (2009) (cit. on p. 35).

BIBLIOGRAPHY

117. Marcovitch, S., Retzker, A., Plenio, M. B. & Reznik, B. Critical and non-critical long-range entanglement in Klein-Gordon fields. *Phys. Rev. A* **80**, 012325. <https://doi.org/10.1103/PhysRevA.80.012325> (2009) (cit. on p. 35).
118. Ruggiero, P., Alba, V. & Calabrese, P. Negativity spectrum of one-dimensional conformal field theories. *Phys. Rev. B* **94**, 195121. <https://doi.org/10.1103/PhysRevB.94.195121> (2016) (cit. on p. 35).
119. Alba, V. Entanglement negativity and conformal field theory: a Monte Carlo study. *J. Stat. Mech.: Theor. Exp.* **2013**, P05013. <https://doi.org/10.1088/1742-5468/2013/05/p05013> (2013) (cit. on p. 35).
120. Chung, C.-M., Alba, V., Bonnes, L., Chen, P. & Läuchli, A. M. Entanglement negativity via the replica trick: A quantum Monte Carlo approach. *Phys. Rev. B* **90**, 064401. <https://doi.org/10.1103/PhysRevB.90.064401> (2014) (cit. on p. 35).
121. Calabrese, P., Cardy, J. & Tonni, E. Finite temperature entanglement negativity in conformal field theory. *J. Phys. A: Math. Theor.* **48**, 015006. <https://doi.org/10.1088/1751-8113/48/1/015006> (2014) (cit. on p. 35).
122. Cornfeld, E., Sela, E. & Goldstein, M. Measuring fermionic entanglement: Entropy, negativity, and spin structure. *Phys. Rev. A* **99**, 062309. <https://doi.org/10.1103/PhysRevA.99.062309> (2019) (cit. on p. 35).
123. Cornfeld, E., Goldstein, M. & Sela, E. Imbalance entanglement: Symmetry decomposition of negativity. *Phys. Rev. A* **98**, 032302. <https://doi.org/10.1103/PhysRevA.98.032302> (2018) (cit. on p. 35).
124. Groisman, B., Popescu, S. & Winter, A. Quantum, classical, and total amount of correlations in a quantum state. *Phys. Rev. A* **72**, 032317. <https://doi.org/10.1103/PhysRevA.72.032317> (2005) (cit. on pp. 36, 90).
125. Wolf, M. M., Verstraete, F., Hastings, M. B. & Cirac, J. I. Area Laws in Quantum Systems: Mutual Information and Correlations. *Phys. Rev. Lett.* **100**, 070502. <https://doi.org/10.1103/PhysRevLett.100.070502> (2008) (cit. on p. 36).

BIBLIOGRAPHY

126. Eisler, V. & Zimborás, Z. Area-law violation for the mutual information in a nonequilibrium steady state. *Phys. Rev. A* **89**, 032321. <https://doi.org/10.1103/PhysRevA.89.032321> (2014) (cit. on p. 36).
127. Kormos, M. & Zimborás, Z. Temperature driven quenches in the Ising model: appearance of negative Rényi mutual information. *J. Phys. A: Math. Theor.* **50**, 264005. <https://doi.org/10.1088/1751-8121/aa70f6> (2017) (cit. on pp. 36, 91).
128. Camilo, G., Landi, G. T. & Eliëns, S. Strong subadditivity of the Rényi entropies for bosonic and fermionic Gaussian states. *Phys. Rev. B* **99**, 045155. <https://doi.org/10.1103/PhysRevB.99.045155> (2019) (cit. on pp. 36, 91).
129. Cardy, J., Castro-Alvaredo, O. & Doyon, B. Form Factors of Branch-Point Twist Fields in Quantum Integrable Models and Entanglement Entropy. *J. Stat. Phys.* **130**, 129–168. <https://doi.org/10.1007/s10955-007-9422-x> (2008) (cit. on p. 39).
130. Calabrese, P., Cardy, J. & Tonni, E. Entanglement Negativity in Quantum Field Theory. *Phys. Rev. Lett.* **109**, 130502. <https://doi.org/10.1103/PhysRevLett.109.130502> (2012) (cit. on pp. 37, 40, 41, 96, 100, 158).
131. P. Calabrese, J. Cardy & E. Tonni. Entanglement negativity in extended systems: a field theoretical approach. *J. Stat. Mech.* **2013**, P02008. <https://doi.org/10.1088/1742-5468/2013/02/p02008> (2013) (cit. on pp. 37, 41, 96, 100, 158).
132. Calabrese, P., Tagliacozzo, L. & Tonni, E. Entanglement negativity in the critical Ising chain. *J. Stat. Mech.* **2013**, P05002. <https://doi.org/10.1088/1742-5468/2013/05/p05002> (2013) (cit. on p. 41).
133. Kinoshita, T., Wenger, T. & Weiss, D. A quantum Newton’s cradle. *Nature* **440**, 900–903. <https://doi.org/10.1038/nature04693> (2006) (cit. on pp. 42, 43).
134. Hofferberth, S., Lesanovsky, I., Fischer, B., Schumm, T. & Schmiedmayer, J. Non-equilibrium coherence dynamics in one-dimensional Bose gases. *Nature* **449**, 324–327. <https://doi.org/10.1038/nature06149> (2007) (cit. on p. 42).

-
135. Cheneau, M., Barmettler, P., Poletti, D., Endres, M., Schauß, P., Fukuhara, T., Gross, C., Bloch, I., Kollath, C. & Kuhr, S. Light-cone-like spreading of correlations in a quantum many-body system. *Nature* **481**, 484–487. <https://doi.org/10.1038/nature10748> (2012) (cit. on p. 42).
136. Trotzky, S., Chen, Y., Flesch, A., McCulloch, I. P., Schollwöck, U., Eisert, J. & Bloch, I. Probing the relaxation towards equilibrium in an isolated strongly correlated one-dimensional Bose gas. *Nature Phys.* **8**, 325–330. <https://doi.org/10.1038/nphys2232> (2012) (cit. on p. 42).
137. Gring, M., Kuhnert, M., Langen, T., Kitagawa, T., Rauer, B., Schreitl, M., Mazets, I., Smith, D. A., Demler, E. & Schmiedmayer, J. Relaxation and Prethermalization in an Isolated Quantum System. *Science* **337**, 1318–1322. <https://doi.org/10.1126/science.1224953> (2012) (cit. on p. 42).
138. Langen, T., Gasenzer, T. & Schmiedmayer, J. Prethermalization and universal dynamics in near-integrable quantum systems. *J. Stat. Mech.* **2016**, 064009. <https://doi.org/10.1088/1742-5468/2016/06/064009> (2016) (cit. on pp. 42, 43).
139. Calabrese, P. Entanglement spreading in non-equilibrium integrable systems. *SciPost Phys. Lect. Notes*, 20. <https://doi.org/10.21468/SciPostPhysLectNotes.20> (2020) (cit. on p. 42).
140. Caux, J.-S. & Essler, F. H. L. Time Evolution of Local Observables After Quenching to an Integrable Model. *Phys. Rev. Lett.* **110**, 257203. <https://doi.org/10.1103/PhysRevLett.110.257203> (2013) (cit. on p. 43).
141. Pozsgay, B. The generalized Gibbs ensemble for Heisenberg spin chains. *J. Stat. Mech.* **2013**, P07003. <https://doi.org/10.1088/1742-5468/2013/07/p07003> (2013) (cit. on p. 43).
142. Lieb, E. & Robinson, D. The Finite Group Velocity of Quantum Spin Systems. *Commun. Math. Phys.* **28**, 251. <https://doi.org/10.1007/BF01645779> (1972) (cit. on p. 43).
143. Eisler, V., Karevski, D., Platini, T. & Peschel, I. Entanglement evolution after connecting finite to infinite quantum chains. *J. Stat. Mech.* **2008**, P01023. <https://doi.org/10.1088/1742-5468/2008/01/p01023> (2008) (cit. on pp. 45, 74, 144).

BIBLIOGRAPHY

144. Stéphan, J.-M. & Dubail, J. Local quantum quenches in critical one-dimensional systems: entanglement, the Loschmidt echo, and light-cone effects. *J. Stat. Mech.* **2011**, P08019. <https://doi.org/10.1088/1742-5468/2011/08/P08019> (2011) (cit. on pp. 46, 74, 75, 96).
145. Gobert, D., Kollath, C., Schollwöck, U. & Schütz, G. Real-time dynamics in spin- $\frac{1}{2}$ chains with adaptive time-dependent density matrix renormalization group. *Phys. Rev. E* **71**, 036102. <https://doi.org/10.1103/PhysRevE.71.036102> (2005) (cit. on p. 46).
146. Eisler, V., Iglói, F. & Peschel, I. Entanglement in spin chains with gradients. *J. Stat. Mech.* **2009**, P02011. <https://doi.org/10.1088/1742-5468/2009/02/p02011> (2009) (cit. on pp. 46, 99, 156).
147. Mossel, J. & Caux, J.-S. Relaxation dynamics in the gapped XXZ spin- $1/2$ chain. *New J. Phys.* **12**, 055028. <https://doi.org/10.1088/1367-2630/12/5/055028> (2010) (cit. on p. 46).
148. Misguich, G., Pavloff, N. & Pasquier, V. Domain wall problem in the quantum XXZ chain and semiclassical behavior close to the isotropic point. *SciPost Phys.* **7**, 25. <https://doi.org/10.21468/SciPostPhys.7.2.025> (2019) (cit. on p. 46).
149. Gruber, M. & Eisler, V. Magnetization and entanglement after a geometric quench in the XXZ chain. *Phys. Rev. B* **99**, 174403. <https://doi.org/10.1103/PhysRevB.99.174403> (2019) (cit. on pp. 63, 99).
150. Iglói, F., Szatmári, Z. & Lin, Y.-C. Entanglement entropy with localized and extended interface defects. *Phys. Rev. B* **80**, 024405. <https://doi.org/10.1103/PhysRevB.80.024405> (2009) (cit. on p. 46).
151. Collura, M. & Calabrese, P. Entanglement evolution across defects in critical anisotropic Heisenberg chains. *J. Phys. A: Math. Theor.* **46**, 175001. <https://doi.org/10.1088/1751-8113/46/17/175001> (2013) (cit. on pp. 46, 111).
152. Vasseur, R., Trinh, K., Haas, S. & Saleur, H. Crossover Physics in the Nonequilibrium Dynamics of Quenched Quantum Impurity Systems. *Phys. Rev. Lett.* **110**, 240601. <https://doi.org/10.1103/PhysRevLett.110.240601> (2013) (cit. on p. 46).

-
153. Vasseur, R. & Saleur, H. Universal Entanglement Dynamics following a Local Quench. *SciPost Phys.* **3**, 001. <https://doi.org/10.21468/SciPostPhys.3.1.001> (2017) (cit. on p. 46).
154. Calabrese, P. & Cardy, J. Quantum quenches in 1+1 dimensional conformal field theories. *J. Stat. Mech.* **2016**, 064003. <https://doi.org/10.1088/1742-5468/2016/06/064003> (2016) (cit. on p. 47).
155. Alba, V., Fagotti, M. & Calabrese, P. Entanglement entropy of excited states. *J. Stat. Mech.* **2009**, P10020. <https://doi.org/10.1088/1742-5468/2009/10/p10020> (2009) (cit. on pp. 47, 120).
156. Mölter, J., Barthel, T., Schollwöck, U. & Alba, V. Bound states and entanglement in the excited states of quantum spin chains. *J. Stat. Mech.* **2014**, P10029. <https://doi.org/10.1088/1742-5468/2014/10/p10029> (2014) (cit. on pp. 47, 120).
157. Caputa, P. & Rams, M. M. Quantum dimensions from local operator excitations in the Ising model. *J. Phys. A: Math. Theor.* **50**, 055002. <https://doi.org/10.1088/1751-8121/aa5202> (2017) (cit. on p. 47).
158. Schuch, N., Wolf, M. M., Verstraete, F. & Cirac, J. I. Entropy Scaling and Simulability by Matrix Product States. *Phys. Rev. Lett.* **100**, 030504. <https://doi.org/10.1103/PhysRevLett.100.030504> (2008) (cit. on p. 53).
159. Verstraete, F. & Cirac, J. I. Matrix product states represent ground states faithfully. *Phys. Rev. B* **73**, 094423. <https://doi.org/10.1103/PhysRevB.73.094423> (2006) (cit. on p. 53).
160. Peschel, I., Kaulke, M. & Legeza, Ö. Density-matrix spectra for integrable models. *Annalen der Physik* **8**, 153–164. [https://doi.org/10.1002/\(SICI\)1521-3889\(199902\)8:2%3C153::AID-ANDP153%3E3.0.CO;2-N](https://doi.org/10.1002/(SICI)1521-3889(199902)8:2%3C153::AID-ANDP153%3E3.0.CO;2-N) (1999) (cit. on pp. 53, 56, 136).
161. Okunishi, K., Hieida, Y. & Akutsu, Y. Universal asymptotic eigenvalue distribution of density matrices and corner transfer matrices in the thermodynamic limit. *Phys. Rev. E* **59**, R6227–R6230. <https://doi.org/10.1103/PhysRevE.59.R6227> (1999) (cit. on pp. 53, 56).

BIBLIOGRAPHY

162. Cirac, J. I. & Verstraete, F. Renormalization and tensor product states in spin chains and lattices. *J. Phys. A: Math. Theor.* **42**, 504004. <https://doi.org/10.1088/1751-8113/42/50/504004> (2009) (cit. on p. 54).
163. Ganahl, M. J. *Dynamics of One Dimensional, Strongly Correlated Quantum Systems using Matrix Product States* PhD thesis (TU Graz, 2014) (cit. on p. 56).
164. Vidal, G. Efficient Classical Simulation of Slightly Entangled Quantum Computations. *Phys. Rev. Lett.* **91**, 147902. <https://doi.org/10.1103/PhysRevLett.91.147902> (2003) (cit. on p. 60).
165. Paeckel, S., Köhler, T., Swoboda, A., Manmana, S. R., Schollwöck, U. & Hubig, C. Time-evolution methods for matrix-product states. *Annals of Physics* **411**, 167998. <https://doi.org/10.1016/j.aop.2019.167998> (2019) (cit. on p. 60).
166. Giamarchi, T. *Quantum Physics in One Dimension* (Clarendon Press, Oxford, 2003) (cit. on pp. 16, 36, 65, 127).
167. Atkinson, K. E. & Shampine, L. F. Algorithm 876: Solving Fredholm Integral Equations of the Second Kind in Matlab. *ACM Trans. Math. Softw.* **34**, 21:1–21:20. <https://doi.org/10.1145/1377596.1377601> (2008) (cit. on p. 66).
168. Fishman, M., White, S. R. & Stoudenmire, E. M. *The ITensor Software Library for Tensor Network Calculations* 2020. arXiv: 2007.14822 (cit. on pp. 66, 107, 122).
169. Eisler, V. & Bauernfeind, D. Front dynamics and entanglement in the XXZ chain with a gradient. *Phys. Rev. B* **96**, 174301. <https://doi.org/10.1103/PhysRevB.96.174301> (2017) (cit. on p. 70).
170. Bulchandani, V. B. & Karrasch, C. Subdiffusive front scaling in interacting integrable models. *Phys. Rev. B* **99**, 121410. <https://doi.org/10.1103/PhysRevB.99.121410> (2019) (cit. on pp. 71, 86).
171. Stéphan, J.-M. Free fermions at the edge of interacting systems. *SciPost Phys.* **6**, 57. <https://doi.org/10.21468/SciPostPhys.6.5.057> (2019) (cit. on pp. 71, 72, 86).

-
172. Antal, T., Rácz, Z., Rákos, A. & Schütz, G. M. Transport in the XX chain at zero temperature: Emergence of flat magnetization profiles. *Phys. Rev. E* **59**, 4912. <https://doi.org/10.1103/PhysRevE.59.4912> (1999) (cit. on p. 74).
173. Antal, T., Krapivsky, P. L. & Rákos, A. Logarithmic current fluctuations in nonequilibrium quantum spin chains. *Phys. Rev. E* **78**, 061115. <https://doi.org/10.1103/PhysRevE.78.061115> (2008) (cit. on pp. 74, 83).
174. Allegra, N., Dubail, J., Stéphan, J. & Viti, J. Inhomogeneous field theory inside the arctic circle. *J. Stat. Mech.* **2016**, 053108. <https://doi.org/10.1088/1742-5468/2016/05/053108> (2016) (cit. on pp. 75, 85, 156).
175. Eisler, V., Legeza, Ö. & Rácz, Z. Fluctuations in subsystems of the zero-temperature XX chain: emergence of an effective temperature. *J. Stat. Mech.* **2006**, P11013. <https://doi.org/10.1088/1742-5468/2006/11/p11013> (2006) (cit. on p. 83).
176. Schönhammer, K. Full counting statistics for noninteracting fermions: Exact results and the Levitov-Lesovik formula. *Phys. Rev. B* **75**, 205329. <https://doi.org/10.1103/PhysRevB.75.205329> (2007) (cit. on p. 83).
177. Eisler, V. & Rácz, Z. Full Counting Statistics in a Propagating Quantum Front and Random Matrix Spectra. *Phys. Rev. Lett.* **110**, 060602. <https://doi.org/10.1103/PhysRevLett.110.060602> (2013) (cit. on pp. 86, 99, 100).
178. Viti, J., Stéphan, J.-M., Dubail, J. & Haque, M. Inhomogeneous quenches in a free fermionic chain: Exact results. *EPL* **115**, 40011. <https://doi.org/10.1209/0295-5075/115/40011> (2016) (cit. on pp. 86, 100).
179. Perfetto, G. & Gambassi, A. Ballistic front dynamics after joining two semi-infinite quantum Ising chains. *Phys. Rev. E* **96**, 012138. <https://doi.org/10.1103/PhysRevE.96.012138> (2017) (cit. on p. 86).
180. Kormos, M. Inhomogeneous quenches in the transverse field Ising chain: scaling and front dynamics. *SciPost Phys.* **3**, 020. <https://doi.org/10.21468/SciPostPhys.3.3.020> (2017) (cit. on p. 86).
181. Fagotti, M. Higher-order generalized hydrodynamics in one dimension: The noninteracting test. *Phys. Rev. B* **96**, 220302(R). <https://doi.org/10.1103/PhysRevB.96.220302> (2017) (cit. on pp. 86, 100).

BIBLIOGRAPHY

182. Tracy, C. A. & Widom, H. Level-spacing distributions and the Airy kernel. *Commun. Math. Phys.* **159**, 151. <https://doi.org/10.1007/BF02100489> (1994) (cit. on p. 86).
183. Gruber, M. & Eisler, V. Time evolution of entanglement negativity across a defect. *J. Phys. A: Math. Theor.* **53**, 205301. <https://doi.org/10.1088/1751-8121/ab831c> (2020) (cit. on p. 87).
184. Fagotti, M. & Calabrese, P. Universal parity effects in the entanglement entropy of XX chains with open boundary conditions. *J. Stat. Mech.* **2011**, P01017. <https://doi.org/10.1088/1742-5468/2011/01/p01017> (2011) (cit. on p. 90).
185. Shapourian, H., Ruggiero, P., Ryu, S. & Calabrese, P. Twisted and untwisted negativity spectrum of free fermions. *SciPost Phys.* **7**, 37. <https://doi.org/10.21468/SciPostPhys.7.3.037> (2019) (cit. on p. 93).
186. Wen, X., Wang, Y. & Ryu, S. Entanglement evolution across a conformal interface. *J. Phys. A: Math. Theor.* **51**, 195004. <https://doi.org/10.1088/1751-8121/aab561> (2018) (cit. on pp. 94, 97, 113).
187. Peschel, I. Entanglement entropy with interface defects. *J. Phys. A: Math. Gen.* **38**, 4327–4335. <https://doi.org/10.1088/0305-4470/38/20/002> (2005) (cit. on pp. 94, 96, 153, 154).
188. Eisler, V. & Peschel, I. Entanglement in fermionic chains with interface defects. *Ann. Phys. (Berlin)* **522**, 679. <https://doi.org/10.1002/andp.201000055> (2010) (cit. on p. 94).
189. Peschel, I. & Eisler, V. Exact results for the entanglement across defects in critical chains. *J. Phys. A: Math. Theor.* **45**, 155301. <https://doi.org/10.1088/1751-8113/45/15/155301> (2012) (cit. on pp. 94, 95).
190. Ossipov, A. Entanglement Entropy in Fermi Gases and Anderson’s Orthogonality Catastrophe. *Phys. Rev. Lett.* **113**, 130402. <https://doi.org/10.1103/PhysRevLett.113.130402> (2014) (cit. on p. 95).
191. Asplund, C. T. & Bernamonti, A. Mutual information after a local quench in conformal field theory. *Phys. Rev. D* **89**, 066015. <https://doi.org/10.1103/PhysRevD.89.066015> (2014) (cit. on p. 96).

-
192. Vidmar, L., Iyer, D. & Rigol, M. Emergent Eigenstate Solution to Quantum Dynamics Far from Equilibrium. *Phys. Rev. X* **7**, 021012. <https://doi.org/10.1103/PhysRevX.7.021012> (2017) (cit. on pp. 99, 156).
193. Bastianello, A., Dubail, J. & Stéphan, J.-M. Entanglement entropies of inhomogeneous Luttinger liquids. *J. Phys. A: Math. Theor.* **53**, 155001. <https://doi.org/10.1088/1751-8121/ab7580> (2020) (cit. on p. 100).
194. Ljubotina, M., Sotiriadis, S. & Prosen, T. Non-equilibrium quantum transport in presence of a defect: the non-interacting case. *SciPost Phys.* **6**, 004. <https://doi.org/10.21468/SciPostPhys.6.1.004> (2019) (cit. on pp. 104, 153, 154).
195. Zhao, J., Peschel, I. & Wang, X. Critical entanglement of XXZ Heisenberg chains with defects. *Phys. Rev. B* **73**, 024417. <https://doi.org/10.1103/PhysRevB.73.024417> (2006) (cit. on p. 112).
196. Kane, C. L. & Fisher, M. P. A. Transmission through barriers and resonant tunneling in an interacting one-dimensional electron gas. *Phys. Rev. B* **46**, 15233–15262. <https://doi.org/10.1103/PhysRevB.46.15233> (1992) (cit. on p. 112).
197. Coser, A., Tonni, E. & Calabrese, P. Partial transpose of two disjoint blocks in XY spin chains. *J. Stat. Mech.* **2015**, P08005. <https://doi.org/10.1088/1742-5468/2015/08/p08005> (2015) (cit. on p. 113).
198. Gruber, M. & Eisler, V. *Entanglement spreading after local fermionic excitations in the XXZ chain* 2020. arXiv: 2010.02708 (cit. on p. 115).
199. De Paula, A. L., Bragança, H., Pereira, R. G., Drumond, R. C. & Aguiar, M. C. O. Spinon and bound-state excitation light cones in Heisenberg XXZ chains. *Phys. Rev. B* **95**, 045125. <https://doi.org/10.1103/PhysRevB.95.045125> (2017) (cit. on p. 118).
200. Alcaraz, F. C., Berganza, M. I. & Sierra, G. Entanglement of Low-Energy Excitations in Conformal Field Theory. *Phys. Rev. Lett.* **106**, 201601. <https://doi.org/10.1103/PhysRevLett.106.201601> (2011) (cit. on p. 120).
201. Berganza, M. I., Alcaraz, F. C. & Sierra, G. Entanglement of excited states in critical spin chains. *J. Stat. Mech.* **2012**, P01016. <https://doi.org/10.1088/1742-5468/2012/01/p01016> (2012) (cit. on p. 120).

BIBLIOGRAPHY

202. Castro-Alvaredo, O. A., De Fazio, C., Doyon, B. & Szécsényi, I. M. Entanglement Content of Quasiparticle Excitations. *Phys. Rev. Lett.* **121**, 170602. <https://doi.org/10.1103/PhysRevLett.121.170602> (2018) (cit. on p. 120).
203. Castro-Alvaredo, O. A., De Fazio, C., Doyon, B. & Szécsényi, I. M. Entanglement content of quantum particle excitations. Part I. Free field theory. *J. High Energy Phys.* **2018**, 39. [https://doi.org/10.1007/JHEP10\(2018\)039](https://doi.org/10.1007/JHEP10(2018)039) (2018) (cit. on p. 120).
204. Sénéchal, D. *An introduction to bosonization* 139–186 (Springer, New York, 2004) (cit. on p. 126).
205. Francesco, P., Mathieu, P. & Sénéchal, D. *Conformal Field Theory* (Springer, New York, 1997) (cit. on p. 130).
206. Calabrese, P., Cardy, J. & Peschel, I. Corrections to scaling for block entanglement in massive spin chains. *J. Stat. Mech.* **2010**, P09003. <https://doi.org/10.1088/1742-5468/2010/09/p09003> (2010) (cit. on p. 136).
207. Zauner, V., Ganahl, M., Evertz, H. G. & Nishino, T. Time evolution within a comoving window: scaling of signal fronts and magnetization plateaus after a local quench in quantum spin chains. *J. Phys.: Condens. Matter* **27**, 425602. <https://doi.org/10.1088/0953-8984/27/42/425602> (2015) (cit. on p. 139).
208. Iorgov, N., Shadura, V. & Tykhyy, Y. Spin operator matrix elements in the quantum Ising chain: fermion approach. *J. Stat. Mech.* **2011**, P02028. <https://doi.org/10.1088/1742-5468/2011/02/p02028> (2011) (cit. on p. 140).
209. Iorgov, N. Form factors of the finite quantum XY-chain. *J. Phys. A: Math. Theor.* **44**, 335005. <https://doi.org/10.1088/1751-8113/44/33/335005> (2011) (cit. on p. 140).
210. Kitanine, N., Maillet, J. & Terras, V. Form factors of the XXZ Heisenberg spin-1/2 finite chain. *Nucl. Phys. B* **554**, 647–678. [https://doi.org/10.1016/S0550-3213\(99\)00295-3](https://doi.org/10.1016/S0550-3213(99)00295-3) (1999) (cit. on p. 140).

-
211. Dugave, M., Göhmann, F., Kozłowski, K. K. & Suzuki, J. On form-factor expansions for the XXZ chain in the massive regime. *J. Stat. Mech.* **2015**, P05037. <https://doi.org/10.1088/1742-5468/2015/05/p05037> (2015) (cit. on p. 140).
 212. Vlijm, R. & Caux, J.-S. Spinon dynamics in quantum integrable antiferromagnets. *Phys. Rev. B* **93**, 174426. <https://doi.org/10.1103/PhysRevB.93.174426> (2016) (cit. on p. 140).
 213. Perk, J. & Capel, H. Time-dependent xx-correlation functions in the one-dimensional XY-model. *Physica A* **89**, 265–303. [https://doi.org/10.1016/0378-4371\(77\)90105-4](https://doi.org/10.1016/0378-4371(77)90105-4) (1977) (cit. on p. 143).
 214. Perk, J., Capel, H. & Siskens, T. Time correlation functions and ergodic properties in the alternating XY-chain. *Physica A* **89**, 304–325. [https://doi.org/10.1016/0378-4371\(77\)90106-6](https://doi.org/10.1016/0378-4371(77)90106-6) (1977) (cit. on p. 143).
 215. Peschel, I. & Schotte, K. Time correlations in quantum spin chains and the X-ray absorption problem. *Z. Phys. B* **54**, 305–311. <https://doi.org/10.1007/BF01485827> (1984) (cit. on p. 143).
 216. Turban, L. Exactly solvable spin-1/2 quantum chains with multispin interactions. *Phys. Lett. A* **104**, 435–437. [https://doi.org/10.1016/0375-9601\(84\)90751-5](https://doi.org/10.1016/0375-9601(84)90751-5) (1984) (cit. on p. 143).
 217. Casini, H., Fosco, C. D. & Huerta, M. Entanglement and alpha entropies for a massive Dirac field in two dimensions. *J. Stat. Mech.* **2005**, P07007. <https://doi.org/10.1088/1742-5468/2005/07/p07007> (2005) (cit. on pp. 158, 159).